Dissertation zur Erlangung des Doktorgrades
der Fakultät für Chemie und Pharmazie
der Ludwig-Maximilians-Universität München

Targeted delivery of magnetic nanocarriers for characterization and therapy in gastro-intestinal cancers

Isabella Stefanie Almstätter geb. Siebert

aus

Gräfelfing, Deutschland

2018

Erklärung

Diese Dissertation wurde im Sinne von §7 der Promotionsordnung vom 29. Januar 1998, zuletzt geändert durch Satzung von 16. August 2010 von Herrn Professor Christian Plank betreut und von Professor Ernst Wagner von der Fakultät für Chemie und Pharmazie vertreten.

Eidesstattliche Versicherung

Diese Dissertation wurde eigenständig und ohne unerlaubte Hilfe erarbeitet.

München, 29. Mai 2018

Isabella Almstätter

Dissertation eingereicht am	12. März 2018
1. Gutachter:	Prof. Ernst Wagner
2. Gutachter:	Prof. Christian Plank
Mündliche Prüfung am	03. Mai 2018

For our beloved Christa

Even the strongest cannot defeat this beast of a cancer.

INDEX

LIST OF FIGURES

LIST OF TABLES

LIST OF ABBREVIATIONS

181P cells	parental human pancreatic adenocarcinoma cells
°C	degrees centigrade
Ad	adenovirus
AFP	alpha-fetoprotein
AMF	alternating magnetic field
ATP	adenosine triphosphate
B_0	constant magnetic field
BHK-21 cells	baby hamster kidney cells
BL/6	C57 black 6 inbred mouse strain (C57BL/6 mouse) widely used as genetic background for genetically engineered mice [1]
BSA	bovine serum albumin
$CaCl_2$	calcium chloride
CAR	coxsackie and adenovirus receptor
$CHCl_3$	chloroform
Chol	cholesterol
CKp53lox mice	$Ptf1\alpha^{wt/Cre}$; $Kras^{wt/LSL\text{-}G12D}$; $p53^{fl/fl}$ mice
cm	centimeter
cm^2	square centimeter
CO_2	carbon dioxide
CPM	counts per minute
CsCl	cesium chloride
CT	computed tomography
ddH_2O	double distilled water
DF-Gold	Dreamfect Gold
DMEM	Dulbecco's Modified Eagle's Medium
DMSO	dimethyl sulfoxide
DOPC	1,2-dioleyl-*sn*-glycero-3-phosphocholine
DOPE	1,2-dioleyl-*sn*-glycero-3-phosphoethanolamine
DOX	doxorubicin
DPPC	1,2-dipalmitoyl-*sn*-glycero-3-phosphocholine
DSPC	1,2-distearoyl-*sn*-glycero-3-phosphocholine
DTT	dithiothreitol
EDTA	ethylene-diamine-tetra-acetic acid
eGFP	enhanced green fluorescent protein
EGFR	epidermal growth factor receptor
EPC	endothelial progenitor cell
EPP85-181P	parental human pancreatic adenocarcinoma cells
EPP85-181RDB	MDR human pancreatic adenocarcinoma cells
EPR	enhanced permeability and retention
ERCP	endoscopic retrograde cholangiopancreatography
EUS	endoscopic ultrasound
EYPC	egg yolk phosphatidylcholine

FCS	fetal calf serum
FDG	fluorine-18-2-fluoro-2-deoxy-D-glucose
Fe	iron
FFE	fast field echo
fg	femtogram
FLT	fluorine-18-2-fluorothymidine
FOV	field of view
FU	fluorouracil
g	gram
Gd	gadolinium
Gd-DTPA	gadopentetic acid
GFP	green fluorescent protein
GMEM	Glasgow's Modified Eagle's Medium
H_2SO_4	sulfuric acid
HCC	hepatocellular carcinoma
HCl	hydrochloric acid
Hep-B/C	hepatitis B/C
HepG2 cells	human hepatocellular carcinoma cell line
HSPC	hydrogenated soy L-α-phosphatidylcholine
HuH-7 cells	human hepatocellular carcinoma cell line
IC_{50}	antagonist dose that causes 50 % growth inhibition
IRE	irreversible electroporation
K	degree Kelvin
kb	kilobases
KD	knock-down
kDa	kilo Dalton
kg	kilogram
kGy	kilo Gray
kHz	kilo Hertz
$KMnO_4$	potassium permanganate
λ	wavelength
LP	liposome
Luc	luciferase
LV	lentivirus
m	meter
M	molar
McA cells	McA-RH7777 Morris hepatocellular carcinoma cells
MDR	multi-drug resistant
MeOH	methanol
MF	magnetic fraction
$MgCl_2$	magnesium chloride
mL	milliliter
mm	millimeter
mmol	millimol

mM	milli molar
MNP	magnetic nanoparticle
MNP-LP	magnetic liposome
MNP-siRNA	magnetic siRNA complex
MNP-VP	magnetic viral complex
MOI	multiplicity of infection
mol	Mol
MR	magnetic resonance
MRI	magnetic resonance imaging
mRNA	messenger RNA
M_s	saturation magnetization
ms	millisecond(s)
MSPC	1-(mono)stearoyl-*sn*-glycero-3-phosphocholine
mT	milli Tesla
MTT	3-(4,5-dimethylthiazole-2-yl)-2,5-diphenyltetrazoliumbromide
M_W	molecular weight
MWA	microwave ablation
μL	microliter
μM	micro molar
NaCl	sodium chloride
NaOH	sodium hydroxide
Ni	nickel
nm	nanometer
NMF	non-magnetic fraction
NMR	nuclear magnetic resonance
OCT4	octamer-binding transcription factor 4
OD	optical density
PALD2-Mag	palmitoyldextran-coated magnetic nanoparticles
PBS	phosphate-buffered saline
PBS-T	phosphate-buffered saline with Tween
PDAC	pancreatic ductal adenocarcinoma
pDNA	plasmid DNA
PEG	polyethylene glycol
PEI	polyethylene imine
PEI-Mag	PEI-coated magnetic nanoparticles
PET	positron emission tomography
PFA	paraformaldehyde
pfu	plaque forming unit
pg	picogram
PGK (promoter)	phosphoglycerate kinase (promoter)
pH	potential of hydrogen
PTC	percutaneous transhepatic cholangiography
PTX	paclitaxel
R_2 / R_2^*	relaxation rate

r_2 / r_2^*	relaxivity
RDB cells	MDR human pancreatic carcinoma cells EPP85-181RDB
RES	reticulo-endothelial system
REV	reverse phase evaporation
RFA	radio frequency ablation
RGD	arginine-glycine-aspartate tripeptide
RNA	ribonucleic acid
RNAi	RNA interference
ROI	region of interest
rpm	rounds per minute
RT	room temperature
SD	standard deviation
SDS	sodium dodecyl sulfate
siRNA	small interfering RNA
SO-Mag	silicium oxide-coated magnetic nanoparticles
SPECT	single photon emission computed tomography
SPIO	superparamagnetic iron oxide
T	tesla
T_1	relaxation time (longitudinal magnetization)
T_2 / T_2^*	relaxation time (transverse magnetization)
T_2w / T_2^*w	T_2- / T_2^*-weighted
T75	cell culture flask of 75 cm^2
TACE	trans-arterial chemoembolization
TE	echo time
T_R	repetition time
$TCID_{50}$	tissue culture infectious dose 50
TEM	transmission electron microscope
TFH	thin film hydration
US	ultrasound
USPIO	ultrasmall superparamagnetic iron oxide
VP	virus particle
VSV	vesicular stomatitis virus
wt	wildtype
wt%	weight percent
w/w	weight ratio
Zonyl® FSA	lithium 3-[2-(perfluoroalkyl)ethylthio]propionate
Zonyl® FSE	ammonium bis[2-(perfluoroalkyl)ethyl]phosphate
ζ	zeta

ABSTRACT

Magnetic nanocarriers are widely explored for improved treatment of diseases like cancer. Their magnetic properties allow for magnetic targeting upon external magnetic field exposure, and in parallel, the nanocarriers can be monitored non-invasively *in vivo* via magnetic resonance imaging (MRI).

Nanocarrier formulations can be tailored regarding application-specific needs. In pre-clinical studies, various viral and non-viral vector systems were already successfully functionalized with target tissue-specific binding moieties, and (co-)loaded with for example nucleic acids or chemotherapeutic drugs. Such active targeting approaches, and the stabilizing and shielding properties of assembled and functionalized complexes help to overcome low delivery rates and reduce unspecific cell uptake compared to conventional therapies.

Nanocarrier systems examined in this study were magnetic complexes with oncolytic viruses, magnetic small interfering ribonucleic acid (siRNA) complexes, and magnetic liposomes.

Core component of all investigated nanocarrier formulations were selected core-shell type magnetic nanoparticles (MNPs). The MNPs assembled with virus particles and siRNA were cationic, the MNPs encapsulated in the magnetic liposomes anionic, enabling electrostatic interactions.

The different magnetic nanocarrier formulations were analyzed regarding their physico-chemical properties such as hydrodynamic diameter, electrokinetic (or zeta) potential, magnetophoretic mobility (magnetic responsiveness) and the stability in the presence of serum. In all regards, they were comparable to formulations presented by other groups.

Transmission electron microscopy (TEM) was used to elucidate the structure of magnetic viral complexes and their intracellular compartmentalization. We proved the assumed layering of MNPs around the virus particles as well as endosomal cell uptake. Based on promising oncolytic potential *in vitro*, especially in the presence of serum and an external magnetic field, we tested the viral complexes in a proof-of-principle *in vivo* study in a rodent model and could show successful magnetic targeting within an orthotopic tumor lesion and efficient virus replication.

With regard to clinical application of such formulations and to identify the influence of compartmentalization on the MRI contrast properties quantitatively, MNPs and magnetic complexes were examined *in vitro* using tissue-mimicking agarose gel phantoms. The chosen MNPs possessed high r_2 und r_2^* relaxivities, and could be detected over the liver-mimicking background even at very low concentrations of 1 μM iron (10^4 cells labeled at 5 pg Fe/cell) with field-independent (1.5 T and 3.0 T) linear dependency of relaxation rate and iron concentration.

Self-assemblies of siRNA and MNPs were analyzed in a proof-of-concept gene-silencing set-up. Gastro-intestinal cancer cell lines were stably transduced with a luciferase-GFP construct as reporter genes and their down-regulation after magnetofection with magnetic complexes carrying anti-luciferase or anti-GFP siRNA was validated.
On this basis, in future approaches, such siRNA complexes could be used for the knock-down of for example oncogenes.

In *in vitro* experiments such as cell labeling and cell viability evaluation, the MNPs chosen for liposome synthesis performed well. To attest their biocompatibility, we evaluated the toxicity of the MNPs *in vivo* in mice. No negative changes hindering further approaches could be detected.
Hence, we assessed different liposome synthesis protocols and compared the resulting magnetic liposomes regarding their physico-chemical characteristics. Thin film hydration and injection method emerged as methods of choice. First *in vivo* experiments in wildtype and tumor-bearing mice demonstrated the capability of magnetic targeting and provided a biodistribution profile with no pathologic alterations due to accumulated liposomes.

ZUSAMMENFASSUNG

Magnetische Nanocarrier sind seit einiger Zeit im Fokus der Forschung, da sie die Lieferung von therapeutischen Formulierungen in ein Zielgewebe verbessern können. Ihre magnetischen Eigenschaften ermöglichen magnetisches Targeting, sobald ein externes Magnetfeld angelegt wird. Gleichzeitig kann der Weg der Nanocarrier *in vivo* nicht-invasiv mittels Magnetresonanztomographie (MRT) verfolgt werden.
Durch anwendungs-spezifische Modifizierungen können solche Nanocarrier-Formulierungen maßgeschneidert werden. Zahlreiche virale und nicht-virale Vektorsysteme wurden in präklinischen Studien bereits erfolgreich mit Zielstruktur-spezifischen Bindungsmolekülen versehen, und konnten zum Beispiel mit Nukleinsäuren oder Chemotherapeutika beladen werden. Ziel solcher aktiven Targeting-Ansätze ist es, die Konzentration der Formulierung am Zielgewebe zu erhöhen. Gleichzeitig können so im Vergleich zu konventionellen Therapien auch Nebenwirkungen durch unspezifische Aufnahme in Nicht-Zielstrukturen verringert werden, auch durch den stabilisierenden und abschirmenden Einfluss der Komplex-Bildung.

Die in dieser Studie untersuchten Nanocarrier-Formulierungen waren Magnetpartikel-Komplexe mit onkolytischen Viren und kleinen eingreifenden (small interfering) Ribonukleinsäuren (siRNA), sowie magnetische Liposomen.
Essentieller Bestandteil aller Formulierungen waren ausgewählte magnetische Kern-Hülle Nanopartikel (magnetic nanoparticles MNPs). Die MNPs in den Komplexen mit Viruspartikeln und siRNA waren positiv, die in den magnetischen Liposomen negativ geladen, das erlaubte die Ausbildung elektrostatischer Wechselwirkungen.
Die verschiedenen magnetischen Nanocarrier-Formulierungen wurden bezüglich ihrer physikalisch-chemischen Eigenschaften wie den hydrodynamischen Durchmessern und elektrokinetischen (oder zeta) Potentialen, der magnetophoretischen Mobilität, und der Stabilität in Anwesenheit von Serum untersucht. Hierbei zeigten sie vergleichbare Eigenschaften wie die Formulierungen anderer Gruppen.

Mittels Transmissions-Elektronenmikroskopie (TEM) wurde die Struktur sowie die intrazelluläre Kompartmentalisierung der magnetischen Viruskomplexe untersucht. So konnte die Umhüllung der Viruspartikel mit Schichten von MNPs und ihre intrazelluläre Akkumulation in Endosomen bestätigt werden. *In vitro* wiesen sich die Komplexe durch ein hohes onkolytisches Potential aus, besonders in der Anwesenheit von Serum und externem magnetischen Feld. Daraufhin wurde eine Proof-of-Principle-Studie *in vivo* in einem Nagermodell durchgeführt, und das erfolgreiche magnetische Targeting innerhalb einer orthotopen Tumorläsion, sowie die anschließende effiziente Virusreplikation gezeigt.
Im Hinblick auf die diagnostische Anwendung und um den Einfluss der Kompartmentalisierung auf MRT-Kontrasteigenschaften quantitativ zu untersuchen, wurden die MNPs und ihre Komplexe *in vitro* in gewebeähnlichen Agarosegel-Phantomen untersucht. Die untersuchten MNPs wiesen hohe r_2 und r_2^* Relaxivitäten auf, und die Nachweisgrenze in diesen Lebergewebe-nachahmenden Phantomen lag bei unter 1 μM

Eisen (10^4 Zellen markiert mit 5 pg Fe/Zelle). Die lineare Abhängigkeit von Relaxationsrate und Eisenkonzentration war dabei Feldstärken-unabhängig (1.5 und 3.0 T).

In einem Proof-of-Concept-Ansatz wurden selbst-assemblierte MNP-siRNA-Komplexe für die Anwendung im Gene-Silencing, der gezielten Abschaltung einzelner Gene, untersucht. Gastro-intestinale Zelllinien wurden zunächst mit einem Luciferase-GFP-Konstrukt als Reportergene stabil transduziert, um anschließend durch deren Herunter-Regulation die erfolgreiche Magnetofection mit anti-Luciferase- oder anti-GFP-siRNA-beladenen magnetischen Komplexen nachzuweisen.
Auf dieser Basis können in zukünftigen Ansätzen solche siRNA-Komplexe zum Beispiel genutzt werden für das gezielte Abschalten von Onkogenen.

In *in vitro* Versuchen wie Zellmarkierung und Vitalitätsprüfung zeigten die ausgewählten MNPs gute Ergebnisse. Um auch ihre Biokompatibilität zu bestätigen, wurden sie *in vivo* in Mäusen auf ihre Toxizität hin untersucht und es konnten keine negativen Auswirkungen festgestellt werden.
Daraufhin wurde die MNPs in verschiedenen Liposom-Synthese-Protokollen verwendet und diese bezüglich ihrer physikalisch-chemischen Eigenschaften untersucht. Auf dieser Basis wurden die Dünnschicht-Hydrierung (thin film hydration) und eine Injektionsmethode als Methoden der Wahl ausgewählt. In ersten *in vivo* Experimenten in Wildtypmäusen und Mäusen mit Tumorläsionen zeigten sich die Liposomen als geeignet für magnetisches Targeting und es konnten keine pathologischen Gewebeveränderungen nach der Liposomenakkumulation festgestellt werden.

1 INTRODUCTION

1.1 Gastro-intestinal cancers

Among estimated new gastro-intestinal cancer cases and cancer-related deaths for the year 2017, pancreatic cancer, in most cases pancreatic ductal adenocarcinoma (PDAC), and primary liver cancer, predominantly hepatocellular carcinoma (HCC), rank on the positions 2 and 3, and the incidences are expected to further rise [2, 3]. So it is of upmost urgency to improve diagnosis and the existing treatment options. Both tumor types share diagnosis in advanced cancer stages, resulting in reduced chance for curative surgical removal of the lesions. In palliative approaches both cancers do not respond well to systemically administered chemotherapeutics and other therapy approaches are limited.

Less than 15 % of HCC patients are curable by liver transplantation, surgical tumor resection, or ablation [4]. The overall resectability rates in PDAC patients are below 20 % at the time of diagnosis [5-7]. Of the as resectable classified PDAC patients, further 30 % emerge as non-resectable after staging laparoscopy due to peritoneal carcinosis [8]. The German incidence (figure 1A) and mortality rates (figure 1B) for HCC and PDAC as well as the survival for ten years after the first diagnosis of liver (figure 1C) and pancreatic cancer (figure 1D) are plotted in figure 1 (modified from [9-11]).

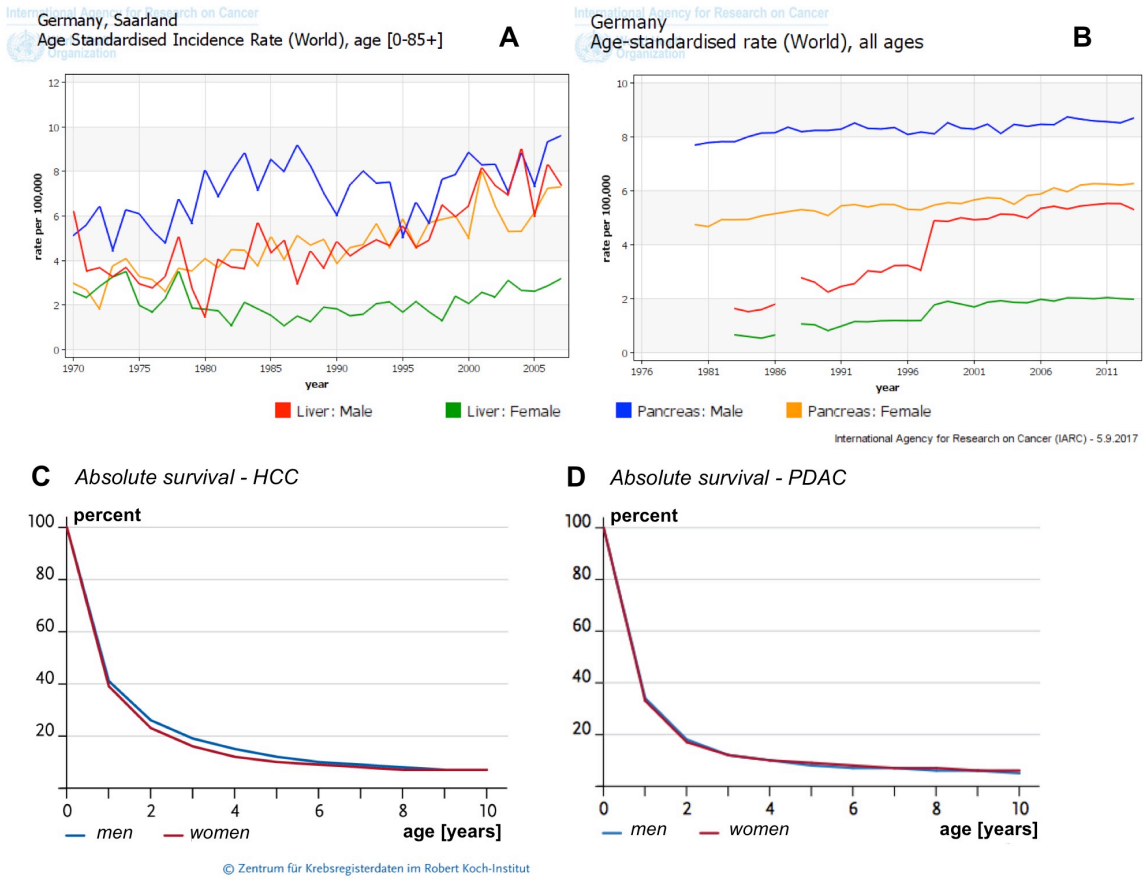

Figure 1: HCC and PDAC: Tumor statistics. German age-standardized incidence **(A**; Saarland**)** and mortality rates **(B)** (International Agency for Research on Cancer; 2017; [9]). Absolute survival for up to ten years after first diagnosis (ICD-10) of HCC **(C)** or PDAC **(D)** in Germany (2013-14; [10, 11]).

1.1.1 Hepatocellular carcinoma (HCC)

1.1.1.1 Risk factors and etiology

A functional liver is necessary for maintenance of a healthy organism. Inter alia, she is responsible for bile secretion into the intestines, production of blood clotting factors, and break down of alcohol, drugs and toxic wastes for renal and intestinal clearance [12]. Due to external influences and intrinsic aspects, many patients suffer from pathologic alterations and comprised liver function. There are several risk factors like chronic viral hepatitis (Hep-B or Hep-C), alcohol abuse, non-alcoholic fatty liver disease (NAFLD), non-alcoholic steatohepatitis (NASH), obesity, type 2 diabetes, aflatoxins (direct exposure or via contaminated foods [13]), exposure to chemicals, rare metabolic diseases, anabolic steroids, and tobacco which could ultimately result in liver cirrhosis [14]. Additional prevalence depends on race or ethnicity (Asian and African roots [15-17]), age (≥ 60 years), and gender (3 times higher risk for men [18]). The liver cirrhosis then presents a frequent precondition of HCC development, 90 % of all HCC patients were diagnosed cirrhotic before the first tumor lesions developed [14]. The etiology of HCC is summarized schematically in figure 2B [17] and tabularized by geographical areas in figure 2C [15].

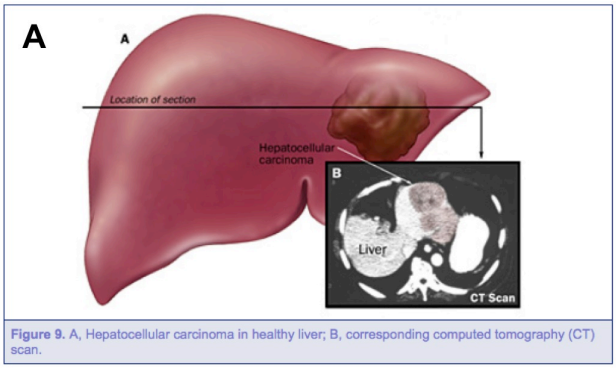

Figure 9. A, Hepatocellular carcinoma in healthy liver; B, corresponding computed tomography (CT) scan.

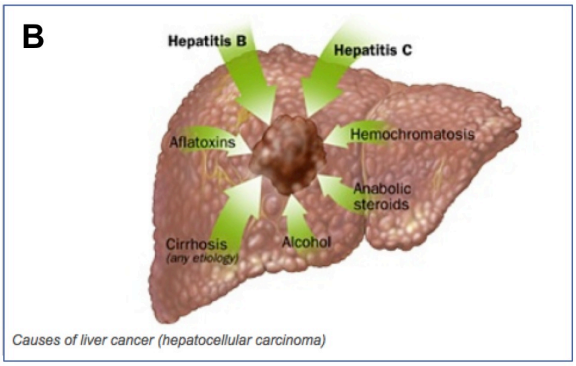

Causes of liver cancer (hepatocellular carcinoma)

C **Likely Etiology of HCC**

Causative Agents	Dominant Geographical Area
Hepatitis B virus	Asia and Africa
Hepatitis C virus	Europe, United States, and Japa
Alcohol	Europe and United States
Aflatoxins	East Asia and Africa

Figure 2: HCC: Pathology and etiology. A: Schematic and CT scan of HCC lesions [17]. **B:** Risk factors [17]. **C:** Regional etiology (National Cancer Institute at the National Institute of Health, USA; [15]).

1.1.1.2 Tumor diagnosis

Patients with comprised liver function are often identified during routine screening examinations by elevated γGT or GPT serum levels. Later-on, several patients develop liver cirrhosis, as cirrhotic diagnosed patients then are monitored more closely depending on the grade of their liver dysfunction. [14]

As not all patients show clear symptoms upon development of HCC, many liver tumors are eventually diagnosed during the periodic routine screening examinations. Diffuse HCC symptoms can be unexplained weight loss, loss of appetite, abdominal discomfort or distention (enlargement), fluid in the abdomen (ascites), gastro-intestinal hemorrhage (blood in the stool), nausea or vomiting, jaundice, weakness or fatigue, pain near the right shoulder blade or in the back, persistent itching, easy bruising and bleeding, or fever [12, 19]. After suspicious ultrasound (US) findings, HCC lesions can be confirmed by further examinations. Additionally, alpha-fetoprotein (AFP), a protein normally only produced by a fetal liver, is commonly secreted from liver cancer cells, and therefore can serve as marker of tumor progression in HCC patients [14].

HCC likely develops from hepatocytes and is a primary cancer originating from and located in the liver (figure 2A; [17]). It can occur as unifocal single tumor mass, or as multifocal HCC of several smaller, often inter- and intra-tumorally heterogenous cancer nodules in the liver [12, 20]. Multifocal nodular HCCs develop mostly in patients with cirrhotic livers [12]. In advanced stages, HCC commonly metastasizes to lungs, lymph nodes, adrenal gland, bones, and seldom into the brain [21].

1.1.1.3 Cancer statistics

Liver tumors were diagnosed more frequently in the recent years, most probably due to both, improved diagnostic tools and the increasing incidence because of growing numbers of cirrhotic HCC risk patients. Worldwide, liver cancer was the sixth most frequent cancer among the newly diagnosed tumors [22]. The relative numbers of newly diagnosed HCC patients in 2014 were 10.7/3.6 per 100,000 (men/women; age adjusted to the European standard) in Germany (GEKID-Atlas 2017; figure 3C; [23]). Incidence rates were steadily increasing as calculations based on the cancer registry data of the federal states demonstrate [23]. The same development could be observed in the United States [2, 3, 24], the UK [16], Europe [11] and worldwide [13, 24, 25] (figure 3A [25] and 3D [11]) with male predominance and in higher ages [11, 16, 24]. In Germany, 1 in 82 men and 1 in 190 women will be diagnosed with liver cancer during their lifetime [11]. The estimated 5-year-survival rate is 14/11 % (men/women) (Robert Koch Institute 2017; [10]) in Germany and 18 % in the United States [2], the 10-year-survival rate was estimated to be 10/9 % (men/women) [10], both getting less optimistic every year [24]. Especially in (South-)East Asia, the incidence rates were three to five times higher than in the European Union in 2013 [24].

Worldwide, liver tumors were the 6th most common cause of cancer related death in 2015/16 [4, 26, 27] (figure 3B; [28]). For 2017, it was predicted to be fifth most common [2, 3], and by 2030, liver tumors are projected to become the 3rd leading cause of cancer related death in the United States [27]. This upwards tendency was also seen in Germany, with a clear male predominance there were 8.2/2.9 victims per 100,000 (male/female; age adjusted to the European standard; figure 43A; [24]) [10].

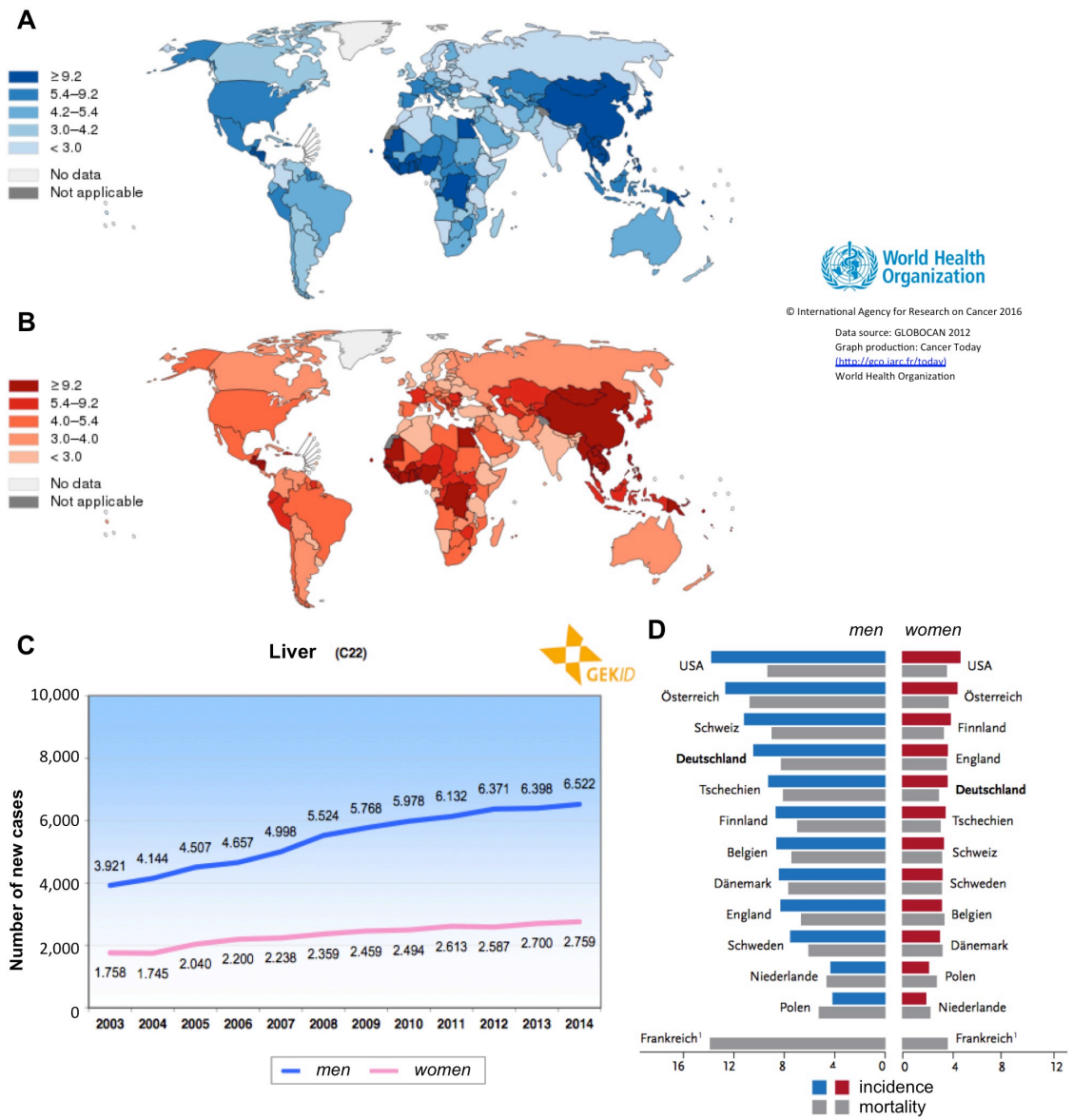

Figure 3: HCC: Incidence and mortality. Estimated worldwide age-standardized incidence **(A**; [25]**)** and mortality **(B**; [28]**)** rates (2012; [29]). **C:** Absolute number of new cases in Germany (2003-14; modified from [23]). **D:** International incidence and mortality rates ([1]France: No data on incidence available; age-standardized per 100,000 residents; 2013-14; modified from [11]).

1.1.2 Pancreatic ductal adenocarcinoma (PDAC)

The pancreas consists of exocrine and endocrine compartments, figure 4 presents its structure and localization within the body [30]. Digestive enzymes released from the exocrine pancreas are produced in the acini and released through ducts into the small intestine. The endocrine pancreas is made up of islets of Langerhans, cell clusters which produce specific and important hormones such as for example insulin, glucagon and somatostatin, all of which contribute to the regulation of metabolic processes in the body [31]. The pancreas is capable to develop either exocrine or endocrine tumors. Exocrine tumors, mostly pancreatic adenocarcinomas, are the most common type of exocrine cancers in general. Usually they originate from the pancreatic ducts, and hence are called pancreatic ductal adenocarcinomas (PDAC).

1.1.2.1 Risk factors and etiology

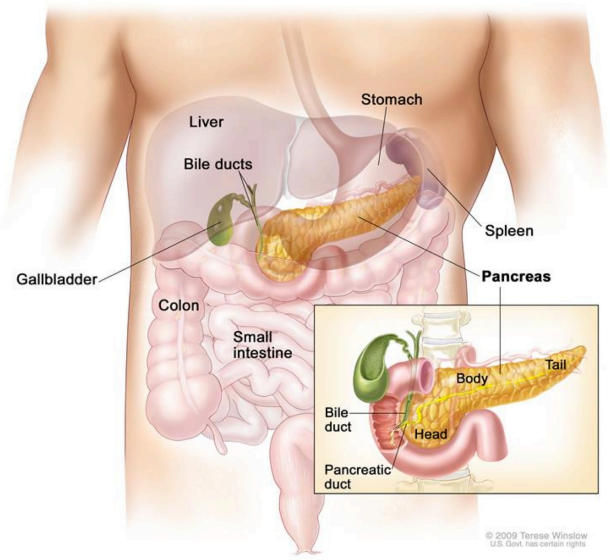

Figure 4: Structure (magnification) **and localization of the pancreas within the body** (big picture) [30]**.**

Risk factors for development of pancreatic cancer are age (90 % are older than 55, 70 % older than 65 years), gender (male predominance), race/ethnicity (Black people more likely than Asian, Hispanic, or White people in the United States [32], and White and Black people more likely than Asians in the UK [33]), tobacco (2-3 times higher risk), obesity, alcohol abuse, diabetes, family history, rare inherited conditions, chronic pancreatitis, exposure to chemicals, bacteria (*Helicobacter pylori*), chronic viral hepatitis (Hep-B), and liver cirrhosis [32].

1.1.2.2 Tumor diagnosis

PDAC gets often diagnosed at late stage due to the diffuse symptom pattern, and therefore, in its early stages is also classified as silent disease. Symptoms and signs of pancreatic tumors could be jaundice, pain in the upper abdomen or upper back, thrombosis in an arm or leg, burning feeling in stomach or other gastro-intestinal discomforts, stomach bloating, floating stools due to bad fat digestion (bad odor, unusual color), weakness, loss of appetite, nausea and vomiting, chills, fever, and unexpected weight loss [34]. Also, the tumor marker carbohydrate antigen 19-9 (CA19-9) is often elevated in PDAC patients [17].

1.1.2.3 Cancer statistics

The German incidence and mortality rates are calculated based on the cancer registries of the federal states (GEKID-Atlas 2017; [23]). Both rates are constantly growing [33], and compared to the development in Scandinavia and the United States, this increase happens faster in Germany (figure 5C; [23, 24]). In 2014, there were 14.1/10.3 new cancer cases per 100,000 Germans (male/female patients; age adjusted to the European standard; figure 5C) [23]. Those numbers represent the European, United States' and worldwide situation for PDAC: it ranks on the 12th position among the newly diagnosed tumors (figure 5A [35] and 5D, [2, 3, 11, 22, 28, 33]. Worldwide there is a slight male predominance (12th versus 11th) [13], whereas in the European countries the predominance is female (9th versus 12th) [23, 33]. The incidence to develop PDAC is higher in the economically developed countries [24], besides other factors this might be due to the increasing numbers of adipose patients and

life expectancies. The latest life time risk estimation to develop PDAC predicts 1 in 57 men and 1 in 59 women (Robert Koch Institute 2017; [10, 11]), this is an increase of about 20 % in the last 10 years [36]. The estimated the 5-year-survival rate in Germany is 8.9/8.8 % (men/women) [11] and 8 % in the United States [2], the 10-year-survival rate is 10.9/11.0 % in Germany [11]. The estimation of Gudjonsson is devastating, as after correcting the numbers for repetitions and the life table percentage, his calculations result in a 5-year-survival rate of hardly more than 0.3 % [37].

In 2016, PDAC was the fourth leading cause of cancer death worldwide (figure 5B; [31, 38]) with rising tendency [2, 22, 36]. In Germany, the tendency for PDAC-related death was significantly rising (13.2/9.8 victims (male/female) per 100,000 in 2015; age adjusted to the European standard; figure 43B; [24]) compared to the previous years [10, 24, 36, 39]. For 2017, PDAC was estimated to be the third most common reason [2, 3], and by 2030 pancreatic cancer was projected to become the second leading cause, all in the United States with a clear male predominance [2, 27, 37, 40]. The average age at cancer-related death in 2014 and 2015 it was 77 (men) and 73 (women) [11].

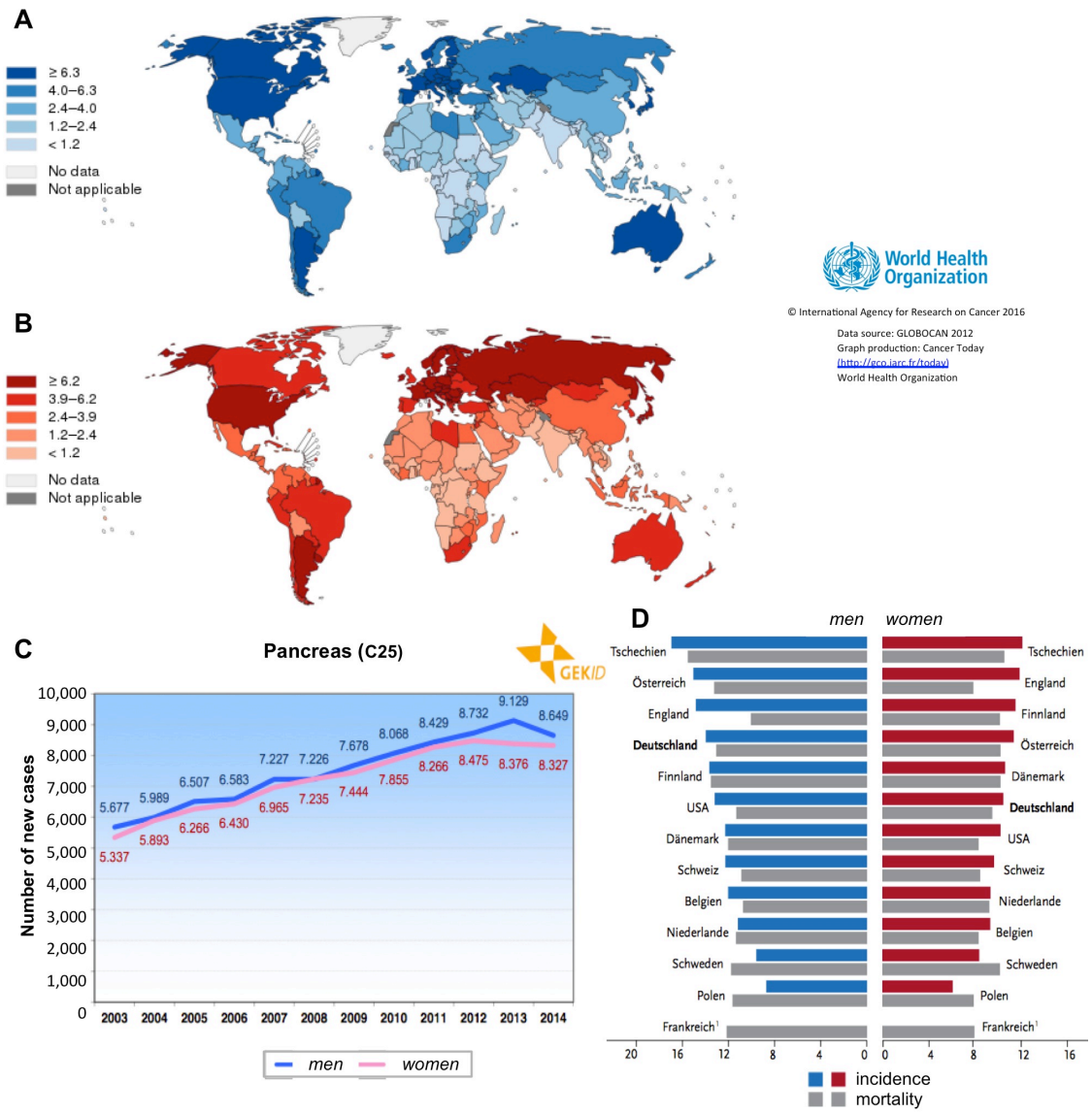

Figure 5: PDAC: Incidence and mortality. Estimated worldwide age-standardized incidence **(A**; [35]**)** and mortality **(B**; [38]**)** rates (2012). **C:** Absolute number of new cases in Germany (2003-14; modified from [23]). **D:** International incidence and mortality rates ([1]France: No data on incidence available; age-standardized per 100,000 residents; 2013-14; modified from [11]).

1.2 Non-invasive imaging for diagnosis and monitoring

Imaging is crucial for reliable diagnosis of several diseases, monitoring during therapy, and long-term follow-up after successful treatment. Available non-invasive imaging modalities include different ultrasound (US) techniques, computed tomography (CT), MRI, and positron emission tomography (PET), alone or in combination. The optimal imaging tool needs to be selected case-specific after careful consideration regarding resolution, acquisition time, utilization of contrast agents, availability, health condition of the patient, and potential risks from radiation load.

Advantage of US is its wide availability in medical offices and high resolution of acquired images. However, US is highly dependent on the examiners skill level. CT uses X-rays, and offers good resolution after a short acquisition time, especially of solid structures like bones. For good soft tissue contrast, CT imaging requires contrast agents which might have side-effects, especially in old patients or patients with co-morbidities like renal dysfunction. MRI provides high tissue resolution and contrast without radiation exposure. For specific questions, there are contrast agents available. Disadvantages are the long acquisition time and relatively high costs per scan. In PET/CT scans, radioactive tracers, such as ^{18}F-fluorodeoxyglucose (FDG), are detected upon accumulation. The tracers can be chosen depending of the target, for example FDG accumulates in metabolically active tissues, such as primary tumors and their metastases. Therefore, PET scans mostly involve whole-body imaging for metastasis identification in distant tissues. The PET signal then gets localized by superimpositioning of the PET scan data with the corresponding anatomical information from CT or MRI scans. Big advantage is the specificity of the tracer molecules, as they could be coupled to target-specific ligands. [7, 41, 42]

1.2.1 Magnetic resonance imaging (MRI)

Since the 1980s, MRI is used for diagnostic approaches and established as one of the imaging columns in modern medicine. Big advantages are the lack of ionizing radiation, excellent soft tissue contrast, high spatial resolution, slice-wise image acquisition of the region of interest (ROI) in any possible orientation, and hence the possibility for post-processing into three-dimensional reconstructions (e.g. maximum intensity projections (MIP)) [43, 44]. With specific scan protocols and data analysis, morphological, metabolic, and functional information can be obtained. Figure 6 shows an exemplary T_2w MR scan of a rat HCC tumor nodule and is an example to illustrate the good resolution in the μm range [45].

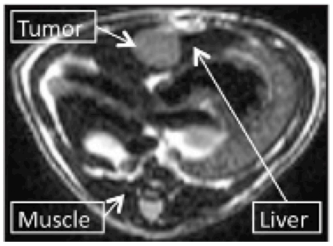

Figure 6: T_2w MRI scan of HCC tumor nodule in rat model [45].

Basic principle behind is the excitation of atomic nuclear spins (most commonly ^{1}H or ^{13}C) in the ROI by application of an external magnetic field and the subsequent detection of tissue-specific relaxation time, the time the spins need to return to their starting orientation. That relaxation consists of longitudinal and transverse components, the relaxation time of the longitudinal component is T_1, and T_2 is the transverse relaxation time. [46] The relaxation times depend on the chemical and physical environments of water protons in tissue, the grades of freedom those molecules have. Thus, T_1 and T_2 relaxation time measurements help to understand water molecular dynamics in biologic systems which can be translated into anatomical tissue information [47]. Differences in the tissue microstructure are the basis of the contrast between normal and pathologic tissue, expressed in relaxation time shifts. Therefore, MRI scans provide for example information about inflammation, tumor malignancy, edemas, infarction, and ischemia [47].

1.2.1.1 Contrast agents

The administration of contrast agents could further increase the contrast of the target structure, and hence could improve the diagnostic efficiency regarding detection sensitivity of (pathologically) altered tissues and lesions. Contrast agents for example accumulate in specific tissues, are not taken up by specific cells or structures, or are taken up in an altered pattern. The altered MRI signal detected in pre- and post-scans can help to clarify several clinical questions. The pioneering idea for the use of magnetic imaging probes with high magnetic moments, and their application for magnetically-guided targeting approaches can be dated back to the early 1960s and Freeman et *al*. [48]. In the late 1970s they were established for MRI due to their ability to shorten T_2 relaxation times [49].

Widely utilized substances are paramagnetic gadolinium (Gd) formulations, which shorten T_1 relaxation time and T_2-reducing superparamagnetic iron oxides (SPIOs). Clinically approved products include the SPIO formulations Resovist® (ferucarbotran; [50]) and Feridex®/ Endorem® (ferumoxides; [51]) for liver-specific contrast enhancement in the diagnosis of HCC [52, 53]. The SPIOs specifically accumulate in Kupffer cells and leave cancerous lesions bright amidst hypointense healthy liver tissue. Sinerem®/Combidex® (USPIO) was applied for the detection of metastatic lymph nodes, but was withdrawn from the market [54-56]. Lumiren®/GastroMARK® is an oral ferumoxsil contrast agent for imaging of the gastro-intestinal tract [56]. Eovist® (gadoxetate disodium) is a Gd preparations used in liver imaging [51]. Other Gd contrast agents are needed for MR-angiography and brain and spine imaging, examples are Gadovist® (gadobutrol; [51]), Magnevist® (Gd-DTPA; [50]), MultiHance® (gadobenate dimeglumine; [57]), and OmniScan™ (gadodiamide; [58]). ProHance® is a liposomal formulation of gadoteridol for brain and spine imaging [57].

In general, MNPs possess ferri- or ferromagnetic properties which generate significant susceptibility effects resulting in strong T_2 and T_2^* contrast. This made them ideal candidates to be examined as sensitive imaging probes in pre-clinical MR imaging approaches, for example in oncologic issues [59] and potential use for clinical approval processes.

1.2.1.2 Sequence optimization and data evaluation

Improvement of diagnosis for better and earlier detection of for example tumor lesions could improve the prognosis of cancer patients [60]. It also relies on development and optimization of application specific scan sequences. As experiments and studies can not be performed on patients, alternatives were needed. Tissue-mimicking phantoms can be equipped to possess close-to-*in vivo* properties and hence provide a convenient tool to improve the MRI scan sequences, to test radiofrequency coils, and to evaluate system performance [60]. In addition, phantoms could be used to elucidate variations between different MRI scanners and/or different field strengths (table 1 [47], and figure 29E+F).

T_2 and T_1 Relaxation Times at 3T and 1.5T Measured at 37°C. Literature data is also shown.

Tissue	T_2—3 T [ms]		T_1—3 T [ms]		T_2—1.5 T [ms]		T_1—1.5 T [ms]	
	This study	Literature	This study	Literature	This study	Literature	This study	Literature
Liver	42 ± 3		812 ± 64		46 ± 6	54 ± 8[35]	576 ± 30	~600[23]
Skeletal muscle	50 ± 4	32 ± 2[25]	1412 ± 13	1420 ± 38[25]	44 ± 6	35 ± 4[25]	1008 ± 20	1060 ± 155[25]
Heart	47 ± 11		1471 ± 31		40 ± 6	44 ± 6[36]	1030 ± 34	
Kidney	56 ± 4		1194 ± 27		55 ± 3	61 ± 11[37]	690 ± 30	709 ± 60[37]
Cartilage 0°	27 ± 3	37 ± 4[25]	1168 ± 18	~1240[25]	30 ± 4	42 ± 7[25]	1024 ± 70	~1060[25]
Cartilage 55°	43 ± 2	45 ± 67[26]	1156 ± 10		44 ± 5		1038 ± 67	
White matter	69 ± 3	56 ± 4[27]	1084 ± 45	1110 ± 45[29]	72 ± 4	79 ± 8[38]	884 ± 50	778 ± 84[38]
Gray matter	99 ± 7	71 ± 10[27]	1820 ± 114	1470 ± 50[29]	95 ± 8	~95[39]	1124 ± 50	1086 ± 228[38]
Optic nerve	78 ± 5		1083 ± 39		77 ± 9		815 ± 30	
Spinal cord	78 ± 2		993 ± 47		74 ± 6		745 ± 37	
Blood	275 ± 50		1932 ± 85	~1550[30]	290 ± 30	327 ± 40[14]	1441 ± 120	~1200[30]

Table 1: Comparison of T_1 and T_2 relaxation times acquired at 3.0 and 1.5 T (table 1 from [47]).

A second aspect is the first *in vitro* evaluation of newly developed contrast agent-loaded formulations regarding their imaging properties [4, 60-64]. Tissue-mimicking phantoms could be used to find out whether the content of imaging probe is high enough to result in a sufficient contrast over baseline tissue relaxation and to identify detection limits. Hence, they may help to reduce the extent of animal testing. Probably, relaxation data from *in vitro* samples embedded in phantoms could also provide the basis for quantitative analysis in according *in vivo* scans.

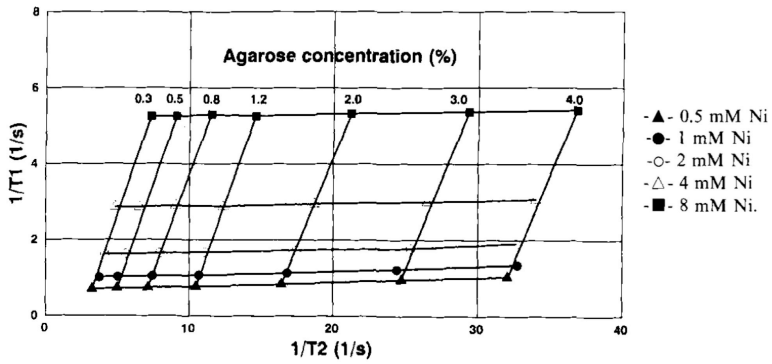

Figure 7: Tissue-mimicking by Ni- and agarose-dependent T_1 and T_2 modulation [65].

Most common material in MRI phantom preparation is agarose [65-68]. General criteria for phantom components are chemical, physical and thermal stability, easy handling regarding plasticity in size and shape, and tolerability regarding ingredients (non-toxicity) at good availability and low price [60, 65]. The T_2 relaxation is modulated by the agarose itself, the addition of superparamagnetic metals like nickel allows T_1 relaxation adjustment [60, 65, 68]. Hence it is possible to obtain independently tune T_1 and T_2 relaxation values to mimick specific body tissues [65]. In figure 7, Christofferson et *al*. graphically demonstrated the influence of varying agarose concentrations on the T_2 relaxation, and nickel-doping on the T_1 values [65]. Advantages of agarose gel phantoms are independency from magnetic flux density and temperature (within the acquisition range). Disadvantageous is that MR-effecting *in vivo* parameters like diffusion, flow, movement and susceptibility effects can not be taken into account [65].

1.2.2 Imaging of HCC

Contrast agent-enhanced US of emerging HCC nodules presents highly vascularized areas within the surrounding tissue [69]. Further applied imaging modalities include CT, multi-detector CT (MDCT), MRI scans, angiography of the abdominal blood vessels and organs, and FDG-PET/CT [14, 69]. In the arterial phase of contrast agent-enhanced MDCT and the arterial phase of gadolinium-enhanced T_1-weighted MRI sequences, a HCC nodule also presents as hyperintense region due to the arterial flush in the highly vascularized tumor [69, 70]. During the portal venous phase and the late arterial phase, the hyperintense MRI signal washes out, resulting in hypointense signals of cancerous tissue [14, 70, 71]. The administration of liver-specific contrast agents such as in bolus intravenously injected SPIOs enables for the detailed visualization of smaller lesions by dynamic (T_2) MRI [14]. The effect of SPIOs on the acquired MR images is primarily the shortening of T_2 relaxation times [72]. Such SPIOs are selectively taken up by the reticulo-endothelial system (RES), about 80 % of an injected dose is taken up by the liver Kupffer cells and 5 – 10 % by the spleen. Most HCC lesions do not have an intact RES, they appear bright among the hypointense liver parenchyma after SPIO uptake [72]. Whole-body FDG-PET/CT is another imaging modality that allows for the parallel detection of both, the primary tumor and, most importantly, distant metastases [73]. The FDG tracer administered for PET accumulates in highly proliferative tissue such as tumors. Combination of FDG-PET imaging with anatomical CT scanning allows for concrete localization of the glucose-active tumor nodules [41]. Cancer imaging has become a valuable and important tool for diagnosis and prediction of the tumors' response to therapeutic approaches. On a molecular basis, HCC lesions are very heterogenous, both, intra- and inter-individually. The tumor nodules present a high grade of vascularity with activated angiogenesis and elevated expression of growth factors [69]. For histo-pathological examination of unclear masses in the liver and to prove the diagnosis HCC, liver biopsies need to be taken. [17]

1.2.3 Imaging of PDAC

Imaging plays a critical role in pancreatic cancer staging and the therapeutic decision process. The imaging modalities used to evaluate PDAC include CT, MDCT, MRI, different US modes, and FDG- / ^{18}F-fluorothymidine (FLT-) PET/CT [7, 74]. CT, and especially MDCT, is the preferred imaging tool for PDAC staging due to its short acquisition time, the robustness, the excellent spatial resolution, and the option for contrast-enhanced imaging of the vasculature [7]. Primary PDACs show a peak enhancement in the late arterial phase (45 – 50 seconds post i.v. contrast agent injection), potential hypodense liver metastases reach optimal enhancement in the portal venous phase after 70 seconds [75]. MRI principally provides the better soft tissue contrast compared to unenhanced CT imaging. Therefore MRI is especially valuable in patients with contraindication for intravenous contrast agent administration, and it provides flow sensitive sequenced and diffusion-weighted imaging [7]. In a recent study it could be shown that MRI improved a lot and thus presents comparable sensitivities and specifities to CT (MRI sensitivity 93 %, specificity 50–75 %; CT sensitivity 87 %, specificity 63–75 %) [76, 77]. Transabdominal US is typically applied in the initial examination of abdominal pain or suspected obstructive jaundice but visualization of the pancreas might be difficult due to body habitus or bowel gas [7]. Endoscopic US (EUS), endoscopic retrograde cholangiopancreatography (ERCP), or percutaneous transhepatic cholangiography (PTC) can help localize, identify and characterize the tumor lesion and support in the guidance during biopsies for histo-pathological tissue evaluation [5, 7, 74]. The sensitivity of EUS for tumors ≤ 2 cm is nearly 100 %, the specificity ≥ 95 % [7, 77]. Besides the role in identification and localization of the primary PDAC, in whole-body examinations FDG-PET/CT can help to detect additional distant metatstases beyond those which can be found applying conventional cross-sectional imaging of the abdomen, pelvis and chest [7, 78]. Detection of distant metastases in as resectable classified patients prevents unnecessary resection [42]. The new tracer FLT evaluates tumor proliferation and has the potential to be more specific than FDG-PET/CT [42]. Both PET tracer help to differentiate benign and malign pancreatic lesions in PET-CT scans, but the specificity of FLT-PET/CT is higher as benign lesions are FLT-uptake-negative with a specificity of 100 % compared to 85 – 97 % for FDG-PET/CT [42].

1.3 Therapeutic approaches

The treatment of several diseases by classical therapies is not as efficient as it should be. After systemic administration, a big problem is the incomplete delivery of the therapeutic agents to the target tissue due to for example short circulation times, early inactivation or degradation in the blood and rapid clearance by immune cells. Off-site delivery and accumulation at for example liver and kidney could lead to tissue damage [49, 79]. Though, as previously mentioned, this clearance by macrophages of the hepatic RES is a wanted

feature when applying SPIO-based contrast agents for liver imaging, it has to be avoided when targeting other tissues.

Targeted approaches are broadly examined to overcome the delivery issues and even reduce administered doses. New therapeutic approaches utilizing nanocarrier formulations and targeting strategies also open the field for new therapies. For example nucleic acid therapies rely on packing into shielding nanocarrier formulations. Targeted delivery could be enhanced by the assembly with MNPs and target cell-specific surface functionalization of the vehicle.

1.3.1 State-of-the-art therapy of HCC

HCC is often difficult to treat or even cure due to late diagnosis or the tumor localization within the liver. Most patients suffer from advanced tumors upon diagnosis and are only eligible to palliative treatments. For the fewer number of patients in earlier stages, possible curative treatments are surgical removal of the tumor mass, liver transplantation, or ablative techniques (radio frequency ablation (RFA), microwave ablation (MWA), irreversible electroporation (IRE) or ethanol injection). Palliative treatments include intra-arterial therapies, chemotherapy, radiation therapy (stereotactic radiation therapy) or combinations thereof. For patients with metastatic spread, the therapeutic options are restricted to palliative therapies [69]. To decide on the optimal therapeutic approach, each patient is staged according to the 8th edition of the TNM (tumor, node, metastases) Classification of malignant Tumors of 2016 [80], compiled in table 2.

Liver transplantation is an option only for individuals of stable health condition and HCC lesion(s) meeting the Milan criteria: i.e. single lesion ≤ 5 cm, or up to three lesions ≤ 3 cm in diameter, each in the absence of tumor vascular invasion or evidence of extra-hepatic metastases [81]. The Milan criteria predict the risk of relapse and survival probability after liver transplantation. Among those patients eligible for transplantation, elevated AFP levels might indicated a higher risk for tumor relapse [82]. The resection of even large liver portions is tolerable depending on the remaining liver volume, as the liver has a high regenerative capacity. Another possibility is the combination of surgery with local ablation techniques (figure 8; [83]). Operating principle behind all ablation methods is the local destruction of all tumor cells. RFA utilizes a needle probe inserted into the tumor nodule, which then heats up by applying an alternating radiofrequency electrical current (figure 8A, [84]). In MWA, the thermal ablation results from electromagnetic energy focused onto the cancerous area [84]. For IRE, also needle probes are used, but in contrast to the thermal RFA approach, the tumor cell death is induced non-thermally using electrical energy to disrupt the cellular membrane integrity with subsequent cell death (figure 8B, [85]). Ablation techniques are generally indicated for treatment of small tumors (≤ 3 cm in diameter) and patients that cannot tolerate an operation.

	T	**Tumor**		
Tx		primary tumor cannot be assessed		
T0		no evidence of primary tumor		
T1		solitary tumor without vascular invasion		
	T1a	solitary tumor ≤ 2 cm in greatest dimension with or without vascular invasion		
	T1b	solitary tumor > 2 cm in greatest dimension without vascular invasion		
T2		solitary tumor with vascular invasion > 2 cm dimension *or* multiple tumors, < 5 cm in greatest dimension		
T3		multiple tumors ≥ 5 cm in greatest dimension		
T4		tumor(s) involving a major branch of the portal or hepatic vein with direct invasion of adjacent organs (including the diaphragm) other than the gallbladder, *or* with perforation of visceral peritoneum		
	N	**Regional lymph nodes**		
Nx		regional lymph nodes cannot be assessed		
N0		no regional lymph node metastases		
N1		metastases in 1 to 3 nodes		
N2		metastases in ≥ 4 nodes		
	M	**Distant metastases**		
Mx		metastases cannot be assessed		
M0		no evidence of metastases		
M1		distant metastases present		
		Stage		
Stage 0		Tis	N0	M0
Stage IA		T1a	N0	M0
Stage IB		T1b	N0	M0
Stage II		T2	N0	M0
Stage IIIA		T3	N0	M0
Stage IIIB		T4	N0	M0
Stage IVA		Any T	N1	M0
Stage IVB		Any T	Any N	M1

Table 2: HCC TNM staging criteria. T (tumor), N (regional lymph nodes), M (distant metastases), and stage criteria of HCC (data from [36]).

Intra-arterial therapies are the most frequently applied palliative options. The success of all intra-arterial approaches is based on the specific blood supply of hepatocellular carcinomas, which is provided almost exclusively by the hepatic artery whereas the healthy hepatic tissue is fed to 75 % by the portal venous system [86, 87]. Therapeutic agents (chemotherapy or β-emitter) are directly delivered to the tumor by placing a catheter into the tumor-feeding artery. Thus, side-effects from off site delivery are strongly reduced. These techniques use X-ray imaging to monitor catheter placement and agent delivery into the tumor specific so-called feeding-arteries. During the trans-arterial procedure, chemotherapy emulsions (TACE, DEB-TACE; figure 8C; [88]) or Yittrium-90 microspheres are administered. The only clinically approved systemic therapy in HCC is sorafenib [69, 89], but others like 5-fluorouracil, oxaliplatin, irinotecan, cetuximab, and avastin are in clinical trials [17].

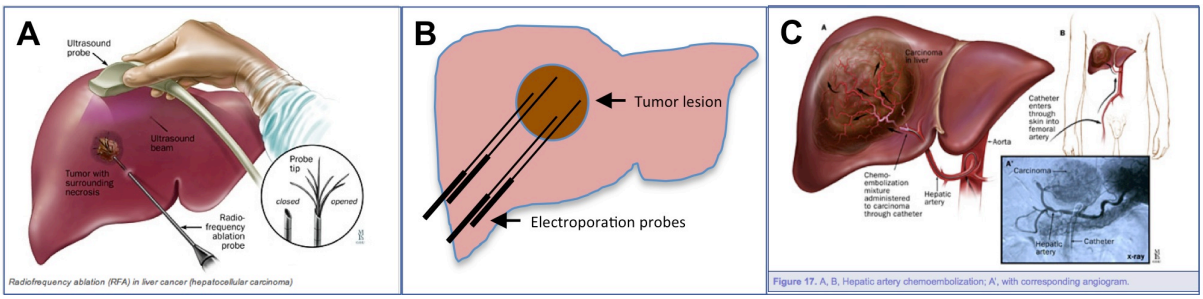

Figure 8: HCC: Treatment options. A: Schematical setup of radiofrequency ablation (RFA) [83]. **B:** Schematical setup of irreversible electroporation (IRE). **C:** Schematical setup of trans-arterial chemoembolization (TACE) [88].

1.3.2 State-of-the-art therapy of PDAC

The treatment options for PDAC patients are very limited, mostly due to the diagnosis in already advanced stages, and the local invasion and distant spread of tumor lesions. After identification, tumors are staged resectable, borderline resectable, locally advanced, or metastatic to decide on the treatment approach. Table 3 summarizes TNM staging criteria for PDAC [80, 90]. In general, possible approaches include surgery, radiation therapy, chemotherapy and targeted therapy.

	T	**Tumor**		
Tx			primary tumor cannot be assessed	
T0			no evidence of primary tumor	
Tis			carcinoma *in situ*	
T1			tumor limited to the pancreas, ≤ 2 cm in greatest dimension	
	T1a		tumor ≤ 0.5 cm in greatest dimension	
	T1b		tumor < 0.5 cm < 1cm in greatest dimension	
	T1c		tumor < 1cm < 2 cm in greatest dimension	
T2			tumor limited to the pancreas, > 2 cm ≤ 4 cm in greatest dimension	
T3			tumor extends beyond the pancreas but without involvement of the celiac axis or the superior mesenteric artery, > 4 cm in greatest dimension	
T4			tumor involves celiac axis, *or* superior mesenteric artery, *and/or* common hepatic artery (unresectable primary tumor)	
	N	**Regional lymph nodes**		
Nx			regional lymph nodes cannot be assessed	
N0			no regional lymph node metastases	
N1			metastases in 1 to 3 nodes	
N2			metastases in ≥ 4 nodes	
	M	**Distant metastases**		
Mx			metastases cannot be assessed	
M0			no evidence of metastases	
M1			distant metastases present	
		Stage		
Stage 0		Tis	N0	M0
Stage IA		T1	N0	M0
Stage IB		T2	N0	M0
Stage IIA		T3	N0	M0
Stage IIB		T1, T2, T3	N1	M0
Stage III		T1, T2, T3	N2	M0
		T4	Any N	M0
Stage IV		Any T	Any N	M1

Table 3: PDAC TNM staging criteria. T (tumor), N (regional lymph nodes), M (distant metastases), and stage criteria of PDAC (data from [36]).

Chemotherapy and targeted therapy can be applied in a neo-adjuvant and/or adjuvant regimen [91]. For patients with small intestine or bile duct stenosis due to the tumor mass, that block might be relieved by mechanical widening of the stenosis or the insertion of stents during ERCP or PTC. The surgical approach includes partial or complete pancreatectomy. The goal is a complete resection, i.e. R0 resection with no residual tumor cells left in the patient. Surgery is an option for only about 20 % of individuals, as in most cases the cancer has already spread to other organs [4-6]. Neo-adjuvant chemotherapy has become an important approach, by which the tumor is downsized and thus made eligible for surgery. The surgical intervention is typically followed by radiation and chemotherapy, the adjuvant therapy.

Aim of radiation therapy is the destruction of tumor cells by high-energy X-rays or other particles, and its therapy regimen consists of several treatments in patient-specific schedules and doses. To exploit the radiosensitization, radiation therapy is often combined with chemotherapeutic treatments, also in patient-specific regimen cycles.
Different regimens are available in the neo-adjuvant and adjuvant setting. The most common agents are Folfirinox® (a combination of fluorouracil (5-FU), irinotecan and oxaliplatin), gemcitabine (Gemzar®), or Nab-paclitaxel (Abraxane®). An agent for targeted therapy is erlotinib (Tarceva®). Erlotinib targets and blocks a cancer cell surface protein, the epidermal growth factor receptor (EGFR). It is always administered in combination with gemcitabine and is an option for advanced PDAC. All chemotherapeutics have unpleasant side-effects that indicate further palliative care. On the other hand, chemotherapeutic drugs could also improve the patient´s general condition, as they could relieve pain and improve digestion, appetite, weight loss, and weakness. [91]

1.3.3 Targeted delivery

Driving idea behind targeting approaches is to increase the efficiency of the therapeutic agent by localized delivery towards the region of interest, and depending on the nanocarrier formulation even the controlled release of its cargo. The reduction of off-site delivery and prevention of inactivation also reduces the amount of therapeutic agent that has to be administered.

1.3.3.1 What does this mean for HCC and PDAC?

For HCC and PDAC clear diagnostic and therapeutic limitations exist and there is high demand for clinically practicable solutions. Biggest obstacles remain diagnosis only in advanced cancer stages and the lack of functional and clinically approved therapies in those often non-resectable patients.
To overcome diagnostic obstacles is difficult, as both cancer types show no clear symptoms in the early stages. A solution might be more frequent medical check-ups in risk patients and the usage of sensitive contrast agents that specifically target cancer cells. Though more frequent screenings would eventually lead to false positive diagnoses and as economic aspect that would mean higher costs for the health care system.
State-of-the-art chemotherapeutic treatments are non-targeted and rely solely on accumulation at the targeted site via the natural so called enhanced permeability and retention (EPR) effect leading to extravasation of particles up to 400 nm through the leaky vasculature into the tumor interstitium due to the increased vessel permeability. Unfortunately, not all tumors and stages, and not all cancer patients exhibit the EPR effect at the same level, for several individuals it is only weak [92]. Due to this limitation and the patients-specific composition of the tumor interstitium the drug delivery rate is only low.

Issues on delivery efficiency can be approached with nanocarrier formulations. By specific functionalization, the loss of therapeutic agent before even reaching the target tissue can be reduced, its circulation time increased, the functionality upon delivery improved and side-effects decreased. Another problem is the heterogeneity of the tumor lesions due to fibrosis. Tumor cell-specific targeting could help to improve the uptake into the cancer cells.
The generation of theranostic formulations combining improved diagnostic agents and encapsulated/assembled therapeutic agents for immediate delivery is a promising strategy. Core component of such theranostics could be MNPs enabling parallel magnetic targeting and MRI monitoring of the circulating nanocarriers.
For the development of new therapeutic approaches in HCC and PDAC there are different animal model systems available. There are two basic concepts of rodent models: on one hand, they are based on orthotopic tumor lesions of (human) cancer cell lines with relatively homogeneous cancer nodules. On the other hand, there are endogenous tumor models with more heterogeneous tumor lesions whose properties are closer to the human pathologic situation. Cancer is then evoked either by exposure of the animals to chemicals or genetic engineering of the mouse strains leading to tumor growth. For both cancers, at the Klinikum rechts der Isar there are several animal models established.

1.3.3.2 Nanocarrier formulations

A nanocarrier formulation is composed of a cargo such as a drug, nucleic acids or an imaging probe, and a structure to protect the cargo. Of course there can be more than one cargo assembled with one or more stabilizing components, and further modifications providing special features. Examples for nanocarrier formulations are viral vectors, non-viral vectors such as lipoplexes and polyplexes, and liposomes.
On the diagnostic side, there are several pre-clinical studies on for example contrast agent-loaded liposomes and nanogels [93] for MRI and fluorescence imaging [94]. The MRI contrast agent ProHance® is a clinically approved liposomal gadoteridol formulation for T_1w imaging of brain, HCC, and spine [95].
Lipsomes are also successfully applied for the delivery of encapsulated doxorubicin (DOX) in a pharmaceutical called Caelyx®/Doxil® [96-99]. Though they are frequently used for tumor therapies, they are non-targeted. Hence, the drug delivery efficiency is limited and need to be improved. Doxil® therapy contributes to an extension of survival, but full recovery is seldom. In pre-clinical research, there are several approaches to prepare complexes loaded with nucleic acids, for example lipoplexes and polyplexes. Such assemblies are stabilizing and prevent from early inactivation of the nucleic acids by nucleases. Another widely utilized nanocarrier for nucleic acids are viruses, also known as viral vectors. The viral capsids can be loaded with additional cargos if necessary, such as imaging probes, and the viral genome can be genetically engineered. For longer circulation times, the surface could be modified with shielding organics such as the polymer PEG or with hyaluronic acid.

1.3.3.3 Strategy: Magnetic targeting

The described nanocarrier systems can all be assembled with magnetic nanoparticles to form magnetic nanocarriers. That enables for two key features: magnetic targeting via magnetofection [100] and non-invasive monitoring *in vivo* by MRI [4].

Suitable core-shell type MNPs form stable complexes with different viral and non-viral particles by self-assembly [101-106] and they can be loaded into liposomes. The integration of MNPs in such nanocarrier formulations resulted in enhanced viral transduction and non-viral transfection efficiency and transgene expression [100, 101, 103-114]. Furthermore, the complex formation with MNPs and shielding with organic molecules minimized the interaction with blood components and cells, and could prevent early inactivation of assembled structures like viruses or nucleic acids [103, 105, 110, 115]. The uptake of magnetic liposomes could also be enhanced in external magnetic fields. In figure 9, the magnetic nanocarrier systems investigated in this work are schematically presented.

Transport to specific targets and controllability of the release of the cargo are two of the most avidly pursued goals in drug delivery research. The advantage in utilization of SPIOs is their ability to acquire net magnetic moment in the presence of an external magnetic field, but return to a non-magnetic state when the external magnet is removed [116]. This is of paramount importance when these particles are introduced into living systems because once the external magnetic field is removed, the magnetization disappears and thus, agglomeration and the possible embolization of capillary vessels could be avoided [116].

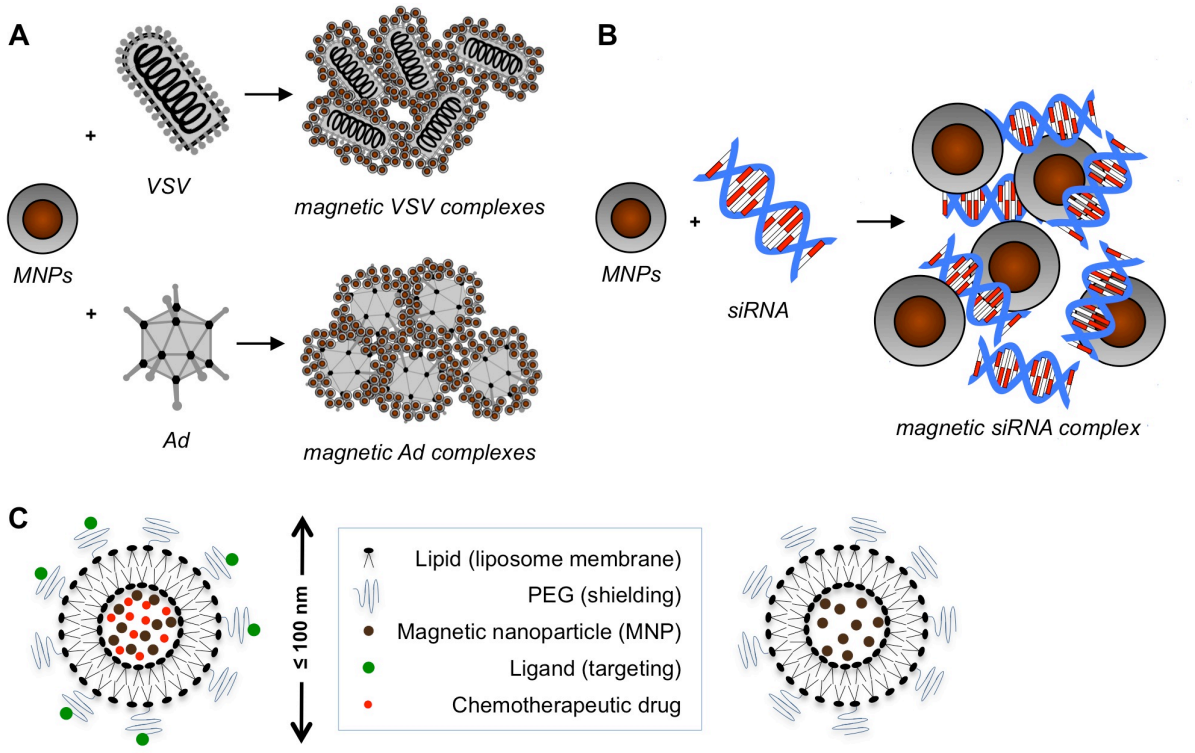

Figure 9: Schematical sketches of the magnetic nanocarrier systems investigated in this work. A: MNP-VP complex self-assembly. **B:** MNP-siRNA complex self-assembly. **C:** MNP-LPs.

The combination of therapeutic and contrast agents in one formulation resulted to the new class of “theranostics” – *thera*peutics and substances for diag*nostics* integrated in one multi-functional formulation [49]. Some assemblies of MNPs with for example pharmaceuticals, viruses or nucleic acids could be applied as such theranostic formulations providing MRI contrast and the delivery of the therapeutic agent at the same time.

1.3.3.3.1 Magnetic nanoparticles (MNPs)

In the last decades, MNPs have been widely employed in the biomedical field, for example in cellular therapy, tissue repair, drug delivery, hyperthermia, biosensors, immunoassays, and magnetic separation [49, 116-120]. In oncology, they are utilized as clinically approved contrast agents in tumor detection [49, 121, 122], and in preclinical approaches in magnetically targeted delivery of magnetic nanocarriers [123-131]. Their broad applicability is based on the magnetic properties, the chemical stability, the biocompatibility, and the tunable size [49, 67, 79, 115, 120, 132, 133]. Great advantage of MNPs is their large specific surface relative to their small size [49, 79, 120]. After cell uptake, SPIOs are metabolized intracellularly in lysosomes into a soluble, non-superparamagnetic form of iron to become part of the normal iron pool in ferritin or haemoglobin [55, 134].

A MNP is comprised of an inorganic magnetic core with a biocompatible surface coating to stabilize the nanoparticle under physiological conditions and enable further application-specific surface modifications with functional ligands for *in vivo* applications [135]. The synthesis of MNPs is possible in aqueous as well as organic phases [49]. Coating materials provide non-immunogenic and non-antigenic properties, could prevent opsonization, and give conjugation sites for example for nucleic acids and viral particles [49, 136]. Often used materials include polysaccharides like dextran, organic polymers like polyethylene glycol (PEG) and polyethylene imine (PEI), or inorganic molecules such as silica [49, 79, 137, 138]. Further moieties could enhance targeting and increase delivery efficiency, examples are bioactive molecules like ligands or receptors, peptides, antibodies, and small molecules like dyes [49, 137]. Figure 10 presents the schematical structure of the core-shell type MNPs PEI-Mag2 (figure 10A), SO-Mag6-11.5 (figure 10B), and the coating components PEI_{Br}-25 kDa, Zonyl® FSA, Zonyl® FSE and palmitoyl dextran PALD2 (figure 10C+D).

Of course MNPs can be used not only in the field of nanocarriers, but offer broad variety of application possibilities besides the biomedical approaches [116]. Further application fields are as various as aeronautic, automotive industry, and storage devices [96, 103, 113, 115, 132, 139-142].

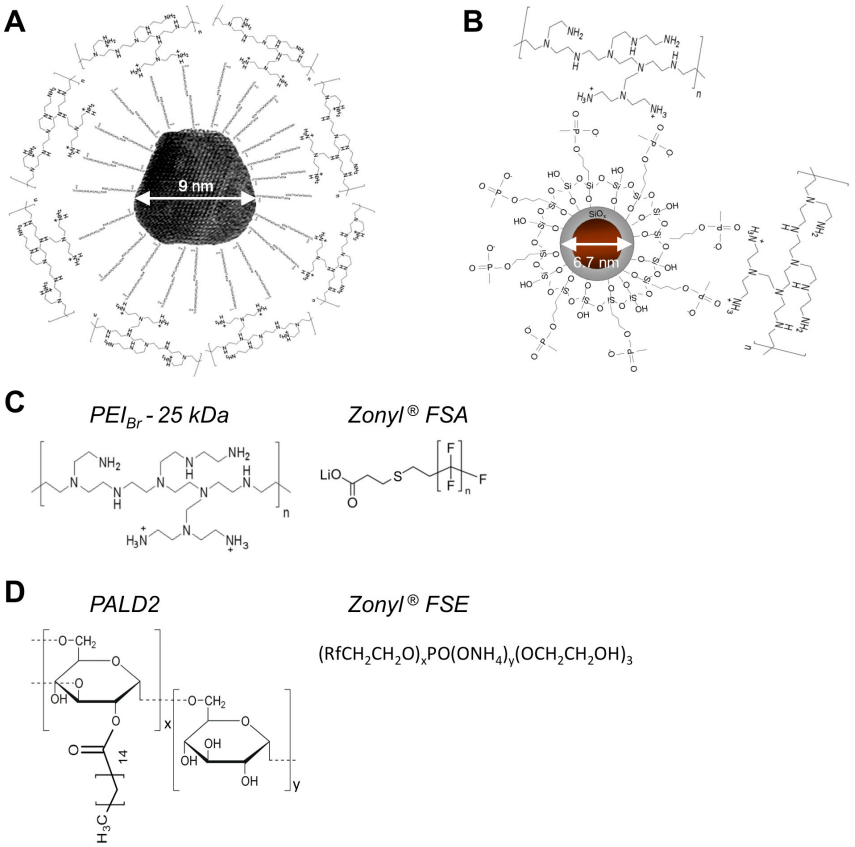

Figure 10: Core-shell type MNPs and their coating components. **A:** PEI-Mag2 particle, the coating comprises 32 mass% PEI$_{Br}$ and 68 mass% Zonyl® FSA. **B:** Silica-iron oxide MNPs SO-Mag6-11.5, decorated with PEI$_{Br}$ in a PEI-to-Fe w/w ratio of 11.5 %. **C:** Structural formulas of PEI$_{Br}$ and the fluoro-surfactant Zonyl® FSA. **D:** PALD2-Mag particles were stabilized using palmitoyldextran PALD2 (32 palmitoyl groups per *100* dextran units) and the anionic phosphate fluoro-surfactant Zonyl® FSE.

1.3.3.3.2 Magnetofection

Magnetofection is the technique of magnetically enhanced delivery of magnetic formulations into cells. It was invented independently in two groups back in the year 2000 for the delivery of small molecules into hard-to-transfect cells. The first references on the topic of magnetofection were conference abstracts by Mah et *al*. [143] and Plank et *al*. [144]. The contributions of Scherer et *al*. [114] on non-viral and viral magnetofection and Mah et *al*. [145] on recombinant adeno-associated virus delivery were among the first articles addressing the new technique. The sketches in figure 11 by Plank et *al*. schematically explain the principle of magnetofection in general (figure 11A; [146]), and for the delivery of nucleic acids in an *in vitro* set-up (figure 11B; [147]).

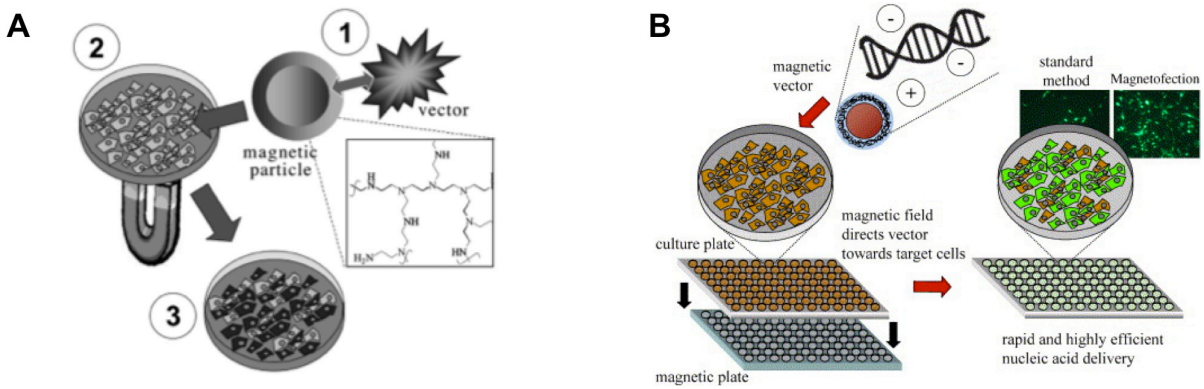

Figure 11: General principle of magnetofection (A; [146]**) and magnetofection for *in vitro* nucleic acid delivery (B;** [147]**)**

Since the pioneering work in our group, this technique was broadly adapted for viral and non-viral transfection with DNA, mRNA and siRNA for example in gene silencing approaches [106, 147-149]. Nowadays, magnetofection is well established for the delivery of nucleic acids under the guidance of an external magnetic field into cells or tissue by association with for example PEI- or silica oxide-coated MNPs [111, 114, 143, 144, 150].
Great advantages over chemical enhancers are easy, non-invasive and effective applicability, without negative effects. Moreover, acceleration of the kinetic course of infection could be useful in avoiding nucleic acid inactivation and immune response [110]. The technique was already tested in *in vivo* approaches, for example feline fibrosarcomas could successfully be treated applying magnetofection for nucleic acid delivery [151]. Progress was also made in the field of aerosol guidance for the treatment of respiratory tract diseases. There, the external magnetic field-mediated guidance could increase the gene delivery from viral and non-viral vectors into the airway epithelium of specific regions of the lung *ex vivo* and *in vivo* [152-154].

1.3.3.3.3 Viral and non-viral vectors

In the treatment of diseases like cancer, genetic disorders, and chronic and acute diseases, viral [155-157] and non-viral vector-mediated nucleic acid therapies [158] are rapidly developing approaches [159]. The assembly of vectors with MNPs is often based on electrostatic interactions [147]. Thus the composition of the MNP-coating could positively influence the association of nucleic acids with the magnetic carrier particles, as for example positively charged PEI facilitates assembly with negatively charged DNA and RNA into stable complexes. In addition, PEI protects the nucleic acids from degradation, enhances the cell uptake via endocytosis, and, inside the endosomes, it enhances the release of the complexes into the cytosol [62, 160-162]. Viral vectors as well as non-viral vectors could be tailored in their composition to the application-specific needs.

1.3.3.3.3.1 Oncolytic viruses

The National Cancer Institute at the National Institutes of Health, USA, defines an oncolytic virus as: *"A type of virus that infects and lyses (breaks down) cancer cells but not normal cells. Oncolytic viruses can occur naturally, or could be made in the laboratory by changing other viruses. Certain oncolytic viruses are being studied in the treatment of cancer. They may make it easier to kill tumor cells with chemotherapy and radiation therapy."*
Often utilized viruses are adenovirus (Ad), herpes simplex virus, Newcastle disease virus and vesicular stomatitis virus (VSV) [163, 164]. Important for efficient delivery of the oncolytic virus particles (VPs) is the assembly into shielded and stabilized formulations, for example with MNPs (figure 9A), especially when administered via the systemic route. Magnetic targeting could further increase local titers in the tumor. The utilization of MNPs for virus functionalization also enables for real-time monitoring of the VP delivery *in vivo* by MRI.

Big advantage of oncolytic viruses is their specificity to tumor cells, it is very unlikely that they infect healthy tissue [155-157, 163, 164]. In addition, they can be genetically engineered to eliminate their pathogenicity without destroying their oncolytic potency, enhance their tumor specificity, and, eventually, to introduce additional application-specific needs [163, 165]. After induction of cancer cell death, new virus particles are released during lysis, and the pro-inflammatory microenvironment might also induce an anti-tumoral response of the immune system [164, 165]. When utilized as nucleic acid nanocarrier, another important aspect of viral vectors is their highly efficient transfection, which could not be achieved with non-viral formulations so far [159, 166]. All this makes oncolytic viruses versatile platforms for molecularly targeted tumor therapies, maybe even more promising than traditional approaches, as such therapy approaches not affected by the increasing problem of cancer cell resistance to chemotherapeutics [165].

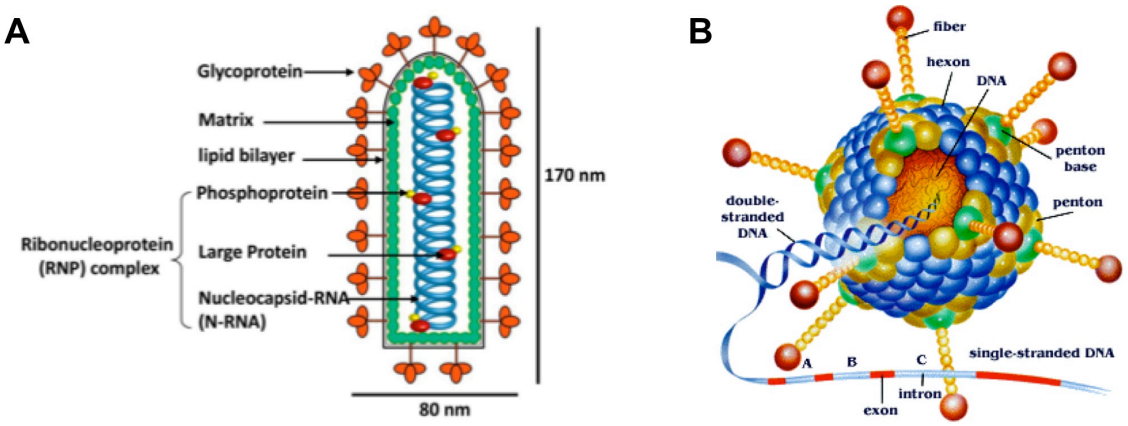

Figure 12: Schematical virus structures: VSV (A; [167]**) and Ad (B;** [168]**).**

1.3.3.3.3.1.1 Vesicular stomatitis virus (VSV)

The vesicular stomatitis virus (figure 12A; [167]) is a negative-stranded RNA virus of the *Rhabdoviridae* family. It specifically replicates in type I interferon deficient cells, a characteristic of several cancer cell types (figure 13; [169]). Natural hosts of the virus are cattle, horses, pigs and insects in which VSV evokes symptoms comparable to foot and mouth disease [164].

VSV has been successfully used pre-clinically for the treatment of various cancers, including multifocal hepatocellular carcinoma lesions (HCC) in rat models [164, 170, 171]. One of its advantages is the short replication cycle, reaching high number of copies within 24 hours post infection, and thus the ability to reach high titers in the microenvironment of many cancers. Representative results of VSV treatment in rat HCC models *in vivo* are summarized in figure 14. A rat bearing multifocal HCC lesions was viro-embolized with VSV by hepatic artery infusion (figure 14A), and compared to control animals, a prolonged survival of treated rats could be achieved (figure 14B) [170].

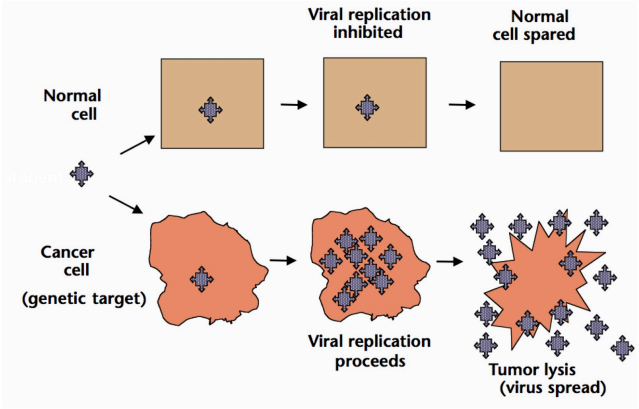

Figure 13: Tumor cell-selective viral replication and oncolysis of VSV [63].

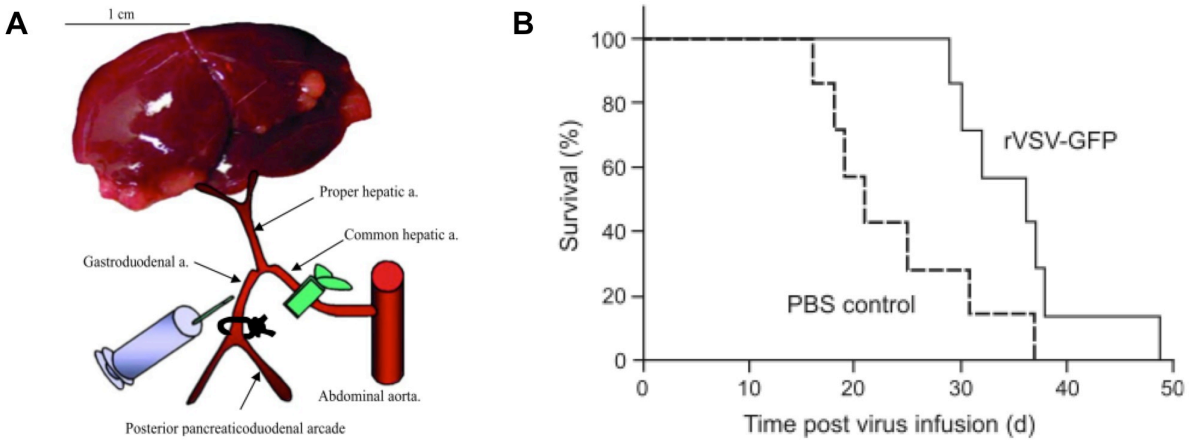

Figure 14: HCC viro-embolization with VSV [170] **A:** Representative picture of a rat liver with multifocal HCC lesions and the schematical representation of the hepatic arterial infusion procedure for administration of VSV. **B:** Rat survival after arterial VSV viro-embolization.

1.3.3.3.3.1.2 Adenovirus (Ad)

Adenoviruses were among the first viral gene vector systems, and due to their long history they are well established [163, 172]. The *Adenoviridae* family comprises more than 50 different serotypes of human adenoviruses and multiple non-human serotypes [173]. The icosaedric virus capsid envelopes the double-strand virus DNA (figure 12B; [168]), which transcribes the ability to transduce both, quiescent and dividing cells, and in addition offers a high cloning capacity of up to 37 kb [174].

Adenoviral vectors are classified among the most powerful gene delivery systems [110], especially when assembled with MNPs for magneto-transduction approaches. That was shown to reduce immune system inactivation and enhance oncolytic potency [114, 175]. Besides the high capacity for modification, the big advantage of adenoviruses is their low oncogenic potential as compared to retro- and lentiviral vectors - they do not insert their genome into the target cell DNA [176]. Adenoviruses have been tested for the treatment of several cancer types [157, 177], and are used in several gene therapy trials. In China, it was approved for the treatment of head and neck cancer [178] and nasopharyngeal cancer [179] in 2005, and pre-clinically tested in glioblastoma und cervical tumors.

1.3.3.3.3.2 Non-viral formulations

Gene therapy is an upcoming alternative to conventional treatments and opens options for previously hard-to-treat genetic and acquired diseases. Obstacle is the delivery of the sensitive nucleic acids to the target tissue without early inactivation in the circulatory system by nucleases. In the recent years, a lot of work was done on non-viral vectors loaded with plasmid DNA (pDNA) or (si)RNA for gene therapy applications [61, 112, 113, 132, 149, 166, 180-182]. The spontaneous assembly of negatively charged nucleic acids with MNPs (figure 9B) and surface modification with for example cationic lipids or polymers such as PEI resulted in biocompatible formulations for targeted delivery approaches [183] and high transfection efficiencies [182-184]. Examples for non-viral nanocarrier structures are lipoplexes, polyplexes and MNP-siRNA complexes [112, 180, 185]. Advantages over viral vectors are their safety, biocompatibility, adaptability and efficiency in large-scale production, size, gene-carrying capacity, specificity through functionalization with targeting ligands, low immunogenicity, stability, and sufficient release into the cytoplasm [159, 166].

First *in vitro* and *in vivo* approaches on non-viral constructs loaded with nucleic acids and coupled to PEI-coated MNPs were performed in the early 2000s [114, 186-189]. Surface functionalization with targeting moieties in combination with magnetofection was revolutionizing regarding nucleic acid delivery. The magnetofection process is pretty fast and in *in vitro* experiments, a few minutes of incubation with a magnetic field applied were sufficient for successful transfection [132, 188, 189]. Successful transfection could easily be proven with nucleic acids coding for reporter genes. Often used reporter genes are (enhanced) green fluorescent protein ((e)GFP) [100, 112, 113, 180] and luciferase [111, 190] as there are several assays available. After successful proof-of-principle studies, Wu et *al*. used RNA interference (RNAi) successfully for target-specific nucleic acid delivery in a murine HCC model. They synthesized multifunctional carriers comprised of siRNA targeting human HCC cells, PEG- and PEI-coated MNPs for MRI contrast, and tripeptide arginine-glycine-aspartic acid (RGD)-functionalization for specific targeting [4].

1.3.3.3.4 Magnetic liposomes

Magnetic liposomes are predominantly examined in the field of liposomal drug delivery [191-194]. As for all nanocarrier formulations, encapsulation helps to stabilize and shield therapeutic agents within the bloodstream to increase their efficacy and decrease side-effects from off-target delivery [195].

Structurally, liposomes consist of a lipid bilayer enclosing a liquid filled core, and thus provide binding sites for both, hydrophilic and lipophilic molecules, during synthesis. Lipophilic molecules can incorporate into the bilayer beneath the lipid chains [196], hydrophilic substances can be encapsulated into the aqueous core liquid [197, 198]. Further liposome functionalizations to increase the EPR-mediated accumulation at the target tissue include loading of MNPs, PEGylation of the surface lipids [92, 199], and coupling of target-

specific moieties (figure 9C). Possible candidates are antibodies [191, 200, 201], the vitamin folic acid [96, 202-206] and the tripeptide RGD [4, 59, 186, 207-210]. Both, folic acid and RGD are potential targets in HCC and PDAC therapy as their pendants folate receptor and $\alpha_v\beta_3$ integrin receptor are up-regulated in tumor cells [4, 59, 96, 186, 202-210]. PEGylation of the surface lipids results in stealth liposomes with increased stability in the blood circulation and reduced uptake into the RES, preventing hepatic drug overload [92, 199]. Labeling of liposomes with MRI probes enables for real-time monitoring of (magnetically enhanced) accumulation at the target site, and hence estimation of delivered drug [63, 139, 211-214].

1.3.3.3.5 Hyperthermia

Magnetic nanocarriers could also be utilized in therapeutic hyperthermia approaches [117-119]. In hyperthermic treatments, the local temperature in cancerous tissue gets elevated by either external heating sources or within the target tissue starting from therapeutic agents. Aim is the temperature-induced irreparable damage or death of tumor cells [59, 215]. In addition, the tumor gets sensitized for parallel radio- or chemotherapy [216]. Therapeutic formulations for hyperthermia treatments include MNPs and thermosensitive liposomes [96, 199, 217].

The delivery of therapeutic agents in hyperthermia approaches is based on the temperature-induced enhancement of natural extravasation into tumor tissue due to increased vessel permeability. At normothermia conditions of up to 39 °C, the EPR allows extravasation of particles up to 100 nm, at hyperthermia conditions above 42 °C, the cut-off for enhanced extravasation increased up to 400 nm due [218-221]. Hyperthermia was also shown to increase the blood flow which additionally could lead to better accumulation [221], especially if further supported by magnetic targeting. Further elevation of the tissue temperature resulted in hemorrhage and stasis in examined vessels [219, 220].

Besides their capability as targeting agent, the MNPs could be exploited as heating source within the target region with an AMF applied [96, 199, 217, 222-224]. AMF for hyperthermia induction was found to even have a better penetration than HIFU, laser, radiofrequency or microwaves [225]. NanoTherm® by MagForce® is the first approved pharmaceutical formulation consisting of SPIOs with aminosilane coating for fine dispersion in water and long-term localization at the target site, allowing for repeated treatments. It is successfully applied in the treatment of glioblastomas. After administration, the patient is exposed to a local alternating magnetic field (AMF) the heat the particles [216].

Thermosensitive liposomes are specifically designed to release the encapsulated cargo at the lipid transition temperature T_m [96, 213, 226-228]. For potential *in vivo* approaches, release should start above 40 °C to prevent unspecific liberation [96, 193, 213, 222, 223, 225, 228-232]. The addition of PEG lowered the transition temperature, and led to faster release at T_m, better stability below T_m and higher drug delivery, also farther from the vessels [221]. The clinically approved thermosensitve liposomes ThermoDOX® were evaluated in

several clinical studies on HCC [233-237] and breast cancer [238-241]. Between 2008 and 2017, there were several phase III studies on HCC, partly in combination with radiofrequency ablation [233-236].

1.4 Aim of the study

Hepatocellular carcinoma and pancreatic ductal adenocarcinoma are severe tumors with high incidence and mortality rates. Both cancers do not present clear symptoms, and therefore are often diagnosed in advanced stages. By then, the tumors of many patients are not capable of resection anymore and palliative and adjuvant treatments are the therapies of choice. Especially in PDAC it is difficult to improve the diagnosis due to its status as silent disease, but HCC patients were mostly cirrhotic before the HCC developed. Improved diagnostic, ideally with parallel delivery of therapeutic agents, could enhance the therapeutic outcome. For PDAC, the main focus was set on the improvement of drug delivery to overcome the poor chemotherapeutic efficiency. In both cancers, tumor cell-specific nanocarriers could improve the non-invasive and non-radiation detection of distant metastasis.
In this study, we aimed to develop nanocarrier formulations for three different therapeutic approaches: MNP-VP complexes with oncolytic viruses to specifically infect tumor cells, MNP-siRNA complexes in a proof-of-principle set-up for future gene-silencing approaches targeting oncogenes, and magnetic liposomes for targeted drug delivery and release. Core component of the magnetic nanocarrier formulations were iron oxide MNPs. The adjustability of surface composition, high surface area-to-volume ratio and magnetic moment made the chosen core-shell type MNPs ideal candidates for the assembly of nanocarrier formulations, magnetically enhanced delivery, magnetofection, and as MRI contrast probes. The latter allow parallel examination of MRI imaging properties due to SPIO-induced T_2 signal attenuation after *in vivo* administration. Figure 15 schematically presents magnetic targeting of our nanocarrier systems *in vivo* in PDAC (figure 15A) and exemplary MRI scans of accumulated MNP-VP complexes in a HCC model (figure 15B).

All *in vitro* experiments were performed in HCC and PDAC cell lines of human and rodent origin. The MNPs were previously synthesized in our lab, viruses were amplified specifically for this study. As all nanocarrier formulations were characterized for their potential transferability into clinical approaches, it was important to test them for potential toxicity in animal models. Thus, PALD2-Mag particles were examined in a mouse study. PEI-Mag and SO-Mag particles were previously used for pre-clinical approaches, the *in vivo* toxicity study was not repeated.

MNP-VP complexes were tested in tumor therapy approaches to utilize the cancer cell-specificity of oncolytic viruses, i.e. Ad and VSV, combined with MNP-based magnetic targeting of the formulation. In *in vitro* and *in vivo* experiments, the viral complexes were

analyzed for their oncolytic activity, virus delivery efficiency and possibility to non-invasively identify the formulation by MRI. Tissue-mimicking *in vitro* phantoms were prepared and characterized for quantification of MRI detection limits regarding the amount of MNPs needed for sufficient contrast, and to provide the basis for estimation of virus delivery efficiency in further *in vivo* approaches. Such MNP-VP complexes are a promising approach especially for the treatment of chemo-resistant tumor lesions in non-resectable patients as well as metastasis detection and treatment in very localized and target tissue-specific manner.

MNP-siRNA complexes are an excellent formulation for the targeted delivery of nucleic acids. In this study, proof-of-principle experiments should show how they enable for the knock-down of reporter genes. In further pre-clinical approaches, the delivery of oncogene-specific nucleic acids towards tumor cells could help to stop tumor expansion, again in a very localized approach due to the magnetic targeting.

Magnetic liposomes provide various options for application-specific tailoring. To identify the optimal synthesis protocol for our liposomes, different methods were compared. They were loaded with chemotherapeutic drug, and MNPs for targeting and monitoring. The lipid bilayer was composed to release the cargo temperature-dependently and further surface functionalization with PEG and a RGD-like structure would stabilize the LPs and enhance tumor cell targeting and, thus, increase drug delivery efficiency. Stabilization of the MNP-LPs, their biodistribution and ability for magnetic targeting were analyzed in proof-of-principle *in vivo* experiments.

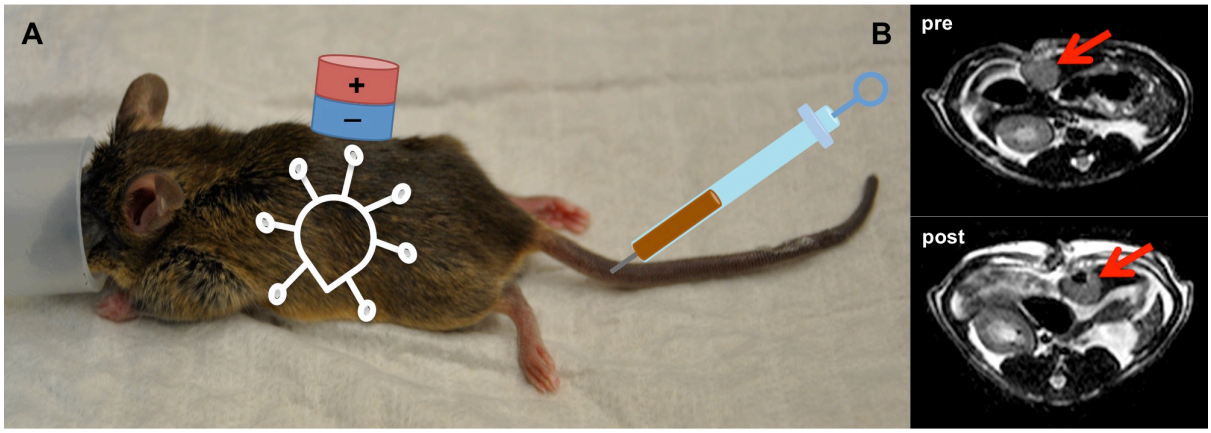

Figure 15: Schematical setup of magnetic targeting in gastro-intestinal cancers. A: Magnetic targeting of a systemically administered nanocarrier formulation in murine PDAC. **B:** Hypointense MRI signal due to MNP-accumulation in a rat HCC tumor nodule (red arrow) before (top) and after (bottom) magnetic targeting.

2 EXPERIMENTAL

2.1 Material

2.1.1 Technical equipment

1.5 T Achieva and 3.0 T Ingenia	Philips Medical Systems, Best, the Netherlands
Beckman DU 640 spectrophotometer	Beckman Coulter Inc., Krefeld, Germany
Infinite M1000Pro	Tecan Trading AG, Switzerland
Malvern 3000 HS Zetasizer	Malvern Instruments Ltd, UK
Microplate Scintillation & Luminescence Counter	Packard Instrument Co., Inc./Canberra Industries, & Meriden, CT, USA
Rotavapor (Rotary evaporator)	Büchi Labortechnik GmbH, Essen, Germany
Wallac 1420 VICTOR^2	PerkinElmer, Waltham, MA, USA
Zeiss Libra 120 Plus (TEM)	Carl Zeiss NTS GmbH, Oberkochen, Germany

All analysis was done using MS Excel (Microsoft Corporation, Redmont, USA) and the graphs were generated with Prism (GraphPad Software, Inc., La Jolla, CA, USA).

2.1.2 Reagents

Agarose	Biozym, Oldendorf, Germany
Isofluorane	VetOne^{TM}, MWI, Meridian
Control (non-sil.) siRNA (5 nm)	Qiagen, Hilden, Germany
GFP-22 siRNA (5 nm)	Qiagen, Hilden, Germany
Luciferase GL3 siRNA (5 nm)	Qiagen, Hilden, Germany
DPPC (1,2-dipalmitoyl-*sn*-glycero-3-phosphocholine)	Avanti Polar Lipids, Inc., Alabaster, Alabama, USA
DSPC (1,2-distearoyl-*sn*-glycero-3-phosphocholine)	Avanti Polar Lipids, Inc., Alabaster, Alabama, USA

If not declared differently, all other chemicals and reagents were purchased from Carl Roth, GmbH & Co. KG (Karlsruhe, Germany), Merck (Darmstadt, Germany), Sigma-Aldrich (Steinheim, Germany), or ThermoFisher Scientific (Darmstadt, Germany).

2.1.3 Media

Dulbecco´s Modified Eagle´s Medium (DMEM), Dulbecco´s phosphate-buffered saline (PBS) (with and w/o Mg^{2+}, Ca^{2+}), fetal calf serum (FCS) and L-glutamine were purchased from Gibco® Life Technologies, Darmstadt, Germany. Non-essential amino acids, penicillin/streptomycin and trypsin/EDTA (0.25%/0.02%) were bought from PAA Laboratories GmbH, Pasching, Austria.

2.1.4 Animals, cells, viruses and vectors

Provided by Dr Altomonte (II. Med Clinic, Gastroenterology, RdI, TUM):

Baby hamster kidney cells BHK-21 (American Type Culture Collection (ATCC), LGC Standards GmbH, Wesel, Germany)

Buffalo rats (Harlan Winkelmann, Borchen, Germany)

HuH-7 human hepatocellular carcinoma cell line

Rat Morris hepatocellular carcinoma cells (McA-RH7777) (American Type Culture Collection (ATCC), LGC Standards GmbH, Wesel, Germany)

Human liver carcinoma cell line HepG2 (HepG2 ATCC® HB-8065TM)

rVSV-GFP

Provided by Dr Heid (Diagnostic and Interventional Radiology, RdI, TUM):

BL/6 CKp53lox mice ($Ptf1\alpha^{wt/Cre}$; $Kras^{wt/LSL\text{-}G12D}$; $p53^{fl/fl}$)

Provided by Dr Mykhaylyk/Dr Holm (Experimental Oncology and Therapy Research, RdI, TUM):

E1A mutant adenovirus dl520

MDR human pancreatic carcinoma cells EPP85-181RDB

Parental human pancreatic carcinoma cells EPP85-181P

Provided by Dr Anton (Experimental Oncology and Therapy Research, RdI, TUM):

LV-PGK-eGFP-Luc-fusion construct

Provided by Dr Trajkovic-Arsic (II. Med Clinic, Gastroenterology, RdI, TUM):

Murine pancreatic ductal adenocarcinoma primary cells from CKp53lox mice ($Ptf1\alpha^{wt/Cre}$; $Kras^{wt/LSL\text{-}G12D}$; $p53^{fl/fl}$)

2.2 Experimental

In this thesis the development and characterization of three different nanocarrier systems, namely MNP-VP complexes, MNP-siRNA complexes and magnetic liposomes, is described. Essential component of all three nanocarrier systems are magnetic nanoparticles. Therefore, in the first section the synthesis of the different MNPs is described. The further experimental chapter is structured into three parts, each describing one nanocarrier system.

2.2.1 MNPs

Core–shell type iron oxide nanoparticles all consist of a magnetic iron core and different surface functionalizations. The composition of those surface modifications influences the charge of the MNPs.

The magnetic core particles were synthesized by precipitation of the Fe(II)/Fe(III) hydroxide from aqueous solution, followed by transformation into magnetic iron oxide in an oxygen-free atmosphere [242]. The condensation of tetraethyl orthosilicate (TEOS) and 3-(trihydroxysilyl)propylmethylphosphonate (THPMP) resulted in the SO-Mag5 particles comprising a surface coating of a silicon oxide layer with surface phosphonate groups (SiO_x/phosphonate) [243].

For assembling with negatively charged nanostructures such as virus particles and nucleic acids, the SO-Mag5 nanoparticles were decorated with PEI. Surface modification at a PEI-to-iron (w/w) ratio of 11.5 % formed the positively charged SO-Mag6-11.5 nanoparticles and further referred to as SO-Mag particles. The exact synthesis procedure was previously described in [115].

The positively PEI-Mag2 nanoparticles, further referred to as PEI-Mag particles, were generated by spontaneous adsorption of the fluorosurfactant lithium 3-[2-(perfluoroalkyl)ethylthio]propionate (Zonyl® FSA) and 25-kDa branched polyethyleneimine ($PEI_{Br\text{-}25}$ kDa) onto the iron oxide core particles as described previously in detail by [100, 113, 243].

Negatively charged MNPs can be used for the inclusion in magnetic liposomes. The detailed synthesis of PALD2-Mag particles was described by [180]. Surface coating of those particles resulted from the spontaneous adsorption of the fluorosurfactant ammonium bis[2-(perfluoroalkyl)ethyl]phosphate (Zonyl® FSE) and the palmitoyl dextran PALD2 [79, 180].

The synthesis of all MNPs was kindly performed by Dr Mykhaylyk, Group of Prof Plank, Department of Experimental Oncology and Therapy Research, Klinikum rechts der Isar der Technischen Universität München.

2.2.2 Magnetic nanocarriers

2.2.2.1 MNP-VP complexes

2.2.2.1.1 Cell culture

The rat Morris hepatocellular carcinoma cells (McA-RH7777), further referred to as McA cells, and the baby hamster kidney cells BHK-21 cells were purchased from the American Type Culture Collection, and were cultured in Dulbecco's modified Eagle's medium (DMEM; ATTC, Manassas, MA, USA) supplemented with 10 % heat-inactivated fetal calf serum (FCS), 100 U mL^{-1} penicillin, and 100 μg mL^{-1} streptomycin. The MDR human pancreatic adenocarcinoma cells EPP85-181RDB, further referred to as RDB cells, were grown in DMEM supplemented with 10 % heat-inactivated FCS and 1 % 2 mM L-glutamine.
The McA cells derive from a female Buffalo rat and show an epithelial morphology with loosely adherent growth, the RDB cell morphology is epithelial with adherent growth. All cell lines were spilt before reaching 100 % confluency. Briefly, the cell culture medium was aspirated and the cell monolayer was washed with pre-warmed PBS to remove any serum. Then pre-warmed trypsin/EDTA (0.25%/0.02%) was added and cell detachment was observed under the microscope (Carl Zeiss, Munich, Germany). Once the cells started to detach, warm culture medium containing serum was added to stop the trypsin reaction and the cells were split 1:4 to 1:6 into new cell culture dishes.
All cell lines were cultured at 37 °C in a humidified atmosphere containing 5 % CO_2.

2.2.2.1.2 Adenovirus and vesicular stomatitis virus

The E1A mutant adenovirus dl520, further referred to as Ad, was kindly provided by Dr Holm [244]. The Ad was expanded in 293 cells and purified by double cesium chloride (CsCl) gradient centrifugation, resulting in a virus stock containing 4.3 x 10^{12} VP/mL and 2.6 x 10^{11} transforming units per mL. Briefly, the 293 cells were infected with adenovirus and harvested when full cytopathic effect was observed. Cells and medium were harvested and centrifuged, then the pellet was resuspended in a smaller volume of the supernatant and the solution underwent freeze-thaw-cycles. After another centrifugation, the virus-containing supernatant was transferred as top layer onto 1.34 g/ml CsCl overlaid with 1.43 g/ml CsCl and centrifuged. The lower band containing intact virus particles underwent a second ultracentrifuge spin in 1.34 g/ml CsCl solution. After desalting using a sephadex PD-10 column, the purified virus stock could be stored at -80 °C [245]. To determine the physical virus particle titer, an aliquot of the virus stock was diluted 1 to 20 in Dulbecco's phosphate buffered saline (PBS) that contained 0.1 % sodium dodecyl sulfate, mixed thoroughly for 2 minutes and centrifuged at 8,000 g for 5 minutes [246]. The optical density (OD) at 260 nm was measured, and the physical virus titer was calculated, taking into account that an OD of 1 corresponds to 1.1 x 10^{12} VP/mL [247]. Aliquots of the stock were stored at -80 °C.

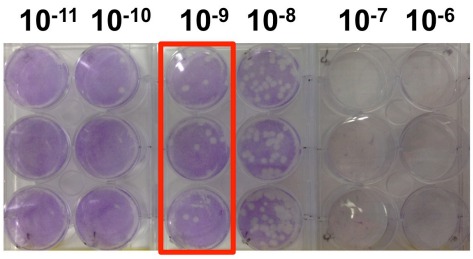

Figure 16: Plaque assay of sucrose-gradient purified VSV-GFP.

The rVSV-GFP, further referred to as VSV, was amplified on BHK-21 cells and the supernatant was purified by sucrose gradient centrifugation [170, 171]. Briefly, BHK-21 cells (90 % confluent) in 15 cm cell culture dishes were infected with VSV at a multiplicity of infection (MOI) of 0.0001 in OptiPRO SFM (ThermoFisher Scientific, Darmstadt, Germany), and 48 hours later the supernatant containing virus particles and floating cells was harvested. The cells were cleared by 10 minutes centrifugation at 1,500 rpm then the virus was pelleted by ultra-centrifugation for 1 hour at 25,000 rpm. The in PBS resuspended virus was layered on top of a 60 % / 30 % / 10 % sucrose gradient and purified by ultra-centrifugation at 25,000 rpm for 1 hour. The band containing the virus was carefully collected with a syringe and 20-gauge needle, and aliquots of the virus stock were stored at -80 °C. This virus stock contained 6.6 x 10^9 pfu/mL as was determined by plaque assay. Briefly, the virus was serial diluted in PBS with 1 mM $MgCl_2$ and $CaCl_2$, then BHK-21 cells (90 % confluent) in 6-well plates were infected with the VSV dilutions for 1 hour. The three times rinsed cell layers were then overlayed with 0.9 % agarose in GMEM (ThermoFisher Scientific, Darmstadt, Germany), and further incubated at 37 °C for 48 hours. After 15 minutes crystal violet staining, the number of plaques could be counted and the titer calculated (average of 5 plaques/10^{-9} dilution means the titer is 5 x 10^9 pfu/mL). Figure 16 shows exemplary photographs of VSV plaque assay plates.

2.2.2.1.3 MNP-VP interaction

The question to be answered was to find a formulation, which could help to facilitate the localization of the oncolytic virus particles in the tumor region after systemic administration. To prepare such formulation, first the virus particles were assembled with magnetic nanoparticles to enable magnetic targeting and real-time monitoring of the applied virus by MRI. Those complexes were examined for their physico-chemical properties to identify the best composition. After this first step, the magnetic viral complexes were tested *in vitro* on cancer cells to evaluate the cell infection efficacy and the oncolytic potential of the formulations. Two types of particles, namely SO-Mag6-11.5 and PEI-Mag2, both positively charged, and two types of cancer cell lines, namely McA hepatoma and RDB pancreatic cancer cells were examined to identify the complex type with the best oncolytic potential for each cell line.

2.2.2.1.3.1 Preparation of magnetic viral complexes

Adenovirus complexes with MNPs were prepared as described previously by Tresilwised et *al.* [105]. Briefly, 10^{11} VP of the Ad diluted in 800 µL PBS were added to 200 µL of PEI-Mag2 or SO-Mag6-11.5 MNPs in ddH_2O containing 500 µg of Fe and mixed, resulting in an iron-to-physical virus particle ratio of 5 fg Fe/VP. The resulting complexes will be further referred to as PEI-Mag-Ad and SO-Mag-Ad complexes.

To prepare magnetic VSV complexes, equal volumes of ddH_2O containing MNPs of 226.8 µg iron and PBS containing 4.5 x 10^8 pfu or 2.3 x 10^8 pfu VSV were mixed in a final volume of 1,380 µL. The resulting ratios of MNP-to-virus were of 500 and 1,000 fg Fe/pfu, respectively, for PEI-Mag2 and SO-Mag6-11.5 particles, respectively. The resulting complexes will be further referred to as PEI-Mag-VSV and SO-Mag-VSV complexes.

After an incubation period of 20 minutes at RT to allow complex assembly, the volume was adjusted with PBS and the freshly prepared complexes were used for characterization of the magnetic vectors, cell infection, phantom preparation, or *in vivo* experiments as described in the following sections.

2.2.2.1.3.2 Titration and characterization of MNP-VP complexes

To identify the optimal iron-to-virus ratio for the magnetic viral complexes, a fix amount of virus was incubated with increasing concentrations of iron.

The titration for the adenovirus complexes was already performed by Tresilwised et *al.* and an optimal ratio of 5 fg Fe/pfu was determined [105].

$TCID_{50}$ assays were performed to identify the optimal condition for the according VSV complexes. Therefore, 10^8 pfu/mL VSV were titrated with increasing amounts of PEI-Mag and SO-Mag, respectively, at iron doses per viral pfu ranging between 0-750 and 0-1,250 fg Fe/pfu VSV. To determine at which iron-to-virus ratio most of the virus was complexed with the MNPs, the mixtures of the magnetic and viral particles were allowed to assemble for 15 minutes and subjected to gradient magnetic field to magnetically separate the magnetic fraction (MF) and the non-magnetic fraction (NMF). Both fractions were used for cell infection. Pure virus at a concentration of 10^8 pfu/mL served as positive control, just MNPs with the same iron concentration as used in the 500 fg Fe/pfu VSV sample as negative control.

Those batches of fractions were serial diluted and used in quadrupels for infection of BHK-21 cells (50 % confluent) in 96-well plates as shown in figure 23A. After 48 hours incubation, the $TCID_{50}$ values were calculated with the Spearman & Kärber algorithm [248]. In addition both, the fresh complex preparation and the magnetic fraction after separation, were analyzed regarding their physico-chemical properties zeta potential and hydrodynamic diameter.

2.2.2.1.3.3 Magnetic cell labeling and infection with magnetic viral complexes

The cells were grown in 75 cm^2 cell culture flasks (Techno Plastic Products, Trasadingen, Switzerland) and loaded with MNPs or infected with magnetic viral complexes when they reached 70 to 80 % confluency (4 - 6 x 10^6 cells per flask). 25 and 10 pg Fe/cell either free MNPs or complexed with Ad or VSV were applied in cell culture medium to the RDB and McA cells, respectively. Adenoviral complexes were applied at MOIs of 120, VSV complexes at MOIs of 20 (PEI-Mag-VSV) and 10 (SO-Mag-VSV). For the magnetofection [100], the magnetic field was applied by incubating the flasks on a magnetic plate (field strength and gradient at the cell layer location of 70–250 mT and of 50–130 T/m, respectively, OZ Biosciences, Marseille, France) for 30 minutes in the case of the RDB cells [105] and 1 hour for the McA cells at 37 °C. Afterwards, the RDB cells were incubated for another 3 hours in the incubator without magnetic field. The now labeled cells were washed with PBS three times to remove any loosely-bound particles or complexes. Next, the cells were trypsinized with 0.25 % trypsin/0.02 % EDTA solution. After washing with PBS, the cells were fixed with BD Cytofix™ (BD Biosciences, Heidelberg, Germany), washed three times with PBS and resuspended in PBS for use in cell characterization or phantom preparation.

2.2.2.1.3.4 Analysis of the exogenic non-heme iron content

The exogenic non-heme iron content of the magnetically (virus-)labeled cells was determined using a modified protocol of the Torrance and Bothwell method [100, 249]. Briefly, approximately 4 x 10^5 trypsinized cells were washed with PBS and pelleted. The in 500 μL acid mixture of 3 M HCl and 0.6 M trichloracetic acid contained resuspended cells were incubated overnight at 65 °C. To remove cell debris, the samples were centrifuged 5 minutes at 14,000 rpm and 50 μL of the clear supernatant were analyzed for the iron content by a colorimetric method with 1,10-phenanthroline. Therefore, the supernatant was mixed with 50 μL sterile water, 20 μL 10 % hydroxylamine-hydrochloride solution, 100 μL ammonium acetate buffer (25 g ammonium acetate and 70 ml glacial acetic acid with a total volume adjusted to 100 ml with ddH_2O), and 50 μL 0.1 % 1,10-phenanthroline solution. After 20 minutes reaction time, the OD was measured at 510 nm, the absorption maximum of the iron(II)-1,10-phenanthroline complex, in a Beckman DU 640 spectrophotometer (Beckman Coulter Inc., Krefeld, Germany). The iron content of the samples could be calculated using a calibration curve, determined from an iron stock solution (392,8 mg ammonium iron(II) sulfate hexahydrate, 2 mL concentrated H_2SO_4 and 10 mL ddH_2O water, titrated with 0.05 N $KMnO_4$ until a faint pink color persisted, followed by volume adjustment to 100 mL). Basal non-heme iron level determined in non-labeled cells was used as a reference.

2.2.2.1.3.5 Sample preparation and transmission electron microscopy (TEM)

For TEM analysis, about 10^5 labeled or infected cells were washed with PBS after trypsinization. Free MNP suspensions and free MNP-VP complexes, both containing about

the same amount of iron as applied to cells, and the cells were pelleted for 5 minutes at 1,600 rpm in beam tubes and the (cell) pellets were fixed with 2.5 % glutaraldehyde in 0.1 M sodium cacodylate buffer pH 7.4 TEM fixation buffer (Electron Microscopy Sciences, Hatfield, USA) at 4 °C. The samples were then post-fixed in 2 % aqueous osmium tetraoxide [250], dehydrated in gradual ethanol (30 – 100 %) and propylene oxide, embedded in Epon and dried for 24 hours at 60 °C. Semithin sections were cut and stained with toluidine blue. Ultrathin sections of 50 nm were collected onto 200 mesh copper grids (Sigma-Aldrich, Steinheim, Germany), stained with uranyl acetate and lead citrate before examination by TEM (Zeiss Libra 120 Plus, Carl Zeiss NTS GmbH, Oberkochen, Germany). Pictures were acquired using a Slow Scan CCD-camera (Olympus Soft Imaging Solutions, Münster, Germany) and the iTEM software (Olympus Soft Imaging Solutions, Münster, Germany).

2.2.2.1.3.6 Characterization of the oncolytic potential of MNP-VP complexes *in vitro*

The RDB cells and McA cells were seeded in 96-well cell culture plates at 10^4 cells per well and incubated at 37 °C 24 hours prior to infection. The cell culture medium in each well was replaced with 150 μL of fresh culture medium containing 10 % FCS or 66.7 % FCS, then 50 μL of virus or the magnetic viral complexes in serum free medium were added. The resulting medium was referred to as the infection medium with final FCS concentrations of 7.5 % or 50 %. To define the concentration required for 50 % cell growth inhibition (IC_{50}) for free virus or viral complexes, 2-to-1 serial dilutions of naked adenovirus ranging from 2.5 – 320 pfu/cell and from 0.625 – 80 pfu/cell for the MNP-Ad complexes, and MOIs of 0.005 - 10 for naked VSV and the MNP-VSV complexes were prepared, all in triplicates. If indicated, a magnetic field was applied by positioning the cell culture plates on a magnetic plate (OZ Biosciences, Marseille, France) for 30 minutes. No medium change was performed and the RDB and McA cells were incubated for 6 days and 24 hours, respectively.

The survival of infected RDB cells was evaluated 6 days after infection using luciferase assay (37). Briefly, the cells, which stably express firefly luciferase, in all wells were washed with PBS and lysed with 100 μL of lysis buffer per well. After incubation for 15 – 20 minutes at RT, 50 μL of cell lysate were transferred to the respective well in a 96-well black flat-bottom plate. Then, 100 μL of luciferin buffer (35 μM D-luciferin (Roche Diagnostics, Mannheim, Germany), 60 mM DTT, 10 mM magnesium sulfate, 1mM ATP, in 25 mM glycyl-glycin-NaOH buffer, pH 7.8) were added. The chemiluminescence intensity was measured in counts per min (CPM) using a Microplate Scintillation & Luminescence Counter (Packard Instrument Co., Inc./Canberra Industries, Meriden, CT, USA). The non-infected cells were used as reference representing 100 % viable cells. For background measurements, 50 μL of lysis buffer and 100 μL of luciferin buffer were used. The cell survival was calculated according to the following equation:

$$\text{Cell survival (\%)} = 100 * (CPM_{\text{infected cells}} - CPM_{\text{blank}}) / (CPM_{\text{uninfected cells}} - CPM_{\text{blank}})$$

The viability of the McA cells was assessed 24 hours after infection by MTT assay, based on reduction of the MTT reagent into formazan by superoxide anion radicals produced in the mitochondrial respiratory chain [251, 252]. Briefly, infected cells were washed with PBS and 100 µL of MTT solution (1 mg/mL MTT in 5 mg/mL glucose) were added per well. After 2 hours incubation at 37 °C, viable cells formed formazan crystals, which were lysed with 100 µL solubilization solution (10 % Triton X-100 in 0.1 N HCl in anhydrous isopropanol) over night, incubation at RT in the dark. The solved crystals, representing the respiration activity of the cells, were quantified using a Wallac 1420 VICTOR^2 microplate reader at a wavelength of 590 nm. To evaluate the effect of free MNPs on the viability, control cells were treated with MNPs in the same concentration range and analyzed under the same conditions. Again non-infected cells were used as reference representing 100 % viable cells; the background was determined from 100 µL MTT solution with 100 µL solubilization solution. The acquired cell survival data were plotted against logarithms of the applied virus dose (pfu/cell) and were fitted using the "DoseResponse" function of OriginPro 9G software (OriginLab Corporation, Northampton, MA, USA) to calculate the needed doses of virus resulting in 50 % cell growth inhibition (IC_{50} values).

2.2.2.1.3.7 Magnetophoretic mobility measurements

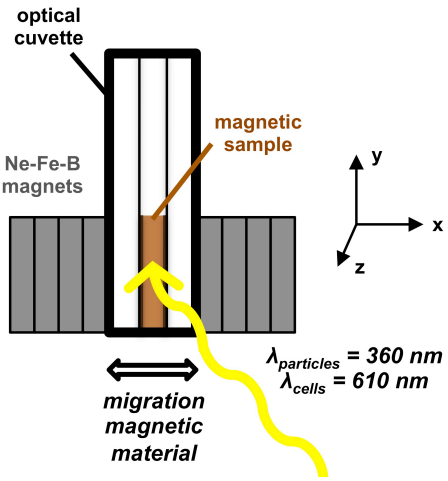

Figure 17: Setup magnetophoretic mobility measurements. Magnetic responsiveness in µm/sec (modified from [67]).

To characterize the magnetic responsiveness of the magnetically labeled cells and the MNP-VP complexes, the time course of the decreasing turbidity of the suspensions when subjected to inhomogeneous magnetic fields was measured [180, 181]. Briefly, a gradient field was generated by positioning two mutually attracting packs of four quadrangular neodymium-iron-boron permanent magnets symmetrically on each side of a cuvette holder, parallel to a beam of light, for optical density measurements. The magnetic field between the magnets was measured with a Hall detector using a grid of step size 1 mm, and the average magnetic field and the resulting field gradient were calculated to be 0.213 T and 4 ± 2 T/m in the direction of the complex movement (figure 17). The complex and cell suspensions were diluted to 500 µL aliquots to achieve a starting OD = 0.3–1 at the analytical wavelength of 610 nm for the labeled cells and 360 nm for the magnetic viral complexes. Optical cuvettes filled with these diluted suspensions were placed in a Beckman DU 640 spectrophotometer and the change in the optical density or turbidity was immediately recorded over 30 minutes.

2.2.2.1.4 Magnetic resonance imaging

Long-term aim was to facilitate the real-time monitoring and localization of the systemically applied oncolytic virus complexes. To examine the MNP-VP complexes for their imaging properties, complexes and infected cells were prepared under the identified most effective conditions. Then tissue-mimicking agarose phantoms were prepared from those complexes as well as from infected cells, both with known iron concentrations and sample material homogenously dispersed in the gel. In addition, there were phantoms prepared with certain iron concentrations either as homogenously dispersed free or cell internalized MNPs in dilution series, and phantoms prepared with clotted sample material.

2.2.2.1.4.1 Cell labeling and infection for phantom preparation

For the MNP-VP complex phantoms (dispersed and clotted), the cells were infected and prepared as described under 2.2.2.1.3.3.

For the MRI phantoms prepared from free MNPs and cells with internalized MNPs, described in figure 28, the cell labeling conditions were identified in saturation experiments. Therefore, McA and murine PDAC cells were magnetofected with increasing amounts of MNPs, and after non-heme iron quantification with 1,10-phenantroline, the internalized/associated iron was plotted against the applied iron. From the saturation curves 100 pg Fe/cell was identified as good labeling condition. Then 511181 cells were seeded at a density of 46,667 cells per cm^2 in a 75 cm^2 dish, while McA cells were seeded at a density of 8 x 10^4 cells per cm^2 in a 75 cm^2 dish. 24 hours post cell seeding, 100 pg Fe/cell SO-Mag6-11.5 particle suspension in cell culture medium was applied. Then, the cell culture flasks were placed on a plate magnet (OZ Biosciences, Marseille, France) for 30 minutes in the incubator. After the magnetofection, cells and MNPs were further incubated for 24 hours. The harvested cells were fixed and stored at 4 °C in PBS/0.5% NaN_3 until usage as previously described. This procedure was performed analogous for all other cell lines, complexes, and the PEI-Mag particles and complexes.

2.2.2.1.4.2 Preparation of calibration phantoms for MRI

Calibration phantoms for MR imaging were prepared with free MNPs, free MNP-VP complexes, cells labeled with MNPs and cells infected with MNP-VP complexes, respectively, all homogeneously dispersed in agarose gel in 24-well plates [67, 115]. Briefly, according to Christoffersson et *al.* tissue-mimicking phantom material can be prepared by using different concentrations of nickel and agarose to modulate the relaxation times of the gel [65]. Increasing nickel(II) ion concentration shifts the T_1 values to longer relaxation times, while increasing agarose concentration results in T_2 relaxation time shortening. The gel phantom mimicking relaxivity of murine liver tissue (T_1 = 550 ms and T_2 = 48 ms; table 4) was prepared with 1.98 mM nickel(II) nitrate, 2.45 % agarose, and 0.5 % sodium azide for preservative purposes [253].

tissue	organism	T_1 [ms]	T_2 [ms]	reference
liver	mouse	550	48	data not shown
liver	mouse	576 ± 30	46 ± 6	Stanisz et al, 2005
PDAC	mouse	1,200	115	data not shown
heart	mouse	1,030 ± 34	40 ± 6	Stanisz et al, 2005
muscle	mouse	1,008 ± 20	44 ± 6	Stanisz et al, 2005
liver	rat	525	49	data not shown
kidney	rat	690 ± 30	55 ± 3	Stanisz et al, 2005
spinal cord	rat	745 ± 37	74 ± 6	Stanisz et al, 2005

Table 4: Relaxation times used for tissue-mimicking: T_1 and T_2 of different body tissues [47].

2-to-3 dilution series were prepared for all samples, in water for free MNPs, and in PBS for free MNP-VP complexes and magnetically labeled and infected cells. The maximal iron [in mM Fe/well] and cell [in cells/mL] concentrations present in well 1, as well as the respective cell labeling [in pg Fe/cell] and labeling efficiencies are summarized in table 5. To prove detectability of the MNP iron in surrounding liver tissue, and to exclude air artifacts during the MR image acquisition, the 12 wells between the sample wells and the cavities between the wells on both sides were filled with the described Ni-containing agarose gel. Figure 18A shows the schematical setup of the phantom plates. For the 11 sample wells and the reference well, gel with 1.5-fold higher concentrations of the nickel salt, agarose (Biozym, Oldendorf, Germany) and sodium azide was prepared and 3 mL of to 60 °C pre-warmed agarose gel were vortex-mixed with 1.5 mL sample in 15 mL falcon tubes to distribute the nanomaterial homogenously, and transferred into the designated well avoiding air bubbles. Well R contained only water/PBS mixed with this agarose gel and served as a reference well for background normalization. To identify potential relaxivity changes caused by the cell background, phantom plates with untreated, fixed cells were prepared. The phantom plates were allowed to cool down slowly to RT, and sealed with parafilm (Brand GmbH & Co. KG, Grafrath, Germany) to avoid evaporation of water during their storage at 4 °C.

In addition to the phantoms with homogenously dispersed sample material, clot phantoms were prepared. Therefore, sample material was mixed to a total volume of 120 µL with 1 % alginate as coagulant agent, 40 mM $CaCl_2$, and PBS/0.5 % NaN_3. To identify optimal clotting conditions, per well 50 µL medium were mixed with 50 µL 2 % alginate and either transferred directly to the wells of a 96-well plate, or added to wells prepared with $CaCl_2$ in increasing volumes ranging from 5 µL to 100 µL; to the wells prepared with the alginate mix, the same increasing volumes of $CaCl_2$ were added (figure 18B, “Ca” means $CaCl_2$ first, “P” means sample first). The clot forming was supported either by incubating the plate on a 37 °C ThermoMixer, or by using a hair dryer for heating. The geling process took about 15 minutes, then the clots could be removed from the wells using a small curved spatula. Optimal clot formation was observed when 100 µL sample were added onto 20 µL $CaCl_2$ followed by short hair dryer heating and incubation for 15 minutes.

Clots were prepared from free MNPs, MNP-VP complexes, and cells with internalized MNP(-VPs). The gelled clots were transferred to a phantom plate prepared with 1.5 mL agarose in

the sample wells, placed in the middle on top of the hardened agarose, and covered with another 1.5 mL agarose gel (figure 18C).

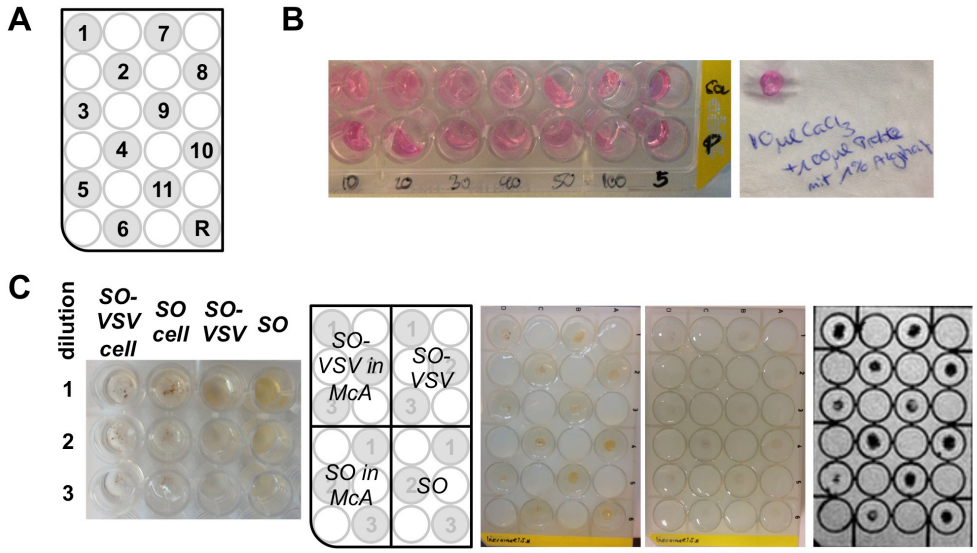

Figure 18: MRI phantom preparation. A: General scheme of MRI phantoms. **B:** Optimization of alginate clot formulation: best result for 0.017 M $CaCl_3$ and 1 % alginate (P: sample first, $CaCl_3$ added; Ca: $CaCl_3$ first, sample added → 20 µl $CaCl_3$ + 100 µl sample with 1 % alginate). **C:** From left to right: MNP(-VP) ± McA cells clots and the according phantoms (set-up, plate ± agarose cover, T_2^*w image (1.5 T Achieva, Philips Medical Systems, Best, the Netherlands)).

Sample	Maximal iron concentration [mM]	Maximal cell concentration [10^6 cells/mL]	Cell labeling [pg Fe/cell]	Applied iron [pg Fe/cell]	Labeling efficiency [%]
PEI-Mag2	0.07	-	-		
SO-Mag6-11.5	0.32	-	-		
PEI-Mag2-VSV	0.11	-	-		
SO-Mag6-11.5-VSV	0.11	-	-		
PEI-Mag2-Ad	0.33	-	-		
SO-Mag6-11.5-Ad	0.33	-	-		
PEI-Mag2 in McA	0.14	1.74	4.5	10	45
SO-Mag6-11.5 in McA	0.2	2.05	5.4	10	54
PEI-Mag2-VSV in McA	0.22	3.88	3.2	10	32
SO-Mag6-11.5-VSV in McA	0.2	4.36	2.5	10	25
McA untreated	-	1.91	-	-	
PEI-Mag2 in RDB	0.79	2.55	17.3	25	69
SO-Mag6-11.5 in RDB	0.72	2.53	15.9	25	64
PEI-Mag2-Ad In RDB	0.11	0.90	6.7	25	27
SO-Mag6-11.5-Ad In RDB	0.14	1.03	7.4	25	30
RDB untreated	-	3.36	-	-	

Table 5: Phantom properties. Phantom plates with MNPs, magnetic viral complexes and magnetically labeled or infected cells. The maximal concentration in well 1 is diluted in a 2-to-3 dilution series.

2.2.2.1.4.3 Magnetic resonance imaging

The imaging experiments were performed on a clinical 1.5 T MRI system (1.5 T Achieva, Philips Medical Systems, Best, the Netherlands) and a clinical 3.0 T MRI system (3.0 T Ingenia, Philips Medical System, Best, the Netherlands) using the 8-channel SENSE head coil (Philips Medical Systems, Best, the Netherlands) for signal reception. The rectangular agarose phantom plates were centrally positioned on the head cushion of the coil.

T_2 and T_2^* maps of the calibration phantoms were measured using the following sequences on the 1.5 T MRI system: for T_2 a multi-spin echo sequence with T_R = 2,000 ms, TE = n x 4.9 ms (n = 1…30), flip angle = 90 °, FOV = 160 x 88, resolution = 1 x 1 x 3 mm^3, 3 slices of 3 mm thickness with gap = 0 mm, scan time = 6:04 minutes and for T_2^* a multi-echo gradient echo sequence (FFE) with T_R = 1000 ms, TE = 2.1 + n x 3.2 ms (n = 0…15), flip angle = 90 °, FOV = 160 x 92, resolution = 1 x 1 x 3 mm^3, 3 slices of 3 mm thickness with gap = 0 mm, scan time = 4:40 minutes.

On the 3.0 T system the sequences were the following: for T_2 a multi spin echo sequence with T_R = 2,200 ms, TE = n x 6.0 ms (n = 1…30), flip angle = 90 °, FOV = 160 x 88, resolution = 1 x 1 x 2 mm^3, 7 slices of 2 mm thickness with gap = 0 mm, NSA = 1, scan time = 5:47 minutes and for T_2^* a FFE with T_R = 1500 ms, TE = 2.2 + n x 2.7 ms (n = 0…15), flip angle = 90 °, FOV = 160 x 92, resolution = 1 x 1 x 2 mm^3, 7 slices of 2 mm thickness with gap = 0 mm, NSA = 2, scan time = 7:28 minutes.

T_2 maps were calculated from the multi-spin echo data using the standard MR scanner mono-exponential fitting routine. For the T_2^* maps, the complex data of the multi-gradient echo sequence were analyzed using the RelaxMapsTool (Philips PRIDE data evaluation software package, Philips Medical Systems, Best, the Netherlands). This tool calculates B_0 maps for all slices and – as a first order deviation from a mono-exponential signal decay – takes into account the sinus-shaped oscillation of the multi-echo signal induced by the through plane B_0 gradient [254].

For analysis, circular ROIs were manually drawn for each well avoiding the rim region with partial volume effects and the mean (± standard deviation (SD)) R_2 values were calculated from the T_2 values. The R_2^* values of the manually drawn ROIs were extracted from the RelaxMapsTool. The mean R_2 and R_2^* values ± SD were calculated over the three slices scanned in all phantoms and the mean values were plotted against the iron concentration to determine the corresponding transverse relaxivities (r_2 and r_2^*, [mM^{-1} Fe s^{-1}]) by linear regression.

Mean basal relaxation rates at 0 μg Fe/mL were: R_{2max} = 3.91 ± 5.77 s^{-1} and R_{2max}^* = 2.51 ± 3.03 s^{-1} for untreated McA cells (maximal cell concentration of 1.91 x 10^6 cells/mL) and R_{2max} = 1.74 ± 0.37 s^{-1} and R_{2max}^* = 5.07 ± 0.86 s^{-1} for untreated RDB cells (maximal cell concentration of 3.36 x 10^6 cells/mL).

2.2.2.1.5 *In vivo* targeting of SO-Mag-VSV complexes

All procedures involving animals were approved and performed according to the guidelines of the Institutional Animal Care and Use Committee, and the local government. Six-week-old male Buffalo rats, weighing 200 g, were purchased from Harlan Winkelmann and housed in a specific pathogen-free environment under standard conditions. 10^6 McA cells suspended in 20 μL of DMEM were implanted orthotopically into the liver. After 10 days, the size of HCC nodules was determined by T_2-weighted MRI scans to be 0.5–1 cm in diameter. 100 μL of complexes consisting of 10^7 pfu VSV and 10 μg iron in form of SO-Mag6-11.5 particles (ratio of 1,000 fg Fe/pfu of virus), or 10^7 pfu of naked VSV were injected intra-tumorally into the orthotopic HCC nodules in the presence of a magnet placed on the surface of the tumor nodule, opposite to the injection site. Magnets were left in place for 30 minutes after injection. To evaluate intra-tumoral virus titer and non-heme iron, animals were sacrificed 30 minutes post infection with SO-Mag-VSV complexes or naked VSV and whole tumors were sampled. To quantify delivered VSV, $TCID_{50}$ analysis was performed on BHK-21 cells with whole tumor extracts. In addition, tumors were processed for quantification of non-heme iron content. An additional group of animals was MR imaged at 24 hours post infection to visualize accumulated SO-Mag-VSV complexes. Subsequently, the animals were sacrificed, and tumor and liver sections were fixed overnight in 4 % PFA for histological and immuno-histochemical analysis. That analysis was kindly performed by Dr Altomonte, II. Med. Clinic, Gastroenterology, Klinikum rechts der Isar der Technischen Universität München.

2.2.2.2 MNP-siRNA complexes

2.2.2.2.1 Cell Culture

The rat Morris hepatocellular carcinoma cells (McA-RH7777), further referred to as McA cells, derive from a female Buffalo rat, and show an epithelial morphology with loosely adherent growth [255]. The human liver carcinoma cell line HepG2 is a perpetual cell line derived from the liver tissue of a 15-year-old Caucasian male who had a well-differentiated hepatocellular carcinoma. The morphology of HepG2 cells is epithelial and they grow adherent as monolayers and in small aggregates [256]. HuH-7 is a well differentiated hepatocyte-derived cellular carcinoma cell line that was originally taken from a liver tumor in a 57-year-old Japanese male. HuH-7 cells have an epithelial-like morphology and grow in 2D monolayers [257]. The McA, HepG2 and HuH-7 cells were purchased from the American Type Culture Collection (LGC Standards GmbH, Wesel, Germany), and were kindly provided by Dr Altomonte. All three cell lines were cultured in DMEM supplemented with 10 % heat-inactivated FCS, 100 U mL^{-1} penicillin, and 100 μg mL^{-1} streptomycin. The human pancreatic adenocarcinoma EPP85-181P cell line, further referred to as 181P cells, is the parental and not daunorubicin-resistant cell line of the MDR human pancreatic adenocarcinoma cells EPP85-181RDB (RDB cells) [258], which were used in the MNP-virus-

complex experiments. The cell morphology is epithelial with adherent growth. The cells were kindly provided by Dr Mykhaylyk and were grown in DMEM supplemented with 10 % heat-inactivated FCS and 1 % 2 mM L-glutamine.

Recombinant cell lines stably expressing luciferase and GFP were McA LV PGKeGFPLuc, 181P LV PGKeGFPLuc, HepG2 LV PGKeGFPLuc and HuH-7 LV PGKeGFPLuc. They could be cultured under identical conditions as the non-transfected control cells not expressing luciferase and GFP.

All cell lines were cultured at 37 °C in a humidified atmosphere containing 5 % CO_2 and spilt before reaching 100 % confluency. Briefly, the cell culture medium was aspirated and the cell monolayer was washed with pre-warmed PBS to remove serum. Pre-warmed trypsin/ EDTA (0.25%/0.02%) was added and cell detachment was observed under the microscope. Once the cells started detaching, warm culture medium containing serum was added to stop the trypsin reaction and the cells were split 1:4 to 1:6 into new cell culture dishes.

2.2.2.2.2 Cell transduction for stable eGFP-Luc-fusion expression

The magnetic siRNA complexes were developed as carrier system to protect the siRNA from early degradation, and in parallel to provide a tool to magnetically target the siRNA to the region of interest after systemic application. Before siRNA could be used for specific knock-down of target genes, the carrier system itself needed to be tested for its functionality. Therefore, luciferase and GFP were chosen as convenient reporter genes in these proof-of-principle experiments. As the cancer cells do not express the genes naturally, lentiviral cell transduction with an eGFP-Luc-fusion construct was performed on several cancer cell lines, and the cells were examined for stable expression of the reporter genes via luciferase assay, GFP assay and microscopy.

2.2.2.2.2.1 Cell transduction with eGFP-Luc-fusion construct

Chosen cells lines for transduction were HepG2, HuH-7 and McA cells, all hepatoma cell lines and the pancreatic adenocarcinoma cell line 181P. For the stable transduction of those cell lines, a lentiviral transfer vector (LV-PGK-eGFPLuc; Figure 19) expressing the eGFP-luciferase fusion protein under the control of a phosphoglycerate kinase (PGK) promoter was chosen [259, 260]. CMS-5 cells served as internal control of the transduction. The positively transduced cell lines were named after the transduction construct: 181P LV PGKeGFPLuc, HepG2 LV PGKeGFPLuc, HuH-7 LV PGKeGFPLuc and McA LV PGKeGFPLuc, and further referred to as 181P eGFPLuc, HepG2 eGFPLuc, HuH-7 eGFPLuc and McA eGFPLuc.

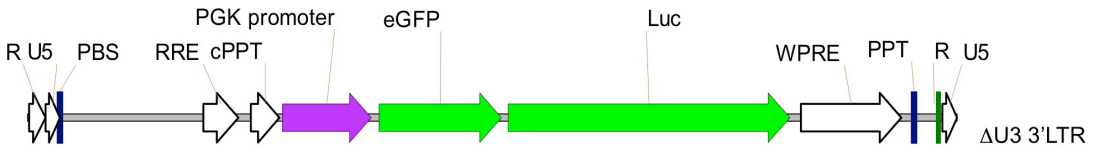

Figure 19: Lentiviral eGFP-Luc-fusion construct (LV PGKeGFPLuc) scheme under PGK promoter control.

The cell transduction experiments were kindly performed by Dr Anton, Department of Experimental Oncology and Therapy Research, now the Institute of Molecular Immunology and Experimental Oncology, Klinikum rechts der Isar der Technischen Universität München.

2.2.2.2.2.2 Reporter gene expression analysis - proof of cell transduction

To examine the cells for successful transduction, the expression of luciferase and GFP reporter genes could be assayed quantitatively. In addition, culture dishes with cell monolayers were qualitatively checked for GFP expression under the fluorescence microscope.

2.2.2.2.2.3 Cell preparation

All cell lines were cultivated as described in the cell culture section. For plating 96-well plates, the respective cells were harvested from T75 flasks and counted using a Neubauer counting chamber. Then the respective volume of cell suspension was transferred into a reagent reservoir containing cell culture medium and mixed well for equal distribution. 150 μL of that cell suspension were transferred per well into flat-bottom clear-walled or clear-bottom black-walled 96-well microplates using a multichannel pipette. The cell culture plates were incubated over night at 37 °C in a 5 % CO_2 atmosphere incubator.
All transduced cell lines were seeded in 96-well microplates at several densities ranging from 1 x 10^3 to 25 x 10^3 to identify the optimal conditions for the knock-down experiments. After 24 hours, the medium was replaced with fresh medium mocking the MNP-siRNA complex treatment in later experiments. 48 hours and 72 hours post-“transfection”, cell lysates were prepared for the quantitative assays. Therefore, the cell monolayers were washed with 150 μL PBS per well using a multichannel pipette. Then, 120 μL lysis buffer (0.1 % Triton X-100 in 250 mM Tris, pH 7.8) were added per well, incubated for 10 minutes at RT. The plates with lysed cells were then placed on ice in a covered box to prevent from GFP and protein degradation.
To qualitatively control GFP expression, culture dishes with cell monolayers were checked for GFP expression under the fluorescence microscope.

2.2.2.2.2.4 Luciferase assay

For the quantification of the luciferase reporter gene expression in the prepared cell lysates, 50 μL from each well were transferred into a new 96-well black flat-bottom microplate. Then, 100 μL luciferin buffer (see 2.2.2.1.3.6.) were added per well and mixed properly with the cell lysate. The chemiluminescence intensity was measured immediately afterwards using a Tecan infinite M1000Pro microplate reader (Tecan Trading AG, Switzerland) and a count time of 0.20 minutes per well with background correction.
For quantification of luciferase in the cell samples, a calibration curve had to be constructed. Therefore, in a new black-walled 96-well plate 50 μL lysis buffer were pipetted per well in

columns 1 and 3, and 40 µL lysis buffer per well in columns 2 and 4. To well A1, 30 µL lysis buffer and 20 µL luciferase standard stock (0.1 mg/mL luciferase (Roche Diagnostics, Mannheim, Germany), 1 mg/mL BSA (bovine serum albumin) in 0.5 M Tris acetate buffer, pH 7.5) were added. Then, 50 µL from A1 were transferred to B1, mixed well, pipetted from B1 to C1, etc. down to H1. That dilution series was continued by pipetting 50 µL from H1 to A3, and continued in column 3 down to G3; H3 was a blank. Then 10 µL of each well were transferred from column 3 to 4, and from column 1 to 2. After addition of 100 µL luciferin buffer to the wells of columns 2 and 4, the chemiluminescence intensity was immediately measured as described above. To construct the calibration curve, the logarithm of luciferase content was plotted against the logarithm of the luminescence intensity (light units). Figure 20 shows the calibration curve acquired via preparing and measuring as described above.

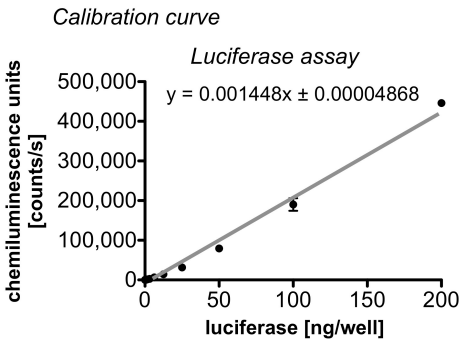

To calculate the actual amount of luciferase in the cell samples, an approximation function, the linear regression, was applied.

Figure 20: Luciferase assay calibration curve.

2.2.2.2.2.5 GFP assay

For the quantification of the GFP reporter gene expression in the prepared cell lysates, 50 µL from each well were transferred into a new 96-well clear-bottom black-walled microplate. Then 100 µL PBS were added per well and mixed with the cell lysate. The fluorescence intensity was measured immediately afterwards at excitation 485 nm / emission 535 nm using a Tecan infinite M1000Pro microplate reader and an acquisition time of 1.0 second per well.

For quantification of GFP in the cell samples, a calibration curve had to be constructed. Therefore, 147 µL lysis buffer were pipetted in well A1, 50 µL lysis buffer to all other wells A2 - A12 of a new 96-well clear bottom black-walled plate. Then, 3 µL GFP stock solution (500 ng GFP per µL PBS) were added and mixed properly. 100 µL were transferred from A1 to A2, mixed well, 100 µL were transferred from A2 to A3, mixed, and so on down to A11. The surplus 100 µL from well A11 were discarded and A12 served as a blank. After addition of 100 µL PBS to each well of row A and mixing, the fluorescence intensity of GFP (485/535 nm) was measured as described above. To construct a calibration curve, the measured fluorescence intensity was plotted as a function of GFP content per well. Using a linear regression of the calibration function, the GFP content in the cell lysate samples could be calculated.

2.2.2.2.3 MNP - siRNA - cell interaction

By assembling magnetic siRNA complexes, it was aimed to construct a tool for siRNA delivery to a target region. The complexation with magnetic nanoparticles provided on one hand a stabilizer for systemic applicability and the formulation, and on the other hand allows for magnetic guidance and monitoring within the organism. In the following section, the complexes were examined for their knock-down capacity in first *in vitro* experiments.

2.2.2.2.3.1 Cell preparation

All cell lines were cultivated as described in the cell culture section. For plating 96-well plates, the respective cells were harvested from T75 flasks and counted using a Neubauer counting chamber. Then the respective volume of cell suspension for 10^4 cells per well was transferred into a reagent reservoir containing cell culture medium and mixed well for equal distribution. 150 µL of that cell suspension were transferred per well into a flat-bottom clear-walled or clear-bottom black-walled 96-well microplate using a multichannel pipette. The cell culture plates were incubated over night at 37 °C in a 5 % CO_2 atmosphere incubator.

2.2.2.2.3.2 Preparation of magnetic siRNA complexes

Magnetic siRNA complexes were prepared from PEI-Mag2 and SO-Mag5 magnetic nanoparticles, siRNAs to be tested were luciferase and GFP, non-coding siRNA served as negative control, and enhancer was Dreamfect Gold (DF-Gold; OZ Biosciences, Marseille, France). Maximal siRNA dose was 16 pg siRNA/cell, the Fe-to-siRNA ratio was 0.5:1, and the enhancer DF-Gold-to-siRNA ratio was 4:1. Analyzed cell lines were McA eGFPLuc, HepG2 eGFPLuc, HuH-7 eGFPLuc, 181P eGFPLuc and 181RDB Luc, all stably expressing the luciferase reporter gene. The siRNA was solved in H_2O as indicated in the producers manual to reach final siRNA stock concentrations of 250 µg/µL. The MNPs were diluted with H_2O to reach 0.1 µg/µL stocks, and DF-Gold was diluted to a 1 mg/mL stock.
To prepare the transfection complexes, first siRNA dilutions of the coding and non-coding control siRNAs were prepared. In numbers, that means per plate (10^5 cells per well) 1.152 µg siRNA (4.61 µL of the previously mentioned 250 µg/µL stock) were diluted in 273.02 µL medium without additives. 5.76 µL of the 0.1 µg/µL MNP stocks were mixed with 4.61 µL DF-Gold and to a final volume of 10.37 µL. Those MNP-DF-Gold dilutions were mixed and the siRNA was added to this solution, mixed well and the 288 µL assembling liquid incubated for 15 minutes at RT for complex assembly. During the incubation time, all wells B to D and F to H in the columns 1, 4 and 7 of a 96-well flat-bottom microplate were filled with 180 µL medium without additives for the 1-to-1 dilution series. The incubated complexes were filled up with medium to the final volume of 360 µL per plate, mixed, and 360 µL of the complex solutions were transferred to the wells A or E of the columns 1, 4 and 7 of each plate. 180 µL each were used for the dilutions series from wells A (E) down to wells D (H). The wells of column 10 A to G were prepared with plain medium without additives and medium w/o /

water instead of siRNA, enhancer and MNPs; the wells H stayed empty and served as background wells in the later luciferase and GFP assays. The plate design for luciferase silencing is presented in table 6 and all plates for the different cell lines were prepared analogous.

pg siRNA/cell	triplex			triplex			duplex (lipoplex)			references			
16	PEI/DF-Gold/ siRNA-Luc			SO/DF-Gold/ siRNA-Luc			DF-Gold/ siRNA-Luc				control		A
8													B
4													C
2													D
16	PEI/DF-Gold/ siRNA-noncoding			SO/DF-Gold/ siRNA-noncoding			DF-Gold/ siRNA-noncoding						E
8													F
4													G
2										background			H
	1	2	3	4	5	6	7	8	9	10	11	12	

Table 6: Color-coded plate design for preparation of magnetic siRNA complexes

2.2.2.2.3.3 Knock-down via magnetofection

The 96-well plates with 24 hours incubated cells were checked under the microscope for cell state and confluency, which should be about 40 to 50 %. The medium was replaced by 150 µL fresh cell culture medium per well, then 50 µL of the respective transfection complex was transferred to the culture plate using a multichannel pipette. The treatment scheme was as follows: mixed dilutions of transfection complex prepared in column 1 of the complex preparation plate were transferred to the wells of columns 1, 2, and 3 (to test each composition and dilution of transfection complex in triplicate) of the cell culture plate. 50 µL from each well of column 4 of the complex preparation plate were transferred to columns 4, 5 and 6 of the cell culture plate, and 50 µL from each well of column 7 of the complex preparation plate to columns 7, 8, and 9 of the cell culture plate. The rows A to G of the columns 10, 11, and 12 of the cell culture plate served as untreated control cells, row H as background. With that transfection scheme, 16, 8, 4 and 2 pg siRNA/well, respectively, were applied to cells in rows A (E), B (F), C (G), and D (H). For magnetofection, the cell culture plates were then placed on a plate magnet (OZ Biosciences, Marseille, France) for 30 minutes in an incubator to create at the cell layer location a permanent magnetic field with a field strength and gradient of 70–250 mT and 50–130 T/m, respectively. After 30 minutes, the magnet was removed and the cell culture plates were incubated for further 48/72 hours at 37 °C until analysis of the gene silencing.

2.2.2.2.3.4 Reporter gene expression analysis

2.2.2.2.3.4.1 Luciferase assay

To quantify the luciferase reporter gene down-regulation, the luciferase expression was determined 48 and 72 hours after MNP-siRNA complex treatment. Therefore, luciferase assays were conducted in cell lysates as described in section 2.2.2.2.2.4. Either the data acquired from cell transfected with the non-coding siRNA, or cell lysates of non-transfected cells served as reference.

To allow the results of the luciferase expression assays to be presented as weight luciferase per weight unit total protein, total protein content in lysate was determined, and the weight luciferase per weight unit total protein was calculated. Again, the results were normalized against the reference data of non-transfected cells. In order to get a dose–response curve, the results were plotted against time post-transfection or against the siRNA dose per well.

2.2.2.2.3.4.2 Protein assay

To correlate the amounts of luciferase and GFP protein, and present them as weight luciferase or GFP per weight unit total protein, the total protein of the cell lysate samples had to be determined. A flat-bottom 96-well plate was prepared with 150 μL ddH_2O per well, then 10 μL cell lysate were transferred using a multichannel pipette. After addition of 40 μL BioRad protein assay reagent (Bio-Rad Laboratories GmbH, Munich, Germany), the plates were mixed well with the pipette or placed on a shaker. Then the absorbance at 590 nm was measured using the Tecan infinite M1000Pro microplate reader, acquisition time was 0.1 second per well.

To calculate the protein amounts in the cell lysate samples, first a calibration curve had to be constructed. Therefore, row A of a new 96-well plate was prepared with 25 μL lysis buffer. Then 50 μL BSA stock solution (1.5 mg/ml BSA in PBS) was added to well A1 and after mixing well, 50 μL were transferred to A2, mixed well, and 50 μL transferred to A3 and so on down to A11; A12 was left as blank. Then 150 μL of water per well were added to another row, for example row B, and 10 μL per well were now transferred from row A to the corresponding well in row B. After addition of 40 μL BioRad protein assay reagent (Bio-Rad Laboratories GmbH, Munich, Germany) and well mixing, the absorbance at 590 nm was measured using the microplate reader as described above. The measured absorbance was plotted against the protein content per well to construct the calibration curve and again linear regression was used to derive the calibration function and therewith to calculate the protein content of the cell lysate samples.

2.2.2.3 Magnetic liposomes

2.2.2.3.1 Pre-studies on the MNPs

MNPs were tested for their characteristics *in vitro* and *in vivo* in the first part of this chapter. After the positive results *in vitro* and no adverse effects in the *in vivo* biodistribution and toxicity experiments, the liposome preparation was started.

2.2.2.3.1.1 Cell culture

Murine pancreatic ductal adenocarcinoma cells were extracted as primary cells from *CKp53lox* mice by Marija Trajkovic-Arsic, II. Med. Clinic, Gastroenterology, Klinikum rechts der Isar der Technischen Universität München, and were cultured in DMEM supplemented with 10% heat-inactivated FCS, 1 % non-essential amino acids, 100 U mL^{-1} penicillin, and 100 μg mL^{-1} streptomycin. The cells were numbered after the animal they were extracted from; namely: 10078 (male), 10083 (male), 10088 (female), 10115 (male), 10123 (female), 10124 (female), 10127 (female), 10135 (male), 511181, 511189, 511677, 512010, 530202.
The rat Morris hepatocellular carcinoma cells (McA-RH7777), further referred to as McA cells, and the baby hamster kidney cells BHK-21 cells were purchased from the American Type Culture Collection, and were cultured in DMEM supplemented with 10 % heat-inactivated FCS, 100 U mL^{-1} penicillin, and 100 μg mL^{-1} streptomycin.
All cell lines were cultured at 37 °C in a humidified atmosphere containing 5 % CO_2.

2.2.2.3.1.2 MNP - cell interaction

To identify and characterize the MNP-uptake behavior of the pancreatic and the hepatic carcinoma cells, all cell types were treated with different iron concentrations, and the cells were analyzed for the internalized iron, and the cytotoxicity of the applied MNPs was evaluated in cell viability assays. Several types of particles, namely SO-Mag6-11.5, PEI-Mag2, PALD2-Mag1 and PALD2-Mag2 were examined to identify the particle type with the best properties.

2.2.2.3.1.2.1 Saturation

Pancreatic cells and McA cells were seeded at densities of 2 x 10^5 and 5 x 10^5 cells per well, respectively, in 6-well plates. 24 hours post seeding, the cell culture medium of each well was changed to a MNPs suspension. Therefore, MNPs were diluted in cell culture medium to the desired applied iron dose. A range of 5 – 80 μg Fe/mL was used for the 511181 cells and 12.5 – 100 μg Fe/mL for the hepatic cells, resulting in an applied iron dose of about 25 to 400 pg Fe/cell in a 1-to-2 dilution series. After 24 hours incubation, the cells were washed with PBS, trypsinized using 0.25 % trypsin/0.02 % EDTA solution, and analyzed for the associated/internalized iron. To evaluate the optimal ratios of applied-to-internalized iron for

the different particles and cells, data of at least three saturation experiments were plotted as applied iron doses versus internalized iron.

2.2.2.3.1.2.2 *Analysis of the cell associated/internalized iron*

To quantify the cell associated/internalized exogenic non-heme iron in magnetically labeled cells, the analysis was performed as described in the first section 2.2.2.1.3.4. Briefly, approximately 2 x 10^5 trypsinized cells were washed with PBS and pelleted. The cell pellet was resuspended in 250-500 µL of an acid mixture containing 3 M HCl and 0.6 M trichloracetic acid. After overnight incubation at 65 °C, the samples were centrifuged, and 50 µL of the clear supernatant was analyzed for its iron content by a colorimetric method with 1,10-phenanthroline using a spectrophotometer [261]. Basal non-heme iron level determined in non-labeled cells was used as a reference.

2.2.2.3.1.2.3 *Cytotoxicity evaluation*

The cytotoxicity of the MNPs on cells was evaluated using the MTT assay which is based on reduction of the MTT reagent into formazan by superoxide anion radicals produced in the mitochondrial respiratory chain [262, 263] and described in section 2.2.2.1.3.6. Briefly, cells were washed with PBS 48 hours post-treatment, the supernatant was discarded and the cells were incubated for 1–2 hours in 100 µL of 1 mg/mL MTT solution. Afterwards, 100 µL solubilization solution were added and incubated at 37 °C, shaking overnight to dissolve the formazan crystals. Those solved crystals were quantified at 590 nm using a microplate reader. Non-treated cells served as a reference representing 100 % viable cells; the background was determined from 100 µL MTT solution with 100 µL solubilization solution.

2.2.2.3.1.3 *In vivo* biodistribution and toxicity study

As there were no detectable adverse effects of the magnetic nanoparticles in the *in vitro* tests, the particles were analyzed for their *in vivo* biodistribution and toxicity in mice.

2.2.2.3.1.3.1 Animals

The genetically engineered animals used in that experimental setup had a pancreas-specific deletion of *p53* (*p53lox*). One group of animals was *wt Kras/wt Cre*, two other groups were heterozygous with either *wt Kras/+/- Cre*, or *+/- Kras/wt Cre*. Those three genotypes were not capable to develop invasive pancreas tumors. In addition, a fourth group of animals had a pancreas-specific activation of oncogenic *KrasG12D* and *p48-Cre (+/- Kras* and *+/- Cre*), and thus, those animals had the genetic prevalence to develop pancreatic tumors. At the day of the MNP injection, the animals were between 37 and 49 days (5 to 7 weeks) old, according to Trajkovic-Arsic et *al*. [209].The administered iron dose was 200 µg per animal via catheter tail vein injection (PALD2-Mag2 in 0.9 % NaCl, PALD2-Mag1 in 6 % HES buffer, maximal volume of 0.2 mL) under isofluorane anesthesia and temgesic analgetics. After the magnetic nanoparticle treatment, the animals were observed for 14 days regarding weight

development, general fitness and behavior, then they were sacrificed and tissue samples underwent histological and biochemical analysis for iron of the magnetic nanoparticles. Sampled tissues were liver, lung, spleen, kidney, pancreas/pancreatic tumor (tumor head and tumor tail), heart, testis/ovary, bone, and tail (injection site). An overview of all animals, their genotypes, and the sampled tissues is shown in the supplemental table 12.
At all times, the animals were treated according to the guidelines of the local Animal Use and Care Committees, and following the welfare guidelines and GV-Solas [264-266]. The scoring sheet used for the daily animal evaluation is attached as supplemental table 13.

2.2.2.3.1.3.2 Histology: Prussian Blue staining

The tissue samples were fixed in formalin over night at 4 °C. The histological processing and evaluation of the tissue samples was kindly conducted by Dr Aichler, Research Unit Analytical Pathology, Institute of Pathology, Helmholtz Zentrum München, Neuherberg, Germany.

2.2.2.3.1.3.3 Non-heme iron quantification

The biochemical analysis for exogenic non-heme iron, the administered magnetic nanoparticles, was performed as described earlier. Briefly, between 20 and 100 mg tissue (sampled, weighed and stored at -80 °C) were thawed and cut with scissors into small pieces. Then the tissue was lysed with 500 µL of an acid mixture (3 M HCl and 0.6 M trichloracetic acid) overnight at 65 °C (18 to 20 hours). To remove debris, the samples were centrifuged 5 minutes at 14,000 rpm and 20 µL of the tissue extract were analyzed for the iron content by a colorimetric method with 1,10-phenanthroline. After 20 minutes reaction time, the OD was measured at 510 nm, the absorption maximum of the iron(II)-1,10-phenanthroline complex, in a Beckman DU 640 spectrophotometer. The iron concentration in the tissue samples could be calculated using a calibration curve, determined from an iron stock solution.

2.2.2.3.1.4 Target-protein expression integrins α_v and β_3

Potential target for surface modification of the multifunctional liposomes was the tumor cell surface protein $\alpha_v\beta_3$ integrin. Therefore, the primary PDAC cell lines were screened for their $\alpha_v\beta_3$ integrin expression by Western blotting. The *CKp53lox* PDAC mice were analyzed for the integrin expression *ex vivo* by immuno-histolgical analysis of tumor tissue, and *in vivo* using MRI for tumor localization and intraoperative fluorescence imaging with the integrin-specific contrast agent integrisense for visualization of $\alpha_v\beta_3$ integrin expressing tumor cells.

2.2.2.3.1.4.1 Western blot in PDAC primary cell lysates

For Western blot analysis, cells were washed with cold PBS and then removed from the culture flask using a cell scraper. After combining those harvested cells with the PBS wash-off from the culture flask in a falcon tube, the cell suspension was centrifuged for 10 minutes

at 5,000 rpm and 4 °C. Then, the PBS supernatant was carefully removed and discarded. At that point, the cell pellets could be stored at -80 °C until further analysis. In case of freezing of the cells pellets, they were thawed on ice. Then the cell pellet was resuspended in 500 µl STEN lysis buffer (50 mM Tris-HCl, 2 mM EDTA, 1 % NP-40, pH 7.6) containing 1 protein-inhibitor tablet/10 mL. After 10 minutes of lysis on ice, the tubes were centrifuged for 10 minutes at 14,000 rpm and 4 °C to pellet the cell debris. The supernatant was transferred to new tubes and the Bradford (BCA) assay kit was used for determination of the protein content in the samples. Desired protein concentrations for Western blot analysis range between 50-80 µg protein in a 7 % SDS gel. Therefore, 40 µL BioRad Bradford reagent (Bio-Rad Laboratories GmbH, Munich, Germany) per well were pipetted into a 96-well microplate. The standard was prepared as follows: 0, 1, 2, 3, 4 and 5 µL of the BSA standard solution (2 mg/mL in NaCl) was pipetted in triplicates onto the Bradford reagent, then 2 µL lysis buffer were added, in the sample wells 2 µL cell lysate were added, and all wells were adjusted to 200 µL final volume with H_2O. The reaction incubated on a ThermoMixer at 400 rpm for about 45-60 minutes at 37 °C. Protein binding of the reagent dye Coomassie led to color-changing from green to purple. The absorbance was analyzed at 570 nm using a microplate reader. According to the protein concentrations, the cell lysates (including the positive and negative control cell lysates) were diluted with STEN buffer to final protein amounts of 60 µg per sample per SDS gel and 14 µL Lämmli buffer were added per sample followed by boiling for 5 minutes. The prepared protein solutions could be stored at -80 °C over night.

The samples were thawed, boiled again, vortexed and centrifuged. Then, either 23.4 µL sample or 15 µL marker were loaded per well on 7 % SDS gels, 15 µL Lämmli buffer served as loading control. The gels ran for about 3 hours at RT, blotting conditions were 150 mA per gel for 2 hours at 4 °C, and blocking was for 1 hour shaking in milk at RT. The primary antibodies (integrin α_v in milk or integrin β_3 in BSA) incubated over night shaking at 4 °C. Chosen antibodies were anti-integrin α_V (T-20): sc-6618 goat polyclonal (Santa Cruz Biotechnology, Inc., Heidelberg, Germany) and anti-integrin beta 3 antibody [EPR2417Y] ab75872 rabbit monoclonal (abcam®, Cambridge, UK) and.

The next day, the membranes were rinsed with PBS-T and the secondary antibodies (anti-goat (Santa Cruz Biotechnology, Inc., Heidelberg, Germany) or anti-rabbit (abcam®, Cambridge, UK)) were added. After rinsing of the membranes, they were developed with enhanced chemiluminescence Western blotting substrate, an enhanced luminol-based chemiluminescent substrate for the detection of horseradish peroxidase (HRP) on immunoblots. After 1 hour exposure, the blots were developed on X-ray films.

2.2.2.3.1.4.2 MRI, intra-operative fluorescence imaging, and immuno-histology of CKp53lox PDAC mice

MRI, intra-operative fluorescence imaging, and immunohistologic experiments were performed, and the results were kindly provided by Dr Trajkovic-Arsic, II. Med. Clinic, Gastroenterology, Klinikum rechts der Isar der Technischen Universität München.

2.2.2.3.2 Magnetic liposomes

2.2.2.3.2.1 Liposome preparation

To generate liposomes of about 100 nm in diameter, three different synthesis protocols were compared. For better stability in the blood circulation und targeting towards the RGD-ligand $\alpha_v\beta_3$ integrin receptor expressed on tumor cell surface *in vivo*, either PEGylated lipids or the new polymer P_3C_{18} of 18 carbon atoms and 7 PEG chains were used. The arrow diagram of figure 21 displays the three synthesis methods, figure 22 shows the structure of the polymer P_3C_{18} consisting of PEG 3 kDa with 6 lysine-serine-serine-C_{18} chains.

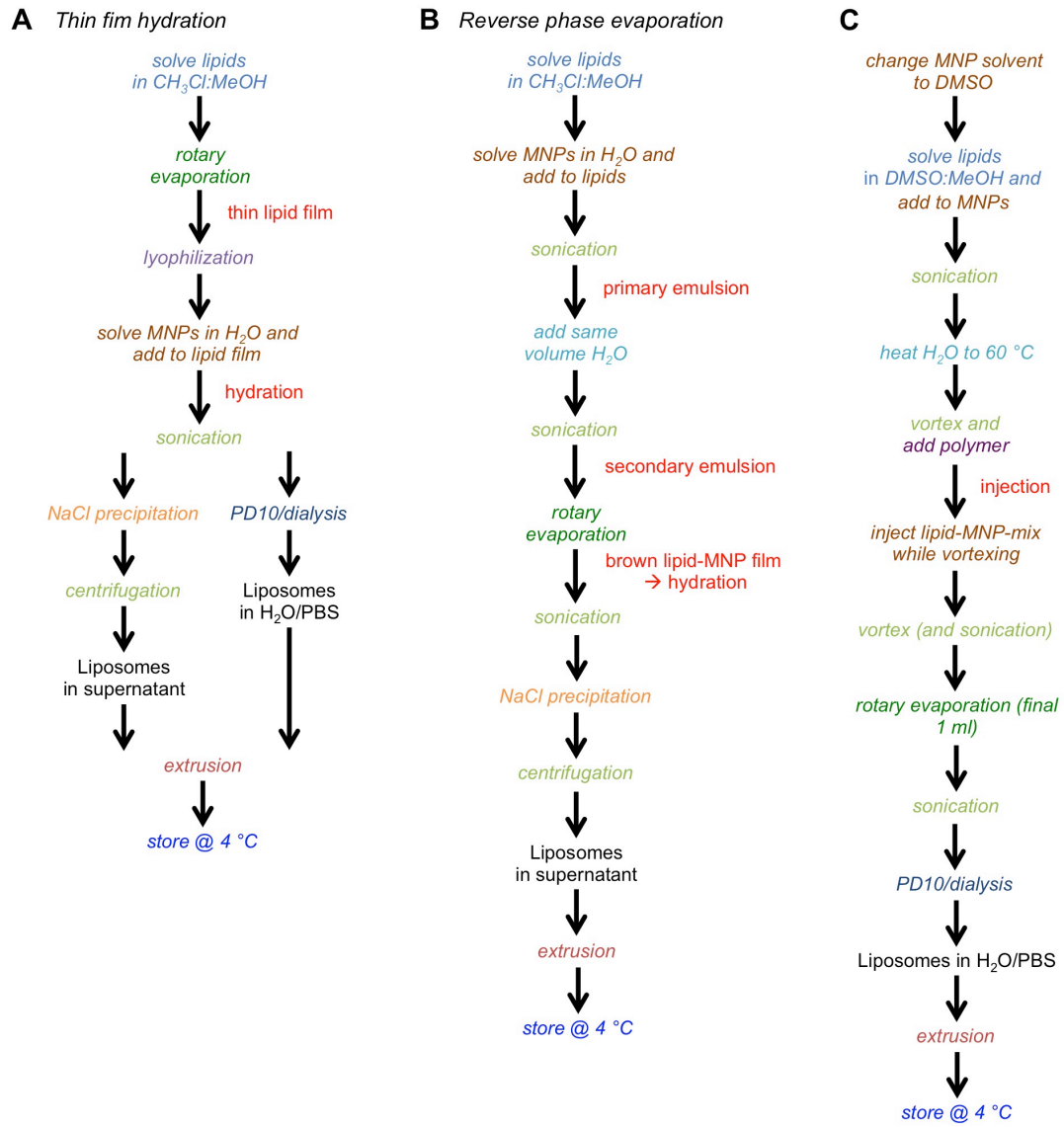

Figure 21: Liposome synthesis protocols. A: Thin film hydration (TFH): lipids are heated to build a lipid film, then the lipid film is hydrated with a MNP solution and sonicated to form liposomes. **B**: Reverse phase evaporation (REV): lipids are mixed with MNPs and sonicated to form the primary emulsion that gets sonicated with more water to form the secondary emulsion. This emulsion is evaporation dried and hydrated to form liposomes. **C:** Injection method: not water but DMSO is the solvent of the MNPs, the MNPs are mixed with solved lipids, sonicated and injected into pre-warmed polymer solution under vigorous condition to form liposomes. MeOH is removed by rotary evaporation. In **A**, **B** and **C**, synthesis is followed by a clean up to remove unbound MNPs and solvent by dialysis or PD10 columns. Liposomes are stored at 4 °C after size optimization via extrusion.

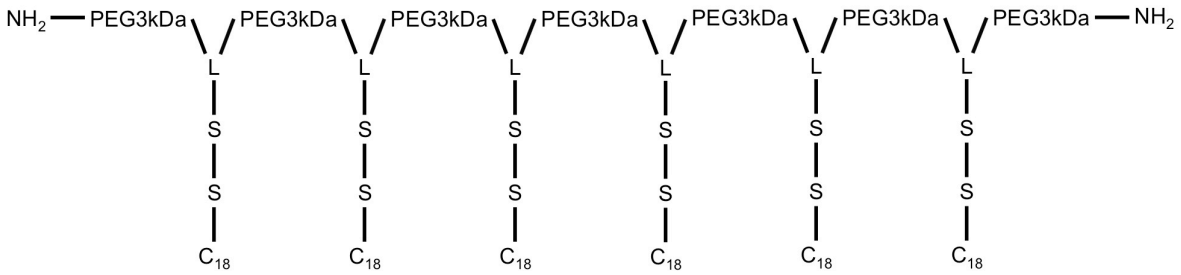

Figure 22: Structure of the P_3C_{18} polymer PEG3kDa with 6 lysine-serine-serine-C_{18} chains

2.2.2.3.2.1.1 Thin film hydration (TFH)

Liposome preparation via thin film hydration (TFH) was performed as described by Pradhan et *al*. [96]. Briefly, a lipid mix of 1,2-dipalmitoyl-*sn*-glycero-3-phosphocholine (DPPC) (M_W = 734.05 g/mol), cholesterol (M_W = 386.66 g/mol), and a functionalized lipid, 1,2-distearoyl-*sn*-glycerol-3-phosphoethanolamine-N-[amino(polyethylene glycol)2000] ammonium salt (DSPC-PEG_{2000}) (M_W = 2790.52 g/mol), were used in a molar ratio of 75:25:5. 11.2 mg total lipid (8.2 mg DPPC, 1.2 mg cholesterol and 1.8 mg DSPC-PEG_{2000}) were solved in 1 mL 2:1 $CHCl_3$:MeOH and transferred into a round-bottom flask. The lipid suspension-containing flask was placed in the rotary evaporator (Rotavapor, Büchi Labortechnik GmbH, Essen, Germany), and the solvent was evaporated to get a dry lipid film on the flask wall at 40 °C. Optionally, the lipid film could be further dried using a lyophilizator. 1 mg iron in form of the palmitoyl dextran magnetic nanoparticles PALD2-Mag1 were suspended in a total volume of 500 µL ddH_2O and added to the lipid film. After 30 minutes lipid film hydration at 40 °C in the water bath, the emulsion was sonicated for 15 minutes. The liposome emulsion was then washed with 500 µL 0.9 % NaCl to precipitate unbound MNPs. After a centrifugation for 10 minutes at 1,000 rpm and 4 °C, the liposome containing supernatant was transferred into a new tube and stored at 4 °C until further usage.

2.2.2.3.2.1.2 Reverse phase evaporation (REV)

For the liposome preparation via reverse phase evaporation (REV), the same lipid mix as for the TFH liposomes was used. The lipids (8.2 mg DPPC, 1.2 mg cholesterol and 1.8 mg DSPC-PEG_{2000}) were solved in 500 µL 2:1 $CHCl_3$:MeOH and transferred into a round-bottom flask. 1 mg iron in form of the palmitoyl dextran magnetic nanoparticles were suspended in a total volume of 500 µL ddH_2O and added to the lipid mix. After 15 minutes of sonication, the same volume (1 mL) ddH_2O was added to this primary emulsion followed by a second sonication step for 15 minutes leading to the secondary emulsion. Then the solvent was removed using a rotary evaporator at 40 °C. The brownish MNP-containing lipid film was then washed with 1 mL 0.9 % NaCl to precipitate unbound MNPs. After a centrifugation for 10 minutes at 1,000 rpm and 4 °C, the liposome containing supernatant was transferred into a new tube and stored at 4 °C until further usage.

2.2.2.3.2.1.3 Injection method

Using the injection method synthesis protocol, 10 mg total lipid DPPC:Chol 80:20 were solved in 1 mL DMSO:MeOH 3:2 at 650 rpm, 70 °C in the ThermoMixer. The polymer P_3C_{18} was solved in ddH_2O at 10 mg/mL and vortex mixed, the molar ratio of the lipids was then DPPC:Chol:P_3C_{18} 80:20:5. The MNPs were stored in H_2O, but before liposome synthesis, the medium had to be changed to DMSO. Therefore, palmitoyl dextran magnetic nanoparticles equivalent to 1 mg iron were centrifuged for 15 minutes at 14,000 rpm, then, the tube was placed on the magnetic rack for another up to 24 hours. After magnetic separation, the water was carefully removed and the MNPs were resuspended in 100 µL DMSO. For liposome synthesis, 2 mL ddH_2O were heated to 60 °C in a round-bottom flask, then the flask was placed on a vortex mixer and fixed. The in DMSO suspended MNPs were sonicated shortly, then the lipids were added, and again the suspension was sonicated. The pre-heated polymer was then added to the water in the round-bottom flask, and then the lipid-MNP suspension was injected using a G23 needle, both under vigorous conditions on a vortex mixer. That vigorous condition allowed for liposome formation. After further vortex mixing and short sonication, the round-bottom flask was connected to a rotary evaporator, and the solvent was reduced to 1 mL at 60 °C. To remove the remaining DMSO, the liposomes were either purified through a PD10 Sephadex column, or the liposomes were dialyzed against ddH_2O over night at 4 °C, stirring, using a Slide-A-Lyzer® 10 K Dialysis Cassette 10,000 MWCO. The column was first equilibrated with 4 volumes PBS, then, the liposome solution was loaded. To push the liposomes through, another volume PBS was layered on top, and the liposome-containing (brown) flow-through was collected in an eppendorf tube. The liposomes then underwent further analysis. After the overnight dialysis, the liposomes were extracted from the dialysis cassette and transferred to a round-bottom flask, placed on the rotary evaporator and the water was completely removed. The dry lipid film was then hydrated with PBS.

2.2.2.3.2.2 Characterization of MNPs and magnetic liposomes

As the planned administration route for magnetic liposomal nanocarriers was systemic injection followed by magnetic targeting towards the tissue of interest, the main goal was a good response of the liposome to external magnetic fields. In this section, the properties in magnetic fields and the physico-chemical properties were observed for particles and liposomes.

2.2.2.3.2.2.1 Non-heme iron determination

To quantify the liposomal iron content, biochemical analysis for exogenic non-heme iron was performed by the procedure described in section 2.2.2.1.3.4. Briefly, 20 µL liposome preparation were lysed with 200 µL concentrated HCl and 280 µl H_2O overnight at 65 °C. Then the samples were centrifuged 5 minutes at 14,000 rpm, and 20 µL of the extract were

mixed with 860 µL sterile water, 20 µL 10 % hydroxylamine-hydrochloride solution, 200 µL ammonium acetate buffer (25 g ammonium acetate and 70 ml glacial acetic acid with a total volume adjusted to 100 ml with ddH_2O), and 80 µL 0.1 % 1,10-phenanthroline solution. After 20 minutes reaction time, the OD was measured at 510 nm, the absorption maximum of the iron(II)-1,10-phenanthroline complex. The iron concentration in the tissue samples could be calculated using a calibration curve, determined from an iron stock solution.

2.2.2.3.2.2.2 Wavelength scan

To visualize the magnetic particles with a spectrophotometer, first the absorption optimum had to be determined. Therefore, MNP suspensions in water underwent wavelength scans in the visible range, with absorptions between 280 and 800 nm. 350 nm was identified as good wavelength for further spectrophotometrical experiments.

2.2.2.3.2.2.3 Magnetophoretic mobility

The magnetophoretic mobility measurements were conducted as described in section 2.2.2.1.3.7. for the magnetic viral complexes. Briefly, the magnetic liposomes were diluted to 500 µL aliquots to achieve a starting OD = 0.3–1 at the analytical wavelength of 360 nm for the magnetic liposomes. A gradient field was generated and optical cuvettes filled with these diluted suspensions were placed in a Beckman DU 640 spectrophotometer, and the change in the turbidity was immediately recorded over 30 minutes. From the decrease in optical density under magnetic field, the average magnetic moment of the complexes and the number of associated magnetic nanoparticles could be calculated.

2.2.2.3.2.2.4 Physico-chemical characterization

Mean hydrodynamic diameter D_h and electrokinetic zeta potential ζ of the liposomes suspended in ddH_2O were measured by photon correlation spectroscopy using a Malvern 3000 HS Zetasizer.

2.2.2.3.2.3 MNP-PTX liposome synthesis

The drug-loaded magnetic liposomes were synthesized applying the TFH technique as described above. Briefly, a lipid mix of DPPC, cholesterol, and a PEG-functionalized molecule, either the lipid DSPC-PEG_{2000} or the polymer P_3C_{18}, at 80:20:5 was mixed with 5 mg paclitaxel, and all was solved in 1 mL 2:1 $CHCl_3$:MeOH. The PTX-lipid film was hydrated with 1 mg iron in PALD2-Mag1, suspended in 1 mL ddH_2O. After 30 minutes lipid film hydration at 60 °C in the water bath, the emulsion was sonicated for 1 minutes, vortexed for 1 minute and sonicated again. The liposome emulsion was then extruded through 400 nm, 200 nm and 100 nm polycarbonate membranes with an extruder (both Avanti Polar Lipids, Inc., Alabaster, Alabama, USA), and over night dialyzed against ddH_2O at 4 °C. Next day, the liposome solutions were sonicated for 5 minutes and 250 µL of each liposome solution were washed with 250 µL 0.9 % NaCl by 10 minutes centrifugation at 1,000 rpm and 4 °C.

2.2.2.3.2.4 Analysis of liposome functionality

In this section, the functionality of the synthesized liposomes was analyzed regarding their thermosensitivity. Therefore, a calcein release assay was performed within a temperature range of 37 to 43 °C, either in PBS, or 50 % FCS in PBS with sampling every 15 minutes over a period of 60 minutes. In addition, it was tried to detect the binding of the chemotherapeutic drug paclitaxel to the magnetic nanoparticles.

2.2.2.3.2.4.1 Thermosensitivity evaluation

The calcein release assay was used to examine the thermosensitivity of the liposome formulation [96]. It was tested at which temperature the lipid shell started to get leaky, and released the content of the liposome. For detection of the release, the fluorescent calcein was encapsulated within the liposome, and its release was detected fluorometrically using a plate reader. Crucial for later administration *in vivo* was a melting temperature surely higher than 37 °C to prevent the liposomes from releasing their content before the external heat treatment at the target site.

Three different lipid compositions and two different synthesis were tested for the thermosensitive decomposition of the liposomes. To reach the melting temperature T_m of 41 °C analog to Pradhan et *al*. [96], the lipids DPPC and cholesterol were used in a 80:20 molar ratio, instead of DSPE-PEG the new P_3C_{18} polymer was used at DPPC:chol:P_3C_{18} = 80:20:5 (= formulation a), total lipid concentration was 10 mg/mL. in the experiments of Tai et *al*. [225], the lipid composition DPPC:DSPC:chol = 10:5:3 weight ratio led to T_m of 40-42 °C. Desiring a similar melting temperature, the polymer P_3C_{18} was used instead of the PEGylated lipid, and the according molar ratio of formulation b was DPPC:DSPC:chol:P_3C_{18} = 68.1:31.6:38.8:5 at 10 mg total lipid. In addition, a variation of Tai´s composition was tested as formulation b*: DPPC:DSPC:chol:P_3C_{18} = 70:30:40:5.

Using the injection method synthesis protocol, 10 mg total lipid of all three lipid compositions were solved in 1 mL DMSO:MeOH 3:2. To ease the solving, the individual lipids were solved in the DMSO:MeOH, then mixed in the desired composition, and the lipid mix was then heated to 60 °C for 10 minutes. The polymer P_3C_{18} was solved in ddH_2O at 10 mg/mL and also heated to 60 °C. As the liposomes were synthesized by the injection method, 2 mL ddH_2O were heated to 60 °C in a round-bottom flask. The pre-heated polymer was added, and then the pre-heated lipids were injected using a G23 needle, both under vigorous conditions on a vortex mixer. After short sonication, the round-bottom flask was connected to a rotary evaporator and the solvent was reduced to 1-2 mL at 60 °C. To get rid of the remaining DMSO, the liposomes were dialyzed over night at 4 °C, stirring, against ddH_2O using a Slide-A-Lyzer® 10 K Dialysis Cassette 10,000 MWCO. Next day, the liposomes were extracted from the dialysis cassette and transferred to a round-bottom flask, placed on the rotary evaporator and the water was completely removed. The dry lipid film was then hydrated with 1 mL sterile filtered calcein solution of 63 mM, pH 7.4. The resuspended

liposomes underwent several extrusion steps, each 11 times through 400 nm, 200 nm and 100 nm.

Preparing the liposomes via thin film hydration, 10 mg total lipids were solved in $CHCl_3$:MeOH = 2:1 in a round-bottom flask, and the polymer in water was added. To get rid of the solvent, the rotary evaporator was used. The dried lipid film was then hydrated with 1 mL 63 mM calcein (sterile filtered) at 60 °C for 15-20 minutes. The resuspension of the liposomes was again followed by extrusion, 11 times each through 400 nm, 200 nm and 100 nm. The liposomes were dialyzed against water over night at 4 °C. The next day, the liposomes were transferred from the dialysis chamber into a new tube with a syringe.

Having the two batches of liposomes prepared, the calcein assay was started. Therefore, 60 µL liposomes were solved in 600 µL either PBS or 50 % FCS in PBS, and incubated at 37 °C, 39 °C, 41 °C and 42 °C. 20 µL samples were taken after 0, 15, 30, 45 and 60 minutes incubation to quantify the released calcein over time in the suspension. The samples were transferred into 24-well plates with 2 mL PBS per well/48-well plates with 1 mL PBS per well, and the calcein fluorescence was detected at 485 nm excitation/520 nm emission (1 second and 0.1 seconds counting time for 24-well plate, 0.1 seconds for 48-well plate) using a Wallac 1420 VICTOR^2 microplate reader (PerkinElmer, Waltham, MA, USA). 100 % release reference suspensions for data normalization were prepared by lysing 60 µL liposomes in 600 µL 1 % Triton X-100 by vortexing 1 minute followed by 30 minutes incubation at 55 °C. The standard curve was prepared from sterile filtered 63 mM calcein in a dilution series in PBS, 50 % FCS in PBS and H_2O; pure PBS and 50 % FCS in PBS served as background blanks.

2.2.2.3.2.4.2 MNP functionalization

In this experimental section it was tried to photometrically detect the paclitaxel (PTX) binding of the palmitoyl dextran magnetic nanoparticles. Paclitaxel was solved in DMSO at a stock concentration of 1 mg/mL and the magnetic nanoparticles were transferred from water to DMSO after magnetic separation for 3 hours and centrifugation for 5 min, 14,000 rpm. 900 µL DMSO with 1 mg iron in from of magnetic nanoparticles were mixed with 200 µL of the PTX stock, sonicated for 5 minutes, and further incubated at 20 °C, 1,000 rpm on the ThermoMixer for 20 minutes. It was assumed that the particles were loaded with drug and therefore, the suspension was placed on the magnetic rack for 1 hour (4 hours) to separate the magnetic fraction from unbound drug. After an additional centrifugation at 14,000 rpm for 5 minutes, the supernatant with unbound drug was carefully removed and the magnetic fraction with MNP-PTX complexes was resuspended in DMSO. Then both, magnetic and non-magnetic fraction, were analyzed from 200 to 800 nm using a Beckman spectrophotometer against pure DMSO as blank, dissolved PTX and pure MNPs served as controls. The samples were diluted with DMSO 1:10 and 1:100.

2.2.2.3.2.5 Magnetic liposomes *in vivo*

To examine the biodistribution and magnetic targeting of the liposomes, in first *in vivo* pilot experiments anesthesized wildtype and tumor bearing PDAC mice were intravenously (tail vein) injected with magnetic liposomes (figure 23A). After sacrifice, tissue samples of the animals underwent histological and biochemical iron analysis. The arrow diagrams of figure 23 show the timeline of the biodistribution (figure 23B) and targeting (figure 23C) experiments.

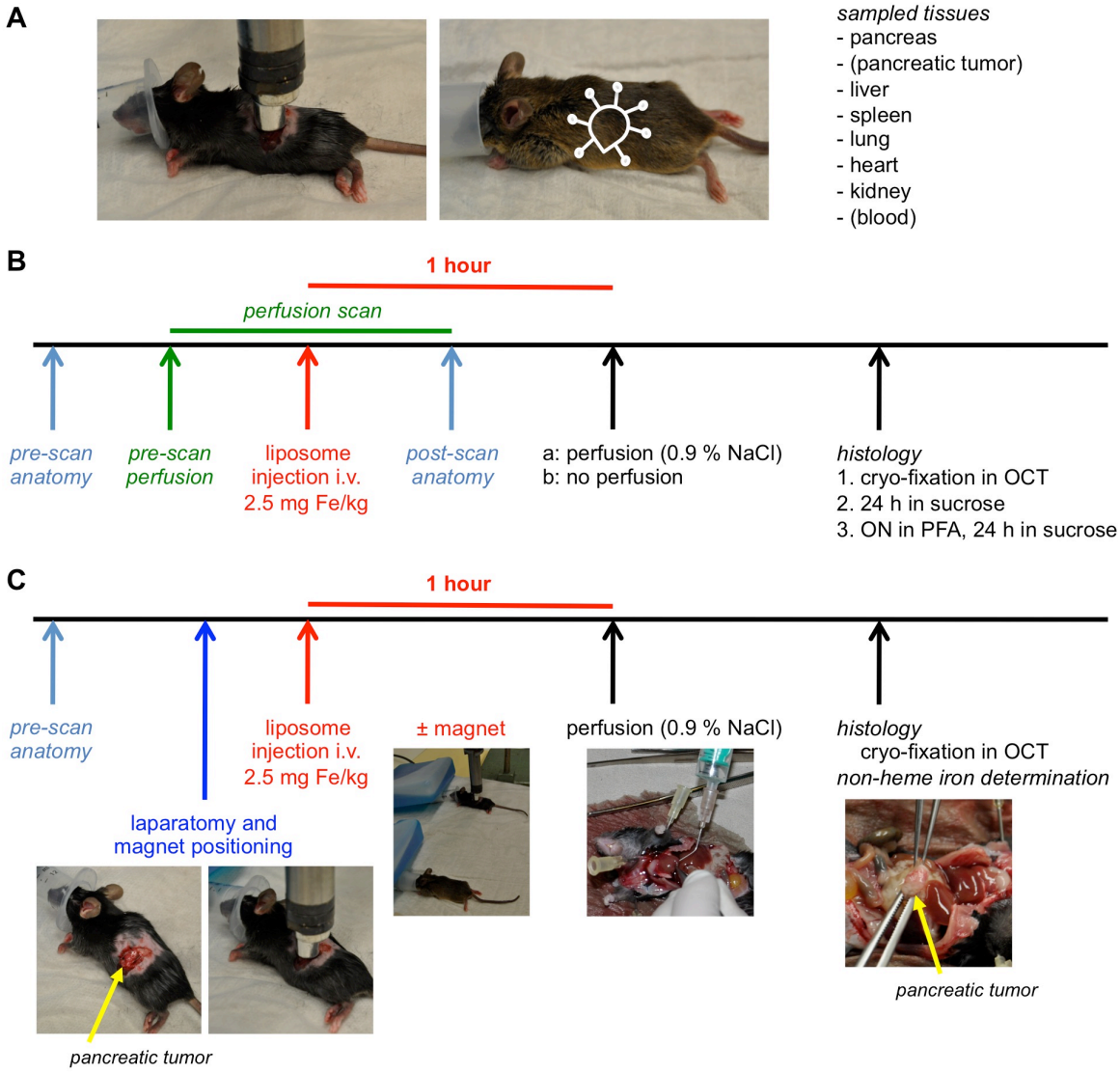

Figure 23: MNP-LP *in vivo* targeting setup: i.v. liposome injection and magnetic targeting after laparotomy. **A:** Targeting setup. **B:** Experimental design LP2: *wt* mice for optimization of PB tissue staining, ± perfusion. **C:** Experimental design LP1: CKp53lox mice, ± magnetic targeting.

2.2.2.3.2.5.1 Biodistribution

2.2.2.3.2.5.1.1 Animals: Wildtype mice

Two 3 months old wildtype mice were injected intravenously with magnetic liposomes in a concentration of 2.5 mg Fe per kg bodyweight in 100 µL NaCl per 20 g bodyweight under isofluorane anesthesia. The liposomes circulated for 1 hour, and as the wildtype animals had

no tumors, there was no magnetic targeting. Then the animals were sacrificed and samples were taken from the following tissues: pancreas, spleen, duodenum, kidney, heart and lung. The tissue samples were either fixed in 4 % PFA over night, 24 hours in sucrose at 4°C, or mounted in OCT for cryoslicing, the samples for non-heme iron determination were stored at -80 °C.

At all times, the animals were treated according to the guidelines of the local Animal Use and Care Committees.

2.2.2.3.2.5.1.2 *Histology: Prussian blue staining*

The fixed tissue samples were sliced and mounted onto glass slides. Then, the dry samples could be stained using the Prussian blue staining to visualize the MNPs with a Kernechtrot tissue counterstaining. The 2 % iron stock solution (20 g potassium hexacyanoferrat(II)-trihydrate dissolved in 1 L ddH_2O) and the 0.2 % Kernechtrot solution (2 g Kernechtrot, 50 g aluminiumsulfat ad 1 L ddH_2O), could be stored at 4 °C. The iron reagent for staining was prepared fresh every day with $^2/_3$ iron stock solution and $^1/_3$ 1 % HCl. Table 7 summarizes the staining protocol.

Step	Reagent	Incubation time
1	xylol	5 minutes
2	xylol	5 minutes
3	xylol	5 minutes
4	ethanol 100 %	1 second
5	ethanol 96 %	1 second
6	ethanol 96 %	1 second
7	ethanol 70 %	1 second
8	ddH_2O	1 second
9	iron reagent	20 minutes
10	ddH_2O	15 seconds
11	Kernechtrot solution	8 minutes
12	ddH_2O	1 second
13	ethanol 96%	1 second
14	ethanol 100%	1 second
15	ethanol 100%	1 second
16	xylol	5 minutes
17	xylol	5 minutes

Table 7: Prussian blue staining protocol.

2.2.2.3.2.5.2 Magnetic targeting

2.2.2.3.2.5.2.1 *Animals: CKp53lox mice*

The genetically engineered animals used in that experimental setup had pancreas-specific activation of oncogenic *KrasG12D* and *p48-Cre (+/- Kras* and *+/- Cre*) and deletion of *p53* (*p53lox*), further referred to as *CKp53lox* mice, and therefore were capable to develop invasive pancreatic adenocarcinomas (PDAC). At the day of the magnetic liposome injection, the animals were 6 weeks old. To examine the magnetic targeting of the liposomes, PDAC mice were intravenously (tail vein) injected with magnetic liposomes under isofluorane anesthesia. Before liposome administration, the animals were divided into two groups. One group (n = 4) underwent magnetic targeting by an above the tumor site (pancreas tumor tail) fixed magnet for 1 hour post liposome injection, the other group (n = 3) served as control with free circulating liposomes without externally applied magnetic field. In addition, there were three control animals without liposome injection. The animals of the magnetic targeting group underwent a laparotomy for better access to the tumor region, figure 23C contains a picture of the experimental setup. As for the wildtype animals in the biodistribution experiment, liposomes were administered in concentrations of 2.5 mg Fe/kg

bodyweight in 100 µL sterile NaCl per 20 g bodyweight. In addition to the aesthesia, the animals got 50 µL Temgesic analgetics. After 1 hour of liposome circulation (and magnetic targeting), the animals were sacrificed, and tissue samples for histological and biochemical iron analysis were taken. Sampled tissues were liver, lung, spleen, kidney, pancreas/pancreatic tumor (tumor head and tumor tail), heart and blood.
At all times, the animals were treated according to the guidelines of the local Animal Use and Care Committees.

2.2.2.3.2.5.2.2 *Histology: Prussian blue staining*

The fixed tissue samples were processed and stained as described in section 2.2.2.3.2.5.1.2.

2.2.2.3.2.5.2.3 *Non-heme iron determination*

To quantify the liposomal iron in tissue samples, biochemical analysis for exogenic non-heme iron was performed as described in section 2.2.2.3.1.3.3. Briefly, between 20 and 100 mg tissue were cut with scissors into small pieces and lysed with 500 µL of an acid mixture overnight at 65 °C (18 to 20 hours). After removal of the cell debris, the samples were analyzed for the iron content by a colorimetric method with 1,10-phenanthroline at 510 nm in a Beckman DU 640 spectrophotometer. The iron concentration in the tissue samples could be calculated using a calibration curve, determined from an iron stock solution.

3 RESULTS

The results section summarizes the outcome of all experiments conducted regarding the development and characterization of the different nanocarrier systems and their components. Again, first the magnetic nanoparticles are described, then the MNP-VP complexes, MNP-siRNA complexes, and magnetic liposomes.

3.1 Magnetic nanoparticles

The core–shell type iron oxide MNPs examined in the experiments of this dissertation were synthesized by precipitation of iron hydroxide from aqueous solution, followed by transformation into magnetite, and spontaneous adsorption of the surface structures/shell components. Those were a silicium oxide layer with surface phosphonate groups (SiO_x/phosphonate) and PEI for SO-Mag nanoparticles, 25-kDa branched polyethyleneimine ($PEI_{Br\text{-}25}$ kDa) for PEI-Mag nanoparticles, or palmitoyl dextran PALD2 for the PALD2-Mag particles.

The selected MNPs exhibited similar core diameters of SO-Mag = 6.7 nm, PEI-Mag = 9.0 nm and PALD2-Mag1 = 4.0 nm. The saturation magnetization of the core material at RT was 94, 62 and 62 $Am^2/kg(Fe)$, respectively, resulting in an average magnetic moment of the insulated particles of 8.7 x 10^{-20}, 5.8 x 10^{-20} and 5.8 x 10^{-20} Am^2 for the SO-Mag, PEI-Mag and PALD2-Mag1 MNPs, respectively [100, 267].

Decoration of SO-Mag MNPs with PEI resulted in SiO_x/Phosphonate-PEI coating of 11.5 w/w% PEI-to-iron [268] (shown schematically in figure 10B) with a silica coating width of approximately 1 nm and a higher mean D_h of 76 ± 27 nm, suggesting small aggregate formation. The average hydrodynamic diameter of the primary non-aggregated SO-Mag-5 core nanoparticle without PEI-modification was D_h = 40 ± 14 nm in water (d = 6.8 nm), indicating there is no aggregate formation prior to surface modification [115].

Surface coating of PEI-Mag MNPs with a self-assembling layer comprising 32 mass% PEI and 68 mass% of the fluorosurfactant Zonyl® FSA (figure 10D) resulted in a mean hydrodynamic diameter D_h = 28 ± 2 nm. In addition, PEI coating led to a highly positive electrokinetic potential (ζ) for both MNPs of 40.4 ± 0.4 mV for SO-Mag and 55.0 ± 0.7 mV for PEI-Mag. The decreased potential of the SO-Mag particles compared to the PEI-Mag particles is due to the lower PEI content and the negatively charged surface phosphonate groups decorating the silica coating.

The mean hydrated particle diameter of the with palmitoyl dextran (PALD2) decorated PALD2-Mag particles was D_h = 55 ± 11 nm, ranging between the other two particles. In contrast to the positively charged SO-Mag and PEI-Mag particles, the electrokinetic zeta potential of the PALD2-Mag particles in water was negative with ζ = -53.7 ± 12.1 mV due to the coating [180]. The physico-chemical properties of the MNPs are compiled in table 8.

Sample	Hydrodynamic diameter D_h [nm]		Electrokinetic potential ζ [mV]	
	Peak position	Peak width	Mean	SD
in water				
PEI-Mag2	28	2	55.0	0.7
SO-Mag6-11.5	76	27	40.4	0.4
in PBS				
Ad	123	33	-9.1	1.3
VSV	175	61	-11.8	0.7
PEI-Mag2-Ad	271	178	14.1	2.2
SO-Mag6-11.5-Ad	609	127	13.6	0.4
PEI-Mag2-VSV	514	99	15.1	0.8
SO-Mag6-11.5-VSV	923	120	-7.1	0.8

Table 8: Hydrodynamic diameter and electrokinetic potential. D_h and zeta potential of free MNPs, viral particles and their complexes.

3.2 Magnetic nanocarriers

3.2.1 MNP-VP complexes

3.2.1.1 *In vitro* characterization of the MNP-VP complexes

3.2.1.1.1 Physico-chemical properties

The properties of the SO-Mag and PEI-Mag nanoparticles were described in the previous chapter, and the corresponding size values for naked virus particles were D_h = 123 ± 33 nm for adenovirus, and D_h = 175 ± 61 nm for VSV. Both viruses had negative zeta potentials in PBS: -9.1 ± 1.3 mV (Ad) and -11.8 ± 0.7 mV (VSV). This enabled the self-assembly of the positively charged MNPs and the negatively charged VPs by electrostatic interactions. Complex formation with PEI-Mag resulted in a net positive charge of the magnetic viral complexes (PEI-Mag-Ad ζ = 14.1 ± 2.2 mV and PEI-Mag-VSV ζ = 15.1 ± 0.8 mV, in PBS). Co-assembly of SO-Mag with Ad also resulted in a net positive charge (SO-Mag-Ad ζ = 13.6 ± 0.4 mV in PBS), while a net negative charge was detected with VSV (SO-Mag-VSV ζ = -7.1 ± 0.8 mV in PBS). ζ and D_h measurements of the different MNP-VP complex suspensions showed neither free MNPs nor naked VPs (data not shown). As expected, MNP-VP complexes were larger compared to naked VPs, and larger for SO-Mag- compared to PEI-Mag-based complexes (PEI-Mag-Ad D_h = 271 ± 178 and PEI-Mag-VSV D_h = 514 ± 99 nm; SO-Mag-Ad D_h = 609 ± 127 nm and SO-Mag-VSV D_h = 923 ± 120 nm). The latter results suggest aggregate formation of SO-Mag-VP complexes in PBS suspensions. Figure 9A schematically presents the self-assembly of MNPs and VPs and the resulting magnetic viral complexes, and table 8 summarizes their physico-chemical properties. After that characterization, the magnetic viral complexes were tested *in vitro* in two cancer cell lines, McA hepatoma regarding the oncolytic effect of the VSV complexes, and RDB pancreatic cancer cells regarding the potential of the Ad complexes.

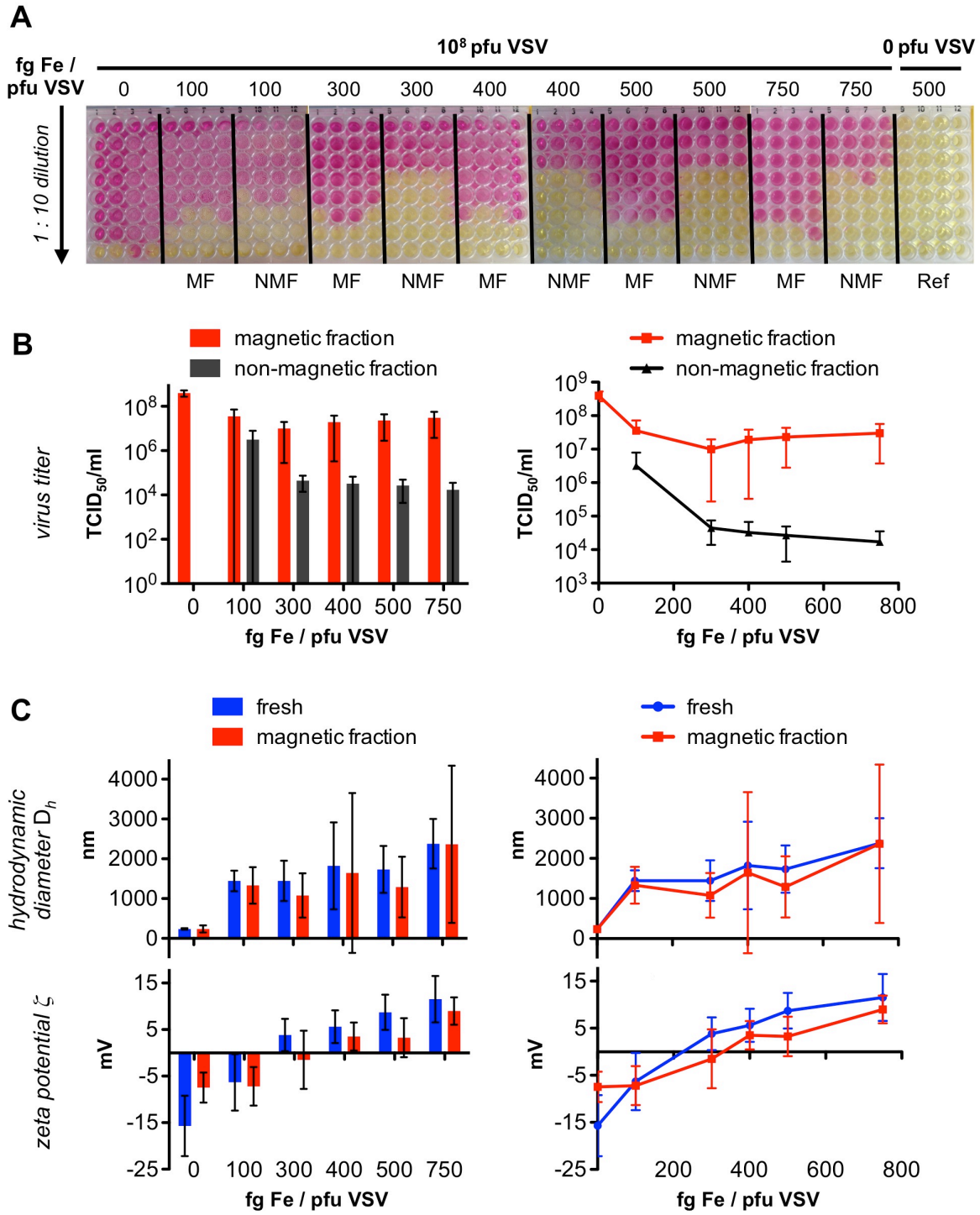

Figure 24: PEI-Mag2-VSV titration at different iron-to-virus ratios. A: Exemplary $TCID_{50}$ assay of magnetic (MF) and non-magnetic fractions (NMF). **B:** $TCID_{50}$ of the MNP-VSV complexes (n_{assay} = 3, all samples in quadrupels). **C:** Physico-chemical characterization: Hydrodynamic diameter D_h and zeta potential of the MNP-VSV complexes (n_{assay} = 3, all samples in quadrupels).

3.2.1.1.2 Titration and characterization of magnetic viral complexes

To identify the optimal iron-to-virus ratio for the magnetic viral complex assembly, virus particles were titrated with increasing amounts of MNPs. As this titration was already performed for the adenovirus complexes by Tresilwised et *al.* [105], and an optimal ratio of 5 fg Fe/pfu was determined, it was conducted only for the MNP-VSV complexes. Exemplary

results of the VSV titration with PEI-Mag particles were summarized in figure 24. Figure 24A shows photographs of the $TCID_{50}$ assay culture plates of magnetic and non-magnetic fractions of complex preparations, for better visibility in the photograph, the plates were left in the incubator after read-out until all medium was consumed by the healthy cells and the medium turned yellow due to pH changes. The medium of the wells with dead cells corresponding to high enough applied virus concentrations was still red. As expected, the medium of the reference wells on the right was used up as only MNPs and no virus were applied. In figure 24B, the $TCID_{50}$ /mL values of the magnetic and non-magnetic fractions were plotted against the applied iron per pfu virus. The optimal binding condition 500 fg Fe/pfu VSV was identified, as there most of the virus was bound to the magnetic nanoparticles in the magnetic fraction relative to the non-magnetic fraction. For the SO-Mag-VSV complexes, 1,000 fg Fe/pfu VSV was identified as optimal iron-to-virus ratio. The physico-chemical characterization was compiled in figure 24C, summarizing the according hydrodynamic diameters D_h and the electrokinetic zeta potentials over the applied iron per pfu virus.

3.2.1.1.3 Highly efficient magnetic cell-labeling with MNPs and MNP-VP complexes

To test cell-labeling efficiency of MNPs and MNP-VP complexes, two cell lines underwent magnetofection. Labeling with both, MNPs or MNP-VP complexes, resulted in high cellular iron loading (2.5 pg Fe/cell up to 17.3 pg Fe/cell upon application of 10 or 25 pg Fe/cell; table 5). No significant differences were detected between PEI-Mag and SO-Mag MNPs regarding that iron loading behavior. However, differences were evident between MNPs and magnetic viral complexes, and between the different cell lines employed: MNP labeling resulted in higher iron loading compared to MNP-VPs (45 – 69 % to 25 – 32 % labeling efficiency, respectively), and RDB cells showed a higher uptake than McA cells for free MNPs (69/64 % to 45/54 % labeling efficiency), but not for MNP-VP-complexes (table 5). To avoid false positive results from background contamination, non-labeled cells were also analyzed for their iron content, and neither cell line revealed detectable levels of exogenic non-heme iron. Based on the obtained iron loading data, an efficient internalization of the magnetic nanomaterial was suggested.

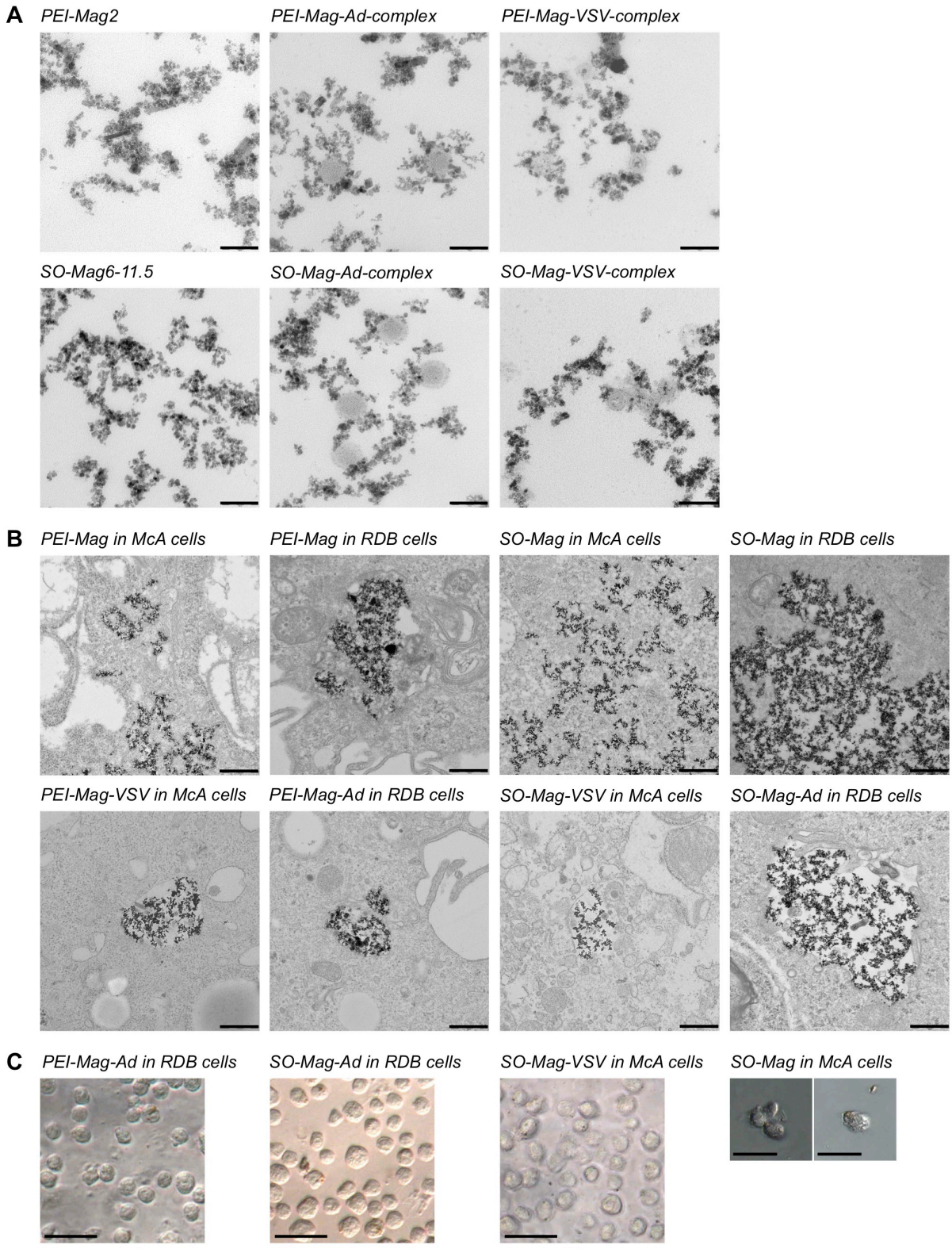

Figure 25: Self-assembly of MNP-VP complexes and their cell uptake. TEM of MNPs and MNP-VP complexes (**A**, scale bar 100 nm) and TEM of cell internalized MNPs and complexes (**B**, scale bar 500 nm). **C:** Microscopy of trypsinized labeled cells (scale bar 50 μm, D_{cell} (181RDB) = 16.5 ± 2.6 μm, D_{cell} (McA) = 16.3 ± 1.8 μm). The cell labelings are: PEI-Mag2-Ad in RDB: 3.9 pg Fe/cell; SO-Mag6-12.5-Ad in RDB: 2.3 pg Fe/cell; SO-Mag6-11.5-VSV in McA: 0.5 pg Fe/cell.

3.2.1.1.4 TEM analysis of internalized MNPs and MNP-VP complexes

To investigate the arrangement and aggregation of free and intracellular MNPs and MNP-VP complexes, as well as their intracellular localization, TEM was performed. Figure 25A shows TEM images of free MNPs and the according MNP-VP complexes for both types of VPs and MNPs. The suspended MNPs and MNP-VP complexes were mostly dispersed. Figure 25B compiles representative photomicrographs of the MNP and MNP-VP complex internalization in both cell lines. Naked MNPs mainly clustered in the cytoplasm, in the RDB cells in endosomes while in McA cells the particles are more dispersed in the cytoplasm (figure 25B, top row). In contrast to the free particles, MNP-VP complexes were localized exclusively in endosomes, independent from the cell type. Inside the endosomes, the magnetic and viral particles were arranged in a similar aggregate structure as the naked MNPs in the cytoplasm.

3.2.1.1.5 Magnetophoretic mobility measurements of MNPs, MNP-VP complexes and labeled cells

As expected, MNPs, MNP-VP complexes, and loaded cells were responsive to an externally applied magnetic field as indicated by a decrease in the relative OD of their suspensions under the magnetic field (figure 26). The decrease in OD of the magnetic samples was due to the accelerated clearance imparted by the magnetic properties, whereas unlabeled cells simply sediment over time. From these turbidity clearance curves, the average magnetophoretic mobility of MNP-VP complexes and MNP- or MNP-VP-labeled cells, and the average number of MNPs associated per complex or cell could be calculated (table 9). Such complexes comprise 2.2 x 10^4 PEI-Mag MNPs per virus particle for the complexes with VSV, and 2.6 x 10^4 MNPs per complex with Ad. The complexes with SO-Mag particles were larger and had more associated MNPs per complex (7.7 x 10^4 MNPs per VSV and 2.2 x 10^5 MNPs per Ad). The mean hydrodynamic diameters of the MNP-VP complexes of about 500 nm, 270 nm, 900 nm, and 600 nm (table 8), respectively, suggest that the complexes consisted of few physical virus particles surrounded with the evaluated number of MNPs. In addition to the information about the complex sizes and compositions, it could be evaluated how many naked and nanoassembled magnetic particles, respectively, were taken up by the cells. There was an uptake of 6.6 x 10^5 to 7.0 x 10^5 MNPs per McA cell (16.3 μm in diameter), and 8.4 x 10^5 to 8.7 x 10^5 free magnetic particles by the RDB cells (16.5 μm in diameter) (table 9). The McA cells were infected with 15 and 36 MNP-VSV complexes and the RDB cells were infected with about 5 and 19 adenoviral SO-Mag- and PEI-Mag-complexes, respectively. The turbidity clearance time course under magnetic field application indicated an optimum of 30 minutes incubation time on the magnet (i.e. time needed for complete magnetic sedimentation) for the *in vitro* labeling and magnetofection experiments.

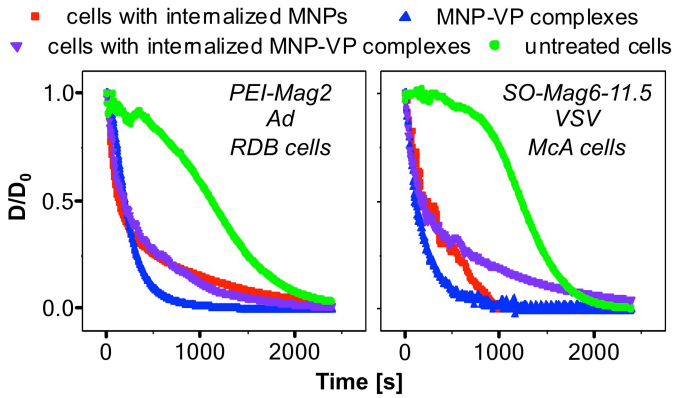

Figure 26: Magnetophoretic mobility of magnetic viral complexes and labeled and infected cells. Decrease of the normalized turbidity (D/D_0) of representative suspensions of untreated cells (green), magnetic viral complexes free (blue) as well as cell internalized (purple), and cells with internalized magnetic nanoparticles (red) in an average magnetic field of B = 0.213 ± 0.017 T with a magnetic field gradient of ∇B = 4 ± 2 T/m. The left panel shows the data set for PEI-Mag particles, Ad and RDB cells, right panel the respective data for SO-Mag particles, VSV and McA cells.

Sample	Time for magnetic sedimentation of 90% of complexes/ cells	Magneto-phoretic mobility	Magnetic moment	Number of associated MNPs
	$T_{0.1}$ [s]	v_z [µm/s][a,b]	M [fAm²][a]	$N = M/m_{eff}$[c]
PEI-Mag2-VSV	575	1.7	1.9	2.2 x 10^4
PEI-Mag2-Ad	513	1.9	2.2	2.6 x 10^4
SO-Mag6-11.5-VSV	441	2.3	4.4	7.8 x 10^4
SO-Mag6-11.5-Ad	85	11.8	405	7.2 x 10^6
PEI-Mag2 in McA	569	1.8	60.0	7.0 x 10^5
SO-Mag6-11.5 in McA	911	1.1	37.5	6.6 x 10^5
PEI-Mag2-VSV in McA	493	3.0	69.3	8.0 x 10^5
SO-Mag6-11.5-VSV in McA	532	1.9	64.3	1.1 x 10^6
PEI-Mag2 in RDB	480	2.1	72.1	8.4 x 10^5
SO-Mag6-11.5 in RDB	706	1.4	49.0	8.7 x 10^5
PEI-Mag2-Ad in RDB	822	1.2	6.9	8.0 x 10^6
SO-Mag6-11.5-Ad in RDB	556	1.8	62.2	1.1 x 10^6

[a] measured at an average magnetic field of B = 0.213 ± 0.017 T.
[b] measured at an average magnetic field gradient of ∇B = 4 ± 2 T/m.
[c] m_{eff} is an average effective magnetic moment of an insulated MNP

Table 9: Physico-chemical characteristics of magnetic viral complexes, MNP-labeled cells and viral complex infected cells.

3.2.1.1.6 Characterization of the oncolytic potential of MNP-VP complexes *in vitro*

Figures 27A and B and table 10A display the virus dose required for 50 % cell growth inhibition/oncolysis (IC_{50}). The curves registered for the concentration-dependent oncolytic effect of magnetic complexes of VSV and Ad with both MNPs were significantly shifted to low applied virus doses relative to the dose-effect-curve of naked virus particles. Even without magnetic field induction, the magnetic complexes were 1.2- to 6-fold more efficient than the virus alone in terms of the IC_{50} values of the applied dose (figure 27C and table 10A). The IC_{50} values of the MNP-VP complexes under magnetic field-guided infection at 7.5

% FCS were 1.6- and 2.5-fold lower for VSV, and 11.8- and 27.4-fold lower for Ad, respectively, than those of the naked virus, emphasizing the higher oncolytic activity of the MNP-VP complexes (figure 27C and table 10A). High serum concentration had a strong inhibitory effect on the oncolytic potency of the naked viruses, and some effect on the complexes when no magnetic field was applied. However, for the magnetic complexes, the magnetic field-influenced oncolytic potency-enhancing effect was about 10-fold and 2-fold for the adenoviral and VSV complexes, respectively (table 10B). This enhancement was true for low and high serum concentrations. The PEI-Mag-Ad complexes were hardly affected by serum in terms of the IC_{50}. High serum had only limited inhibitory effect on the IC_{50} of the SO-Mag-Ad and magnetic VSV complexes. Thus, the *in vitro* results demonstrated enhancement of the oncolytic efficacy of the studied magnetic VSV and Ad complexes in McA and RDB cells at both, low and high serum concentrations.

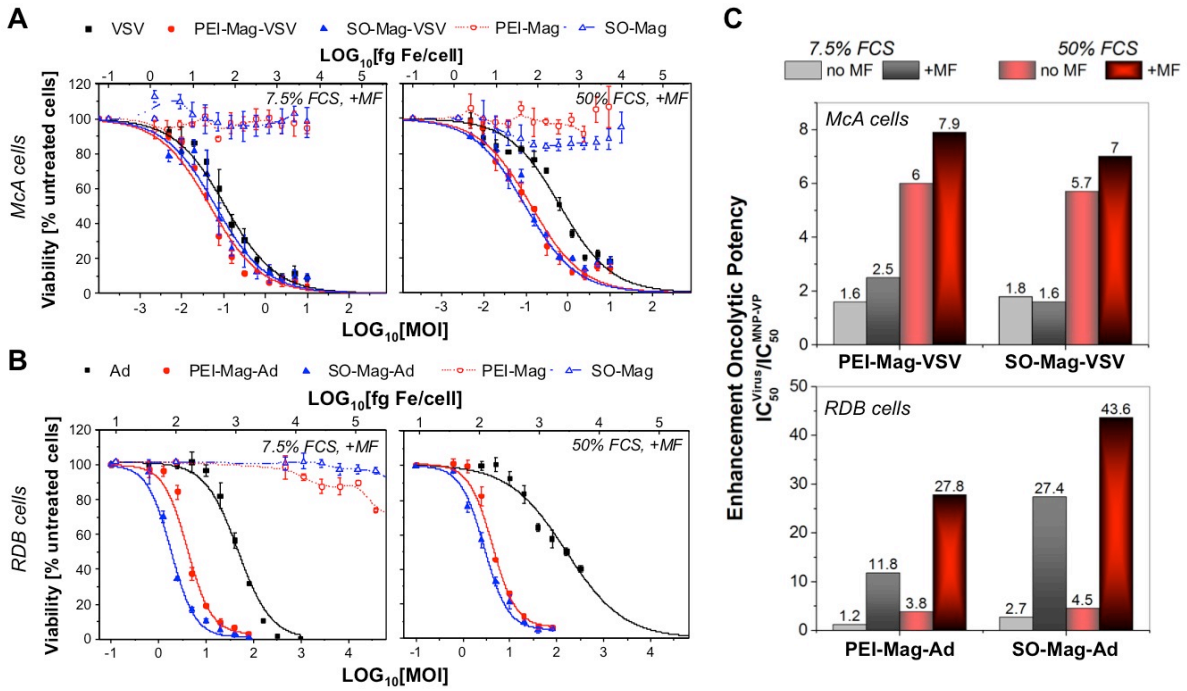

Figure 25: Oncolytic activity of the MNP-VP complexes at moderate and high FCS concentrations. McA (**A**) and RDB (**B**) cells were infected with naked virus or MNP-VP complexes at different virus doses under magnetic field application (+MF) for 30 minutes at FCS concentrations of 7.5 % (left panels) and 50 % (right panels). Oncolytic activity of the viruses and their magnetic complexes was assessed by measuring cell viability 24 hours after infection of McA cells using the MTT assay and 6 days after infection of the RDB cells expressing firefly luciferase using luciferase assay and expressed as a percentage using the untreated cells as a reference (mean ± SD; n = 3). Cell viabilities after treatment with equivalent doses of free MNPs are given as references. Naked virus is plotted in black, SO-Mag particles and their complexes in blue and PEI-Mag particles and their complexes in red. Panel **C** represents enhancement of oncolytic activity of the virus due to assembling with magnetic nanoparticles calculated as $IC_{50}^{virus}/IC_{50}^{MNP\text{-}VP}$, where IC_{50}^{virus} and $IC_{50}^{MNP\text{-}VP}$ are virus doses per cell required for 50 % cell growth inhibition/oncolysis after infection with virus or its magnetic complexes deduced from the dose-response curves registered after infection under magnetic field (+MF, data shown in figures **A** and **B**) or without magnetic field (no MF, data not shown) application and different FCS concentrations (grey bars: 7.5 % FCS, red bars: 50 % FCS).

A

Sample	magnetic field		no magnetic field	
	7.5 % FCS	50 % FCS	7.5 % FCS	50 % FCS
	IC_{50} in McA cells			
VSV	0.106 ± 0.011	0.684 ± 0.167	0.155 ± 0.031	1.020 ± 0.139
PEI-Mag2-VSV	0.042 ± 0.003	0.087 ± 0.015	0.094 ± 0.013	0.169 ± 0.024
SO-Mag6-11.5-VSV	0.067 ± 0.0134	0.098 ± 0.021	0.085 ± 0.0107	0.180 ± 0.025
	IC_{50} in RDB cells			
Ad	48.7 ± 2.0	122.2 ± 31.9	44.3± 2.5	163.2± 3.8
PEI-Mag2-Ad	4.1 ± 0.3	4.4 ± 0.3	36.6 ± 3.4	43.2 ± 1.8
SO-Mag6-11.5-Ad	1.8 ± 0.1	2.8 ± 0.24	16.0 ± 0.8	36.5± 2.0

B

Sample	magnetic field		no magnetic field	
	7.5 % FCS	50 % FCS	7.5 % FCS	50 % FCS
	IC_{50}^{virus} /IC_{50}^{MNP-VP} in McA cells			
VSV	1	1	1	1
PEI-Mag2-VSV	2.5	7.9	1.6	6.0
SO-Mag6-11.5-VSV	1.6	7.0	1.8	5.7
	IC_{50}^{virus} /IC_{50}^{MNP-VP} in RDB cells			
Ad	1	1	1	1
PEI-Mag2-Ad	11.8	27.8	1.2	3.8
SO-Mag6-11.5-Ad	27.5	43.6	2.8	4.5

Table 10: Oncolytic activity (IC_{50}). A: Virus dose required for 50% cell growth inhibition/oncolysis (IC_{50}) 24 hours after infection of McA cells with VSV vectors and 6 days after Infection of RDB cells with Ad vectors for the virus alone and its complexes with MNPs. Effect of the magnetic field and fetal calf serum (FCS) concentrations. **B:** Enhancement of oncolytic activity of magnetic virus complexes relative the virus alone. Effect of the magnetic field and fetal calf serum (FCS) concentrations.

3.2.1.1.7 Quantitative MRI analysis

MRI was performed to examine the visibility of the complexes under tissue-mimicking conditions, to determine the MR detection limit for the non-invasive monitoring of MNP and MNP-VP complexes, and to quantify the effect of cluster formation or intracellular compartmentalization on measured tissue relaxivities.

The visual iron detection limit in the R_2^* maps was as low as 0.003 – 0.008 mM Fe, representing 0.76 x 10^5 labeled cells per mL at a loading of 2.5 pg iron per cell (SO-Mag-VSV in McA cells), 0.24 x 10^5 labeled cells per mL at a loading of 6.7 pg iron per cell (PEI-Mag-Ad in RDB cells), or 0.36 x 10^5 labeled cells per mL at a loading of 5.4 pg iron per cell (SO-Mag in McA cells). A MR detection limit could not be determined as all dilutions of the magnetic nanomaterial were clearly detectable above the background of mimicked liver tissue and untreated carcinoma cells, and therefore it was below 0.001 mM Fe, the lowest measured iron dilution.

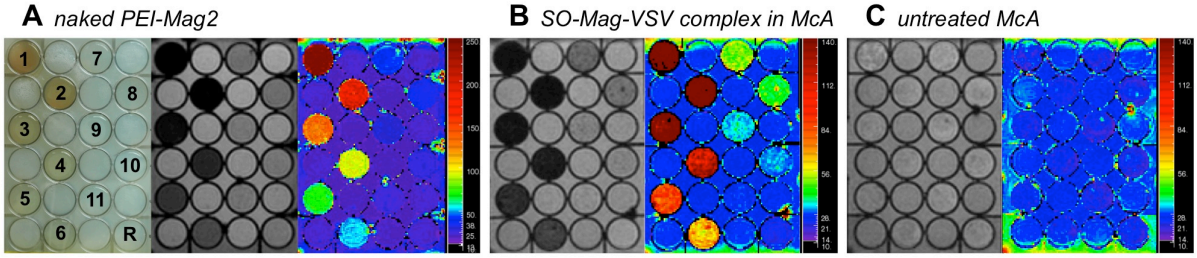

Figure 28: MRI of exemplary liver-mimicking phantoms. Panels show (from left to right) a photograph of the phantom, a T_2^* echo image, and the respective R_2^* map. The phantoms are loaded with PEI-Mag2 (**A**), SO-Mag-VSV-complexes in McA cells (**B**), and untreated McA cells (**C**). All phantoms were prepared from a 2-to-3 dilution series of the magnetic nanomaterial in the wells 1-11 and reference material in well R, on a 1.5 T Achieva MRI system.

Figure 28 compiles image sets of exemplary phantoms with (a photograph of the plate,) a T_2^* echo image, and the corresponding R_2^* map. Figure 28A shows the phantom with homogenously dispersed PEI-Mag particles, panel 28B presents the phantom prepared with SO-Mag-VSV complexes internalized in McA cells, and the image set figure 28C shows the background phantom of untreated McA cells with no detectable iron signal. The fading brown color in the photograph, the black-to-grey signal increase and the red-to-blue signal transition in the R_2^* map in all three panels mirror the decrease of magnetic material. Both, the R_2 and the R_2^* relaxation rates linearly increased with increasing iron concentrations in the range of 0.001 to 0.34 mM Fe of free, assembled, and intracellular MNPs. The measured R_2 or R_2^* transverse relaxation rates and respective iron concentrations were plotted in figure 28 for the 1.5 T (figures 29A and 29B) and 3 T (figures 29C and 29D) acquisition.

The assembly of MNP-VP complexes and further cell internalization led to 47 - 97 % reduction of r_2 and 14 - 82 % increase of r_2^* after internalization compared to free particles, which both yielded the highest r_2 and lower r_2^* relaxivities. Cell internalization of free particles reduced the r_2 relaxivities by 79 – 92 %, while the internalization of the corresponding MNP-VP complexes reduced the r_2 relaxivity in the same range (79 – 94 %), with the exception of the PEI-Mag-Ad complexes (47 %). In summary, the calculated r_2^* values were higher than r_2 values, and SO-Mag exhibited higher r_2^* relaxivities compared to PEI-Mag MNPs, while the r_2 relaxivities were in the same range. Internalized or complexed MNPs yielded lower r_2 values compared to freely dispersed naked MNPs. In contrast, r_2^* relaxivities increased after nanoassembly and/or cell internalization. Our r_2 relaxivities were between 10 and 286 mM^{-1} Fe s^{-1}, and therefore comparable to clinical contrast agents [269]. The r_2^* to r_2 ratio after particle assembly and/or cell internalization compared to free, suspended particles was dramatically increased. The variation was 2- to 33-fold for PEI-Mag and 3- to 56-fold for SO-Mag samples. Table 11 summarizes those r_2 and r_2^* relaxivities, ratios of the complexed and/or internalized MNPs relative to the naked MNPs, iron loading per cell, and r_2^*/r_2 ratios acquired on a 1.5 T clinical MRI system (corresponding 3.0 T MRI data in supplemental table 14). Figures 29E and 29F clearly demonstrates the comparability of data acquired either on a 1.5 T or a 3.0 T clinical MRI system.

Figure 29G shows the relaxivity plots for the data set of SO-Mag5 particles (from figure 9 of [115]), the magnetite core of the SO-Mag6-11.5 particles, and naked and cell internalized SO-Mag6-11.5 particles in McA cells and a primary murine PDAC cell line in liver tissue-mimicking phantoms. The maximal iron concentration was 72 μg Fe/mL (1.3 μM Fe) for all three phantoms, free particles and labeled cells.

Sample	PEI-Mag2					SO-Mag6-11.5				
	r_2 [mM^{-1} Fe s^{-1}]	ratio [%]	r_2^* [mM^{-1} Fe s^{-1}]	ratio [%]	r_2^*/r_2	r_2 [mM^{-1} Fe s^{-1}]	ratio [%]	r_2^* [mM^{-1} Fe s^{-1}]	ratio [%]	r_2^*/r_2
MNP	215 ± 9	100	441 ± 20	100	2.1	286 ± 7	100	851 ± 13	100	3.0
MNP in McA	45 ± 4 *(4.5 pg Fe/cell)*	21	585 ± 15 *(4.5 pg Fe/cell)*	133	13.0	30 ± 2 *(5.4 pg Fe/cell)*	10	787 ± 14 *(5.4 pg Fe/cell)*	92	26.2
MNP-VSV	45 ± 7	21	541 ± 23	123	12.0	32 ± 4	11	1030 ± 32	121	32.2
MNP-VSV in McA	18 ± 3 *(3.2 pg Fe/cell)*	8	595 ± 7 *(3.2 pg Fe/cell)*	135	33.1	55 ± 2 *(2.5 pg Fe/cell)*	19	1450 ± 57 *(2.5 pg Fe/cell)*	170	26.4
MNP in RDB	17 ± 1 *(17.3 pg Fe/cell)*	8	546 ± 37 *(17.3 pg Fe/cell)*	124	32.1	36 ± 1 *(15.9 pg Fe/cell)*	13	1209 ± 136 *(15.9 pg Fe/cell)*	142	33.6
MNP-Ad	115 ± 10	53	503 ± 11	114	4.4	18 ± 2	6	1020 ± 31	120	56.7
MNP-Ad in RDB	28 ± 5 *(6.7 pg Fe/cell)*	13	801 ± 23 *(6.7 pg Fe/cell)*	182	28.6	10 ± 6 *(7.4 pg Fe/cell)*	3	442 ± 17 *(7.4 pg Fe/cell)*	52	44.2

Table 11: r_2 and r_2^* relaxivities of the MNP assemblies. The table compiles the r_2 and r_2^* relaxivity data of the free MNPs and all magnetic viral complex assemblies in liver-mimicking agarose phantoms, the ratios of the nanoassembly relaxivity normalized to the relaxivity of free MNPs (r_2/r_2(MNP) and r_2^*/r_2^*(MNP), respectively), and the r_2^* / r_2 ratios. All measurements were performed using a clinical 1.5 T Achieva MRI system.

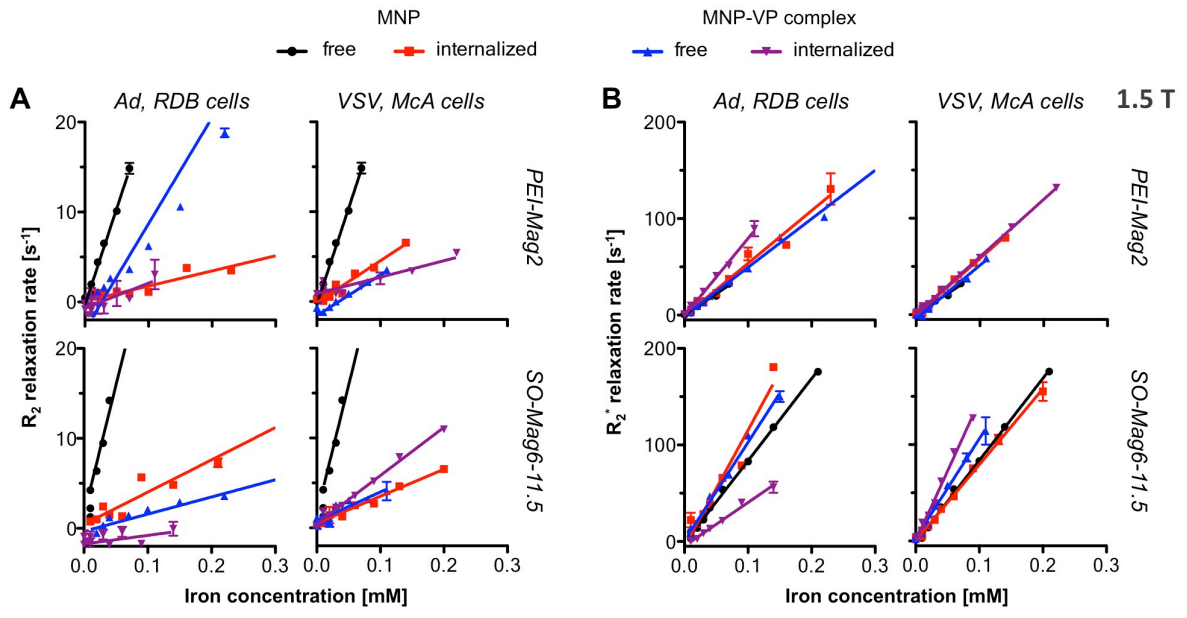

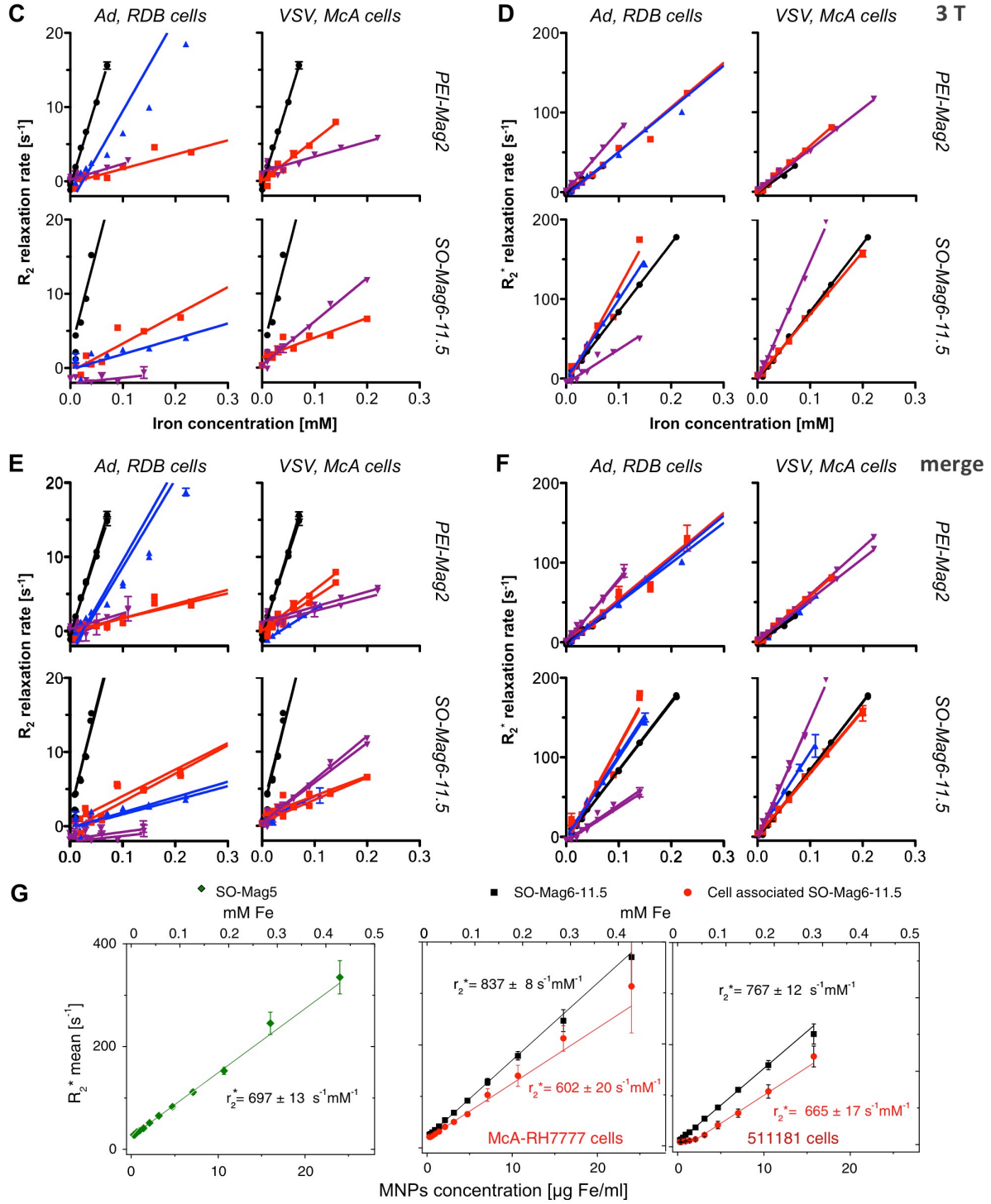

Figure 29: r_2 and r_2^* relaxivity plots. A-D: 1.5 T (A-B) and 3 T(C-D), **E-F:** merge of the 1.5 and 3 T data. **G:** r_2^* plots of free and cell associated MNPs (SO-Mag5/SO-Mag6-11.5) acquired at 1.5 T (from figure 9 [115]).

Figure 30B shows the corresponding saturation curves of SO-Mag particles in those two cell lines with internalized/associated iron plotted against the applied iron. The saturation curves of figure 30A show the results for both, SO-Mag and PEI-Mag particles in McA cells and three primary murine PDAC cell lines. Exogenic non-heme iron analysis elucidated SO-Mag particle loadings of 27 and 39 pg Fe/cell for 511181 and McA cells, respectively. Therefore, calibration phantoms for MR imaging were prepared with maximal final cell concentrations of

8.6 x 10^5 cells/mL in the 511181 cell PDAC phantom, and 6.2 x 10^5 cells/mL in the McA cell liver phantoms.

Due to the MRI signal "blooming" effect it was not possible to quantitatively analyze the phantoms prepared with clotted MNP(-VP complexe)s, neither naked or cell internalized (figure 18C). The concentration of the sample material into a small alginate clot and embedding of that clots in agarose phantoms instead of homogenous dispersion of the sample in the whole volume agarose led to very high punctual iron concentrations and very strong hypointense signals.

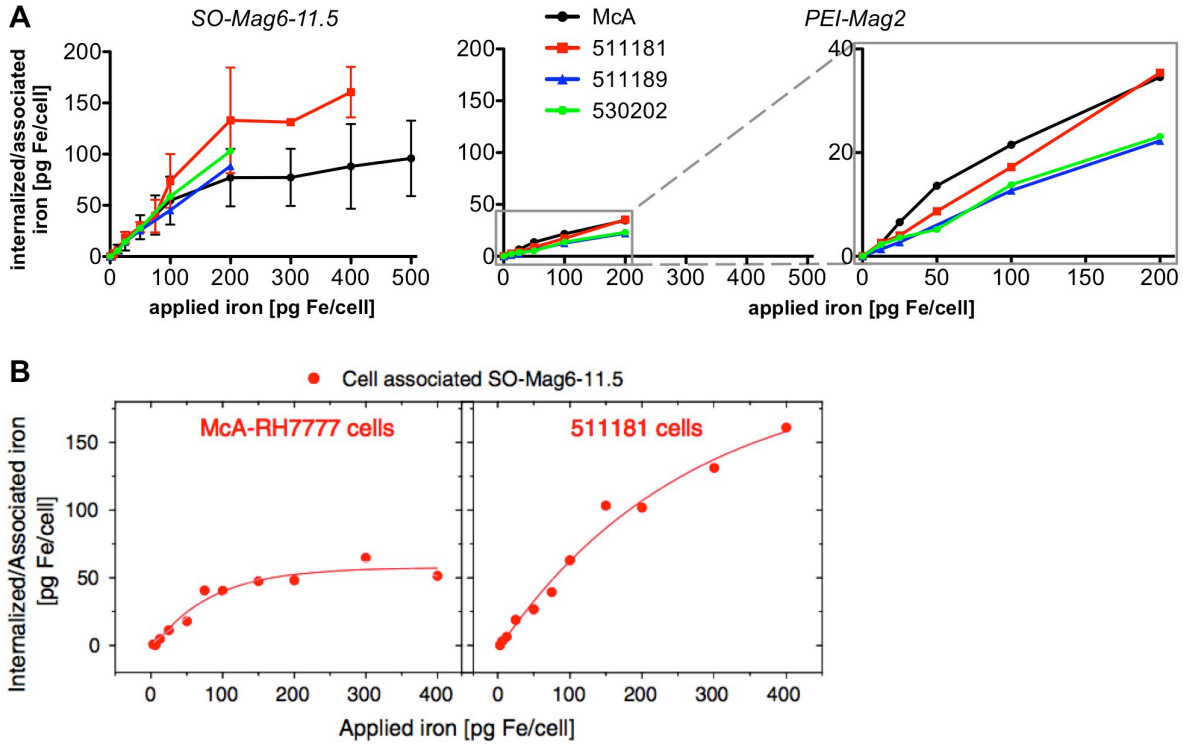

Figure 30: Saturation curves.

3.2.1.2 *In vivo* targeting of SO-Mag-VSV complexes

To test targeting and non-invasive detectability of MNP-VP *in vivo*, orthotopic HCC bearing rats were intra-tumorally injected with SO-Mag-VSV complexes in the presence of an external magnetic field. Anatomical T_2-weighted MR imaging at 24 hours post injection clearly revealed intra-tumoral drop in signal intensity (figure 31A top). Regional histogram analysis of the hypointense parts graphically depicted the signal intensity shift of SO-Mag-VSV complex-injected tumors in the lower signal range (figure 31A right). Histological analysis showed MNP-VP complex accumulation at the side of magnet placement (figure 31B). *Ex vivo* analysis confirmed increased VSV titer and non-heme iron content of SO-Mag-VSV complex-injected compared to naked VSV-injected tumors (figure 31C).

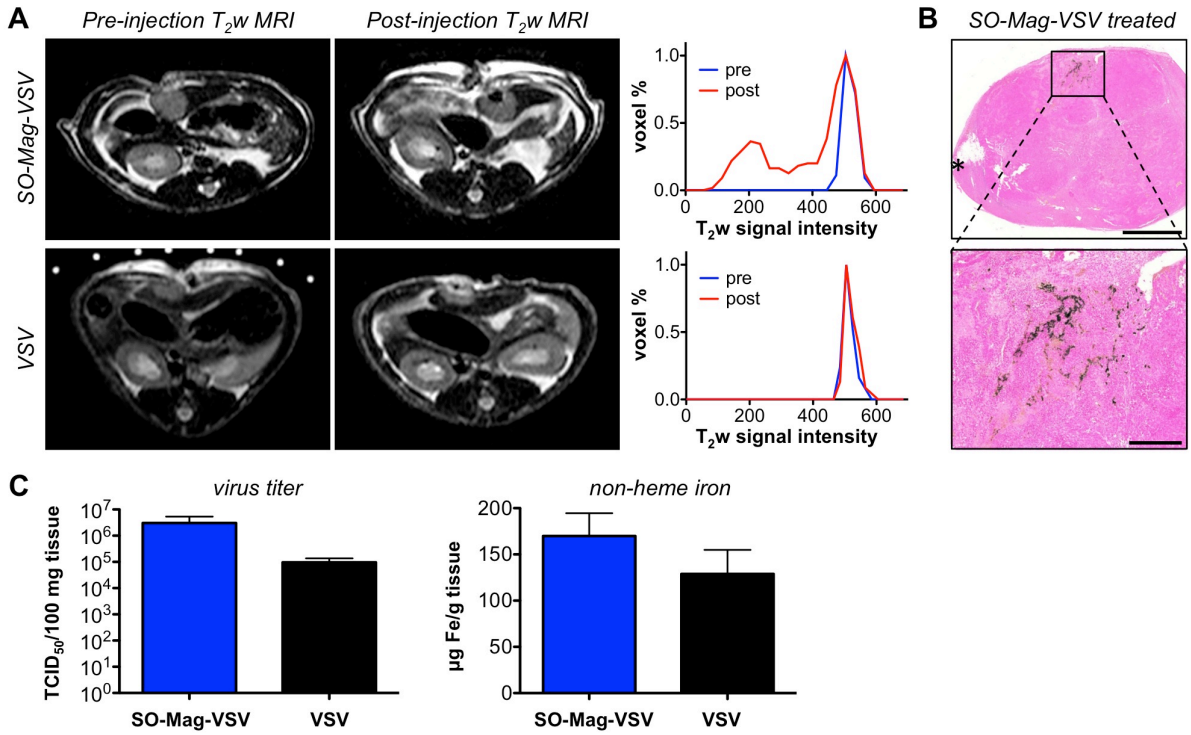

Figure 31: ***In vivo*** **targeting of SO-Mag-VSV complexes. A:** Pre- and 24 hour post-injection T_2-weighted anatomical MR images of orthotopic HCC after SO-Mag-VSV complex (top row) or naked VSV (bottom row) injection. The corresponding histograms (**A**, right) illustrate the signal loss after magnetic complex application in an emerging signal shoulder in the lower signal range. **B:** Overview (top) and high magnification micrographs of Prussian blue staining 24 hours after SO-Mag-VSV complex injection. The asterisk marks the injection site and the magnet was placed above the boxed area (top); scale bars 2,000 μm (top) and 500 μm (bottom), respectively. **C:** Intra-tumoral virus titer and non-heme iron of whole tumors sampled 30 minutes post infection with SO-Mag-VSV complexes (n=4, blue) and naked VSV (n=3, black).

3.2.2 MNP-siRNA complexes

Pre-clinical siRNA-based approaches were examined in various studies in the recent years. For *in vivo* applications, the siRNA needs to be enveloped with a carrier system to stabilize those small molecules and prevent from early degradation in the blood circulation.

In our nanocarrier system, the siRNA was assembled with magnetic nanoparticles and an enhancer, which in parallel provides the opportunity to monitor and magnetically target the siRNA complexes after administration in future *in vivo* trials. The MNP-siRNA constructs were *in vitro* tested for their capability to down-regulate specific genes in cancer cells in a poof-of-principle study. Test systems for the knock-down experiments were stably luciferase and GFP expressing cell lines. SO-Mag and PEI-Mag particles were chosen as they easily assemble with negatively charged siRNA due to their own positive surface charge.

3.2.2.1 Cell transduction for stable eGFP-Luc-fusion protein expression

Selected pancreatic and hepatic cancer cell lines were transduced with the eGFP-luciferase-fusion reporter gene construct, and were analyzed for their capability to express those new

proteins. First, the cells were checked for GFP expression qualitatively under the fluorescence microscope. Compared to the non-transduced cells on the left, all transduced cells exhibited fluorescence as the right column of the photograph panel in figure 32A shows clearly. For quantitative analysis, luciferase and GFP assays were performed, and the expression levels were measured after 48 and 72 hours at different cell seeding concentrations. The read out was plotted as chemiluminescence/fluorescence units in counts per second over the number of cells seeded to identify the cell density needed for reliable assay results. The first McA cell transduction did not work properly, therefore there were three batches of cells tested, cells of the first transduction (48 h and 72 h samples), “new” (same transduction conditions as before; 72 hours) and “double” transduced cells (underwent two sequential transductions; 72 hours). Those double-transduced cells were chosen for the further experiments, and from this point on referred to as McA eGFPLuc. For all other cell lines, the first transduction already resulted in positive GFP and luciferase expression. The luciferase and GFP expression levels varied between the different cell lines with the highest luciferase and GFP expression in the HuH-7 cells relative to the number of cells seeded. For the further knock-down experiments with MNP-siRNA complexes, and subsequent luciferase and protein assays, 10^4 cells per well, and 72 hours incubation after treatment were identified as optimal conditions. Figure 32B shows the calibration curves of luciferase plotted as chemiluminescence units over the luciferase concentration in ng/well. Those calibration curves were used for calculation of the cell expression levels via linear regression.

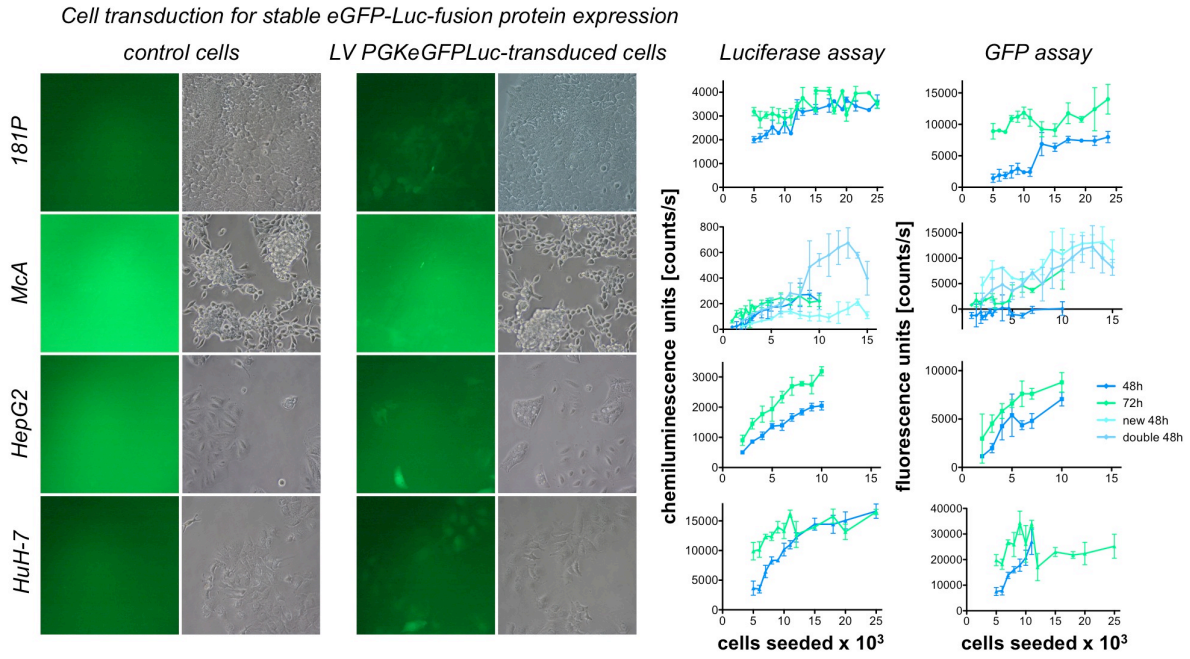

Figure 32: Luciferase and GFP assay – proof of cell transduction with eGFP-Luc-fusion-construct. Fluorescence/brightfield microscopy of LV PGKeGFPLuc-transduced vs. non-tranduced control cells and the according luciferase and GFP assay data (from left to right).

3.2.2.2 *In vitro* knock-down via magnetofection with MNP-siRNA complexes

The down-regulation of luciferase expression after magnetofection with MNP-siRNA complexes is complied in figure 33. For all cells, the luciferase expression level of untreated cells corresponded to the data acquired from the luciferase assays presented in figure 33A. Analogous to the magnetic viral complexes, siRNA complexes of both magnetic nanoparticles, SO-Mag and PEI-Mag, were tested for their enhancing potential. To evaluate the enhancing effect of magnetofection using magnetic complexes instead of non-magnetic lipoplexes in those knock-down experiments, DF-siRNA lipoplexes were tested in parallel to the magnetic lipoplexes (red and blue curves), and the green curves in all graphs represent the data acquired for those reference lipoplexes.

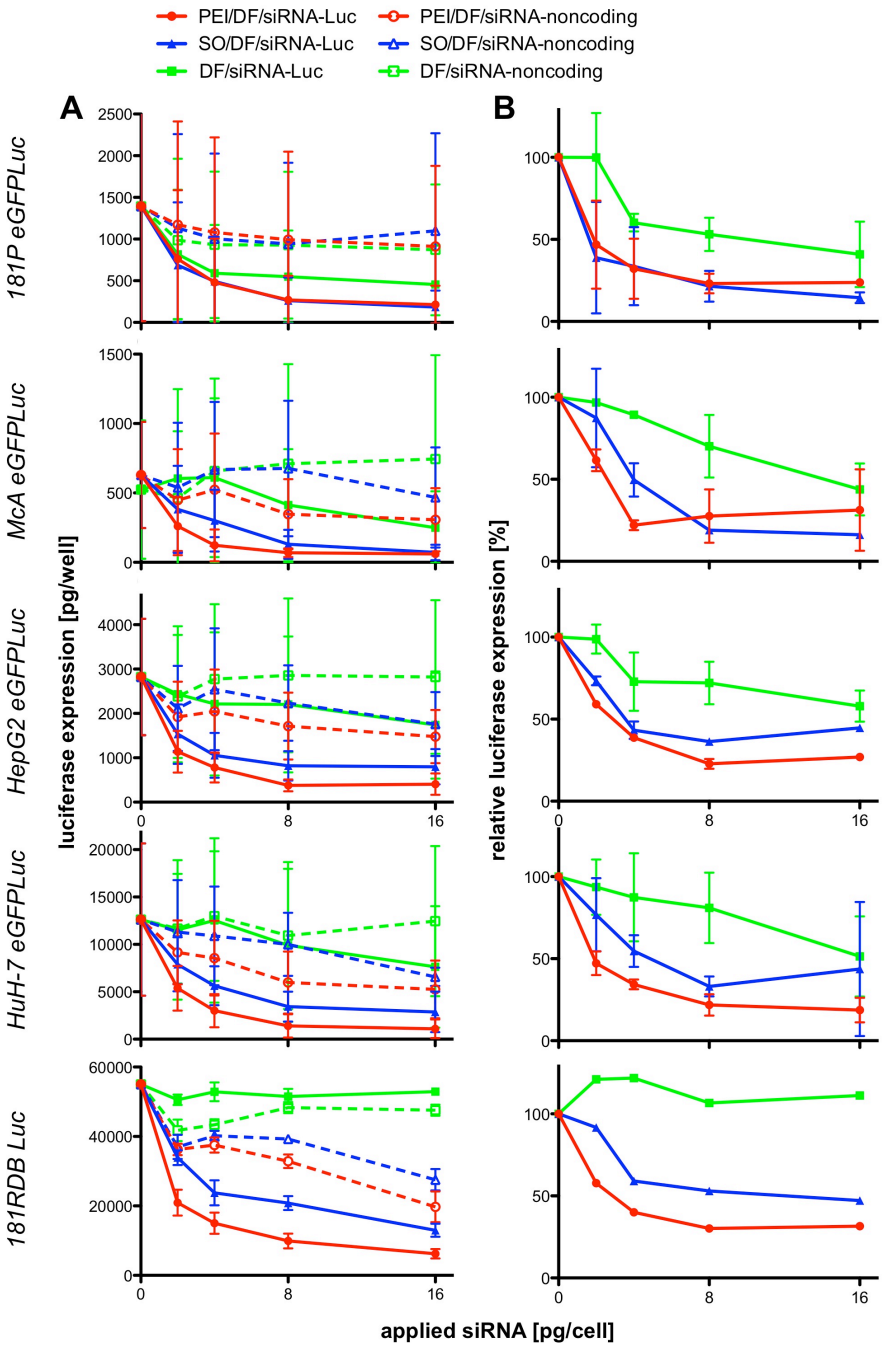

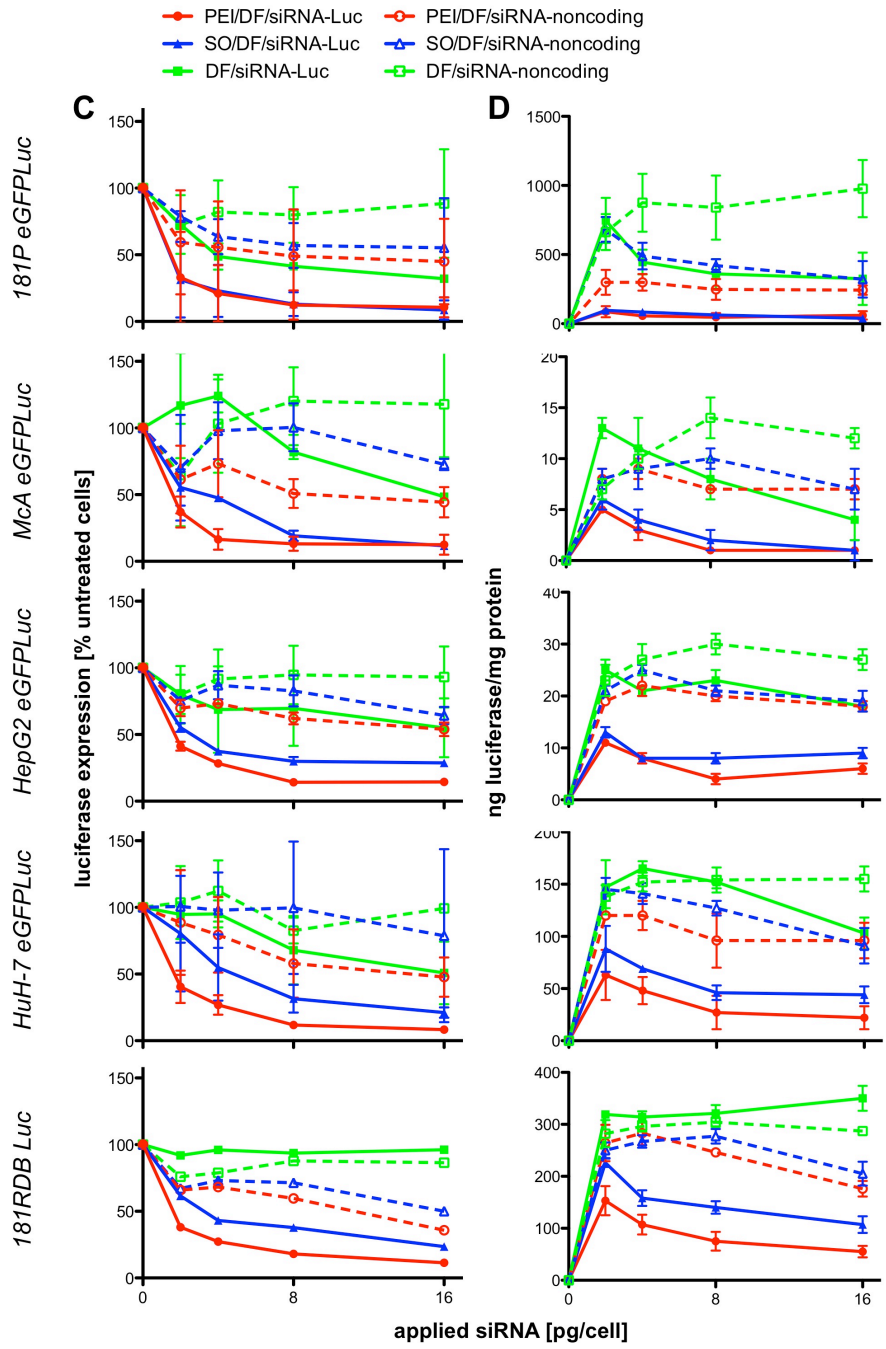

Figure 33: siRNA knock-down via magnetofection. A: Absolute luciferase expression in pg per well of the different tested cell lines. **B:** Luciferase expression of siRNA-Luc transfected cells relative to the luciferase expression in with non-coding siRNA transfected negative control cells. **C:** Luciferase expression of transfected cells relative to untreated cells. **D:** Luciferase expression relative to the total protein.

In all tested cell lines, transfection with PEI-Mag-siRNA complexes (red curves) resulted in higher down-regulation of the luciferase expression than with SO-Mag-siRNA complexes (blue curves). The down-regulative effect of the lipoplexes was a lot weaker than both magnetic complexes in all cell lines, especially in the 181RDB Luc cells. The graphs of figure 33A present the total luciferase expression in pg per well. The expression levels were calculated from the chemiluminescence units detected using the calibration curve (figure 20). In addition to the absolute expression levels, the luciferase expression and more important

its down-regulation after transfection could be presented in two different ways depending on the reference values used. To derive the true down-regulation of the target protein expression, it might be better to use the values of the respective negative control siRNA complexes (figure 33B) rather than untreated cell data (figure 33C) as reference. But using untreated cells as reference allows to qualitatively evaluate the general effect of the transfection on the cells as even non-coding siRNA complexes led to slight down-regulation of the luciferase expression. Furthermore, in figure 33D the total amount of luciferase is presented graphically in ng luciferase per mg total protein.

3.2.3 Magnetic liposomes

3.2.3.1 Pre-studies on the MNPs

The pre-studies were conducted to describe the *in vitro* and *in vivo* behavior of the palmitoyl dextran magnetic nanoparticles. They were characterized regarding their cell interaction and uptake, their MR imaging properties, and their toxicity *in vitro* in cancer cell lines and *in vivo* in mice.

3.2.3.1.1 MNP – cell interaction

The cell lines chosen for the *in vitro* tests were rat hepatic carcinoma cells and primary murine pancreatic adenocarcinoma cells as in both cancer types liposomal chemotherapy would be a convenient medication, and the rodent tumor models were established.

3.2.3.1.1.1 MNP uptake and cytotoxicity evaluation

To identify optimal labeling conditions, several primary murine PDAC cells and the rat HCC cell line McA were treated with increasing amounts of magnetic nanoparticles. Figure 34A of two exemplary cell lines shows photographs of pelleted labeled cells and micrographs of the corresponding MNP-loaded cell monolayers. The color of the cell pellets shifted from white to brown with increasing amounts of internalized iron particles (figure 34A, two top photographs, each from right 0 pg Fe/cell to left 400 pg Fe/cell). In the four picture sets below, the MNP aggregates could be identified in the magnification as clearly visible brownish spheres within the labeled cells but not in the non-treated reference cells of the according micrographs. Quantification of the exogenic iron was performed using a colorimetric method with 1,10-phenanthroline, and the saturation effect with MNPs at between 200 and 800 pg applied iron per cell was visualized by plotting the internalized/associated iron over the applied iron dose (figure 34B; magnification for the concentration range 0 – 400 pg Fe/cell for PALD2-Mag1). The plateau labeling concentrations ranged between 20 and 80 pg Fe/cell for the pancreatic and 125 pg Fe/cell for the hepatic cells in case of PALD2-Mag1, and 70 and 185 pg Fe/cell for the PALD2-Mag2 nanoparticles in the pancreatic cells. To evaluate the cytotoxicity of the applied magnetic

nanoparticles on the cells, MTT assays were performed in that same iron concentration range; figure 34C summarizes those viability assay data. In the tested cell lines, the MNP treatment led to reduced cell viability in the 512010 and 530202 cells in a dosage range of 25 – 800 pg Fe/cell applied iron with viabilities of 54.1 % (530202) and 52.1 ± 6.5 % (512010) at the highest applied iron dose of 800 pg Fe/cell. For the other tested cell lines, there were no strong adverse effects on cell viability with 73.8 ± 25.8 % for 511181 cells and 84.7 ± 20.1 % for 511677 cells even at 800 pg Fe/cell. There was a first viability drop for all cell lines up to 25 pg Fe/cell (12.5 pg Fe/cell for 511181), then an increase, and then the viability was slowly decreasing again for all iron doses up to 800 pg Fe/cell (except for 511677 with viability improvement between 400 and 800 pg Fe/cell treatment) as the graph and its magnification in figure 34C show.

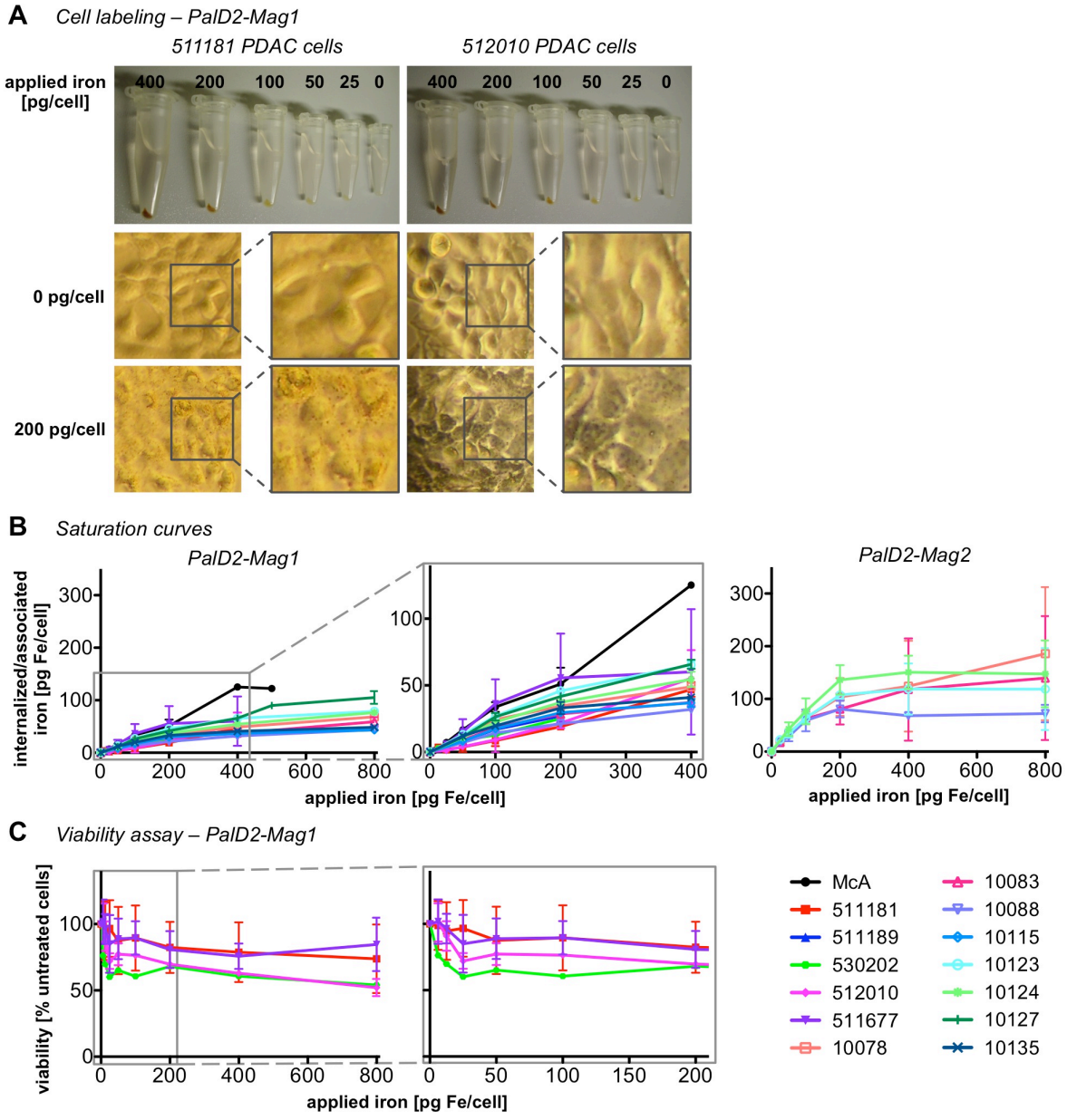

Figure 34: *In vitro* MNP-uptake and cytotoxicity evaluation: PALD2-Mag. A: Images of cells labeled with PALD2-Mag1: cell pellets in the top row and light microscopy of labeled cell monolayers

beyond, labeled and non-labeled cells both in sets with the two-fold magnification. **B:** Mean all saturation curves. **C:** MTT assay of PALD2-Mag1 particles in PDAC cell lines.

3.2.3.1.2 *In vivo* biodistribution and toxicity study

The *in vitro* MNP-uptake and cytotoxicity evaluation exhibited no adverse effects, so the particles were analyzed for their *in vivo* biodistribution and toxicity in mice. After intravenous administration of both types of magnetic palmitoyl functionalized nanoparticles, the mice were observed for 14 days regarding weight development, general fitness and behavior. Then they were sacrificed and tissue samples underwent histological and biochemical analysis for exogenic iron from the magnetic nanoparticles; figure 35 summarizes all analysis results of both treatment groups (PALD2-Mag1 and PALD2-Mag2). The weight development was plotted for both MNPs as weight over age for female and male animals in figure 35A (PALD2-Mag1 male n = 6, PALD2-Mag1 female n = 7, PALD2-Mag2 male n = 4, PALD2-Mag2 female n = 10). All animals presented a healthy gain of weight; the weight of the PALD2-Mag2 injected female animals was slightly higher as they were 10 days older than the PALD2-Mag1 injected females (supplemental table 12). Regarding the weight development and the scoring of general fitness and behavior, no impact of the MNP treatment was suggested as the animals showed no signs of health alteration such as cachexia, reduced mobility or behavioral changes. For the histological (figure 35C) and biochemical (figure 35B) evaluation sampled tissues were liver, lung, spleen, kidney, pancreas/pancreatic tumor (tumor head and tumor tail), heart, testis/ovary, bone and tail (injection site). In figure 35B the quantitative analysis of the Prussian blue stained tissue area (left) was compared with the biochemical analysis for non-heme tissue iron (right), both plotted for all sampled tissues and averaged over all animals per treatment group and sex analogous to figure 35A (exogenic iron quantification: control male n = 6, control female n = 10, PALD2-Mag2 male n = 4, PALD2-Mag2 female n = 10; Prussian blue: control male n = 7, control female n = 11, PALD2-Mag1 male n = 8, PALD2-Mag1 female n = 11, PALD2-Mag2 male n = 4, PALD2-Mag2 female n = 10). Figure 35C compiles exemplary histology results of liver, lung, spleen, kidney and pancreas samples in PALD2-Mag2-injected mice versus the untreated control, both in female and male mice. In the liver samples of treated (97 %) as well as untreated (19 %) animals, positive iron staining was mainly detectable in the periportal zone of the liver lobule. In detail, iron was found in the sinusoidal cells in most cases but also in single hepatocytes. Eosinophilic crystals which stained positive for iron were found in the lung tissue samples of 85 % of the treated animals. These crystals were needle-shaped and were present in the cytoplasm of alveolar macrophages as well as free-lying within alveoli. Positive staining for iron was also found in alveolar cells, but there were no pathological findings in the lungs. Hemosiderin is an iron-positive pigment derived from erythrocytes. The presence of hemosiderin in the spleen is considered normal and can be seen in macrophages mainly in the red pulp but also in the white pulp, so the staining is also not necessarily related to the MNP administration as the staining was found in 100 % of the

treated and 81 % of the untreated animals spleen tissue samples. The iron particles stained in the kidney samples of 52 % of the treated animals were mainly found in the glomeruli and tubules of the cortex region. In the pancreas of 32 % of the treated animals, iron particles were mainly found in endothelial cells of the vessels as well as in the interstitium between acinus cells. In 16 % of the treated animals there were iron positive pancreatic lymphnodes, while the pancreatic tissue was iron-negative. In PDAC samples positive iron staining was localized focally in the tumor stroma.

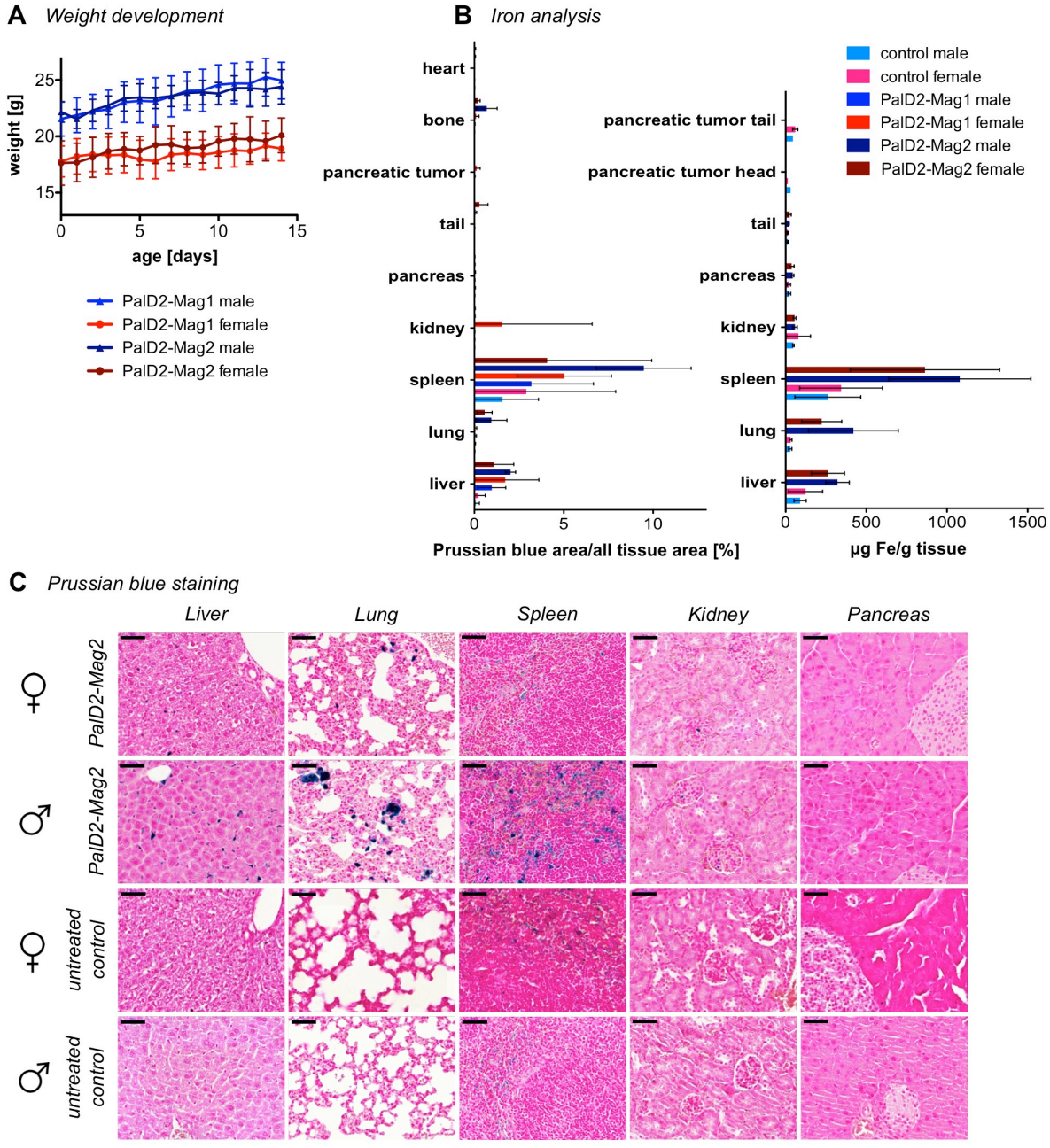

Figure 35: MNP biodistribution and toxicity *in vivo*: PALD2-Mag. PALD2-Mag1 (200 µg in 200 µL NaCl) and PALD2-Mag2 (200 µg Fe in 100/200 µL NaCl). **A:** Weight development after MNP administration. **B:** Prussian Blue are/all tissue area [%] vs. non-heme iron quantification [µg Fe/g tissue] with non-heme iron determination. **C:** Exemplary Prussian blue stained tissue samples, bar 50 µm. Control male: n=6, Control female: n=10, PALD2-Mag2 male: n=4, PALD2-Mag2 female: n=10; Prussian Blue staining: Control male: n=7, Control female: n=11, PALD2-Mag1 male: n=8, PALD2-Mag1 female: n=11, PALD2-Mag2 male: n=4, PALD2-Mag2 female: n=10; Weight development:

PALD2-Mag1 male: n=6, PALD2-Mag1 female: n=7, PALD2-Mag2 male dark: n=4, PALD2-Mag2 female 7w light: n=4, PALD2-Mag2 female 5.5w dark: n=6.

Positive staining for iron was mainly found in the interstitial cells of the heart of 39 % of the treated animals. Some ovary samples of female treated (57 %) as well as untreated (22 %) animals showed positive staining for iron particles in the ovarial stroma, whereas no specific staining could be found in the testis samples. By nature, most absorbed iron is utilized in bone marrow for erythropoiesis. A few animals, treated (72 %) and untreated (7 %), showed focal iron positive staining in the periosteum of the inspected bone sample. In a few treated animals (21 %) the tail vein showed a positive iron staining because of the intravenous administration of the MNPs via a tail vein catheter. The only pathological findings were areas of focal inflammation and/or microgranuloma and/or focal necrosis in many liver tissue samples of treated (85 %) and untreated (69 %) animals with which can be a common finding in BL/6 mice, and the pancreatic tumors, fibrotic tissue and focal areas of inflammation in the pancreas samples of PDAC positive mice. Over all other tissues there were no pathological findings.

3.2.3.1.3 Target-protein expression: integrins α_v and β_3

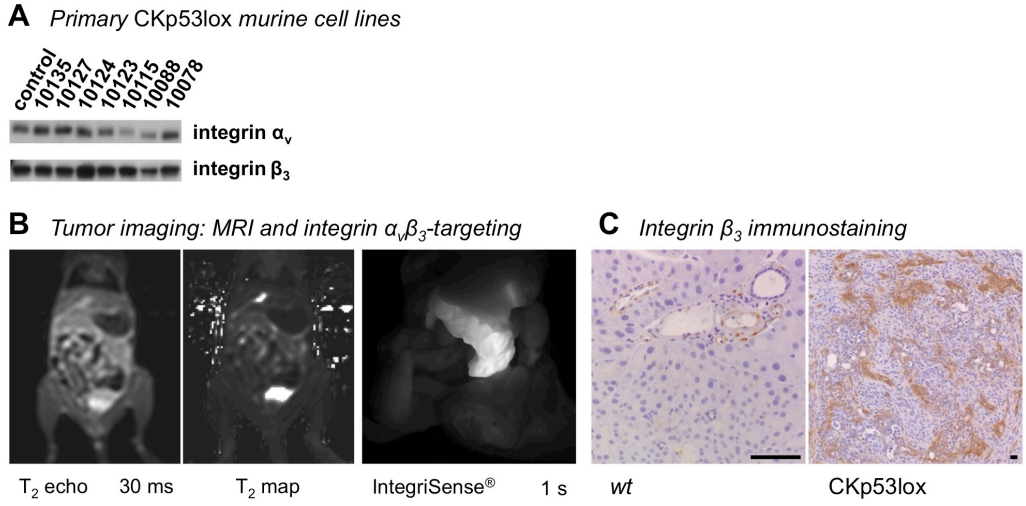

Figure 36: Target-protein expression in PDAC. A: Western blot of primary murine pancreatic cancer cell lines for integrin β_3 and integrin α_v. **B:** Magnetic resonance (left, middle) and intraoperative fluorescence imaging (right) in a PDAC-bearing mouse: The bright abdominal MR signal on the coronal slice in the T_2 echo after 30 ms (left) as well as the T_2 map (middle) and the $\alpha_v\beta_3$-expressing tissue labeled with IntegriSense® (right) mark the tumor. **C:** Immunostaining of integrin β_3 (brown) in murine pancreatic tissue around the vessels of a wildtype mouse (left) and throughout the whole tumor of a tumor mouse (right). Images from B and C kindly provided by Dr Trajkovic-Arsic

The tumor cell surface protein $\alpha_v\beta_3$ integrin receptor was chosen as potential target structure and its expression on the primary PDAC cell lines was proven qualitatively by Western blotting. Figure 36A shows blots for the integrins α_v and β_3 in the PDAC cell lysates and a positive control lysate. Unfortunately, the antibody of the loading control Hsp90 did not work properly, but as it was only a qualitative expression control and no quantitative analysis, the

assay was not repeated. The T_2 echo MR image (36B left) of a PDAC bearing mouse and the corresponding T_2 map (36B middle) of the anatomy scan enabled the localization of the tumor for the intraoperative fluorescence imaging (36B right). The binding of the $\alpha_v\beta_3$ integrin-targeting contrast agent IntegriSense® 680 resulted in a bright signal of the tumor. The *ex vivo* immunostaining in figure 36C shows the normal expression of β_3 integrin (brownish) around the vessels of a healthy *wt* mouse compared to the expression throughout the whole tumor tissue in a *CKp53lox* PDAC mouse. The data of figures 36B and C were kindly provided by Dr Trajkovic-Arsic, II. Med. Clinic, Gastroenterology, Klinikum rechts der Isar der Technischen Universität München. Detailed results are presented in Trajkovic-Arsic et *al*. [209].

3.2.3.2 Magnetic liposomes

3.2.3.2.1 Liposome synthesis and characterization

Liposomes were synthesized using three different protocols: thin film hydration, reverse phase hydration, and the injection method. Desired liposome size was about 100 nm in diameter, and the surface should be PEG-functionalized for stabilization, either as lipid moiety or using the polymer P_3C_{18}. Advantage of the polymer was its capability to bind $\alpha_v\beta_3$ integrins, expressed specifically on tumor cells. Figure 37 compiles exemplary results of the palmitoyl dextran MNP and MNP-LP characterization. The optimal wavelength for photometrical analysis was examined in wavelength scans of the magnetic nanoparticles. For both PALD2-Mag particles, 350 nm was determined as appropriate (37A of an exemplary PALD2-Mag1 scan). In figure 37B, the decrease of turbidity was plotted over time for magnetic TFH liposomes consisting of DPPC:Chol:DSPE-PEG_{2000} at 80:20:5 prepared with PALD2-Mag1 particles versus naked PALD2-Mag1 particles. The schematic explains magnetophoretic mobility as the liposome migration towards the magnets on both sides, and thus the clearance of the suspension in the cuvette, detected as signal decrease. Liposomes synthesized following the injection method protocol met those criteria with 119 ± 57 nm (100.1 nm in one respective measurement, figure 37C) in diameter and a slightly anionic zeta potential of - 10 ± 6 mV (ζ = -9.96 mV, 36C) after magnetic separation, as did the TFH liposomes with D_h = 92 ± 65 nm and an anionic ζ of - 55 ± 8 mV. Exemplary zetasizer measurements of the physico-chemical properties of magnetic liposomes, size and charge, are presented in figure 37C. The left graphs show the size (upper graph) and the zeta potential (bottom graph) of the magnetic fraction, and the right two graphs present the corresponding data of the non-magnetic fraction. Those exemplary injection method liposomes were prepared from DPPC:Chol:P_3C_{18} at 80:20:5 and PALD2-Mag1 particles. A negative charge ζ of -9.96 mV and the size of 100.1 nm indicated, that the injection method could be technique of choice for preparation of magnetic liposomes as size and charge meet the set criteria, as well as the TFH liposomes did with similar values (data not shown). The

magnetic separation into magnetic and non-magnetic fraction helped to remove bigger non-magnetic liposomes, only a very small fraction of 2.2 % was left in the MNP-LP fraction and could be removed via extrusion. Figure 37D compiles phase contrast and fluorescence microscopic images of liposomes synthesized by the injection method and with P_3C_{18} polymer (20 % of it conjugated with atto550 fluorescence dye) in 40-fold magnification. The micrographs nicely show the behavior of the magnetic liposomes before (figure 37D left) and after (figure 37D right) an external magnetic field was applied, the magnetic liposomes instantly moved towards the magnet.

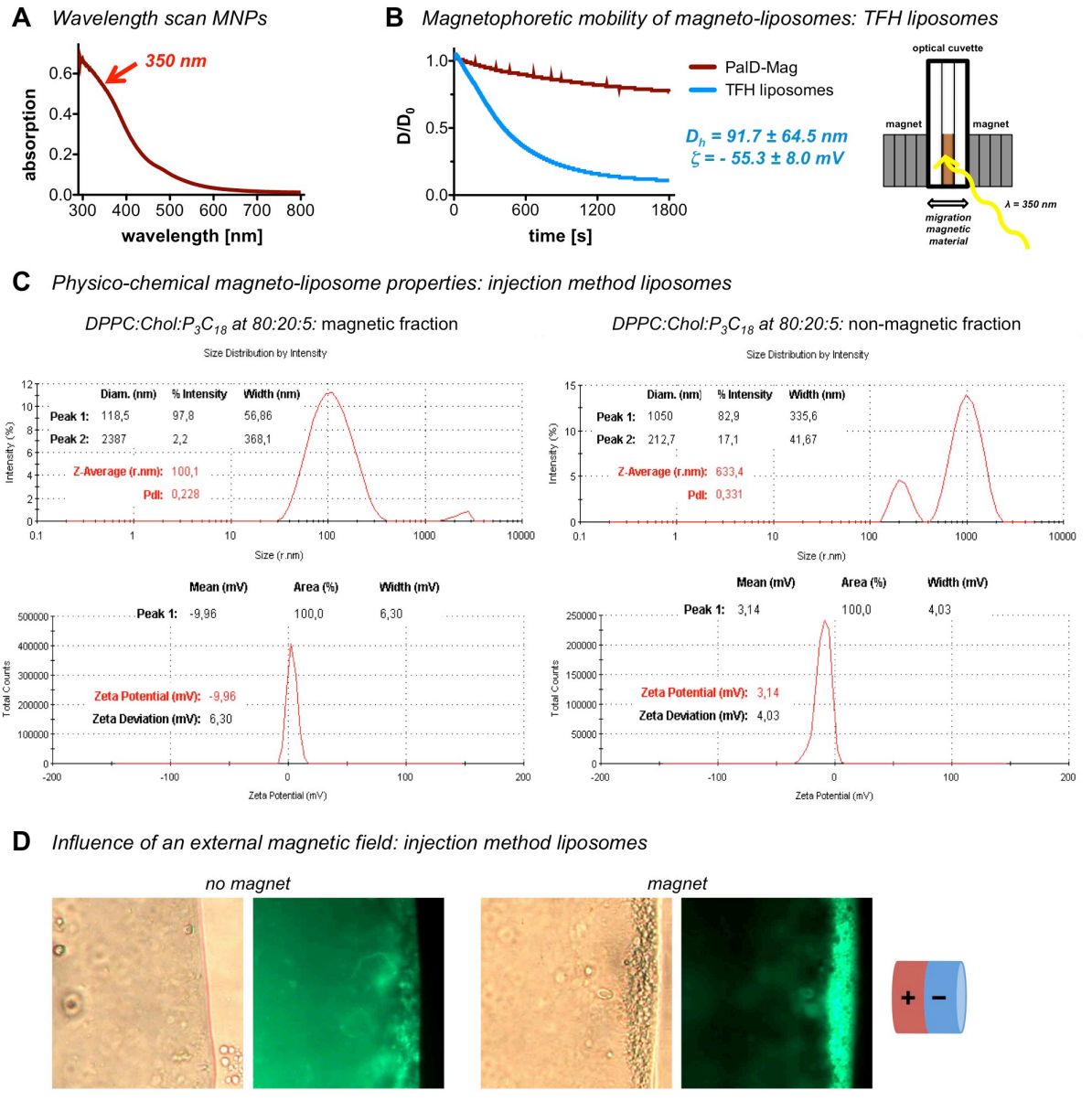

Figure 37: MNP and MNP-LP characterization. A: Wavelength scan of PALD2-Mag1. **B:** Magnetophoretic mobility measurement: exemplary TFH liposomes of DPPC:cholesterol:DSPE-PEG_{2000} 80:20:5 with PALD2-Mag1 and naked PALD2-Mag1 particles at λ = 350 nm. **C:** Physico-chemical characterization of exemplary injection method liposomes: measurement data of size by intensity and charge. **D:** Microscopy of liposomes: phase contrast and fluorescence mode in 40-fold magnification.

3.2.3.2.2 Thermosensitive LPs

Advantage of a liposomal formulation is the possibility to choose the lipids according to the application specific needs. In this study, the lipid shell formulation allowed for targeted release of the liposomes content triggered by temperature. When the liposomal solution was heated up above a specific temperature, the thermosensitive lipid layer started to get leaky and released the encapsulated liquid. Depending on the chosen lipid composition, that melting temperature T_m could be tuned. For this test, three different lipid compositions with proposed melting temperatures ranging between 39 and 42 °C were analyzed. The liposomes were filled with a calcein solution whose release could be quantified fluorometrically in the surrounding medium (PBS/50% FCS in PBS). To identify the specific wavelength for such quantification, first a wavelength scan was performed, and 496 nm was identified as calcein absorption maximum (figure 38A). Measurement of the standard curves in different media revealed that both, PBS and 50 % FCS in PBS could be used (figure 38A), whereby the FCS solution is closer to *in vivo* conditions. In addition, the extinction coefficients $\varepsilon_{calcein}$ in the different media were determined to be $\varepsilon_{calcein}$(PBS) = 2,801 $cm^{-1}M^{-1}$, $\varepsilon_{calcein}$(50 % FCS) = 2,932 $cm^{-1}M^{-1}$ and $\varepsilon_{calcein}$(H_2O) = 2,567 $cm^{-1}M^{-1}$ (figure 38A). Figure 38B summarizes calcein release assay data for two different liposome synthesis protocols, TFH (top graphs) and injection method (bottom graphs), and two different media, PBS (on the left) and the more physiological 50 % FCS in PBS (on the right). For all temperatures, the calcein release in % was plotted over time (temperature color code legend on the right; for all: circles represent lipid preparation a, squares composition b, and triangles lipid mix b*). Figure 44 in the supplement presents the release data for both types of liposomes in separate graphs for each temperature. Lowest incubation temperature was body temperature 37 °C to prove that none of the calcein would be released directly after an *in vivo* application before even reaching the target region, the other incubation temperatures were 39 °C, 41 °C and 42 °C, and the release was calculated relative to the 100 % release control samples lysed with Triton X-100. In general, the assay worked only for the TFH liposomes. For the liposomes synthesized using the injection method, the temperature-dependent calcein release could not be shown properly. In PBS, the best calcein release levels from the TFH liposomes over all temperatures were gained for composition a, the DPPC:Chol:P_3C_{18} liposomes. Melting temperature with high release levels above 50 % already after 15 minutes was T_m = 42 °C, at 41 °C the release started after 30 min and at 39 °C it started after 45 minutes. For the two other lipid compositions, the temperature response pattern was the same but the release levels were lower. In 50 % FCS in PBS, the release levels and timing were comparable for all three lipid compositions, also with about 50 % release after 15 minutes exposure to 42 °C, 30 minutes to 41 °C and 45 minutes to 39 °C.

Incubation at increased temperatures revealed no clear calcein release from the injection liposomes for all three lipid compositions and in both media.

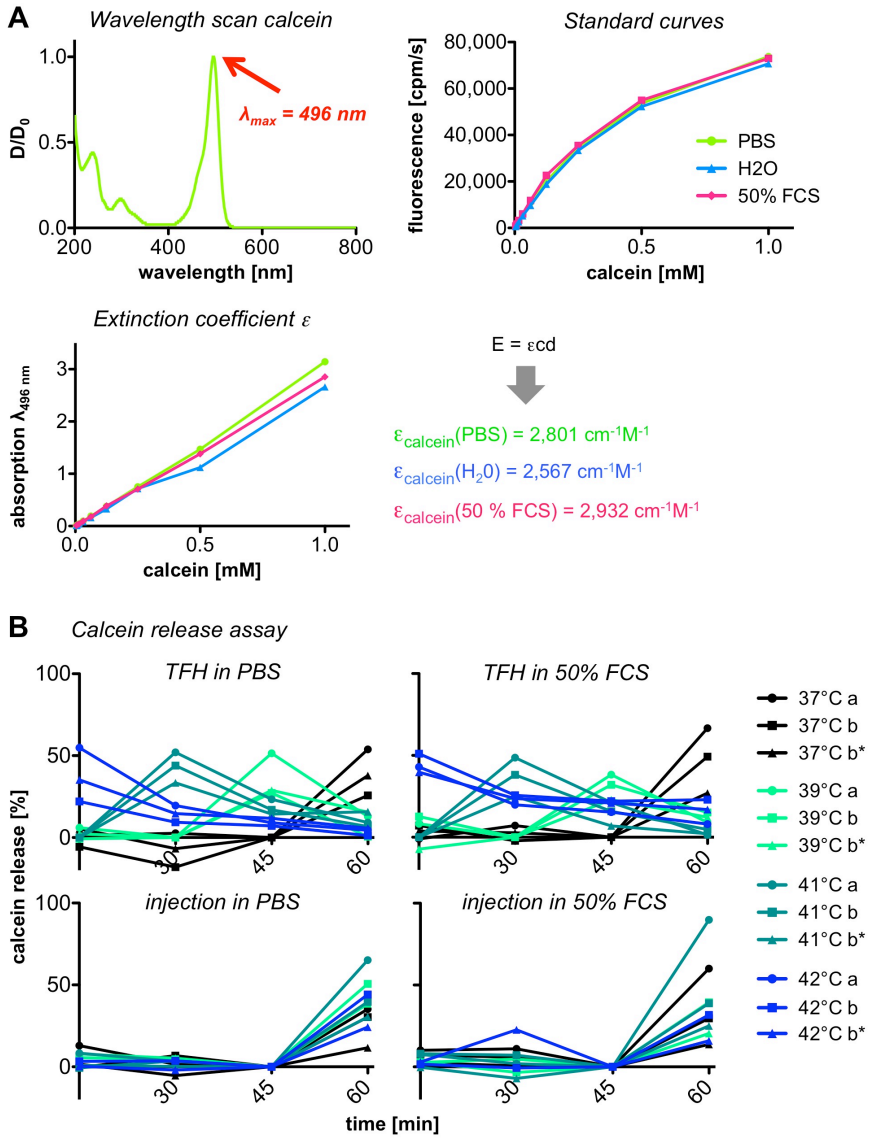

Figure 38: Calcein release assay of thermosensitive liposomes. A: Calcein wavelength scan, standard curves and determination of extinction coefficient. **B:** Calcein release assay of TFH liposomes and injection method liposomes in PBS and 50% FCS.

3.2.3.2.3 Drug loaded MNP-LPs

3.2.3.2.3.1 MNP-PTX liposomes

Liposomes co-loaded with the chemotherapeutic drug paclitaxel (PTX) and the PALD2-Mag1 nanoparticles were synthesized following the TFH protocol. Figure 39 compiles the appearance of those liposomes prepared with PEGylated lipid vs. the polymer P_3C_{18}, drug loaded and without PTX, and before and after dialysis and magnetic separation. The liposomes prepared with the polymer were perfectly magnetically separable as it can be seen on the right picture of figure 39D.

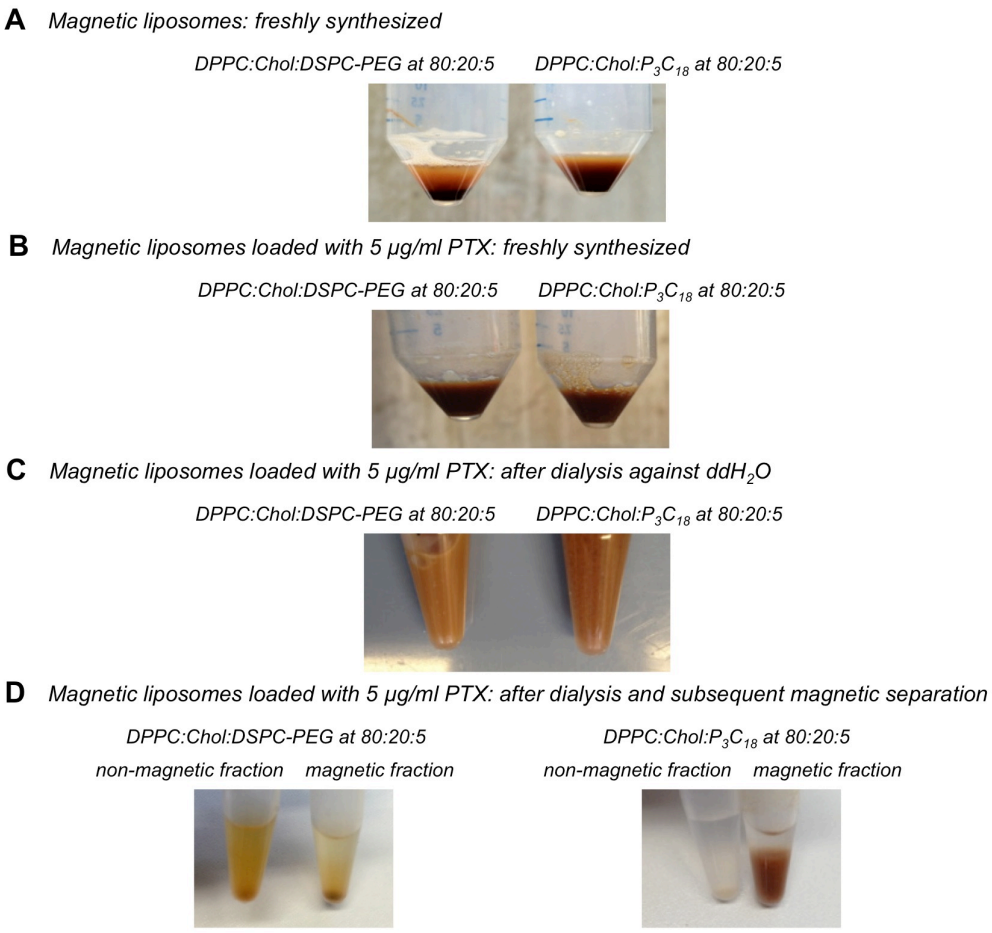

Figure 39: Liposome synthesis and processing: TFH liposomes comprising DPPC:cholesterol:DSPE-PEG_{2000} 80:20:5 or DPPC:cholesterol:P_3 C_{18} 80:20:5 and loaded with PALD2-Mag1 (and PTX). **A:** freshly synthesized MNP-LPs. **B:** freshly synthesized magnetic liposomes co-loaded with PTX. **C:** MNP-PTX-liposomes after ON dialysis against ddH_2O, 4 °C. **D:** magnetic separation of both types of MNP-PTX-liposomes.

3.2.3.2.3.2 MNP functionalization

For further functionalization of the liposomes, the chemotherapeutic drug paclitaxel (PTX) should be encapsulated into the liposomes. Therefore, the positively charged magnetic nanoparticles were complexed with the PTX and binding should be quantified using the photometer. First, the absorption maxima of both, MNPs and PTX, were determined. In addition, the magnetic and the non-magnetic fractions of drug-loaded MNPs underwent wavelength scans. Unfortunately both, MNPs and PTX showed an absorption peak at 275 nm, therefore it was not possible to reliably quantify the coupling of PTX to the MNPs photometrically. In figure 40, the absorption was plotted over the wavelength, and all samples, the free components as well as the drug-loaded complexes and the unbound drug in the non-magnetic fraction, show high absorption at 275 nm. From the close proximity of the free MNP-curve and the MNP-PTX magnetic fraction curve and the high values of the non-magnetic fraction it could be assumed that only a small amount of drug had bound to the particles.

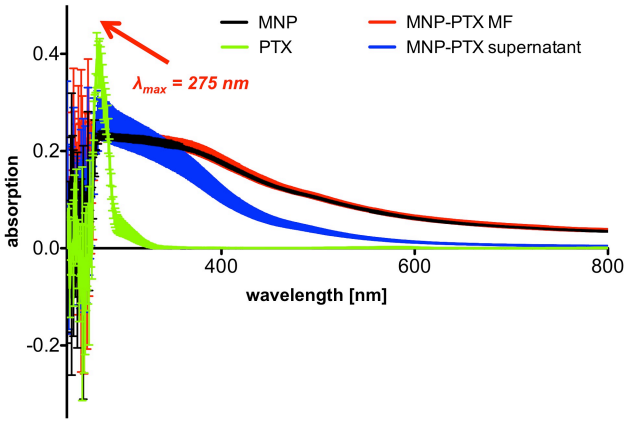

Figure 40: MNP functionalization with PTX.

3.2.3.2.4 *In vivo* evaluation of MNP-LPs

3.2.3.2.4.1 Biodistribution

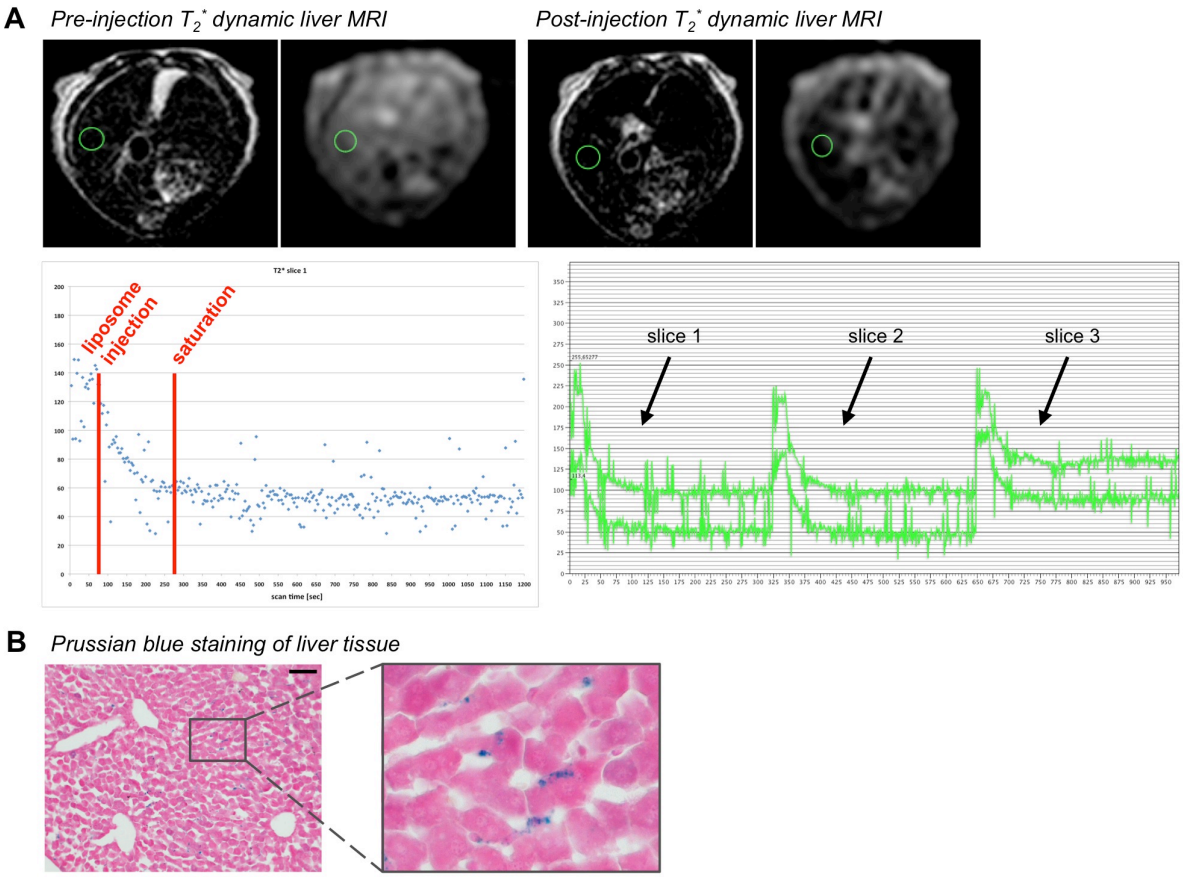

Figure 41: MNP-LPs *in vivo* in wildtype mice. A: T_2^* dynamic MRI scans pre- and post-injection of magnetic liposomes (1.5 T clinical MRI system). The left image in both datasets is the anatomy scan to identify the iron accumulating hypointense tissue in the right images as liver. The histograms in the bottom row plot the signal drop over time after liposome injection for slices 1(, 2 and 3). **B:** Prussian blue staining of liver tissue for ferric iron and the corresponding 5x-fold magnification of stained iron particles, probably in Kupffer cells, bar 50 μm.

In the biodistribution experiment, wildtype mice were treated with magnetic liposomes. The liposomes were administered intravenously via tailvein catheter, and meanwhile the liver of the animal was real-time monitored applying MRI. Figure 41A shows pre- and post-injection liver T_2^* scan image sets in the top row, and in the bottom row the according histograms plotting T_2^* relaxation rates over time, the left graph for slice 1, marked with liposome injection and start of saturation, and the right graph compiling the subsequent acquisition of the slices 1, 2 and 3. The right anatomy scans in the top row image sets helped to localize the liver. The scan sequence protocol used for acquisition of the right images was sensitive for iron-containing magnetic contrast agents, and thus clearly showed a signal decrease in the liver after magnetic liposome injection. The graphs mirror that signal drop throughout the tissue slices. The histological localization of the magnetic nanoparticles was facilitated by Prussian blue staining of the tissue ferric iron in the liver samples. Figure 41B shows an exemplary micrograph and its magnification wherein the MNPs could be identified as blue spots within the liver tissue.

3.2.3.2.4.2 Magnetic targeting

In contrast to the biodistribution experiment, not wildtype but pancreatic tumor-bearing mice were used in this study, and there was no MRI-facilitated monitoring of the animals due to the experimental setup with external magnets. Again, the mice were anesthesized using isoflurane, and the liposomes were administered via tailvein catheters. Then, in one group the magnetic liposomes were targeted towards the pancreatic tumors using an external magnetic field. Therefore, the magnets were fixed above the tumor region. After 1 hour of liposome circulation (and targeting in the magnetic targeting group), the animals were sacrificed and tissue samples were taken. Those samples underwent histological and biochemical analysis. Figure 42A compiles exemplary micrographs of the Prussian blue staining for magnetic nanoparticles in several tissues for all treatment groups (liposome + magnet (top row); liposome, no magnet (middle row); control (no liposome or magnet, bottom row). As expected, there was some positive staining in liver and spleen. Kidney and pancreas showed no positive staining, but in the tumor tissue of all liposome-treated animals (with and without additional magnetic targeting) some positive staining could be identified. Figure 42B shows exemplary micrographs of a liposome-treated mouse (no magnet) in a lower magnification, showing the positive staining in liver, spleen and tumor tissue more clear. In the histogram of figure 42C, the results of the corresponding non-heme iron analysis were plotted as μg iron per gram tissue for all sampled tissues. That biochemical iron analysis mirrors the histological results with relative high levels in spleen and liver, and elevated iron levels in pancreatic tumor compared to healthy pancreatic tissue.

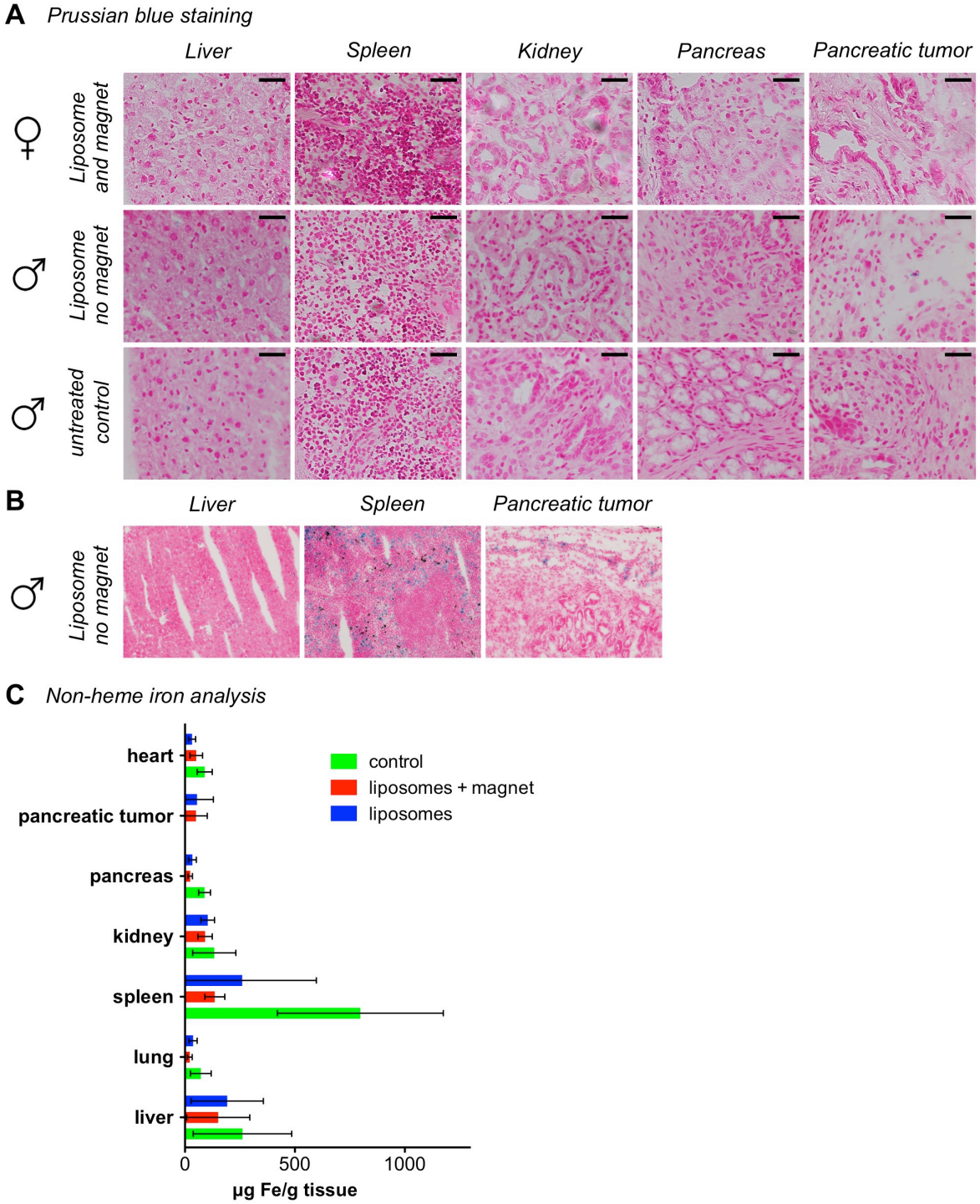

Figure 42: MNP-LPs *in vivo* in CKp53lox PDAC mouse model: LPs i.v. ± 1h magnet. A: Exemplary Prussian blue staining micrographs of several tissues over both treatment groups and control animals, bar 50 *µ*m. **B:** Exemplary Prussian blue staining micrographs (liver, spleen and pancreatic tumor) of liposome-treated mouse in lower magnification. Iron could nicely be localized in the pancreatic tumor tissue (right micrograph), the positive staining in the spleen (middle) is most probably not due to the liposome treatment but could be found in all animals. The liver section shows some positive staining for iron, but from the biodistribution experiment in wildtype mice a little more was expected. Probably it was washed out already as the liposomes circulated for 1 hour prior to sacrifice and the contrast-agent effect of the liposomes was MR imaged in real-time acquisition. **C:** Non-heme iron determination: biochemical tissue-iron quantification from sampled tissues

4 DISCUSSION

4.1 Magnetic nanoparticles

The differences in the mean hydrodynamic diameters and specific magnetization of the selected core–shell type iron oxide MNPs resulted in different magnetic moments of the cores. The differences in the electrokinetic potentials were mainly due to the surface compositions. Small average hydrodynamic diameters of the PEI-Mag particles indicate single particles in aqueous suspension. Whereas the SO-Mag particles with the larger average hydrodynamic diameters suggest particle aggregation into small assemblies due to increased magnetic dipole-dipole interactions [103, 105]. The hydrodynamic diameter of the PALD2-Mag nanoparticles ranked between the PEI-Mag and SO-Mag particles [113].

The MNPs (PEI-Mag and SO-Mag) selected for viral and siRNA complexes both comprised branched PEI in their coating, and were therefore highly positively charged when suspended in water. Such PEI-stabilized particles were eligible for association with negatively charged VPs and siRNA, respectively, into efficient complexes at (virus-)specific and -optimized iron-to-virus and iron-to-siRNA ratios, respectively, resulting in high cell labeling and magnetofection efficacies [103, 141, 270]. The self-assembly into stable MNP-VP or MNP-siRNA complexes was of predominantly electrostatic nature. Such self-assembly is known to modify the magnetic behavior relative to that of isolated particles and often happens in liquid medium [271].

In contrast to SO-Mag and PEI-Mag particles, PALD2-Mag particles exhibit negative electrokinetic potential and are therefore especially suitable for the integration in liposomal formulations [96, 272] or lipoplexes [113], but they were also successfully used for viral [102] and non-viral siRNA complexes [100, 112, 180].

4.2 Magnetic nanocarriers

4.2.1 MNP-VP complexes

The central questions when developing oncolytic virus therapies are: What happens with the virus after administration? And is it possible to localize the oncolytic virus at the tumor site and therefore enhance its oncolytic potential? – The coupling of virus particles to magnetic nanoparticles is one possible approach to address both issues. The viral complexes can be monitored after administration via MRI, and targeting towards the region of interest applying an external magnetic field increases delivery efficiency.

This section discusses on the physico-chemical and imaging characteristics of the selected MNPs and derived complexes with Ad and VSV, and their *in vitro* and *in vivo* evaluation regarding oncolytic activity and tissue virus titer. PEI-Mag2 and SO-Mag6-11.5 particles possessed highly positive electrokinetic potentials, enabling self-assembly based mainly on

electrostatic interaction with negatively charged VPs. TEM was used to visualize complex and cluster formation of free magnetic material and upon cellular uptake. Quantitative MRI of gel phantoms revealed decreased r_2 and increased r_2^* values upon complexation and clusterization. First *in vivo* application of VSV-based MNP-VP complexes demonstrated their targeting and imaging properties.

In many studies, MNP-VP complexes were used for the targeted delivery of nucleic acids to target tissues, and to utilize the uptake-enhancing effect of magneto-transduction in an external magnetic field [101, 145, 270, 273-278]. The physico-chemical properties of our MNP-Ad complexes were consistent with earlier studies on such complexes by Tresilwised et *al.* [103, 105]. Comparing the electrokinetic potential, magnetophoretic mobility and magnetic moment of our adenoviral complexes with lentiviral complexes with PEI-Mag and SO-Mag particles [102], the data for the PEI-Mag-Ad complexes were in the same range, whereas the SO-Mag-Ad complex data exhibited higher values in our study, indicative of aggregation as already postulated [139]. Using MNP-Ad complexes and applying magnetofection could successfully help overcome the transduction resistance in skeletal muscle cells compared to naked virus [277].
Besides the self-assembly of our MNP-VP complexes, also surface moieties could be used for complexation. Pandori et *al.* developed a method for coupling of adenoviral vectors to silica microbeads via streptavidin and its ligand biotin. No negative effects on the infectivity after conjugation of adenovirus virions to solid silica microbeads or paramagnetic microparticles via biotin-(strept)avidin interaction could be detected. On the contrary, the combination of those streptavidin-coated MNPs, biotinylated adenovirus and magnetic force resulted in high infection rates under magnetically controlled conditions [273]. We were the first group to couple VSV to MNPs for magnetically guided delivery and monitoring of the oncolytic virus particles. Regarding size and charge, the MNP-VSV complexes were within the same size range as the MNP-Ad complexes.

Analogous to Trueck et *al.*, we identified the optimal MNP-to-VP ratio for complex formation by titration of a fixed amount of VPs with increasing amounts of MNPs [102]. They analyzed the bound amount of virus by lentiviral capsid protein quantification from the non-magnetic supernatants by ELISA, whereas we quantified the remaining virus particles using $TCID_{50}$ assays. In addition to the supernatant analysis, we also analyzed the virus content in the magnetic fraction. The optimal iron-to-virus ratio identified for the PEI-VSV complexes was 500 fg Fe/VP which was comparable to the lentiviral PEI-Mag complexes with 300 fg Fe/VP [102], although Wenzel et *al.* performed their experiments with PEI-Mag-LV complexes comprising only 40 fg Fe/VP [101]. Their titration experiments affirmed our choice to utilize electrostatic interactions between MNPs and VPs for self-assembly. There was a clear better binding efficiency of negatively charged lentivirus particles to positively charged MNPs [102].

As expected, MNPs and MNP-VP complexes both displayed high cell labeling and infection efficiencies with the magnetofection method applied [100]. The magnetic cell labeling with and without an externally applied magnetic field was previously tested in RDB cells [103, 105], and within this work tested in McA cells [115, 139]. The total labeling was between 2.5 and 5.4 pg Fe/cell in McA cells, and 6.7 and 17.3 pg Fe/cell in RDB cells after application of 10 and 25 pg Fe/cell, respectively, indicating that the labeling efficiencies ranged between 25 % and 69 % [139] and 39 % under higher applied iron doses of SO-Mag particles in McA cells [115].

The high transduction rates with the MNP-VP complexes could be explained by the surface modification of both magnetic particles with PEI, as this component is known to stimulate cell internalization of the complexes [102]. During complex assembly, it enhances the binding of VPs to MNPs leading to a high amount of viral particles per magnetic complex [102].

In addition, the magnetofection-mediated MNP-VP complex uptake is more efficient and faster than the uptake of naked adenovirus via coxsackie and adenovirus receptor (CAR)-mediated endocytosis [276]. In detail, the entry of both, wildtype and recombinant adenovirus, into cells comprises a two-step sequence involving different membrane proteins: a high-affinity primary receptor, the CAR, that mediates the attachment of virus to the cell surface, and lower-affinity secondary receptors ($\alpha_v\beta_3$ and $\alpha_v\beta_5$ integrins) that allow internalization of the viral particles [279]. Additionally supportive are high expression levels of $\alpha_v\beta_3$ integrins on the surface of several tumor cell types including HCC and PDAC [209, 280-283]. Also, magnetofection utilizes the natural uptake pathway of endocytosis, resulting in high post-transfection cell viability [148].

The localization and aggregation state of MNPs and MNP-VP complexes after cell internalization, as well as their appearance in suspended form was elucidated by transmission electron microscopy. TEM images revealed that MNPs were most probably arranged in layers around the VPs due to predominantly electrostatic interactions and magnetic dipole-dipole interaction between the particles as shown earlier [105, 139]. A similar corona of multiple MNPs surrounding a VP has previously proven as effective defense against virus neutralizing antibodies [103]. On the TEM photomicrographs of naked MNPs and MNP-VP, both samples were more or less dispersed, and single self-assembled complexes could easily be identified.

As expected [284], the cell-internalized complexes were encapsulated in endosomes, whereas the free MNPs were mostly clustered within the cytoplasm and only few in endosomes. Cytoplasmic localization [285, 286] and endosomal encapsulation [287] of the internalized MNPs was also observed in other experiments with MNP-labeled cells. We assume that the compartmentalization, clusterization and distribution of MNPs and MNP-VP complexes in cells depended on the uptake mechanism. From the TEM photomicrographs, we speculate that the uptake of complexes was not receptor mediated, and therefore, cell-bound complexes were most probably endocytosed. In contrast, naked MNPs might have

been taken up directly into the cytoplasm and aggregated there. In earlier studies, cell uptake and transfection with enclosed plasmid DNA of magnetic lipoplexes was very efficient. The sizes of these lipoplexes were comparable or bigger than our complexes, but also the bigger lipoplexes of about 2 micron were efficiently internalized [113]. Others found the larger complex size even advantageous for good internalization and transfection [288-290] which could not be confirmed by Sanchez-Antequera et *al*. [113]. In contrast to the cytoplasmic localization of MNPs in our study, others found iron oxide particles to be localized intracellularly primarily in the tubular lysosomal compartment [291, 292]. Sun et *al.* identified the non-facilitated endocytosis of small particles into human hepatocellular liver carcinoma cells from TEM images [293]. Chemically modified dextran-coated iron oxide particles were internalized through receptor-mediated endocytosis into highly specialized cells such as hepatocytes [294, 295] or pancreatic acinar cells [296].

In vitro infection experiments have shown that exposure of the MNP-VP complexes to 50 % FCS resulted in considerable inhibition of the oncolytic activity of the naked virus, for both, VSV and Ad. In contrast, the oncolytic potency was not dramatically altered after assembling with selected MNPs at optimal iron-to-virus ratios and remained high even at high serum concentration for viral complexes with both, VSV and Ad (table 10 and figure 27). The stability of MNP-VP complexes in the presence of high serum concentration could also be shown for lentiviral complexes when utilizing the same MNPs chosen in this study [101, 102]. Our findings promised enhancement of oncolytic potency due to assembling with MNPs, especially under application of a magnetic field.

In addition to their physico-chemical properties D_h and ζ, the selected core-shell MNPs and their optimized self-assembled complexes with VPs were characterized for their magnetic responsiveness in applied magnetic fields [180, 181]. This step is crucial to ensure that the magnetic moment of such complexes is high enough for magnetic targeting even under physiological flow stress [102].
Therefore, the turbidity clearance curves were plotted and extrapolated to calculate the magnetophoretic mobility and the number of associated MNPs per VP applying the method by Wilhelm et *al.* [297]. The results were comparable to those of previous studies on MNP-VP complexes [103, 105]. Flow experiments of Wenzel et *al*. and Trueck et *al.* revealed the magnetic moment of SO-Mag-LV complexes to be higher than that of PEI-Mag-LV complexes. Solely their SO-Mag-LV complexes could successfully internalize into endothelial cells [101, 102]. Therefore, in cell replacement experiments in an *ex vivo* murine aorta model, endothelial cells were transduced with MNP-LV complexes and loaded with SO-Mag5 particles for higher a magnetic moment of the cells. Such approach could be used for the combination of nucleic acid transfer and cell replacement or seeding of cells on cellular grafts in patients suffering from vascular disease. Lentiviral complexes with other MNPs were tested for *in vitro* transduction efficiency in several endothelial cell lines and *ex*

vivo under non-permissive conditions (hydrodynamic forces, shear stress induced by blood flow) in an aorta model and regarding targeting and transduction capacity in an injured common carotid artery model *in vivo* [106]. Another application of lentiviral vectors is the gene delivery into airway epithelium using polycation-coated iron oxide NPs non-covalently bound to LV particles. *In vitro* magneto-transduction with GFP as reporter gene led to high transduction efficiency of MNP-LV complexes compared to naked LV [298]. Such approaches are also an option for our MNP-Ad complexes. The most important application of our MNP-VSV complexes would lie in the treatment of HCC.

Non-invasive MRI is a very important monitoring and diagnosis tool as clinical MRI scanners providing 1.5 to 3.0 T are capable of μm resolution in soft tissue imaging [43]. SPIOs have proven as negative MRI contrast agents *in vitro*, and will be used in *in vivo* labeling and tracking experiments, but challenging remains the quantification [64]. From first our experiments we knew that the selected core-shell type SO-Mag MNPs showed excellent r_2 and r_2^* relaxivities, both free and cell-internalized [115]. To further determine the efficacy of naked and cell-internalized MNP-VP complexes as contrast agents for MRI, and to identify the detection limit of iron in the different assemblies, tissue-mimicking MRI phantoms with homogeneously distributed nanomaterial were prepared.

Although Kuhlpeter et *al.* found no differences in the R_2 and R_2^* effect comparing low quantities of highly iron-loaded cells and high quantities of low iron-loaded cells with comparable average iron concentrations per sample [211], we decided to use comparable iron loadings and cell numbers per concentration. Also because Hardy and Henkelman predicted a difference from numerical simulations, i.e. smaller particles in a larger number should be more efficient than larger particles in a smaller number [299]. Therefore, to identify the detection limit we prepared phantoms from cells with similar iron loadings and phantoms with the respective amounts of naked MNPs and complexes. All samples were diluted and homogenously distributed and embedded in the agarose gel phantoms.

The linear increase of the R_2 and R_2^* relaxation rates with increasing iron concentrations is in concordance with previous findings for iron oxides [67, 115, 300, 301]. The chosen baseline relaxation mimicked by the phantom [211] was that of normal liver tissue, as HCC and PDAC develop in and often metastasize to the liver, respectively. That should enable the transfer of the *in vitro* iron quantification data to *in vivo* studies.

Our r_2 relaxivities (10 to 286 mM^{-1} Fe s^{-1}) were within the range or even higher than those of clinically used contrast agents which range between 10 – 150 mM^{-1} Fe s^{-1} [269] with for example 60 mM^{-1} Fe s^{-1} for Combidex®/Sinerem®, 98.3 mM^{-1} Fe s^{-1} for Feridex® and 151.0 mM^{-1} Fe s^{-1} for Resovist® [55]. The r_2^* relaxivities calculated from our phantoms measurements were higher than the r_2 relaxivities, as it was shown by Shapiro et *al.* and Kuhlpeter et *al*. with significant r_2 relaxivity reduction and r_2^* relaxivity amplification upon aggregation, the assembly of MNP-VP complexes and/or further cell internalization [211, 269], always compared to the relaxivities of the respective amount naked MNPs. Perez et *al.*

also found the T_2 signal intensity to decrease upon nanoassembly of herpes simplex or adenovirus particles and MNPs labeled with virus-specific antibodies [302, 303]. Others, too, saw reduced r_2 relaxation rates relative to free particles induced by the intracellular iron particle clusterization [211, 285-287, 304, 305]. As reported by others [304], the r_2^* to r_2 ratio after particle assembly and/or cell internalization compared to free, suspended particles was dramatically increased, especially for the SO-Mag samples (PEI-Mag: 2- to 33-fold, SO-Mag: 3- to 56-fold). These variations in r_2 and r_2^* relaxivity could be explained by the restricted diffusion of water-protons. The lower r_2 relaxivities were in concordance with the motional narrowing effect [306], the effect of restricted water/proton diffusion after compartmentalization [305] and reduced proton relaxation [287]. It was induced by the clusterization of MNPs around VPs and/or intracellular compartmentalization. The increased diffusion distance of protons along intracellularly clustered MNPs decreased the r_2 relaxivities and increased the r_2^* relaxivities. In addition, the relatively small field inhomogenities induced by small free MNPs in the nanometer range, are potentiated in clustered particles of viral complexes and intracellular aggregates that occur in the high nm or μm range. Both factors lead to incoherent spin dephasing, and the outer-sphere relaxation theory could be applied to explain the r_2 relaxivity drop [285]. The static dephasing regime theory says that large compartmental magnetic moments produce a strong enough outer-sphere dipolar field so that diffusion has a minimal effect on the MR signal decay, and this decay is unaffected by details of the compact magnetic aggregate shape [304, 307]. Hence the aggregation state directly modulated the intracellular relaxivity of the cell and complex samples in comparison to free MNPs dispersed in agarose gel. Therefore, r_2 is influenced by the concentration and the assembly state of the MNPs, r_2^* is mainly sensitive towards the iron concentration, and thus R_2^*-weighted acquisition was assumed to be the potentially most sensitive method to identify the presence of iron-oxide particles and labeled cells [211, 304]. Therefore, the increased r_2^* relaxivity of MNP-VP complexes should further enhance their non-invasive detectability by MRI. Differences in R_2^* and r_2^* between the two particles could be explained by D_h-dependent higher diffusion restriction in SO-Mag MNPs as they tend to aggregate, even in the dispersed state [103].

Leung et *al.* also analyzed clustered, MNP-labeled cells for their T_2 relaxation times. Their “blooming” effect of MRI signals [182] was comparable to the signal effects we detected in our MRI phantoms of clotted MNPs, MNP-VP complexes, and labeled/infected cells thereof in the high iron-load samples (figure 18C). Such blooming of hypointense signals whose sizes overran the physical sizes of the samples was also observed in the phantom measurements of Pouponneau et *al.* with a 1.5 T clinical MRI scanner. For their T_2^*w image acquisition they concentrated microcarriers and iron-cobalt-NPs at the bottom of 1.5 mL tubes, covered the samples with 2 % agarose gel containing manganese(II) chloride hydrate to mimic the relaxation properties of liver tissue, and embedded the tubes in the same agarose gel [308].

In general, the local concentration of a contrast agent required for signal detection is a limiting factor in its application [132]. In our *in vitro* liver mimicking phantoms, iron concentrations as low as 3 – 8 μM per 10^5 labeled cells/mL agarose gel were visually detectable above the phantom background with sufficient image contrast [139]. Hence the detection was more sensitive compared to previous results (25 μM Fe for SO-Mag particles [115] and 21 μM Fe for NDT-Mag1 particles [67]; 1.5 T MRI) or the detection limit of for example 10^6 Endorem®-labeled cells per mL gelantin at comparable cell iron loading (25 pg Fe/cell 448 μM iron, 3.0 T clinical MRI system) [309]. Our detection limit was within the same range as small iron oxide particles (D_h = 17.1 ± 0.9 nm) prepared by Weissleder et *al*. with 2 μM Fe in evenly distributed (5 x 10^6 cells/mL) or pelleted (10^5 in 20 μL) cells in 2 % agarose gel using a 1.5 T MRI system [292]. Focusing on the determined relaxivities, our phantom measurements were comparative. The r_2 relaxivity of our virus-complex-labeled McA cells with 2.5 pg Fe/cell was 55 mM^{-1} Fe s^{-1} (1.5 T MRI), Estapor® labeled neutrophils with 2 pg Fe/cell had a r_2 relaxivity of 74 mM^{-1} Fe s^{-1} (4.0 T MRI) [310].

In our measurements, we could show that the data acquired from phantom scans at 1.5 and 3 T clinical MRI systems were comparable. Field strength independency for T_2 relaxation times with alterations less than 5 % was also shown by Tofts et *al*. for their Ni-doped agarose gel phantoms with MRI systems from 0.5 to 2.0 T [68]. Stanisz et *al*. had constant data for their comparative measurements from 1.5 to 3 T [47], which is consistent with the magnetic field-independent T_2 relaxation times observed by Bottomley et *al*. [311], whereas De Bazelaire et *al*. found the T_2 relaxation times to be generally lower at 3.0 T than at 1.5 T with tissue-dependent variations in the magnitude of change [312].

In future *in vivo* studies, in particular on viral cancer therapy, such tissue-mimicking phantoms could be used in preliminary *in vitro* tests and applied for the non-invasive quantification of exogenic iron from magnetic nanoassemblies by MRI *in vivo*. For example for calibration in studies on orthotopic McA tumor nodules in rats, the described phantoms could be used, as this model lacks the underlying liver damage of the human condition and the surrounding liver tissue is relatively homogenous [20]. Thereby it should be taken into account that such phantoms do not exactly represent the *in vivo* heterogeneity of human HCC. Most HCC patients also suffer from liver cirrhosis, therefore acquired images show different signal patterns compared to healthy individuals and between the different patients [14, 69]. Pathologic liver tissue is not homogenous throughout, there might be fibrotic strands, which result in MR signal drop or void due to the restricted diffusion [313]. Also, natural iron content of the livers of patients with varying clinical backgrounds is diverse and could lead to different baseline relaxivities. Thus, ideally for each patient, specific phantoms with the individual baseline relaxivity would be an option for correct quantification of delivered MNP-VP complexes. Calibration measurements should be performed using phantoms prepared from cells with internalized complexes rather than from complexes alone or naked particles, as this is more close to the cell internalized situation *in vivo*.

In general, all four complex derivates assembled in this study were suitable for *in vivo* applications regarding their size as small vessels typically have a diameter of 7 µm [314]. We chose the SO-Mag-VSV complexes in orthotopic HCC liver lesion bearing Buffalo rats. In this proof-of-principle study we could show the *in vivo* applicability of the magnetic viral complexes regarding detection and virus delivery.

Tumor bearing rats were injected with either naked VSV or SO-Mag-VSV complexes and after 30 minutes of magnetic targeting, the virus titer in MNP-VSV complex treated animals was higher than the titers in animals treated with naked virus. 24 hours after infection, there was still a clearly detectable iron-induced MRI signal loss in the tumor lesions of SO-Mag-VSV complex treated animals, whereas the naked VSV-treated control animal showed no signal alteration in their tumors. The same effect of enhanced oncolytic potential of the MNP-VP complexes over naked virus was shown in *in vivo* experiments on local application of the magnetic complexes of the oncolytic adenovirus in a murine tumor model [103].

4.2.2 MNP-siRNA complexes

Pre-clinical siRNA-based approaches were examined in various studies in the recent years. In our nanocarrier system, the siRNA was assembled with an enhancer and magnetic nanoparticles, which in parallel enable magnetic targeting and monitoring of the complexes after administration in future *in vivo* applications. In this study, the MNP-siRNA constructs were tested for their capability to down-regulate specific genes in cancer cells in a poof-of-principle study *in vitro*. Test systems for the knock-down experiments were stably luciferase and GFP expressing cell lines. SO-Mag and PEI-Mag particles were chosen as they easily assemble with negatively charged siRNA due to their own positive surface charge.

Non-viral vectors are an interesting and thoroughly tested approach for targeted nucleic acid delivery. In several studies, non-viral nanocarriers were loaded with plasmid DNA (pDNA) or (si)RNA for therapeutic applications [61, 112, 113, 132, 149, 166, 180-182]. Again, magnetic nanoparticles were the core structure facilitating magnetic targeting, and hence contributing to transfection enhancement. In addition, they provided stabilization for the sensitive nucleic acids. As our selected core-shell type MNPs, in other studies the MNPs were mostly coated with cationic polymers or peptides for better binding of the negatively charged DNA and RNA molecules via electrostatic interaction [132, 274]. PEI was a widely used molecule [61, 100, 113, 132, 166] and was also chosen for the surface functionalization of PEI-Mag and SO-Mag particles [115, 315]. Another exploited feature of PEI was the capability to promote endocytosis of particles resulting in rapid and efficient transfection [184], also in HCC cells [182]. The influence of sedimentation and magnetofection on the endocytosis was tested in various cell lines with PEI-coated SPIO-pDNA complexes. Huth et *al.* could show that endocytosis is not influenced directly by the magnetic field, but indirectly as it accelerates the sedimentation onto the cell surface, and thereby enhances the endocytic uptake taking place via clathrin-dependent and caveolae-mediated endocytosis [316].

Our study and many others were first proof-of-principle experiments on the capability of the new carrier systems to efficiently deliver nucleic acids to a target tissue [100, 112, 180]. There, a convenient marker for successful transfection is the expression of reporter genes [67, 100, 112, 113, 189]. We chose the widely used reporter genes firefly luciferase and the (e)GFP as there are various reporter assays available. Luciferase can easily be quantified for example applying luciferase assay for quantitative analysis either after transfection as reporter gene [113] or as target in knock-down experiments [100, 112, 180]. In *ex vivo* and *in vivo* studies, the luciferase expression can be monitored based on its intrinsic capability for bioluminescence imaging [111, 190] with subsequent histo-pathologic luciferase staining. Techniques to quantify the GFP expression *in vitro* and *ex vivo* are for example GFP assay, FACS and fluorescence microscopy [112], *in vivo*, it could serve as an intrinsic fluorescent probe for fluorescence imaging [182].
Human (HepG2 and HuH-7) and rodent (McA-RH7777) HCC, and human PDAC (EPP85-181P and EPP85-181RDB) cell lines were analyzed *in vitro* for the capability to be transfected with MNP-siRNA complexes to down-regulate the expression of previously inserted firefly luciferase and eGFP reporter genes. A lentiviral vector with the luciferase-GFP-fusion construct was chosen for this transduction and resulted in stable expression of both proof-of-principle target proteins.

Utilizing magnetic siRNA complexes, we could show strong luciferase down-regulation after magnetofection compared to non-magnetic DF-Gold-siRNA lipoplexes. The successful knock-down was in concordance with previous results on MNP-siRNA complexes. Mykhaylyk et *al.* assembled magnetic siRNA complexes following the same protocol, and tested them *in vitro* in different cell lines [112, 180]. The magnetic MNP-siRNA complexes with the enhancer DF-Gold were most efficient for transfection experiments exposed to external magnetic fields. Sanchez-Antequera et *al*. used (magnetic) firefly luciferase pDNA-loaded complexes for transfection of Jurkat T cells, and compared the transfection efficiencies of magnetofection and lipofection [113]. Again, the luciferase expression enhancement was better for magnetic MNP-DF-Gold-siRNA complexes compared to DF-Gold-siRNA lipoplexes. Magnetofection allowed for pDNA delivery to primary mouse embryonic fibroblasts and porcine fetal fibroblasts even at low doses of nucleic acid per cell bound in magnetic complexes with SO-Mag5 and PEI-Mag2 [150]. Zhao et *al.* analyzed MNPs with PEI-coating and surface-bound pDNA on morphology, assembling structure and nucleic acid delivery abilities regarding transfection efficiency, as the MNPs increase DNA concentration and prevent DNA from degradation at low toxicity. They found the MNP-to-DNA ratio to be crucial for the transfection efficiency in mammalian somatic cells [317].

There were several studies using nucleic acid-MNP complexes in HCC cell lines such as HepG2 cells *in vitro* and *in vivo* in xenograft models for reporter gene expression [182, 186, 190], as gene silencing has significant therapeutic promise for the genetic treatment of HCC

[4]. The MNPs one hand enabled for magnetic targeting and on the other hand for *in vivo* monitoring of the nanocarrier formulation after administration [4, 182]. Next step after such proof-of-principle experiments would be the replacement of the reporter genes by application-specific target genes. In HCC and PDAC therapy, a potential target gene for therapeutic knock-down approaches is the octamer-binding transcription factor 4 (OCT4). This factor is associated with the self-renewal and differentiation of cancer stem cells and hence is crucial for the progression of several cancer types [318-320]. Its involvement in the tumorigenesis, proliferation and invasion of pancreatic and hepatic cancer cells was shown in several studies based on elevated expression levels compared non-cancerous cells [318, 319, 321, 322]. In HCC, its function is based on a positive feedback loop with the oncogene c-JUN [323], in PDAC with AKT pathway-mediated proliferating cell nuclear antigen (PCNA) and matrix-metalloproteinase-2 (MMP-2) expression [318]. The knock-down of OCT4 could inhibit the proliferation and invasion for example in the human HCC cell line Hep-G2 [323] and human PDAC cells Panc-1 [318].

4.2.3 Magnetic liposomes

Magnetic liposomes are the third nanocarrier formulation for targeted delivery examined in this study. Liposomal formulations are especially eligible for the delivery of drugs to a target tissue. In clinical approaches, the stabilization of the (free) therapeutic agent within the bloodstream for longer circulation times, targeted delivery to the destined tissue, and the prevention of early inactivation or degradation before even reaching the region of interest are driving forces [195]. Functionalized liposomes were examined to address those issues, delivery efficacy can be increased, and toxic side-effects decreased [195]. Consisting of a lipid bilayer enclosing a liquid filled core, during synthesis a liposome provides binding sites for both, hydrophilic and hydrophobic molecules. Hydrophobic molecules can incorporate into the lipid bilayer beneath the lipid chains, hydrophilic substances can be encapsulated into the aqueous core liquid [197].

Three different protocols, thin film hydration [96, 208], reverse phase hydration [191], and the injection method, were used to synthesize our magnetic liposomes which all had an aqueous core. The additional inclusion of SPIOs made our liposomal formulation suitable for magnetic targeting and as MRI-visible probe as it was previously shown by others [4]. To support the magnetically targeted delivery, our MNP-LPs were functionalized with tumor cell-binding surface moieties binding the $\alpha_v\beta_3$ integrin receptor as ligand. The $\alpha_v\beta_3$ integrin receptor, an angiogenesis marker, is up-regulated in PDAC and HCC, and in its expression level often correlated to the tumor grade [4, 59, 208-210]. Surface PEGylation can increase liposomal stability in the circulatory system *in vivo*. The inclusion of the polymer P_3C_{18} into the lipid bilayer provided both, PEG groups and an $\alpha_v\beta_3$ integrin-binding motif. To fully exploit the potential of the targetable MNP-LPs, they had to be loaded with a chemotherapeutic drug for targeted delivery. The encapsulated drug, PTX in our case, thus would be shielded

from clearance and stabilized for longer circulation times. Hence the efficacy after targeted delivery could be increased, off-site delivery decreased [195]. Local hyperthermia was evaluated for the treatment of cancer cells [59]. Designing the lipid composition of the drug-loaded MNP-LP accordingly, a controllable temperature-dependent release of the liposomal core liquid could further increase the specificity of the formulation and enable local liberation of the cargo. To determine the lipid transition temperature of our liposome formulations, the calcein release assay was our method of choice [96, 227, 324-327].

First step in our study was to analyze the MNP-cell interaction. Therefore, several primary murine PDAC cell lines and the rat HCC cell line McA were treated with naked PALD2-Mag particles and exposed to an external magnetic field. The cells were then analyzed regarding cell labeling capacity and iron saturation behavior. MTT viability tests were performed to clarify the effect of increasing iron loads. The obtained good labeling capacities at low toxicity were comparable to the results obtained analyzing PEI decorated SO-Mag particles [115] and provided the basis for further experiments.

Thus after those promising *in vitro* tests, the MNPs were tested for their toxicity and biodistribution *in vivo* in mice. The animals were intravenously injected with PALD2-Mag particles, and after 14 days of careful observation regarding behavioral or physiological changes, the animals were sacrificed. Tissue samples from various organs underwent quantitative iron analysis and histological Prussian blue staining.
There were no major MNP-treatment-related alterations. Solely, a few treated animals accumulated iron particles in the tail vein at the injection site, probably due to too fast injection. As expected the PDAC-positive mice had pancreatic tumors, fibrotic tissue and focal areas of inflammation in the pancreas samples. Even without targeting, some of those mice accumulated MNPs in their pancreatic cancer nodules. Nearly all liver samples (treated and control animals) showed areas of focal inflammation and/or microgranuloma and/or focal necrosis, a common finding in BL/6 mice. Almost all animals in the treatment and a fifth in the control group had slightly elevated iron levels in the biochemical and histological liver tissue analysis, but without pathological tissue changes. The accumulation of SPIOs in the liver was expected as this uptake is widely exploited when utilizing the particles as MRI contrast agents, later-on the SPIOs would have been metabolized into a soluble, non-paramagnetic form of iron that become part of the normal iron pool [52, 55]. In spleen samples, hemosiderin derived from erythrocytes is considered normal in both, red and white pulp, so the positive staining for iron is also not necessarily treatment-related, and was found in all treated and almost all untreated animals. Yang et *al.*, too, found high levels of Prussian blue-positive cells in the liver and spleen samples of MNP-treated mice when they sacrificed the animals 48 hours post-injection [328]. Eosinophilic crystals, which stained positive for iron, were found in the lung tissue samples. These needle-shaped crystals were found in the cytoplasm of alveolar macrophages as well as free-lying within alveoli, again a structure

mainly found in mouse strains on a BL/6 background. It is discussed if they are representing eosinophilic granules at various stages of degeneration [329] or hemoglobin breakdown following uptake by macrophages [330]. Positive staining for iron was also found in lung alveolar cells, and glomeruli and tubules of the kidney cortex region, of our samples, but there were no pathological findings. Besides the positive staining in spleen and liver, there were also a few animals with scattered iron-positive cells in lung and kidney tissue samples of Yang et *al*. [328].
Summarizing this biodistribution and toxicity experiment, there were no pathological findings induced by the administered iron particles in the tissue analysis. All animals showed a healthy gain of weight and there were no behavioral changes of the animals indicating no MNP-related (negative) side-effects.

The cell surface receptor integrin $\alpha_v\beta_3$ is an angiogenesis marker expressed on activated endothelial cells of new vessels. It is up-regulated in newly synthesized tumor blood vessels and crucial for tumor metastasis [187]. This, and the expression on tumor cells of various cancers such as PDAC and HCC made it a very interesting binding molecule for targeted delivery of diagnostic probes and drugs [209, 280-283]. In liver cancer, its expression is limited to HCC cells with very rare expression on healthy hepatocytes [4, 187], the same pattern could be shown in PDAC patients [209]. Hence the liposomes in our study carried an $\alpha_v\beta_3$ integrin-binding molecule.
To prove the existence of the integrins α_v and β_3 on the surface of the chosen primary murine PDAC cell lines, the expression of these target structures was tested by Western blotting. As described previously [209], we found the integrin β_3 expression to be higher than the integrin α_v expression.
An established $\alpha_v\beta_3$-binding molecule is the tripeptide RGD that can be coupled to the liposome surface for tumor targeting [4, 186, 207, 208, 331-333]. In our MNP-LPs, the RGD-like $\alpha_v\beta_3$ integrin receptor binding motif lysine-serine-serine-C_{18} (LSS-C_{18}) was integrated in the P_3C_{18} polymer and included into the lipid bilayer of the liposome. Their surface was modified with 6 such LSS-C_{18} chains and 7 PEGs per polymer molecule. The polymer chains surrounded the liposome in a bow-like manner, and *in vivo* the PEG molecules in the P_3C_{18} polymer coating would shield the liposomes to prevent from early RES-phagocytosis. That probably could increase the circulation time 2- to 3-fold for target tissue delivery via EPR [198]. Caldorera-Moore et *al*. postulated the $\alpha_v\beta_3$ integrin to be an optimal targeting ligand for their theranostic liposomes loaded with an imaging probe and a drug. Hence, the surface was modified with an RGD peptide [334], a setup comparable to our magnetic liposome design. Additional coating of the liposome with PEI could optimize the cellular uptake as it was shown for RGD motif-containing peptides [132, 335]. Conjugation of the RGD peptide onto PEI enabled targeting for liposomal luciferase pDNA delivery *in vitro* into HepG2 cells [186] or siRNA to the human HCC cell line Bel-7402 in an *in vivo* nude mouse xenograft model [4].

After the preliminary experiments regarding the tolerability of the PALD2-Mag particles *in vitro* and *in vivo*, and the proof of $\alpha_v\beta_3$ integrin receptor expression in the chosen cancer cell lines, magnetic liposomes were synthesized and examined using three different protocols. Most common technique for liposome synthesis used in the literature is the thin film hydration [96, 193, 208, 213, 214, 223, 225, 325, 336-339]. Another protocol is the reverse phase hydration [191, 222, 232, 340]. The third technique, the injection method, was developed in our lab.

The size of our magnetic liposomes was around 100 nm to exploit the EPR effect applicable for particles smaller than 200 nm [341]. The commercially available and clinically used liposomal doxorubicin-loaded formulation Caelyx®/Doxil® has a size of 86 ± 1 nm, being slightly smaller than we intended our liposomes to be [96-98]. 100 nm as optimal liposome size was supported by Kono et *al*.s finding of better accumulation at the tumor site for liposomes of around 100 nm in diameter rather than for 50 nm liposomes [229].

As the magnetic liposomes would be utilized for magnetic targeting, their responsiveness in external magnetic fields had to be ensured. Hence for characterization of the MNP-LPs, the optimal wavelength for photometrical analysis of the PALD2-Mag particles and formulations encapsulating them had to be identified. Analogous to the SO-Mag and PEI-Mag particles [115, 139, 180], an analytical wavelength of 350 nm was determined from wavelength scans [112]. Then the magnetophoretic mobility of the liposomes was tested in the same setup as the magnetic viral complexes [105, 112, 113, 139, 342]. The detected magnetic sedimentation behavior of the MNP-LPs was comparable to the data of magnetic lipoplexes of Sanchez-Antequera et *al*. [113], the very slow sedimentation of naked, suspended MNPs was comparable to that of the MNP-VP complexes with the lowest virus load of Tresilwised et *al*. [105] and the PALD2-Mag-siRNA complexes of Mykhaylyk et *al*. [112]. In addition, the influence of an external magnetic field on a suspension of magnetic liposomes was visualized under the microscope. MNP-LPs were prepared with atto550 fluorescent dye coupled to 20 % of the deployed P_3C_{18} polymer. The magnet was placed besides the sample slide and the liposomes immediately started moving towards it and accumulated at the air-liquid-interface next to the magnet. The same behavior was observed by Pradhan et *al*. [272]. Those results strongly suggested the capability of our magnetic liposomes to be used as vehicle for magnetic drug targeting approaches.

Besides the possibility to magnetically alter the MNP-LP distribution and accumulation *in vivo* after administration, the MNPs themselves could serve as contrast agents for non-invasive monitoring via MRI. There were several studies deploying liposome encapsulated MNPs as imaging probes in T_2 and T_2^* imaging to real-time follow their localization [4, 191, 343, 344]. In *in vivo* experiments on the biodistribution of non-targeted MNP-LPs, we could show the accumulation of non-targeted liposomes in the liver tissue of wildtype mice by T_2^* MR imaging and the results correlated with the corresponding Prussian blue staining

histology. As expected [63, 139, 211], they accumulated in the liver and led to hypointense signal in T_2^* dynamic MRI scans.

In a second *in vivo* approach on the magnetic targeting of MNP-LPs, we could show the accumulation of the liposomes in endogenous pancreatic tumors, though there was no further improvement between the magnetically targeted and the non-targeted liposome control groups. Compared to the first non-targeted biodistribution experiment, there was less accumulation in the livers indicating an overall successful targeting towards the PDAC within the circulation time (1 hour) at reduced unspecific liver uptake. For example Wu et *al*. could also successfully target their magnetic liposomes towards HCC xenograft lesions [4]. Babinkova et *al*. were among the first applying MRI probe-labeled liposomes for real-time monitoring *in vivo*. They were able to show their accumulation at the target site and that success encouraged further magnetic targeting approaches to increase the amount of accumulated nanocarriers [212].

Without stabilizing PEG, magnetic liposomes were metabolized by cells of the mononuclear phagocyte system and accumulated in liver, spleen and bone marrow. There, they were used for tumor detection, especially in liver diseases [345]. Inclusion of PEGylated lipids such as DSPE-PEG_{2000} prevented opsonization via “mushroom brush boundary”-formation [346, 347]. Yang et *al*. PEGylated their MNP-LPs for reduced liver macrophage phagocytosis, confirmed by less T_2 signal reduction in the liver, and thus prolonged circulation times to provide a higher chance of target binding, [224]. In *in vitro* and *in vivo* PDAC models of human Panc-1 cells and xenograft tumors in mice, USPIO-loaded LPs were successfully applied as contrast probes in MRI [191]. Besides the utilization of SPIOs, Gd-chelates are applied as contrast agent in several studies on pre-clinical liposomes [206, 207, 213, 214, 229, 230, 324, 348]. Lorenzato et *al*. tested dually functionalized liposomes loaded with USPIOs and Gd-chelates for MR-guided focused US and hyperthermia-induced drug release [231]. Recently, Martinez-Gonzalez et *al*. found SPIONs to be less toxic than Gd-DTPA [231], nevertheless liposomes loaded with gadolinium were widely used for T_1 weighted imaging and accumulation monitoring *in vivo* [214].

To further improve the (magnetic) liposome properties for clinical demands, lipids can be selected to form thermosensitive lipid bilayers. This makes the LPs eligible in hyperthermia applications. Hyperthermic treatment of tumor lesions is a common therapeutic approach as the heating of tumor cells was shown to induce cell death [59] and to increase the vessel permeability for increased EPR-mediated drug delivery [221]. Thermosensitive liposomes release their load at the target site after local temperature increase, and by that increase drug delivery efficiency and reduce side-effects from drug release at non-target tissues.

A convenient approach to prove the temperature-dependent release of the core liquid is the encapsulation of a fluorescent probe [225]. Due to its water solubility, for example calcein could be loaded into the liposomes during synthesis, and its liberation detected fluometrically [96, 227, 324-327]. In our calcein release assay, tested aspects were the comparison of

different lipid compositions and determination of the respective lipid transition temperatures T_m., calcein release in the presence of serum, and different synthesis protocols. Therefore, liposomal suspensions were incubated at the chosen temperatures and samples were taken in 15-minute-intervals at different incubation temperatures ranging from 37 to 42 °C.

We determined the lipid transition temperature to be 42 °C for all three lipid compositions a, b and b*. Though for lipid formulation b, we expected T_m to be 41 °C analogue to Tai et *al*. [225]. Most probably the temperature shifted due to the P_3C_{18} polymer in the liposome bilayer that was used instead of the PEGylated lipid. The presence of FCS had only minor influence on the calcein release. Whereas the preparation technique emerged as crucial, calcein encapsulation was not successful applying the injection method. The calcein release from TFH liposomes started after 60 minutes incubation time at 37 °C, which should allow circulating LPs to reach the target region in *in vivo* approaches. At higher incubation temperatures, the release started earlier: Per 1 °C increased temperature, released calcein could be detected 15 minutes earlier. Calcein release beginning between 37 and 39 °C after 60 and 45 minutes incubation, respectively, was in concordance with results on similar liposomal preparations [324].

An overall aim in thermosensitive LPs was to tune the drug release above 40 °C to prevent unspecific liberation before reaching the target region [96, 193, 213, 222, 223, 225, 228-232]. With T_m values above 40 °C in all tested formulations, we could meet this criteria. *In vivo*, the fast and controlled release of encapsulated substances at the target site could be facilitated by local hyperthermia treatments for example via external water baths, heat pads, near-infrared laser pulsed or pulsed high-intensity focused ultrasound (HIFU) [226]. Even if the release would start 1-2 °C below T_m as shown by Kong et *al*. [349], there would be only little drug leakage after administration *in vivo*, as normal body temperature lies between 36 and 37 °C.

ThermoDOX® is a clinically approved, thermosensitive formulation of DOX loaded liposomes. In several clinical trials, is was tested for application in (metastatic) HCC [233-237], partly in combination with RFA, and breast cancer patients [238-241]. Transition temperature of the preparation consisting of DPPC:MSPC:PEG at 86.5:9.7:3.8 is T_m = 41.3 °C, therefore it is suitable for mild hyperthermia treatment at 41 – 42 °C [221]. In general, thermosensitivity could be tuned by including DPPC and cholesterol with transition temperatures of T_m = 41.5 – 41.6 °C (peak 38 – 42 °C) for DPPC [96, 221] and T_m = 39.7 °C (peak 36 – 48 °C) for cholesterol [96]. Other possible lipids are DSPE-PEG with T_m = 41.3 °C (37 – 49 °C), DSPE-PEG-folate with T_m = 41.1 °C (37 – 49 °C) [96], HSPC with T_m = 54 °C [208] and DSPC with a T_m of 43 – 45 °C [350]. The addition of PEG lowered the transition temperature, and led to faster release at T_m, better stability below T_m and higher drug delivery, also farther from the vessels [221]. There also seemed to be an inverse correlation of the phase transition temperature of the main lipid component and the toxicity of the formulation [198].

To obtain therapeutic liposomes, (chemotherapeutic) drugs can be incorporated during liposome synthesis. Commercially examined and approved options for drug-loading into liposomes were paclitaxel (EndoTAG™ [351]) and doxorubicin (Caelyx®/Doxil® [99]), but both are non-targeted formulations relying on tumor cell delivery via the EPR effect. Hydrophilic drugs can be loaded into the liposomes during synthesis by solving them in the liquid phase, hydrophobic drugs need either to be modified to hydrophilic pro-drugs or partition into the lipid bilayer during synthesis. An example for hydrophilic pro-drugs are 4-(N)-acyl-gemcitabine derivates [352, 353]. PTX is water-soluble and could directly be encapsulated during liposome synthesis [204, 354, 355]. For the lipophilic drug DOX, gradient encapsulation led to better drug retention in the liposome [198]. We decided to use paclitaxel as chemotherapeutic drug, as the EndoTAG™ liposomes were examined in a controlled phase II clinical trial with advanced PDAC patients in a combination approach with gemcitabine. Löhr et *al*. could show reduced side-effects and improved survival of the patient cohort [351]. We received best qualitative results for MNP-LPs loaded with paclitaxel in a 1:33 PTX:lipid molar ratio. EndoTAG™ liposomes are prepared at 1:32 PTX:lipid molar ratio [351], comparable to our PTX-loaded MNP-LPs. In other pre-clinical studies on PTX-loaded liposomes, the drug content varied between up to 1:3 PTX:lipid [356], 1:5 [223], 1:20 [357], 1:30 [358] and 1:33 [204, 354, 355], to 1:40 [359, 360], 4 mol% [361] and only 1 % w/w [362]. Our PTX-loaded MNP-LPs were synthesized from DPPC/Chol/ P_3C_{18} applying the TFH method and proven to be stable for at least two weeks at 4 °C after qualitative storability monitoring. The loading of MNPs with PTX before loading both components into the liposomes could not be shown properly. Cholesterol was included in the lipid mix in DOX liposomes, as the absence of cholesterol was found to lead to destabilization and toxicity, whereas increasing acyl-chain length and saturation enhanced the drug encapsulation capacity [198].

Generally, drug-loaded MNP-LPs are an interesting formulation. Zhang et *al*. postulated greater potency over just drug-loaded liposomes based on a more gradual and less abrupt drug release due to the iron oxide core from their *in vivo* data on a breast cancer model [363]. Due to the shift of emphasis during this thesis project, that formulation was not tested *in vitro* or *in vivo* for its anti-tumoral efficiency.

Taking together the examined functionalization possibilities of MNP-LP formulations, applied *in vivo* they enable for the MRI-guided visualization of biodistribution and delivery, supportive magnetic targeting by external magnetic fields, enhanced binding at the target tissue due to the $\alpha_v\beta_3$ integrin receptor binding motif, and temperature-induced drug release from thermosensitive liposomes at mild hyperthermia of 42 °C. Similar approaches led to successful studies *in vitro* and tumor specific targeted delivery *in vivo* in rodent HCC and PDAC models [213, 214, 226, 229, 230, 343, 350].

5 CONCLUSION and OUTLOOK

This work on three different types of magnetic nanocarriers, namely MNP-VP complexes, MNP-siRNA complexes and magnetic liposomes, was done to identify and examine the potential of each formulation in diagnosis and therapy of gastro-intestinal cancers, especially HCC and PDAC. Core component of all magnetic nanocarriers were MNPs. The magnetic moment and high surface area-to-volume ratio made the chosen core-shell type iron oxide MNPs ideal candidates for nanocarrier assembly, and as imaging probe for non-invasive and real-time monitoring of the formulation via MRI.

Summarizing, it can be said that the variety of carrier formulations equipped with different properties allow for the application in various clinical questions, as each holds specific advantages.
The approach to treat tumors with oncolytic viruses is still limited by the inactivation of virus particles in the circulatory system. The delivery efficiency could greatly be enhanced by assembly with magnetic nanoparticles and magnetic targeting towards the region of interest.
MNP-VP complexes have shown efficient transfection rates and oncolytic activity in *in vitro* assays with HCC and PDAC cell lines. Tissue-mimicking *in vitro* phantoms of free and cell-internalized MNP-VP complexes revealed excellent MRI properties for very sensitive imaging in future *in vivo* therapy monitoring. The agarose phantoms could serve as tool to optimize scan protocols and to evaluate nanocarrier concentrations needed for sufficient imaging contrast in *in vivo* applications. *In vivo*, the viral vectors were magnetically targetable towards orthotopic HCC lesions after intra-hepatic injection, and followed by successful virus replication within the tumor cells. In further approaches, the MNP-VP complexes could be shielded for example with organic structures to achieve a stable formulation for intra-arterial or systemic intravenous administration. Thereby, the diagnosis and treatment of metastases could be improved over the state-of-the-art therapy.

Non-viral magnetic complexes with nucleic acids were successfully applied for gene silencing in *in vitro* model cancer cell lines, and have the potential for nucleic acid therapy approaches in clinical questions when loaded with target-specific nucleic acids. The packing of nucleic acids with MNPs and eventual further functionalization of those assemblies again shields the sensitive nucleic acids from early degradation and enables for targeted delivery.
Examined MNP-siRNA complexes successfully could be applied for knock-down experiments in (primary) HCC and PDAC cell lines *in vitro*. Analogue to the formulations in those proof-of-principle experiments, MNP-siRNA complexes for oncogene down-regulation could be assembled in future experiments. Potential target gene in the therapy of HCC and PDAC is the octamer-binding transcription factor 4 (OCT4).

Magnetic liposomes can be loaded with drugs and synthesized to carry surface binding sites required for target tissue-specific delivery. Such nanocarrier formulations allow for long

circulation times, utilizing local accumulation via the EPR effect in tumor tissue. Additional accumulation is facilitated by the surface moieties binding to target cells and magnetic targeting. The therapeutic cargo can be released from the thermosensitive liposomes by exposure to local hyperthermia.

Naked MNPs and magnetic liposomes were tested *in vitro* and *in vivo* regarding their biodistribution, toxicity and targeting capability. No pathologic MNP-induced tissue alterations could be detected among the treated wildtype and endogenous PDAC-bearing model mice. Thermosensitive PTX-loaded MNP-LPs, partly functionalized with a $\alpha_v\beta_3$ integrin receptor binding motif, were characterized for their physico-chemical properties. They had the desired size of about 100 nm in diameter, and their surface was PEG-functionalized for stabilization, either as lipid moiety or from the polymer P_3C_{18}, which was incorporated in the lipid bilayer. Advantage of the polymer was its capability to bind $\alpha_v\beta_3$ integrins, expressed on HCC and PDAC cells. Thermosensitive LPs are capable of temperature-dependent release of encapsulated drugs with good local controllability. T_m of our tested liposomes was 42 °C, a temperature clinically used in mild hyperthermia treatment regimes. The release at temperatures below T_m started only after long circulation times, giving tolerable time windows for sufficient accumulation at the target site *in vivo*. In further experiments, the anti-tumoral efficiency of drug-loaded MNP-LPs has to be examined in detail *in vitro* and *in vivo*.

6 SUPPLEMENT

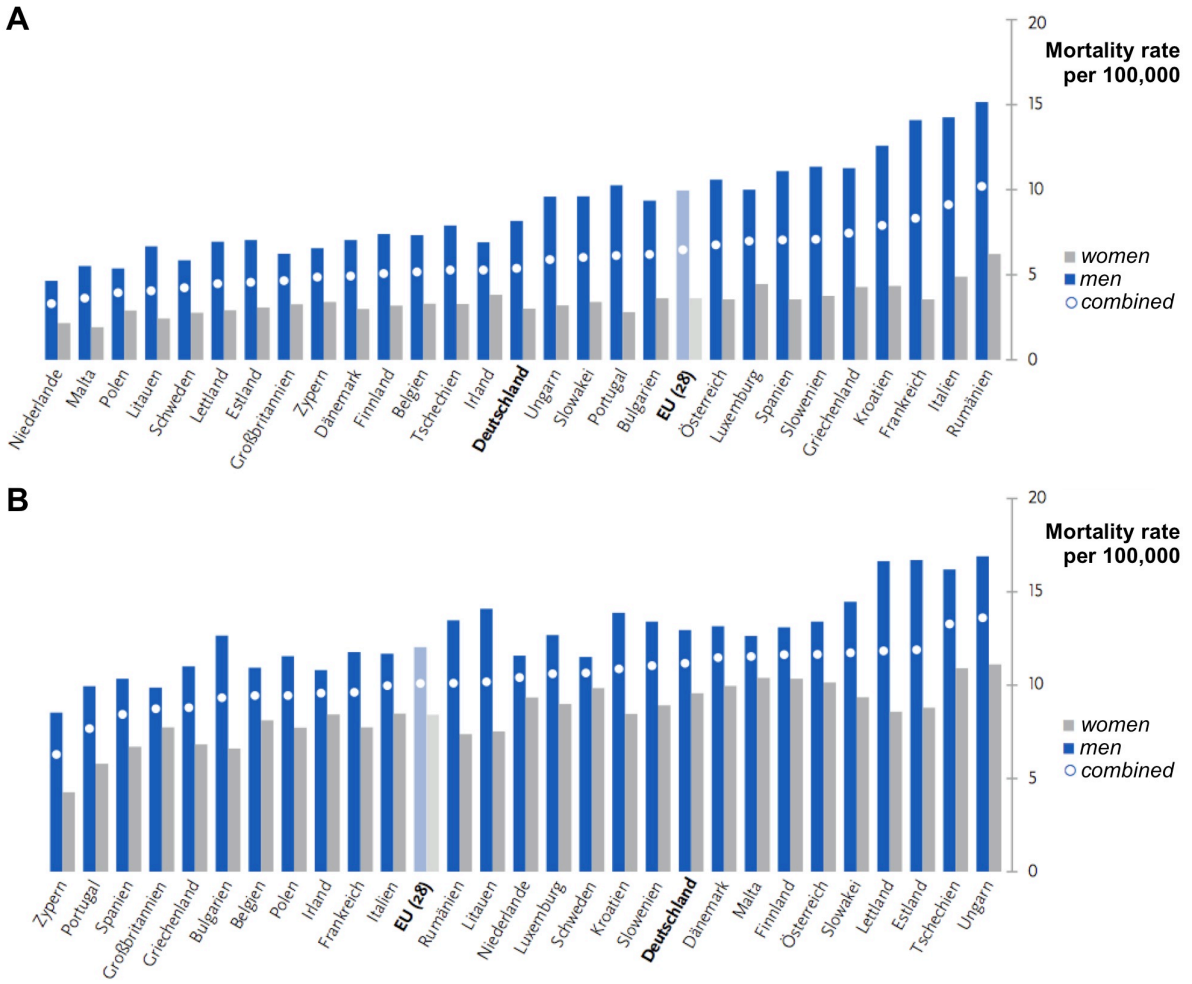

Figure 43: Cancer mortality rates in the European Union (per 100,000 with age adjusted to the European standard; 2011-13). **A:** HCC, **B:** PDAC (modified from [9-11])

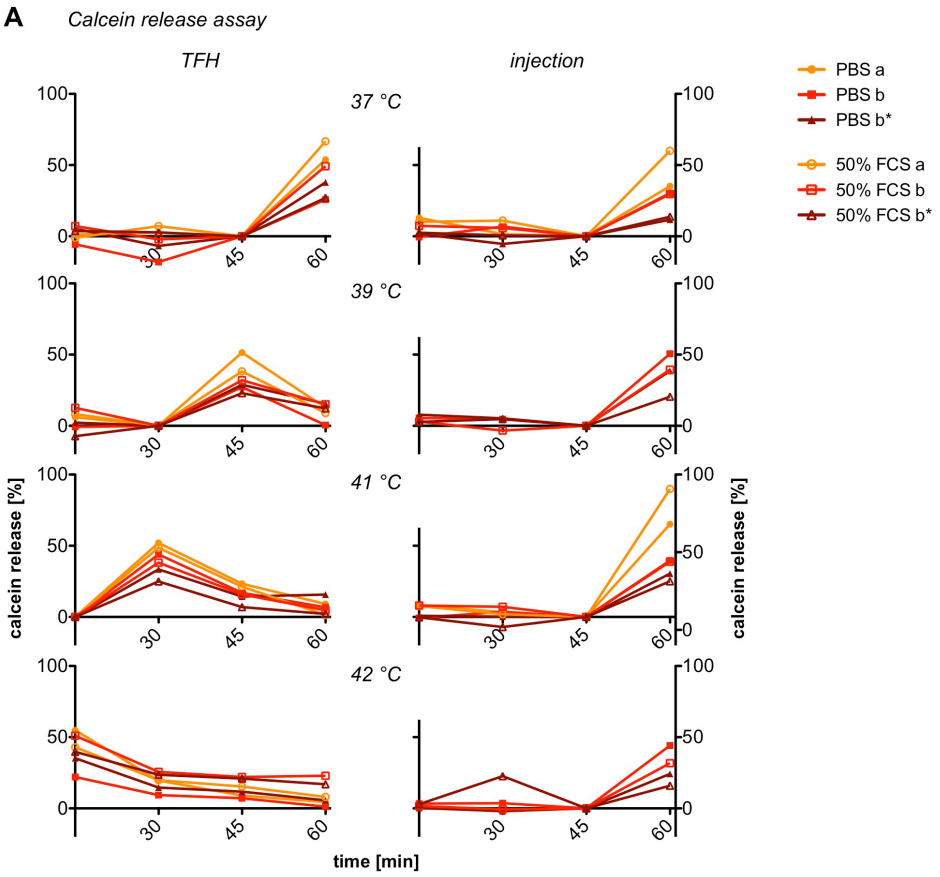

Figure 44: Calcein release assay of thermosensitive liposomes. Calcein release assay of TFH (left column) and injection method (right column) liposomes in PBS and 50% FCS plotted as calcein release versus time for all temperatures.

mouse	mother	father	sex	date of birth	treatment	sacrifice	study [days]	age [days]		Genotype			sampled tissues						
								start	end	Cre p48	Kras G12D	p53LOX	liver	lung	spleen	kidney	pancreas	tumor head	tumor tail	tail
10243	10061	10023	m	08.03.12	PalD2-Mag1	20.04.12	**4**	39	43	+/-	+/-	LOX	✓	✓	✓	✓		✓	✓	✓
10244	10061	10023	m	08.03.12	PalD2-Mag1	30.04.12	**14**	39	53	wt	wt	LOX	✓	✓	✓	✓	✓			✓
10245	10025	10016	m	09.03.12	PalD2-Mag1	30.04.12	**14**	38	52	wt	+/-	LOX	✓	✓	✓	✓	✓			✓
10246	10025	10016	m	09.03.12	PalD2-Mag1	30.04.12	**14**	38	52	wt	+/-	LOX	✓	✓	✓	✓	✓			✓
10247	10025	10016	m	09.03.12	PalD2-Mag1	30.04.12	**14**	38	52	wt	wt	LOX	✓	✓	✓	✓	✓			✓
10248	10025	10016	m	09.03.12	PalD2-Mag1	29.04.12	**13**	38	51	+/-	+/-	LOX	✓	✓	✓	✓		✓	✓	✓
10249	10025	10016	m	09.03.12	PalD2-Mag1	30.04.12	**14**	38	52	wt	+/-	LOX	✓	✓	✓	✓	✓			✓
10257	10087	10059	m	10.03.12	PalD2-Mag1	30.04.12	**14**	37	51	+/-	wt	LOX	✓	✓	✓	✓	✓			✓
10239	10061	10023	f	08.03.12	PalD2-Mag1	01.05.12	**15**	39	54	+/-	wt	LOX	✓	✓	✓	✓	✓			✓
10240	10061	10023	f	08.03.12	PalD2-Mag1	01.05.12	**15**	39	54	+/-	+/-	LOX	✓	✓	✓	✓	✓			✓
10241	10061	10023	f	08.03.12	PalD2-Mag1	01.05.12	**15**	39	54	wt	+/-	LOX	✓	✓	✓	✓	✓			✓
10242	10061	10023	f	08.03.12	PalD2-Mag1	30.04.12	**14**	39	53	+/-	+/-	LOX	✓	✓	✓	✓		✓	✓	✓
10250	10025	10016	f	09.03.12	PalD2-Mag1	30.04.12	**14**	38	52	wt	wt	LOX	✓	✓	✓	✓	✓			✓
10251	10025	10016	f	09.03.12	PalD2-Mag1	30.04.12	**14**	38	52	wt	wt	LOX	✓	✓	✓	✓	✓			✓
10252	10025	10016	f	09.03.12	PalD2-Mag1	30.04.12	**14**	38	52	+/-	+/-	LOX	✓	✓	✓	✓		✓	✓	✓
10254	10086	10059	f	09.03.12	PalD2-Mag1	01.05.12	**14**	38	53	+/-	wt	LOX	✓	✓	✓	✓	✓			✓
10255	10086	10059	f	09.03.12	PalD2-Mag1	24.04.12	**8**	38	46	+/-	+/-	LOX	✓	✓	✓	✓		✓	✓	✓
10263	10008	10035	f	10.03.12	PalD2-Mag1	01.05.12	**14**	37	52	+/-	wt	LOX	✓	✓	✓	✓	✓			✓
10269	10008	10035	f	10.03.12	PalD2-Mag1	01.05.12	**14**	37	52	+/-	+/-	LOX	✓	✓	✓	✓		✓	✓	✓
10203	10007	10037	f	09.02.12	PalD2-Mag2	03.04.12	**15**	39	54	+/-	wt	LOX	✓	✓	✓	✓	✓			✓
10202	10007	10037	f	09.02.12	PalD2-Mag2	03.04.12	**15**	39	54	wt	wt	LOX	✓	✓	✓	✓	✓			✓
10200	10007	10037	f	09.02.12	PalD2-Mag2	03.04.12	**15**	39	54	wt	+/-	LOX	✓	✓	✓	✓	✓			✓
10198	10007	10037	f	09.02.12	PalD2-Mag2	03.04.12	**15**	39	54	+/-	wt	LOX	✓	✓	✓	✓	✓			✓
10191	10031	10027	f	09.02.12	PalD2-Mag2	03.04.12	**15**	39	54	wt	+/-	LOX	✓	✓	✓	✓	✓			✓
10190	10031	10027	f	09.02.12	PalD2-Mag2	03.04.12	**15**	39	54	wt	wt	LOX	✓	✓	✓	✓	✓			✓
10183	10032	10027	f	02.02.12	PalD2-Mag2	02.04.12	**14**	46	60	wt	+/-	LOX	✓	✓	✓	✓	✓			✓
10181	10032	10027	f	02.02.12	PalD2-Mag2	02.04.12	**14**	46	60	+/-	wt	LOX	✓	✓	✓	✓	✓			✓
10178	10028	10017	f	31.01.12	PalD2-Mag2	02.04.12	**14**	48	62	wt	wt	LOX	✓	✓	✓	✓	✓			✓
10176	10028	10017	f	31.01.12	PalD2-Mag2	02.04.12	**14**	48	62	wt	wt	LOX	✓	✓	✓	✓	✓			✓
10188	10032	10027	m	02.02.12	PalD2-Mag2	02.04.12	**14**	46	60	wt	+/-	LOX	✓	✓	✓	✓	✓			✓
10172	10008	10035	m	30.01.12	PalD2-Mag2	02.04.12	**14**	49	63	+/-	wt	LOX	✓	✓	✓	✓	✓			✓
10171	10008	10035	m	30.01.12	PalD2-Mag2	02.04.12	**14**	49	63	wt	wt	LOX	✓	✓	✓	✓	✓			✓
10169	10008	10035	m	30.01.12	PalD2-Mag2	02.04.12	**14**	49	63	+/-	wt	LOX	✓	✓	✓	✓	✓			✓
10259	10087	10059	m	10.03.12	control	01.05.12			53	+/-	wt	LOX	✓	✓	✓	✓	✓			✓
10260	10008	10035	m	10.03.12	control	01.05.12			53	wt	+/-	LOX	✓	✓	✓	✓	✓			✓
10261	10008	10035	m	10.03.12	control	02.05.12			54	wt	wt	LOX	✓	✓	✓	✓	✓			✓
10262	10008	10035	m	10.03.12	control	01.05.12			53	wt	+/-	LOX	✓	✓	✓	✓	✓			✓
10271	10021	10024	m	10.03.12	control	01.05.12			53	+/-	+/-	LOX	✓	✓	✓	✓		✓	✓	✓
10274	10028	10017	m	14.03.12	control	01.05.12			53	wt	wt	LOX	✓	✓	✓	✓	✓			✓
10253	10025	10016	f	09.03.12	control	02.05.12			54	wt	wt	LOX	✓	✓	✓	✓	✓			✓
10256	10086	10059	f	09.03.12	control	02.05.12			54	wt	wt	LOX	✓	✓	✓	✓	✓			✓
10264	10008	10035	f	09.03.12	control	02.05.12			54	+/-	wt	LOX	✓	✓	✓	✓	✓			✓
10265	10008	10035	f	09.03.12	control	02.05.12			54	wt	+/-	LOX	✓	✓	✓	✓	✓			✓
10266	10008	10035	f	09.03.12	control	02.05.12			54	+/-	wt	LOX	✓	✓	✓	✓	✓			✓
10267	10008	10035	f	09.03.12	control	01.05.12			55	+/-	wt	LOX	✓	✓	✓	✓	✓			✓
10268	10008	10035	f	09.03.12	control	01.05.12			54	wt	+/-	LOX	✓	✓	✓	✓	✓			✓
10270	10008	10035	f	10.03.12	control	01.05.12			53	+/-	+/-	LOX	✓	✓	✓	✓		✓	✓	✓
10272	10021	10024	f	10.03.12	control	26.04.12			52	+/-	+/-	LOX	✓	✓	✓	✓	✓	✓	✓	✓
10273	10021	10024	f	10.03.12	control	01.05.12			53	wt	wt	LOX	✓	✓	✓	✓	✓			✓

tumor
no tumor

Table 12: MNPs *in vivo*: genetic background of the treated mice and experimental setup.

Scoring Sheet Mouse

Animal No.:	animal species:	breed:	sex:	weight:	Surgery: Date/ Kind:										
		date/time	date/time	date/time	date/time	date/time	date/time	date/time	date/time	date/time	date/time	date/time	date/time	date/time	date/time
behaviour	sleepy														
	awake														
	attentive														
	aggressive														
	depressive														
natural behaviour	normal														
	sligth changes														
	less mobile, isolated														
	vocalization,														
	self mutilation														
	.....														
coat of hair	straight														
	sligth stand on end														
	stand on end														
	dirty														
	.....														
posture	upright														
	arched														
eyes	clear														
	dirty														
	dull														
	dark														
	anemic														
	.....														
orifice	clear														
	dirty														
	.....														
claws	rose														
	pale														
	dark														
		date/time	date/time	date/time	date/time	date/time	date/time	date/time	date/time	date/time	date/time	date/time	date/time	date/time	date/time
respiratory rate	normal														
	slight changes														
	increased up to 30%														
	increased up to 50%														
	and more														
	.....														
body weight	in g														
	decreased, < 5%														
	decreased, < 10%														
	decreased, < 15%														
	decreased, < 20%														
	.....														
medication	when ?														
	what ?														
	how much ?														

Table 13: Scoresheet for evaluation of the animals in *in vivo* studies.

Sample	PEI-Mag2					SO-Mag6-11.5				
	r_2 [mM^{-1} Fe s^{-1}]	ratio [%]	r_2^* [mM^{-1} Fe s^{-1}]	ratio [%]	r_2^*/r_2	r_2 [mM^{-1} Fe s^{-1}]	ratio [%]	r_2^* [mM^{-1} Fe s^{-1}]	ratio [%]	r_2^*/r_2
MNP	238 ± 11	100	476 ± 58	100	2.0	274 ± 10	100	857 ± 12	100	3.1
MNP in McA	55 ± 5 *(4.5 pg Fe/cell)*	23	584 ± 17 *(4.5 pg Fe/cell)*	123	10.6	37 ± 3 *(5.4 pg Fe/cell)*	14	788 ± 12 *(5.4 pg Fe/cell)*	92	21.3
MNP-VSV										
MNP-VSV in McA	23 ± 3 *(3.2 pg Fe/cell)*	10	518 ± 8 *(3.2 pg Fe/cell)*	109	22.5	57 ± 2 *(2.5 pg Fe/cell)*	21	1494 ± 42 *(2.5 pg Fe/cell)*	174	26.2
MNP in RDB	19 ± 1 *(17.3 pg Fe/cell)*	8	560 ± 23 *(17.3 pg Fe/cell)*	118	29.5	38 ± 2 *(15.9 pg Fe/cell)*	14	1203 ± 118 *(15.9 pg Fe/cell)*	140	31.7
MNP-Ad	124 ± 13	52	542 ± 19	114	4.4	18 ± 2	7	1004 ± 32	117	55.8
MNP-Ad in RDB	21 ± 3 *(6.7 pg Fe/cell)*	9	757 ± 22 *(6.7 pg Fe/cell)*	159	36.0	8 ± 6 *(7.4 pg Fe/cell)*	3	412 ± 26 *(7.4 pg Fe/cell)*	48	51.5

Table 14: r_2 and r_2^* relaxivities of the MNP assemblies. Analogue to table 11, this table compiles the r_2 and r_2^* relaxivity data in liver-mimicking agarose phantoms, the ratios of the nanoassembly relaxivity normalized to the relaxivity of free MNPs (r_2/r_2(MNP) and r_2^*/r_2^*(MNP), respectively), and the r_2^* / r_2 ratios. All measurements were performed using a clinical 3.0 T Ingenia MRI system.

7 REFERENCES

1. Mekada, K., Abe, K., Murakami, A., Nakamura, S., Nakata, H., Moriwaki, K., Obata, Y., and Yoshiki, A. (2009) Genetic differences among C57BL/6 substrains. *Exp Anim* **58**, 141-149
2. cancerstatisticscenter.cancer.org. Vol. 2017
3. Siegel, R., Miller, K., and Jemal, A. (2017) Cancer statistics, 2017. *CA Cancer J Clin* **67**, 7-30
4. Wu, C., Gong, F., Pang, P., Shen, M., Zhu, K., Cheng, D., Liu, Z., and Shan, H. (2013) An RGD-modified MRI-visible polymeric vector for targeted siRNA delivery to hepatocellular carcinoma in nude mice. *PLoS One* **8**, e66416
5. Andersson, R., Vagianos, C., and Williamson, R. (2004) Preoperative staging and evaluation of resectability in pacreatic ductal adenocarcinoma. *HPB (Oxford)* **6**, 5-12
6. Radiology, A. C. o. (2017) ACR Appropriateness Criteria. In *Staging of Pancreatic Ductal Adenocarcinoma*
7. Qayyum, A., Tamm, E., Kamel, I., Allen, P., Arif-Tiwari, H., Chernyak, V., Gonda, T., Grajo, J., Hindman, N., Horowitz, J., Kaur, H., McNamara, M., Noto, R., Srivastava, P., and Lalani, T. (2017) Staging of prancreatic ductal adenocarcinoma. In *ACR Appropriateness Criteria*, American College of Radiology
8. Seufferlein, T., Porzner, M., Heinemann, V., Tannapfel, A., Stuschke, M., and Uhl, W. (2014) Duktales Adenokarzinom. *Dtsch Arztebl* **111**, 396-404
9. IARC. graph4. Vol. 2017
10. Robert-Koch-Institut. (2017) Bericht zum Krebsgeschehen in Deutschland 2017 - C22. Vol. 2018, Berlin
11. Robert-Koch-Institut. (2017) Bericht zum Krebsgeschehen in Deutschland 2017. Vol. 2018, Berlin
12. cancer.org. Vol. 2017
13. WCRF. liver cancers. Vol. 2017
14. Malek, N., Schmidt, S., Huber, P., Manns, M., and TF, G. (2014) Diagnose und Therapieoptionen beim hepatozellulären Karzinom. *Dtsch Arztebl* **111**, 101-109
15. cancer.gov. table HCC. Vol. 2014
16. cancerresearchuk. liver cancer. Vol. 2017
17. hopkinsmedicine. HCC. Vol. 2017
18. cancer.net. liver - cancer statistics. Vol. 2017
19. cancer.net. liver cancer - symptoms and signs. Vol. 2017
20. Groß, C., Steiger, K., Sayyed, S., Heid, I., Feuchtinger, A., Walch, A., Heß, J., Unger, K., Zitzelsberger, H., Settles, M., Schlitter, A., Dworniczak, J., Altomonte, J., Ebert, O., Schwaiger, M., Rummeny, E., Steingoetter, A., Esposito, I., and Braren, R. (2015) Model Matters: Differences in Orthotopic Rat Hepatocellular Carcinoma Physiology Determine Therapy Response to Sorafenib. *Clin Cancer Res* **21**, 4440-4450
21. Kummar, S., and Shafi, N. (2003) Metastatic Hepatocellular Carcinoma. *Clin Oncol* **15**, 288-294
22. WCRF. http://www.wcrf.org/int/cancer-facts-figures/worldwide-data. Vol. 2017
23. GEKID. (2017) Atlas der Krebsinzidenz und Krebsmortalität der Gesellschaft der epidemiologischen Krebsregister in Deutschland e.V. - "Der GEKID Atlas" Ergebnisse der Hochrechnungen für Deutschland. Vol. Datenlieferung: Juli 2017, http://www.gekid.de, Lübeck
24. Robert-Koch-Institut. (2016) Bericht zum Krebsgeschehen in Deutschland 2016. Vol. 2018, Berlin
25. IARC. http://gco.iarc.fr/today/online-analysis-map?mode=population&mode_population=continents&population=900&sex=0&cancer=9&type=1&statistic=2&prevalence=0&color_palette=default&projection=natural-earth. Vol. 2017
26. WGO-foundation. http://www.wgofoundation.org/wdhd-2013.html. Vol. 2014
27. Rahib, I., Smith, B., Aizenberg, R., Rosenzweig, A., Fleshman, J., and Matrisian, L. (2014) Projecting cancer incidence and deaths to 2030: the unexpected burden of thyroid, liver, and pancreas cancers in the United States. *Cancer Res* **74**, 2913-2921
28. IARC. http://gco.iarc.fr/today/online-analysis-map?mode=population&mode_population=continents&population=900&sex=0&cancer=9&type=0&statistic=2&prevalence=0&color_palette=default&projection=natural-earth. Vol. 2017
29. IARC. http://gco.iarc.fr/today/online-analysis-map?mode=population&mode_population=continents&population=900&sex=0&cancer=7&type=0&statistic=2&prevalence=0&color_palette=default&projection=natural-earth. Vol. 2017
30. cancer.gov. PDAC.
31. cancer.net. pancreatic cancer. Vol. 2017
32. cancer.net. pancreatic cancer - risk factors. Vol. 2017
33. cancerresearchuk. pancreatic cancer. Vol. 2017
34. cancer.net. pancreatic cancer - symptoms and signs. Vol. 2017
35. IARC. http://gco.iarc.fr/today/online-analysis-map?mode=population&mode_population=continents&population=900&sex=0&cancer=7&type=1&statistic=2&prevalence=0&color_palette=default&projection=natural-earth. Vol. 2017
36. Robert-Koch-Institut. (2010) Bericht zum Krebsgeschehen in Deutschland 2010. Vol. 2018, Brelin
37. Gudjonsson, B. (2016) Pancreatic cancer: 80 years of surgery - percentages and repetitions. *HPB Surgery*
38. IARC. http://gco.iarc.fr/today/online-analysis-map?mode=population&mode_population=continents&population=900&sex=0&cancer=7&type=2&statistic=2&prevalence=1&color_palette=default&projection=natural-earth. Vol. 2017

39. Robert-Koch-Institut. (2017) Bericht zum Krebsgeschehen in Deutschland 2017 - C25. Vol. 2018, Berlin
40. Siegel, R., Miller, K., and Jemal, A. (2015) Cancer statistics, 2015. *CA Cancer J Clin* **65**, 5-29
41. Cho, E., Jun, C., Kim, B., Son, D., Choi, W., and Choi, S. (2015) 18F-FDG PET CT as a prognostic factor in hepatocellular carcinoma. *Turk J Gastroenterol* **26**, 344-350
42. Pinho, D., and Subramaniam, R. (2017) PET-COmputed Tomography and Precision Medicine in Pancreatic Adenocarcinoma and Pancreatic Neuroendrocrine Tumors. *Pet Clinics* **12**
43. Caravan, P., Ellison, J., McMurry, T., and Lauffer, R. (1999) Gadolinium(III) chelates as MRI contrast agents: structure, dynamics, and applications. *Chem Rev* **99**, 2293-2352
44. Zhang, C., Wängler, B., Morgenstern, B., Zentgraf, H., Eisenhut, M., Untenecker, H., Krüger, R., Huss, R., Seliger, C., Semmler, W., and Kiessling, F. (2007) Silica- and alkoxysilane-coated ultrasmall superparamagnetic iron oxide particles: a promising tool to label cells for magnetic resonance imaging. *Langmuir* **23**, 1427–1434
45. Braren, R., Altomonte, J., Settles, M., Neff, F., Esposito, I., Ebert, O., Schwaiger, M., Rummeny, E., and Steingoetter, A. (2011) Validation of preclinical multiparametric imaging for prediction of necrosis in hepatocellular carcinoma after embolization. *Journal of hepatology* **55**, 1034-1040
46. Möller, H. (Grundlagen der MRT)
47. Stanisz, G., Odrobina, E., Pun, J., Escaravage, M., Graham, S., Bronskill, M., and Henkelmann, R. (2005) T1, T2 Relaxation and Magnetization Transfer in Tissue at 3T. *Magn Reson Med* **54**, 507-512
48. Freeman, M., Arrot, A., and Watson, H. (1960) Magnetism in medicine. *J Appl Phys* **31**, S404
49. McCarthy, J., and Weissleder, R. (2008) Multifunctional magnetic nanoparticles for targeted imaging and therapy. *Advanced drug delivery reviews* **60**, 1241-1251
50. Schering. Vol. 2018
51. Bayer. Vol. 2018
52. Wang, Y., Hussain, S., and Krestin, G. (2001) Superparamagneticironoxidecontrastagents: physicochemical characteristics and applications in MR imaging. *European radiology* **11**, 2319-2331
53. Bonnemain, B. (1998) Superparamagnetic agents in magnetic resonance imaging: physi- cochemical characteristics and clinical applications — a review. *J Drug Target* **6**, 167-174
54. Harisinghani, M. G., Barentsz, J., Hahn, P. F., Deserno, W. M., Tabatabaei, S., Hulsbergen van de Kaa, C., de la Rosette, J., and Weissleder, R. (2003) Noninvasive detection of clinically occult lymph-node metastases in prostate cancer. *New Engl J Med.* **348**, 2491-2499
55. Wang, Y. (2011) Superparamagnetic iron oxide based MRI contrast agents: Current status of clinical application. *Quant Imaging Med Surg* **1**, 35-40
56. Guerbet. Vol. 2018
57. Bracco. Vol. 2018
58. Healthcare, G. Vol. 2018
59. Peng, X.-H., Qian, X., Mao, H., Wang, A., Chen, Z., Nie, S., and Shin, D. (2008) Targeted magnetic iron oxide nanoparticles for tumor imaging and therapy. *International journal of nanomedicine* **3**, 311-321
60. Mazzara, G., Briggs, R., Wu, Z., and Steinbach, B. (1996) Use of a modified polysaccharide gel in developing a realistic breast phantom for MRI. *Magn Reson Imaging* **14**, 639-648
61. Lin, G., Zhu, W., Yang, L., Wu, J., Lin, B., Xu, Y., Cheng, Z., Xia, C., Gong, Q., Song, B., and Ai, H. (2014) Delivery of siRNA by MRI-visible nanovehicles to overcome drug resistance in MCF-7:ADR human breast cancer cells. *Biomaterials* **35**, 9495-9507
62. Liu, G., Xie, J., Zhang, F., Wang, Z., Luo, K., Zhu, L., Quan, Q.-M., Niu, G., Lee, S., Ai, H., and Chen, X. (2011) N-Alkyl-PEI-functionalized iron oxide nanoclusters for efficient siRNA delivery. *Small* **7**, 2742-2749
63. Kim, D., Chen, J., Omary, R., and Larson, A. (2015) MRI Visible Drug Eluting Magnetic Microspheres for Transcatheter Intra-Arterial Delivery to Liver Tumors. *Theranostics* **5**, 477-488
64. Wang, L., Potter, W., and Zhao, Q. (2015) In vivo quantification of SPIO nanoparticles for cell labeling based on MR phase gradient images. *Contrast Media Mol Imaging* **10**, 43-50
65. Christoffersson, J., Olsson, L., and Sjöberg, S. (1991) Nickel-Doped Agarose Gel Phantoms in MR Imaging. *Acta Radiologica* **32**, 426-431
66. Ericsson, A., Lönnemark, M., Hemmingsson, A., and Bach-Gansmo, T. (1991) Effect of superparamagnetic particles in agarose gels. *Acta Radiologica* **32**, 74-78
67. Mykhaylyk, O., Steingötter, A., Perea, H., Aigner, J., Botnar, R., and Plank, C. (2009) Nucleic Acid Delivery to Magnetically-Labeled Cells in a 2D Array and at the Luminal Surface of Cell Culture Tube and Their Detection by MRI. *Journal of Biomedical Nanotechnology* **5**, 692-706
68. Tofts, P., Shuter, B., and Pope, J. (1993) Ni-DTPA doped agarose gel - a phantom material for Gd-DTPA enhancement measurements. *Magn Reson Imaging* **11**, 125-133
69. Trojan, J., Hammerstingl, R., Strey, C., Vogl, T., Bechstein, W.-O., and Zeuzern, S. (2007) Fortschritte in der bildgebenden Diagnostik und Therapie des hepatozellulären Karzinoms. *Dtsch Arztebl* **104**, A3326-3333
70. Hecht, E., Holland, A., Israel, G., Hahn, W., Kim, D., West, A., Babb, J., Taouli, B., Lee, V., and Krinsky, G. (2006) Hapatocellular carcinoma in the cirrhotic liver: gadolinium-enhanced 3D T1-weighted MR imaging as a stand-alone sequence for diagnosis. *Radiology* **239**, 438-447
71. Bruix, J., and Sherman, M. (2005) Practice Guidelines Committee, American Association for the Study of Liver Diseases: Management of Hepatocellular Carcinoma. *Hepatology* **42**, 1208-1236
72. Bellin, M.-F. (2006) Metastatic Hepatocellular Carcinoma. *Eur J Radiol* **60**, 314-323

73. Talbot, J.-N., Fartoux, L., Balogova, S., Natal, V., Kerrou, K., Gutman, F., Huchet, V., Ancel, D., Grange, J.-D., and Rosmorduc, O. (2010) Detection of Hepatocellular Carcinoma with PET/CT: A Prospective Comparison of 18F-Fluorocholine and 18F-FDG in Patients with Cirrhosis and Chonic Liver Disease. *J Nucl Med* **51**, 1699-1706
74. cancer.net. pancreatic cancer - dignosis. Vol. 2017
75. Lu, D., Vedantham, S., Krasny, R., Kadell, B., Berger, W., and Reber, H. (1996) Two-phase helical CT for pancreatic tumors: pancreatic versus hepatic phase enhancement of tumor, pancreas and vascular structures. *Radiology* **199**, 697-701
76. Koelblinger, C., Ba-Ssalamah, A., Goetzinger, P., Puchner, S., Weber, M., Sahora, K., Scharitzer, M., Plank, C., and Schima, W. (2011) Gadobenate dimeglubine-enhanced 3.0-T MR imaging versus multiphasic 64-detector row CT: prospective evaluation in patients suspected of having pancreatic cancer. *Radiology* **259**, 757-766
77. Hrikhande, S., Barreto, S., Goel, M., and Arya, S. (2012) Multimodality imaging of pancreatic ductal adenocarcinoma: a review of the literature. *HPB (Oxford)* **14**, 658-668
78. Farma, J., Santillan, A., Melis, M., Walters, J., Belinc, D., Chen, D., Elkman, E., and Malafa, M. (2008) PET/CT fusion scan enhances CT staging in patients with pancreatic neoplasms. *Ann Surg Oncol* **15**, 2465-2471
79. Sun, C., Lee, J., and Zhang, M. (2008) Magnetic nanoparticles in MR imaging and drug delivery. *Advanced drug delivery reviews* **60**, 1252-1265
80. (2016) TNM Classification of Malignant Tumours 8th edition. Vol. 2018 p. ppt presentation, https://http://www.google.de/url?sa=t&rct=j&q=&esrc=s&source=web&cd=5&ved=0ahUKEwiNr_GsvtXYAhXLCuwKHbTPBDkQFghLMAQ&url=https%3A%2F%2Fwww.uicc.org%2Fsites%2Fmain%2Ffiles%2Fatoms%2Ffiles%2FTNM_Classification_of_Malignant_Tumours_8th_edition_NEW_updated_0.pptx&usg=AOvVaw1vntWLU0o0OjOV65XR-Sje
81. Mazzaferro, V., Regalia, E., Doci, R., Andreaola, S., Pulivirenti, A., Bozzetti, F., Montalto, F., Ammatuna, M., Morabito, A., and Gennari, L. (1996) Liver transplantation for the treatment of small hepatocellular carcinomas in patients with cirrhosis. *N Engl J Med* **334**, 693-699
82. Duvoux, C., Roudot-Thoraval, F., Decaens, T., Pessione, F., Badran, H., Piardi, T., Francoz, C., Compagnon, P., Vanlemmens, C., Dumortier, J., Dharancy, S., Gugenheim, J., Bernard, P., Adam, R., Radenne, S., Muscari, F., Conti, F., Hardwigsen, J., Pageaux, G., Chazouillierez, O., Salame, E., Hilleret, M., Lebray, P., Abergel, A., Debatte-Gratien, M., Kluger, M., Mallat, A., Azoulay, D., Chergui, D., and Group, L. T. F. (2012) Liver transplantation for hepatocellular carcinoma: a model including a-fetoprotein improves the performance of Milan criteria. *Gastroenterology* **143**, 986-994
83. hopkinsmedicine. HCC - RFA. Vol. 2017
84. Salati, U., Barry, A., Chou, F., Ma, R., and Liu, D. (2017) State of the ablation nation: a review of ablative therapies for cure in the treatment of hepatocellular carcinoma. *Future Oncol* **13**, 1437-1448
85. Scheffer, H., Melenhorst, M., Echenique, A., Nielsen, K., van Tilborg, A., van den Bos, W., Vroomen, L., van den Tol, P., and Meijerink, M. (2015) Irreversible Electroporation for Colorectal Liver Metastases. *Tech Vasc Interv Radiol* **18**, 159-169
86. Ackerman, N. (1972) Experimental studies on the circulation dynamics of intrahepatic tumor blood supply. *Cancer* **29**, 435-439
87. Brader, P., Riedl, C., Woo, Y., Ponomarev, V., Zanzonico, P., Wen, B., Cai, S., Hricak, H., Fong, Y., Blasberg, R., and Serganova, I. (2007) Imaging of hypoxia-driven gene expression in an orthotopic liver tumor model. *Mol Cancer Ther* **6**, 2900-2908
88. hopkinsmedicine. HCC - intraarterial therapies. Vol. 2017
89. Llovet, J., Ricci, S., Mazzaferro, V., Hilgard, P., Gane, E., Blanc, J., de Oliveira, A., Santoro, A., Raoul, J., Forner, A., Schwartz, M., Porta, C., Zeuzern, S., Bolondi, L., Greten, T., Galle, P., Seitz, J., Borbath, I., Häussinger, D., Giannaris, T., Shan, M., Moscovici, M., Voliotis, D., Bruix, J., and Group, S. I. S. (2008) Sorafenib in advanced hepatocellular carcinoma. *N Engl J Med* **359**, 378-390
90. cancer.net. pancreatic cancer - stages. Vol. 2017
91. cancer.net. pancreatic cancer - treatment options. Vol. 2017
92. Nobuto, H., Sugita, T., Kubo, T., Shimose, S., Yasunaga, Y., Murakami, T., and Ochi, M. (2004) Evaluation of systemic chemotherapy with magnetic liposomal doxorubicin and a dipole external electromagnet. *International journal of cancer. Journal international du cancer* **109**, 627-635
93. Wang, H., Mukherjee, S., Yi, J., Banerjee, P., Chen, Q., and Zhou, S. (2017) Biocompatible Chitosan–Carbon Dot Hybrid Nanogels for NIR-Imaging-Guided Synergistic Photothermal–Chemo Therapy. *ACS Appl Mater Interfaces* **9**, 18639-18649
94. Peyron, P., Marionneau-Parini, I., and Stegmann, T. (2001) Fusion of human neutrophil phagosomes with lysosomes in vitro: involvement of tyrosine kinases of the Src family and inhibition by mycobacteria. *J Biol Chem* **276**, 35512-35517
95. Bracco. (2017) Fachinformation (ZUSAMMENFASSUNG DER MERKMALE DES ARZNEIMITTELS). **2017-11-28_ProHance_SmPC**
96. Pradhan, P., Giri, J., Rieken, F., Koch, C., Mykhaylyk, O., Döblinger, M., Banerjee, D., Bahadur, D., and Plank, C. (2010) Targeted temperature sensitive magnetic liposomes for thermo-chemotherapy. *Journal of controlled release : official journal of the Controlled Release Society* **142**, 108-121
97. Fetterly, G., and Straubinger, R. (2003) Pharmacokinetics of paclitaxel-containing liposomes in rats. *Pharm Sci* **5**, 32-42

98. Haran, G., Cohen, R., Bar, L., and Barenholz, Y. (1993) Transmembrane ammonium sulfate gradients in liposomes produce efficient and stable entrapment of amphipathic weak bases. *Biochim Biophys Acta* **1151**, 201-215
99. Doxil.com. https://http://www.doxil.com. Vol. 2017
100. Mykhaylyk, O., Sanchez-Antequera, Y., Vlaskou, D., and Plank, C. (2007) Generation of magnetic nonviral gene transfer agents and magnetofection in vitro. *Nature protocols* **2**, 2391-2411
101. Wenzel, D., Rieck, S., Vosen, S., Mykhaylyk, O., Trueck, C., Eberbeck, D., Trahms, L., Zimmermann, K., Pfeifer, A., and Fleischmann, B. (2012) Identification of magnetic nanoparticles for combined positioning and lentiviral transduction of endothelial cells. *Pharmaceutical research* **29**, 1242-1254
102. Trueck, C., Zimmermann, K., Mykhaylyk, O., Anton, M., Vosen, S., Wenzel, D., Fleischmann, B., and Pfeifer, A. (2012) Optimization of magnetic nanoparticle-assisted lentiviral gene transfer. *Pharmaceutical research* **29**, 1255-1269
103. Tresilwised, N., Pithayanukul, P., Holm, P., Schillinger, U., Plank, C., and Mykhaylyk, O. (2011) Effects of nanoparticle coatings on the activity of oncolytic adenovirus-magnetic nanoparticle complexes. *Biomaterials* **33**, 256-269
104. Mannell, H., Pircher, J., Räthel, T., Schilberg, K., Zimmermann, K., Pfeifer, A., Mykhaylyk, O., Gleich, B., Pohl, U., and Krötz, F. (2012) Targeted endothelial gene delivery by ultrasonic destruction of magnetic microbubbles carrying lentiviral vectors. *Pharmaceutical research* **29**, 1282-1294
105. Tresilwised, N., Pithayanukul, P., Mykhaylyk, O., Holm, P. S., Holzmüller, R., Anton, M., Thalhammer, S., Adigüzel, D., Döblinger, M., and Plank, C. (2010) Boosting oncolytic adenovirus potency with magnetic nanoparticles and magnetic force. *Mol Pharm* **7**, 1069-1089
106. Hofmann, A., Wenzel, D., Becher, U., Freitag, D., Klein, A., Eberbeck, D., Schulte, M., Zimmermann, K., Bergemann, C., Gleich, B., Roell, W., Weyh, T., Trahms, L., Nickenig, G., Fleischmann, B., and Pfeifer, A. (2009) Combined targeting of lentiviral vectors and positioning of transduced cells by magnetic nanoparticles. *Proceedings of the National Academy of Sciences of the United States of America* **106**, 44-49
107. Plank, C., Zelphati, O., and Mykhaylyk, O. (2011) Magnetically enhanced nucleic acid delivery. Ten years of magnetofection-Progress and prospects. *Adv Drug Deliv Rev* **63**, 1300-1331
108. Trueck, C., Zimmermann, K., Mykhaylyk, O., Anton, M., Vosen, S., Wenzel, D., Fleischmann, B. K., and Pfeifer, A. (2012) Optimization of Magnetic Nanoparticle-Assisted Lentiviral Gene Transfer. *Pharm Res*
109. Raty, J. K., Liimatainen, T., Wirth, T., Airenne, K. J., Ihalainen, T. O., Huhtala, T., Hamerlynck, E., Vihinen-Ranta, M., Narvanen, A., Yla-Herttuala, S., and Hakumaki, J. M. (2006) Magnetic resonance imaging of viral particle biodistribution in vivo. *Gene Ther* **13**, 1440-1446
110. Sapet, C., Pellegrino, C., Laurent, N., Sicard, F., and Zelphati, O. (2012) Magnetic nanoparticles enhance adenovirus transduction in vitro and in vivo. *Pharmaceutical research* **29**, 1203-1218
111. Badieyan, Z., Pasewald, T., Mykhaylyk, O., Rudolph, C., and Plank, C. (2017) Efficient ex vivo delivery of chemically modified messenger RNA using lipofection and magnetofection. *Biochem Biophys Res Commun* **482**, 796-801
112. Mykhaylyk, O., Sanchez-Antequera, Y., Vlaskou, D., Cerda, M., Bokharaei, M., Hammerschmid, E., Anton, M., and Plank, C. (2015) Magnetic Nanoparticle and Magnetic Field Assisted siRNA Delivery In Vitro. *Methods Mol Biol* **1218**, 53-106
113. Sanchez-Antequera, Y., Mykhaylyk, O., Thalhammer, S., and Plank, C. (2010) Gene delivery to Jurkat T cells using non-viral vectors associated with magnetic nanoparticles. *Int J Biomed Nanosci Nanotech* **1**, 202-229
114. Scherer, F., Anton, M., Schillinger, U., J, H., Bergemann, C., A, K., B, G., and Plank, C. (2002) Magnetofection: Enhancing and targeting gene delivery by magnetic force in vitro and in vivo. *Gene Ther* **9**, 102-109
115. Mykhaylyk, O., Sobisch, T., Almstätter, I., Sanchez-Antequera, Y., Brandt, S., Anton, M., Döblinger, M., Eberbeck, D., Settles, M., Braren, R., Lerche, D., and Plank, C. (2012) Silica-iron oxide magnetic nanoparticles modified for gene delivery: a search for optimum and quantitative criteria. *Pharmaceutical research* **29**, 1344-1365
116. Arruebo, M., Fernandez-Pacheco, R., Ibarra, M., and Santamaria, J. (2007) Magnetic nanoparticles for drug delivery. *Nanotoday* **2**, 22-32
117. Kettering, M., Richter, H., Wiekhorst, F., Bremer-Streck, S., Trahms, L., Kaiser, W., and Hilger, I. (2011) Minimal-invasive magnetic heating of tumors does not alter intra-tumoral nanoparticle accumulation, allowing for repeated therapy sessions: an in vivo study in mice. *Nanotechnology* **22**, 505102
118. Giustini, A., Ivkov, R., and Hoopes, P. (2011) Magnetic nanoparticle biodistribution following intratumoral administration. *Nanotechnology* **22**, 345101
119. Dennis, C., Jackson, A., Borchers, J., Hoopes, P., Strawbridge, R., Foreman, A., van Lierop, J., Gruttner, C., and Ivkov, R. (2009) Nearly complete regression of tumors via collective behavior of magnetic nanoparticles in hyperthermia. *Nanotechnology* **20**, 395103
120. Kittel, C. (1949) Physical theory of ferromagnetic domains. *Rev Mod Phys* **21**, 541-583
121. Strijkers, G. J., Mulder, W. J., van Tilborg, G. A., and Nicolay, K. (2007) MRI contrast agents: current status and future perspectives. *Anticancer Agents Med Chem* **7**, 291-305
122. Carr, D. (1984) The use of iron and gadolinium chelates as NMR contrast agents: animal and human studies *Physiol Chem Phys Med NMR* **16**, 137-144

123. Child, H. W., del Pino, P. A., De La Fuente, J. M., Hursthouse, A. S., Stirling, D., Mullen, M., McPhee, G. M., Nixon, C., Jayawarna, V., and Berry, C. C. (2011) Working together- the combined application of a magnetic field and penetratin for the delivery of magnetic nanoparticles to cells in 3D. *ACS Nano* **5**, 7910-7919
124. Cole, A., David, A., Wang, J., Galban, C., Hill, H., and Yang, V. (2011) Polyethylene glycol modified, cross-linked starch-coated iron oxide nanoparticles for enhanced magnetic tumor targeting. *Biomaterials* **32**, 2183-2193
125. Cole, A., David, A., Wang, J., Galban, C., and Yang, V. (2011) Magnetic brain tumor targeting and biodistribution of long-circulating PEG-modified, cross-linked starch-coated iron oxide nanoparticles. *Biomaterials* **32**, 6291-6301
126. Cole, A., Yang, V., and David, A. (2011) Cancer theranostics: the rise of targeted magnetic nanoparticles. *Trends in biotechnology* **29**, 323-332
127. Levy, M., Luciani, N., Alloyeau, D., Elgrabli, D., Deveaux, V., Pechoux, C., Chat, S., Wang, G., Vats, N., Gendron, F., Factor, C., Lotersztajn, S., Luciani, A., Wilhelm, C., and Gazeau, F. (2011) Long term in vivo biotransformation of iron oxide nanoparticles. *Biomaterials* **32**, 3988-3999
128. Pouponneau, P., Leroux, J., Soulez, G., Gaboury, L., and Martel, S. (2011) Co-encapsulation of magnetic nanoparticles and doxorubicin into biodegradable microcarriers for deep tissue targeting by vascular MRI navigation. *Biomaterials* **32**, 3481-3486
129. Santra, S., Kaittanis, C., Grimm, J., and Perez, J. (2009) Drug/dye-loaded, multifunctional iron oxide nanoparticles for combined targeted cancer therapy and dual optical/magnetic resonance imaging. *Small* **5**, 1862-1868
130. Wang, C., Zhang, H., Chen, B., Yin, H., and Wang, W. (2011) Study of the enhanced anticancer efficacy of gambogic acid on Capan-1 pancreatic cancer cells when mediated via magnetic Fe3O4 nanoparticles. *International journal of nanomedicine* **6**, 1929-1935
131. Yallapu, M., Othman, S., Curtis, E., Gupta, B., Jaggi, M., and Chauhan, S. (2011) Multi-functional magnetic nanoparticles for magnetic resonance imaging and cancer therapy. *Biomaterials* **32**, 1890-1905
132. Estelrich, J., Escribano, E., Queralt, J., and Busquets, M. (2015) Iron oxide nanoparticles for magnetically-guided and magnetically-responsive drug delivery. *Int J Mol Sci* **16**, 8070-8101
133. Chanana, M., Mao, Z., and Wang, D. (2009) Using Polymers to Make Up Magnetic Nanoparticles for Biomedicine. *Journal of Biomedical Nanotechnology* **5**, 652-668
134. Schreiber-Mojdehkar, B., Sturm, B., Plank, L., Kryzer, I., and Goldenberg, H. (2003) Influence of parenteral iron preparations on non-transferrin bound iron uptake, the iron regulatory protein and the expression of ferritin and the divalent metal transporter DMT-1 in HepG2 human hepatoma cells. *Biochem Pharm* **65**, 1973-1978
135. Shao, H., Yoon, T., Liong, M., Weissleder, R., and Lee, H. (2010) Magnetic nanoparticles for biomedical NMR-based diagnostics. *Beilstein J Nanotechnol* **1**, 142-154
136. Chatterjee, K., Sarkar, S., Jagajjanani Rao, K., and Paria, S. (2014) Core/shell nanoparticles in biomedical applications. *Adv Colloid Interface Sci* **209**, 8-39
137. Shubayev, V., Pisanic, T., and Jin, S. (2009) Magnetic nanoparticles for theragnostics. *Advanced drug delivery reviews* **61**, 467-477
138. Akinc, A., Thomas, M., Klibanov, A., and Langer, R. (2005) Exploring polyethylenimine-mediated DNA transfection and the proton sponge hypothesis. *The journal of gene medicine* **7**, 657-663
139. Almstätter, I., Mykhaylyk, O., Settles, M., Altomonte, J., Aichler, M., Walch, A., Rummeny, E., Ebert, O., Plank, C., and Braren, R. (2015) Characterization of magnetic viral complexes for targeted delivery in oncology. *Theranostics* **5**, 667-685
140. Pfeifer, A., Zimmermann, K., and Plank, C. (2012) Magnetic Nanoparticles for Biomedical Applications. *Pharmaceutical research* **29**, 1161-1164
141. Sanchez-Antequera, Y., Mykhaylyk, O., van Til, N., Cengizeroglu, A., de Jong, J., Huston, M., Anton, M., Johnston, I., Pojda, Z., Wagemaker, G., and Plank, C. (2011) Magselectofection: an integrated method of nanomagnetic separation and genetic modification of target cells. *Blood* **117**, e171-181
142. Vlaskou, D., Mykhaylyk, O., Krötz, F., N, H., R, R., Schillinger, U., Gleich, B., A, H., G, S., K, H., and Plank, C. (2010) Magnetic and Acoustically Active Lipospheres for Magnetically Targeted Nucleic Acid Delivery. *Adv Funct Mater* **20**, 3881-3894
143. Mah, C., Zolotukhin, I., Fraites, T., Dobson, J., Batich, C., and Byrne, B. (2000) Microsphere-mediated delivery with magnetic particles under the influence of a magnetic field. *Molecular therapy : the journal of the American Society of Gene Therapy* **1**, S239
144. Plank, C., Scherer, F., Schillinger, U., and Anton, M. (2000) Magnetofection: Enhancement and localization of gene delivery with magnetic particles under the influence of a magnetic field. *The journal of gene medicine* **2 (Suppl.)**, 24
145. Mah, C., Fraites, T., I, Z., Song, S., Flotte, T., Dobson, J., Batich, C., and Byrne, B. (2002) Improved Method of Recombinant AAV2 Delivery for Systemic Targeted Gene Therapy. *Molecular therapy : the journal of the American Society of Gene Therapy* **6**, 106-112
146. Plank, C., Schillinger, U., Scherer, F., Bergemann, C., Rémy, J., Krötz, F., Anton, M., Lausier, J., and Rosenecker, J. (2003) The magnetofection method: using magnetic force to enhance gene delivery. *Biol Chem* **384**, 737-747
147. Schillinger, U., Brill, T., Rudolph, C., Huth, S., Gersting, S., Krötz, F., Hirschberger, J., Bergemann, C., and Plank, C. (2005) Advances in magnetofection—Magnetically guided nucleic acid delivery. *J Magn Magn Mater* **293**, 501-508

148. Laurent, N., Sapet, C., Le Gourrierec, L., Bertosio, E., and Zelphati, O. (2011) Nucleic acid delivery using magnetic nanoparticles: the MagnetofectionTM technology. *Ther Deliv* **2**, 471–482
149. Plank, C., Zelphati, O., and Mykhaylyk, O. (2011) Magnetically enhanced nucleic acid delivery. Ten years of magnetofection-progress and prospects. *Advanced drug delivery reviews* **63**, 1300-1331
150. Grzeskowiak, B., Sanchez-Antequera, Y., Hammerschmid, E., Döblinger, M., Eberbeck, D., Wozniak, A., Slomski, R., Plank, C., and Mykhaylyk, O. (2015) Nanomagnetic Activation as a Way to Control the Efficacy of Nucleic Acid Delivery. *Pharmaceutical research* **32**, 103-121
151. Jahnke, A., Hirschberger, J., Fischer, C., Brill, T., Kostlin, R., Plank, C., Kuchenhoff, H., Krieger, S., Kamenica, K., and Schillinger, U. (2007) Intra-tumoral gene delivery of feIL-2, feIFN-gamma and feGM-CSF using magnetofection as a neoadjuvant treatment option for feline fibrosarcomas: a phase-I study. *Journal of veterinary medicine. A, Physiology, pathology, clinical medicine* **54**, 599-606
152. Dames, P., Gleich, B., Flemmer, A., Hajek, K., Seidl, N., Wiekhorst, F., Eberbeck, D., Bittmann, I., Bergemann, C., Weyh, T., Trahms, L., Rosenecker, J., and Rudolph, C. (2007) Targeted delivery of magnetic aerosol droplets to the lung. *Nat Nanotechnol* **2**, 495-499
153. Xenariou, S., Griesenbach, U., Ferrari, S., Dean, P., Scheule, R., Cheng, S., Geddes, D., Plank, C., and Alton, E. (2006) Using magnetic forces to enhance non-viral gene transfer to airway epithelium in vivo. *Gene Ther* **13**, 1545-1552
154. Gersting, S., Schillinger, U., Lausier, J., Nicklaus, P., Rudolph, C., Plank, C., Reinhardt, D., and Rosenecker, J. (2004) Gene delivery to respiratory epithelial cells by magnetofection. *The journal of gene medicine* **6**, 913-922
155. Campbell, S., and Gromeier, M. (2005) Oncolytic viruses for cancer therapy I. Cell-external factors: virus entry and receptor interaction. *Onkologie* **28**, 144-149
156. Davis, J., and Fang, B. (2005) Oncolytic virotherapy for cancer treatment: challenges and solutions. *The journal of gene medicine* **7**, 1380-1389
157. Liu, T., Galanis, E., and Kirn, D. (2007) Clinical trial results with oncolytic virotherapy: a century of promise, a decade of progress. *Nature clinical practice. Oncology* **4**, 101-117
158. Schellingerhout, D., and Bogdanov, A. J. (2002) Viral imaging in gene therapy noninvasive demonstration of gene delivery and expression. *Neuroimaging Clin N Am* **12**, 571-581
159. Goodwin, T., and Huang, L. (2014) Nonviral vectors: we have come a long way. *Adv Genet* **88**, 1-12
160. Godbey, W., Wu, K., and Mikos, A. (1999) Poly(ethylenimine) and its role in gene delivery. *Journal of controlled release : official journal of the Controlled Release Society* **60**, 149-160
161. Demeneix, B., and Behr, J. (2005) Polyethylenimine (PEI). *Adv Genet* **53**, 217-230
162. Boussif, O., Lezoualc´h, F., Zanta, M., Mergny, M., Schwerman, D., Demeneix, B., and Behr, J. (1995) A versatile vector for gene and oligonucleotide transfer into cells in culture and in vivo: polyethylenimine. *PNAS* **92**, 7297-7301
163. Kelly, E., and Russell, S. (2007) History of Oncolytic Viruses: Genesis to Genetic Engineering. *Molecular therapy : the journal of the American Society of Gene Therapy* **15**, 651-659
164. Russell, S., Peng, K., and Bell, J. (2012) Oncolytic virotherapy. *Nature biotechnology* **30**, 658-670
165. Seymour, L., and Fisher, K. (2016) Oncolytic viruses:finally delivering. *Br J Cancer* **114**, 357-361
166. Li, D., Tang, X., Pulli, B., Lin, C., Zhao, P., Cheng, J., Lv, Z., Yuan, X., Luo, Q., Cai, H., and Ye, M. (2014) Theranostic nanoparticles based on bioreducible polyethylenimine-coated iron oxide for reduction-responsive gene delivery and magnetic resonance imaging. *International journal of nanomedicine* **9**, 3347-3361
167. Li, J., and Zhang, Y. (2012) *Messenger RNA Cap Methylation in Vesicular Stomatitis Virus, a Prototype of Non-Segmented Negative-Sense RNA Virus, Methylation - From DNA, RNA and Histones to Diseases and Treatment*
168. Martin, M., Knipe, D., Fields, B., Howley, P., Griffin, D., and Lamb, R. (2007) *Fields' virology*, Wolters Kluwer Health/Lippincott Williams & Wilkins, Philadelphia
169. Kirn, D., Martuza, R., and Zwiebel, J. (2001) Replication-selective virotherapy for cancer- Biological principles, risk management and future directions.
170. Shinozaki, K., Ebert, O., Kournioti, C., Tai, Y., and Woo, S. (2004) Oncolysis of multifocal hepatocellular carcinoma in the rat liver by hepatic artery infusion of vesicular stomatitis virus. *Molecular therapy : the journal of the American Society of Gene Therapy* **9**, 368-376
171. Altomonte, J., Braren, R., Schulz, S., Marozin, S., Rummeny, E., Schmid, R., and Ebert, O. (2008) Synergistic antitumor effects of transarterial viroembolization for multifocal hepatocellular carcinoma in rats. *Hepatology* **48**, 1864-1873
172. Zhang, W. (1999) Development and application of adenoviral vectors for gene therapy of cancer. *Cancer Gene Ther* **6**, 113-138
173. Davison, A., Benko, M., and Harrach, B. (2003) Genetic content and evolution of adenoviruses. *J Gen Virol* **84**, 2895-2908
174. Palmer, D., and Ng, P. (2003) Improved system for helper-dependent adenoviral vector production. *Molecular therapy : the journal of the American Society of Gene Therapy* **8**, 846-852
175. Sacha, J., Giraldo-Vela, J., Buechler, M., Martins, M., Maness, N., and Chung, C. (2009) Gag- and Nef-specific CD4+ T cells recognize and inhibit SIV replication in infected macrophages early after infection. *PNAS* **106**, 9791-9796
176. Russell, W. (2000) Update on adenovirus and its vectors. *J Gen Virol* **81**, 2573-2604

177. Khuri, F., Nemunaitis, J., Ganly, I., Arseneau, J., Tannock, I., Romel, L., Gore, M., Ironside, J., MacDougall, R., Heise, C., Randlev, B., Gillenwater, A., Bruso, P., Kaye, S., Hong, W., and Kirn, D. (2000) A controlled trial of intratumoral ONYX-015, a selectively-replicating adenovirus, in combination with cisplatin and 5-fluorouracil in patients with recurrent head and neck cancer. *Nat Med* **6**, 879–885
178. Garber, K. (2006) China approves world's first oncolytic virus therapy for cancer treatment. *JNCI* **98**, 298-300
179. medscape. Vol. 2014
180. Mykhaylyk, O., Zelphati, O., Hammerschmid, E., Anton, M., Rosenecker, J., and Plank, C. (2009) Recent advances in magnetofection and its potential to deliver siRNAs in vitro. *Methods Mol. Biol.* **487**, 111-146
181. Mykhaylyk, O., Zelphati, O., Rosenecker, J., and Plank, C. (2008) siRNA delivery by magnetofection. *Curr. Opin. Mol. Ther.* **10**, 493-505
182. Leung, K.-F., Wong, C.-H., Zhu, X.-M., Lee, S.-F., Sham, K., Lai, J., Chak, C.-P., Wang, Y.-X., and Cheng, C. (2013) Ternary hybrid nanocomposites for gene delivery and magnetic resonance imaging of hepatocellular carcinoma cells. *Quant Imaging Med Surg* **3**, 302-307
183. Xing, R., Liu, G., Hou, Y., and Chen, X. (2014) Functional magnetic nanoparticles for non-viral gene delivery and MR imaging. *Pharmaceutical research* **31**, 1377-1389
184. Dobson, J. (2006) Gene therapy progress and prospects: Magnetic nanoparticle-based gene delivery. *Gene Ther* **13**, 283-287
185. Felgner, P., Gadek, T., Holm, M., Roman, R., Chan, H., Wenz, M., Northrop, J., Ringold, G., and Danielsen, M. (1987) Lipofection: a highly efficient, lipid-mediated DNA-transfection procedure. *PNAS* **84**, 7413-7417
186. Xing, H.-B., Pan, H.-M., Fang, Y., X-Y, Z., Pan, Q., and Li, D. (2014) Construction of a tumor cell-targeting non-viral gene delivery vector with polyethylenimine modified with RGD sequence-containing peptide. *Oncology letters* **7**, 487-492
187. Kumar, C. (2003) Intergrin alpha v beta 3 as a therapeutic target for blocking tumor-induced angiogenesis. *Curr Drug Targets* **4**, 123-131
188. Krötz, F., deWit, C., Sohn, H., Zahler, S., Gloe, T., Pohl, U., and Plank, C. (2003) Magnetofection - A highly efficient tool for antisense oligonucleotide delivery in vitro and in vivo. *Molecular therapy : the journal of the American Society of Gene Therapy* **7**, 700-710
189. Plank, C., Anton, M., Rudolph, C., Rosenecker, J., and Krötz, F. (2003) Enhancing and targeting nucleic acid delivery by magnetic force. *Expert Opin Biol Ther* **3**, 745-758
190. Yuan, C., An, Y., Zhang, J., Li, H., Zhang, H., Wang, L., and Zhang, D. (2014) Magnetic nanoparticles for targeted therapeutic gene delivery and magnetic-inducing heating on hepatoma. *Nanotechnology* **25**, 345101-345113
191. Deng, L., Ke, X., He, Z., Yang, D., Gong, H., Zhang, Y., Jing, X., Yao, J., and Chen, J. (2012) A MSLN-targeted multifunctional nanoimmunoliposome for MRI and targeting therapy in pancreatic cancer. *International journal of nanomedicine* **7**, 5053-5065
192. Chen, Y., Chen, Y., Xiao, D., Bose, A., Deng, R., and Bothun, G. (2014) Low-dose chemotherapy of hepatocellular carcinoma through triggered-release from bilayer-decorated magnetoliposomes. *Colloids Surf B Biointerfaces* **116**, 452-458
193. Peng, Z., Wang, C., Fang, E., Lu, X., Wang, G., and Tong, Q. (2014) Co-delivery of doxorubicin and SATB1 shRNA by thermosensitive magnetic cationic liposomes for gastric cancer therapy. *PLoS One* **9**, e92924-92933
194. Ye, H., Tong, J., Liu, J., Lin, W., Zhang, C., Chen, K., Zhao, J., and Zhu, W. (2016) Combination of gemcitabine-containing magnetoliposome and oxaliplatin-containing magnetoliposome in breast cancer treatment: A possible mechanism with potential for clinical application. *Oncotarget* **7**, 43762-43778
195. Kono, K. (2001) Thermosensitive polymer-modified liposomes. *Advanced drug delivery reviews* **53**, 307-319
196. Mayer, L., Tai, L., Bally, M., Mitilenes, G., Ginsberg, R., and Cullis, P. (1990) Characterization of liposomal systems containing doxorubicin entrapped in response to pH gradients. *Biochim Biophys Acta* **1025**, 143-151
197. Koning, G., Eggermont, A., Lindner, L., and ten Hagen, T. (2010) Hyperthermia and thermosensitive liposomes for improved delivery of chemotherapeutic drugs to solid tumors. *Pharmaceutical research* **27**, 1750-1754
198. Tardi, P., Boman, N., and Cullis, P. (1996) Liposomal Doxorubicin. *J Drug Target* **4**, 129-140
199. Soenen, S., Hodenius, M., and De Cuyper, M. (2009) Magnetoliposomes: versatile innovative nanocolloids for use in biotechnology and biomedicine. *Nanomedicine* **4**, 177-191
200. Koning, G., Kamps, J., and Scherphof, G. (2002) Efficient intracellular delivery of 5-fluorodeoxyuridine into colon cancer cells by targeted immunoliposomes. *Cancer Detection Prevention* **26**, 299-307
201. Martina, M., Nicolas, V., Wilhelm, C., Menager, C., Barrat, G., and Lesieur, S. (2007) the in vitro kinetics of the interactions between PEGylated magnetic-fluid-loaded liposomes and macrophages. *Biomaterials* **28**, 4143-4153
202. Low, P., and Antony, A. (2004) Folate receptor-targeted drugs for cancer and inflammatory diseases *Advanced drug delivery reviews* **56**, 1055-1058
203. Gabizon, A., Horowitz, A., Goren, D., Tzemach, D., Shmeeda, H., and Zalipsky, S. (2003) In vivo fate of folate-targeted polyethylene-glycol liposomes in tumor-bearing mice. *Clin Cancer Res* **9**, 6551-6559
204. Wu, J., Liu, Q., and Lee, R. (2006) A folate receptor-targeted liposomal formulation for paclitaxel. *Int J Pharm* **316**, 148-153

205. Ross, J., Chaudhuri, P., and Ratnam, M. (1994) Differential regulation of folate receptor isoforms in normal and malignant tissues in vivo and in established cell lines. Physiologic and clinical implications. *Cancer* **73**, 2432-2443
206. Puri, A., Loomis, K., Smith, B., Lee, J.-H., Yavlovich, A., Heldman, E., and Blumenthal, R. (2009) Lipid-based nanoparticles as pharmaceutical drug carriers: from concept to clinic. *Crit Rev Ther Drug Carrier Syst* **26**, 523-580
207. Mulder, W., Strijkers, G., Habets, J., Bleeker, E., van der Schaft, D., Storm, G., Koning, G., Griffioen, A., and Nicolay, K. (2005) MR molecular imaging and fluorescence microscopy for identification of activated tumor endothelium using a bimodal lipidic nanoparticle. *FASEB J* **19**, 2008-2010
208. Nallamothu, R., Wood, G., Kiani, M., Moore, B., Horton, F., and Thoma, L. (2006) A targeted liposome delivery system for combretastatin A4: formulation optimization through drug loading and in vitro release studies. *J Pharm Sci Technol* **60**, 144-155
209. Trajkovic-Arsic, M., Mohajerani, P., Sarantopoulos, A., Kalideris, E., Steiger, K., Esposito, I., Ma, X., Themelis, G., Burton, N., Michalski, C., Kleeff, J., S, S., Beer, A., Pohle, K., Wester, H.-J., Schmid, R., Braren, R., Ntziachristos, V., and Siveke, J. (2014) Multimodal Molecular Imaging of Integrin avb3 for In Vivo Detection of Pancreatic Cancer. *J Nucl Med* **55**, 446-451
210. Zhang, C., Jugold, M., Woenne, E., Lammers, T., Morgenstern, B., Mueller, M., Zentgraf, H., Bock, M., Eisenhut, M., Semmler, W., and Kiessling, F. (2007) Specific targeting of tumor angiogenesis by RGD-conjugated ultrasmall superparamagnetic iron oxide particles using a clinical 1.5-T magnetic resonance scanner. *Cancer Res* **67**, 1555-1562
211. Kuhlpeter, R., Dahnke, H., Matuszewski, L., Persigehl, T., von Wallbrunn, A., Allkemper, T., Heindel, W., Schaeffter, T., and Bremer, C. (2007) R2 and R2* Mapping for Sensing Cell-bound Superparamagnetic Nanoparticles: In Vitro and Murine in Vivo Testing. *Radiology* **245**, 449-457
212. Babincova, M., and Babinec, P. (1995) Possibility of magnteic targeting of drugs using magnetoliposomes. *Pharmazie* **50**, 828-829
213. de Smet, M., Heijman, E., Langereis, S., Hijnen, N., and Grüll, H. (2011) Magnetic resonance imaging of high intensity focused ultrasound mediated drug delivery from temperature-sensitive liposomes: an in vivo proof-of-concept study. *Journal of controlled release : official journal of the Controlled Release Society* **150**, 102-110
214. Xiao, Y., Liu, Y., Yang, S., Zhang, B., Wang, T., Jiang, D., Zhang, J., Yu, D., and Zhang, N. (2016) Sorafenib and gadolinium co-loaded liposomes for drug delivery and MRI-guided HCC treatment. *Colloids Surf B Biointerfaces* **141**, 83-92
215. Gneveckow, U., Jordan, A., Scholz, R., Brüss, V., Waldöfner, N., Ricke, J., Feussner, A., Hildebrand, B., Rau, B., and Wust, P. (2004) Description and characterization of the novel hyperthermia- and thermoablation-system MFH 300F for clinical magnetic fluid hyperthermia. *Med Phys* **31**, 1444-1451
216. MagForce. NanoTherm. Vol. 2018
217. de Cuyper, M., and Joniau, M. (1988) Magnetoliposomes. Formation and structural characterization. *European biophysics journal : EBJ* **15**, 311-319
218. Storm, F. (1989) Clinical hyperthermia and chemotherapy. *Radiol Clin North Am* **27**, 621-627
219. Kong, G., Braun, R., and Dewhirst, M. (2001) Characterization of the effect of hyperthermia on nanoparticle extravasation from tumor vasculature. *Cancer Res* **61**, 3027-3032
220. Kong, G., Braun, R., and Dewhirst, M. (2000) Hyperthermia enables tumor-specific nanoparticle delivery: effect of particle size. *Cancer Res* **60**, 4440-4445
221. Landon, C., Park, J.-Y., Needham, D., and Dewhirst, M. (2011) Nanoscale Drug Delivery and Hyperthermia: The Materials Design and Preclinical and Clinical Testing of Low Temperature-Sensitive Liposomes Used in Combination with Mild Hyperthermia in the Treatment of Local Cancer. *Open Nanomed J* **3**, 38-64
222. Viroonchatapan, E., Sato, H., Ueno, M., Adachi, I., Murata, J., Saiki, I., Tazawa, K., and Horikoshi, I. (1998) Microdialysis assessment of 5-fluorouracil release from thermosensitive magnetoliposomes induced by an electromagnetic field in tumor-bearing mice. *J Drug Target* **5**, 379-390
223. Wang, L., Zhang, J., An, Y., Wang, Z., Liu, J., Li, Y., and Zhang, D. (2011) A study on the thermochemotherapy effect of nanosized As2O3/MZF thermosensitive magnetoliposomes on experimental hepatoma in vitro and in vivo. *Nanotechnology* **22**, 315102-315110
224. Yang, R., An, L., Mio, Q., Li, F., Han, Y., Wang, H., Liu, D., Chen , R., and Tang, S. (2016) Effective elimination of liver cancer stem-like cells by CD90 antibody targeted thermosensitive magnetoliposomes. *Oncotarget* **7**, 35894-35916
225. Tai, L.-A., Tsai, P.-J., Wang, Y.-C., Wang, Y.-J., Lo, L.-W., and Yang, C.-S. (2009) Thermosensitive liposomes entrapping iron oxide nanoparticles for controllable drug release. *Nanotechnology* **20**, 135101-135109
226. Dromi, S., Frenkel, V., Luk, A., Traughber, B., Angstadt, M., Bur, M., Poff, J., Xie, J., Libutti, S., Li, K., and Wood, B. (2007) Pulsed-high intensity focused ultrasound and low temperature-sensitive liposomes for enhanced targeted drug delivery and antitumor effect. *Clin Cancer Res* **13**, 2722-2727
227. Wu, N., Braun, R., Gaber, M., Lin, G., Ong, E., Shan, S., Papahadjopoulos, D., and Dewhirst, M. (1997) Simultaneous measurement of liposome extravasation and content release in tumors. *Microcirculation* **4**, 83-101
228. Kono, K., Ozawa, T., Yoshida, T., Ozaki, F., Ishizaka, Y., Maruyama, K., Kojima, C., Harada, A., and Aoshima, S. (2010) Highly temperature-sensitive liposomes based on a thermosensitive block copolymer for tumor-specific chemotherapy. *Biomaterials* **31**, 7096-7105

229. Kono, K., Nakashima, S., Kokuryo, D., Aoki, I., Shimomoto, H., Aoshima, S., Maruyama, K., Yuba, E., Kojima, C., Harada, A., and Ishizaka, Y. (2011) Multi-functional liposomes having temperature-triggered release and magnetic resonance imaging for tumor-specific chemotherapy. *Biomaterials* **32**, 1387-1395
230. Peller, M., Schwerdt, A., Hossann, M., Reinl, H., Wang, T., Sourbron, S., Ogris, M., and Lindner, L. (2008) MR Characterization of Mild Hyperthermia-Induced Gadodiamide Release From Thermosensitive Liposomes in Solid Tumors. *Invest Radiol* **43**, 877-892
231. Lorenzato, C., Oerlemans, C., van Elk, M., Geerts, W., de Senneville, B., Moonen, C., and Bos, C. (2016) MRI monitoring of nanocarrier accumulation and release using Gadolinium-SPIO co-labelled thermosensitive liposomes. *Contrast Media Mol Imaging* **11**, 184-194
232. Maruyama, K., and Iwatsuru, M. (1994) Doxorubicin Encapsulated in Long-Circulating Thermosensitive Liposomes. *Journal of liposome research* **4**, 513-527
233. ClinicalTrials.gov. (2010) Phase 3 study of ThermoDox with radiofrequency ablation (RFA) in treatment of hepatocellular carcinoma (HCC). http://www.clinicaltrials.gov/ct2/show/NCT00617981?term=NCT00617981&rank=1, updated 2010 Aug 10; cited 2010 Aug 30
234. Celsion Corporation, I. ThermoDox - release detail. Vol. 2017
235. ClinicalTrials.gov. NCT00617981. Vol. 2017
236. ClinicalTrials.gov. NCT02112656. Vol. 2017
237. ClinicalTrials.gov. (2009) A study of ThermoDoxTM in combination with radiofrequency ablation (RFA) in primary and metastatic tumors of the liver. http://www.clinicaltrials.gov/ct2/show/NCT00441376?term=thermodox+RFA+liver&rank=1, updated 2009 Dec 16; cited 2010 Aug 30
238. Celsion Corporation, I. (updated 2010 March 10), Celsion Corporation, Inc., Columbia
239. ClinicalTrials.gov. (2009) Phase 1/2 study of ThermoDox with approved hyperthermia in treatment of breast cancer recurrence at the chest wall (DIGNITY). http://www.clinicaltrials.gov/ct2/show/NCT00826085?term=thermodox+rcw&rank=1, updated 2010 May 24; cited 2010 Aug 30
240. ClinicalTrials.gov. NCT00826085. Vol. 2017
241. Celsion Corporation, I. ThermoDox. Vol. 2017
242. Kowalski, J. B., and Tallentire, A. (1999) Substantiation of 25 kGy as a sterilization dose: a rational approach to establishing verification dose. . *Radiat Phys Chem* **54**, 55-64
243. Mykhaylyk, O., Sanchez-Antequera, Y., Vlaskou, D., Hammerschmid, E., Anton, M., Zelphati, O., and Plank, C. (2010) Liposomal magnetofection. *Methods Mol Biol* **605**, 487-525
244. Holm, P. S., Lage, H., Bergmann, S., Jurchott, K., Glockzin, G., Bernshausen, A., Mantwill, K., Ladhoff, A., Wichert, A., Mymryk, J. S., Ritter, T., Dietel, M., Gansbacher, B., and Royer, H. D. (2004) Multidrug-resistant cancer cells facilitate E1-independent adenoviral replication: impact for cancer gene therapy. *Cancer Res* **64**, 322-328
245. Duffy, A., O'Doherty, A., O'Brien, T., and Strappe, P. (2005) Purification of adenovirus and adeno-associated virus: comparison of novel membrane-based technology to conventional techniques. *Gene Ther* **12**, S62-S72
246. Mittereder, N., March, K., and Trapnell, B. (1996) Evaluation of the Concentration and Bioactivity of Adenovirus Vectors for Gene Therapy. *Journal of virology* **70**, 7498-7509
247. Mittereder, N., March, K. L., and Trapnell, B. C. (1996) Evaluation of the concentration and bioactivity of adenovirus vectors for gene therapy. *J Virol* **70**, 7498-7509
248. Hierholzer, and Killington. (1996) Virology Methods Manual. p. 374
249. Torrance, J. D., and Bothwell, T. H. (1981) Tissue iron stores. In *Methods in hematology: iron* (JD, C., ed) pp. 90-115, Churchill Livingstone, New York
250. Dalton, A. (1973) A chrome-osmium fixative for electron microscopy. *Anat. Rec*
251. Berridge, M., Herst, P., and Tan, A. (2005) Tetrazolium dyes as tools in cell biology: new insights into their cellular reduction. *Biotechnol Annu Rev* **11**, 127-152
252. Mueller, H., Kassack, M., and Wiese, M. (2004) Comparison of the usefulness of the MTT, ATP, and calcein assays to predict the potency of cytotoxic agents in various human cancer cell lines. *J Biomol Screen* **9**, 506-515
253. Kato, H., Kuroda, M., Yoshimura, K., Yoshida, A., Hanamoto, K., Kawasaki, S., Shibuya, K., and Kanazawa, S. (2005) Composition of MRI phantom equivalent to human tissues. *Med Phys* **32**, 3199-3208
254. Dahnke, H., and Schaeffter, T. (2005) Limits of detection of SPIO at 3.0 T using T2 relaxometry. *Magn Reson Med* **53**, 1202-1206
255. ATCC. http://www.lgcstandards-atcc.org.
256. hepgs.com. http://www.hepg2.com.
257. huh7.com. http://www.huh7.com.
258. Holm, P., Scanlon, K., and Dietel, M. (1994) Reversion of multidrug resistance in the P-glycoprotein-positive human pancreatic cell line (EPP85-181RDB) by introduction of a hammerhead ribozyme *Br J Cancer* **70**, 239-243
259. van Til, N., Stok, M., Aerts Kaya, F., de Waard, M., Farahbakhshian, E., Visser, T., Kroos, M., Jacobs, E., Willart, M., van der Wegen, P., Scholte, B., Lambrecht, B., Duncker, D., van der Ploeg, A., Reuser, A., Verstegen, M., and Wagemaker, G. (2010) Lentiviral gene therapy of murine hematopoietic stem cells ameliorates the Pompe disease phenotype. *Blood* **115**, 5329-5337
260. Wübbenhorst, D., Dumler, K., Wagner, B., Wexel, G., Imhoff, A., Gänsbacher, B., Vogt, S., and Anton, M. (2010) Tetracycline-Regulated Bone Morphogenetic Protein 2 Gene Expression in Lentivirally Transduced Primary Rabbit Chondrocytes for Treatment of Cartilage Defects. *Arthritis & Rheumatism* **62**, 2037-2046

261. Mykhaylyk, O., Antequera, Y. S., Vlaskou, D., and Plank, C. (2007) Generation of magnetic nonviral gene transfer agents and magnetofection in vitro. *Nat Protoc* **2**, 2391-2411
262. Berridge, M. V., Herst, P. M., and Tan, A. S. (2005) Tetrazolium dyes as tools in cell biology: new insights into their cellular reduction. *Biotechnol Annu Rev* **11**, 127-152
263. Mueller, H., Kassack, M. U., and Wiese, M. (2004) Comparison of the usefulness of the MTT, ATP, and calcein assays to predict the potency of cytotoxic agents in various human cancer cell lines. *Journal of Biomolecular Screening* **9**, 506-515
264. GV-Solas. (2010) Empfehlungen zum Transport transgener Mäuse und Ratten. http://www.gv-solas.de
265. GV-Solas. (2010) Empfehlung Schmerztherapie bei Versuchstieren. http://www.gv-solas.de
266. GV-Solas. (2010) Empfehlung zur Substanzapplikation bei Versuchstieren. http://www.gv-solas.de
267. Mykhaylyk, O., Vlaskou, D., Tresilwised, N., Pithayanukul, P., Moller, W., and Plank, C. (2007) Magnetic nanoparticle formulations for DNA and siRNA delivery. *Journal of Magnetism and Magnetic Materials* **311**, 275-281
268. Mykhaylyk, O., Sobisch, T., Almstatter, I., Sanchez-Antequera, Y., Brandt, S., Anton, M., Doblinger, M., Eberbeck, D., Settles, M., Braren, R., Lerche, D., and Plank, C. (2012) Silica-Iron Oxide Magnetic Nanoparticles Modified for Gene Delivery: A Search for Optimum and Quantitative Criteria. *Pharm Res*
269. Shapiro, M., Atanasijevic, T., Faas, H., Westmeyer, G., and Jasanoff, A. (2006) Dynamic imaging with MRI contrast agents: quantitative considerations. *Magn Reson Imaging* **24**, 449-462
270. Anton, M., Wolf, A., Mykhaylyk, O., Koch, C., Gansbacher, B., and Plank, C. (2012) Optimizing adenoviral transduction of endothelial cells under flow conditions. *Pharmaceutical research* **29**, 1219-1231
271. Majetich, S., Wen, T., and Booth, R. (2011) Functional magnetic nanoparticle assemblies: formation, collective behavior, and future directions. *ACS Nano* **5**, 6081-6084
272. Pradhan, P., Banerjee, R., Bahadur, D., Koch, C., Mykhaylyk, O., and Plank, C. (2017) Targeted Magnetic Liposomes Loaded with Doxorubicin. *Methods Mol Biol* **1522**, 257-272
273. Pandori, M., Hobson, D., and Sano, T. (2002) Adenovirus–microbead conjugates possess enhanced infectivity: A new strategy for localized gene delivery. *Virology* **299**, 204-212
274. Nayerossadat, N., Maedeh, T., and Ali, P. (2012) Viral and nonviral delivery systems for gene delivery. *Adv Biomed Res* **1**, 1-11
275. Varma, N., Barton, K., Janic, B., Shankar, A., Iskander, A., Ali, M., and Arbab, A. (2013) Monitoring adenoviral based gene delivery in rat glioma by molecular imaging. *World J Clin Oncol* **4**, 91-101
276. Choi, J.-W., Park, J., Na, Y., Jung, S.-J., Hwang, J., Choi, D., Lee, K., and Yun, C. (2015) Using a magnetic field to redirect an oncolytic adenovirus complexed with iron oxide augments gene therapy efficacy. *Biomaterials* **65**, 163-174
277. Pereyra, A., Mykhaylyk, O., Lockhart, E., Taylor, J., Delbono, O., Goya, R., Plank, C., and Herenu, C. (2016) Magnetofection Enhances Adenoviral Vector-based Gene Delivery in Skeletal Muscle Cells. *J Nanomed Nanotechnol* **7**, 364
278. Heun, Y., Hildebrand, S., Heidsieck, A., Gleich, B., Anton, M., Pircher, J., Ribeiro, A., Mykhaylyk, O., Eberbeck, D., Wenzel, D., Pfeifer, A., Woernle, M., Krötz, F., Pohl, U., and Mannell, H. (2017) Targeting of Magnetic Nanoparticle-coated Microbubbles to the Vascular Wall Empowers Site-specific Lentiviral Gene Delivery in vivo. *Theranostics* **7**, 295-307
279. Wickham, T., Mathias, P., Cheresh, D., and Nemerow, G. (1993) Integrins alpha v beta 3 and alpha v beta 5 promote adenovirus internalization but not virus attachment. *Cell* **73**, 309-319
280. Desgrosellier, J., and Cheresh, D. (2010) Integrins in cancer: biological implications and therapeutic opportunities. *Nature reviews. Cancer* **10**, 9-22
281. Beer, A., and Schwaiger, M. (2008) Imaging of integrin alphavbeta3 expression. *Cancer Metastasis Rev* **27**, 631-644
282. Desgrosellier, J., Barnes, L., Shields, D., Huang, M., Lau, S., Prevost, N., Tarin, D., Shattil, S., and Cheresh, D. (2009) An integrin alpha(v)beta(3)-c-Src oncogenic unit promotes anchorage-independence and tumor progression. *Nat Med* **15**, 1163-1169
283. Hosotani, R., Kawaguchi, M., Masui, T., Koshiba, T., Ida, J., Fujimoto, K., Wada, M., Di, R., and Imamura, M. (2002) Expression of integrin alphaVbeta3 in pancreatic carcinoma: relation to MMP-2 activation and lymph node metastasis. *Pancreas* **25**, e30-e35
284. Oh, N., and Park, J. (2014) Endocytosis and exocytosis of nanoparticles in mammalian cells. *International journal of nanomedicine* **9(Suppl 1)**, 51-63
285. Klug, G., Kampf, T., Bloemer, S., Bremicker, J., Ziener, C., Heymer, A., Gbureck, U., Rommel, E., Noth, U., Schenk, W., Jakob, P., and Bauer, W. (2010) Intracellular and extracellular T1 and T2 relaxivities of magneto-optical nanoparticles at experimental high fields. *Magn Reson Med* **64**, 1607-1615
286. Rogers, W., Meyer, C., and Kramer, C. (2006) Technology insight: in vivo cell tracking by use of MRI. *Nature clinical practice. Cardiovascular medicine* **3**, 554-562
287. Billotey, C., Wilhelm, C., Devaud, M., Bacri, J., Bittoun, J., and Gazeau, F. (2003) Cell internalization of anionic maghemite nanoparticles: quantitative effect on magnetic resonance imaging. *Magn Reson Med* **49**, 646-654
288. Li W, I. T., Okada Y, Oku, N, Kiwada H. (2005) Increased gene expression by cationic liposomes (TFL-3) in lung metastases following intravenous injection. *Biol Pharm Bull* **28**, 701-706
289. Ross, P., and Hui, S. (1999) Lipoplex size is a major determinant of in vitro lipofection efficiency. *Gene Ther* **6**, 651–659

290. Ogris, M., Steinlein, P., Kursa, M., Mechtler, K., Kircheis, R., and Wagner, E. (1998) The size of DNA/transferrin-PEI complexes is an important factor for gene expression in cultured cells. *Gene Ther* **5**, 1425-1433
291. Schulze, E., Ferrucci, J., Poss, K., LaPointe, L., Bogdanova, A., and Weissleder, R. (1995) Cellular uptake and trafficking of a prototypical magnetic iron oxide label in vitro. *Invest Radiol.* **30**, 604-610
292. Weissleder, R., Cheng, H.-C., Bogdanova, A., and Bogdanov, J. A. (1997) Magnetically labeled cells can be detected by MR imaging. *J Magn Reson Imaging.* **7**, 258-263
293. Sun, R., Dittrich, J., Le-Huu, M., Mueller, M., Bedke, J., Kartenbeck, J., Lehmann, W., Krueger, R., Bock, M., Huss, R., Seliger, C., Gröne, H., Misselwitz, B., Semmler, W., and Kiessling, F. (2005) Physical and biological characterization of superparamagnetic iron oxide- and ultrasmall superparamagnetic iron oxide-labeled cells: a comparison. *Invest Radiol.* **40**, 504-513
294. Weissleder, R., Bogdanov, A., and Papisov, M. (1992) Drug targeting in magnetic resonance imaging. *Magn Reson Q* **8**, 55-63
295. Schaffer, B. K., Linker, C., Papisov, M., Tsai, E., Nossiff, N., Shibata, T., Bogdanov, J. A., Brady, T. J., and Weissleder, R. (1993) MION-ASF: biokinetics of an MR receptor agent. *Magn Reson Imaging* **11**, 411- 417.
296. Shen, T. T., Bogdanov, J. A., Bogdanova, A., Poss, K., Brady, T. J., and Weissleder, R. (1996) Magnetically labeled secretin retains receptor affinity to pancreas acinar cells. *Bioconjug Chem.* **7**, 311-316
297. Wilhelm, C., Gazeau, F., and Bacri, J. (2002) Magnetophoresis and ferromagnetic resonance of magnetically labeled cells. *European biophysics journal : EBJ* **31**, 118-125
298. Orlando, C., Castellani, S., Mykhaylyk, O., Copreni, E., Zelphati, O., Plank, C., and Conese, M. (2010) Magnetically guided lentiviral-mediated transduction of airway epithelial cells. *The journal of gene medicine* **12**, 747-754
299. Hardy, P., and Henkelmann, R. (1989) Transverse relaxation rate enhancement caused by magnetic particulates. *Magn Reson Imaging* **7**, 265-275
300. Tanimoto Akihiro, M., Oshio Koichi, M., PhD, Suematsu Makoto, M., Pouliquen Daniel, P., and Stark David D., M. (2001) Relaxation effect of clustered particles. *J Magn Reson Imaging.* **14**, 72-77
301. Majumdar, S., Zoghbi, S., and Gore, J. (1989) The influence of pulse sequence on the relaxation effects of superparamagnetic iron oxide contrast agents. *Magn Reson Med.* **10**, 289-301
302. Perez, J. M., Simeone, F. J., Saeki, Y., Josephson, L., and Weissleder, R. (2003) Viral-induced self-assembly of magnetic nanoparticles allows the detection of viral particles in biological media. *J Am Chem Soc.* **125**, 10192-10193
303. Perez, J., Josephson, L., O'Loughlin, T., Högemann, D., and Weissleder, R. (2002) Magnetic relaxation switches capable of sensing molecular interactions. *Nature biotechnology* **20**, 816-820
304. Bowen, C., Zhang, X., Saab, G., Gareau, P., and Rutt, B. (2002) Application of the static dephasing regime theory to superparamagnetic iron-oxide loaded cells. *Magn Reson Med* **48**, 52-61
305. Simon, G., Bauer, J., Saborovski, O., Fu, Y., Corot, C., Wendland, M., and Daldrup-Link, H. (2006) T1 and T2 relaxivity of intracellular and extracellular USPIO at 1.5T and 3T clinical MR scanning. *European radiology* **16**, 738-745
306. Koenig, S. (1998) Solvent relaxation by uniformly magnetized solute spheres. The classical-quantal connection. *Invest Radiol.* **33**, 822-827
307. Yablonskiy, D., and Haacke, E. (1994) Theory of NMR Signal Behavior in Magnetically Inhomogeneous Tissues: The Static Dephasing Regime. *Magn Reson Med* **32**, 749 –763
308. Pouponneau, P., Soulez, G., Beaudoin, G., Leroux, J.-C., and Martel, S. (2014) MR Imaging of Therapeutic Magnetic Microcarriers Guided by Magnetic Resonance Navigation for Targeted Liver Chemoembolization. *Cardiovasc Intervent Radiol* **37**, 784-790
309. Verdijk, P., Scheenen, T., Lesterhuis, W., Gambarota, G., Veltien, A., Walczak, P., Scharenborg, N., Bulte, J., Punt, C., Heerschap, A., Figdor, C., and de Vries, I. (2007) Sensitivity of magnetic resonance imaging of dendritic cells for in vivo tracking of cellular cancer vaccines. *International journal of cancer. Journal international du cancer* **120**, 978-984
310. Krieg, F. M., Andres, R. Y., and Winterhalter, K. H. (1995) Superparamagnetically labelled neutrophils as potential abscess-specific contrast agent for MRI. *Magnetic Resonance Imaging* **13**, 393–400
311. Bottomley, P., Foster, T., Argersinger, R., and Pfeifer, L. (1984) A review of normal tissue hydrogen NMR relaxation times and relaxation mechanisms from 1–100 MHz: dependence on tissue type, NMR frequency, temperature, species, excision, and age. *Med Phys* **11**, 1184-1197
312. de Bazelaire, C., Duhamel, G., Rofsky, N., and Alsop, D. (2004) MR Imaging Relaxation Times of Abdominal and Pelvic Tissues Measured in Vivo at 3.0 T: Preliminary Results. *Radiology* **230**, 652-659
313. Luciani, A., Vignaud, A., Cavet, M., Nhieu, J., Mallat, A., Ruel, L., Laurent, A., Deux, J., Brugieres, P., and Rahmouni, A. (2008) Liver cirrhosis: intravoxel incoherent motion MR imaging-pilot study. *Radiology* **249**, 891-899
314. Benninghoff, A., and Drenckhahn, D. (2004) *Makroskopische Anatomie, Embryologie und Histologie des Menschen* Vol. 16, Elsevier, München
315. Mykhaylyk, O., Sanchez-Antequera, Y., Tresilwised, N., Döblinger, M., Thalhammer, S., Holm, P., and Plank, C. (2010) Engineering magnetic nanoparticles and formulations for gene delivery. *Journal of controlled release : official journal of the Controlled Release Society* **148**, e63-64
316. Huth, S., Lausier, J., Gersting, S., Rudolph, C., Plank, C., Welsch, U., and Rosenecker, J. (2004) Insights into the mechanism of magnetofection using PEI-based magnetofectins for gene transfer. *The journal of gene medicine* **6**, 923-936

317. Zhao, X., Cui, H., Chen, W., Wang, Y., Cui, B., Sun, C., Meng, Z., and Liu, G. (2014) Morphology, structure and function characterization of PEI modified magnetic nanoparticles gene delivery system. *PLoS One* **9**, e98919
318. Lin, H., Sun, L., Han, W., He, T., Xu, X., Cheng, K., Geng, C., Su, L., Wen, H., Wang, X., and Chen, Q. (2014) Knockdown of OCT4 suppresses the growth and invasion of pancreatic cancer cells through inhibition of the AKT pathway. *Mol Med Rep* **10**, 1335-1342
319. Nio, K., Yamashita, T., and Kaneko, S. (2017) The evolving concept of liver cancer stem cells. *Mol Cancer* **16**, 4
320. Wang, Y., Cai, N., Wu, X., Cao, H., Xie, L., and Zheng, P. (2013) OCT4 promotes tumorigenesis and inhibits apoptosis of cervical cancer cells by miR-125b/BAK1 pathway. *Cell Death Dis* **4**, e760
321. Wu, G. (2015) Oct4 Is a Reliable Marker of Liver Tumor Propagating Cells in Hepatocellular Carcinoma. *Discov Med* **20**, 219-229
322. Iki, K., and Pour, P. (2006) Expression of Oct4, a Stem Cell Marker, in the Hamster Pancreatic Cancer Model. *Pancreatology* **6**, 406-413
323. Kuo, K., Lee, K., Chen, K., Yang, Y., Lin, Y., Tasi, M., Wuputra, K., Lee, Y., Ku, C., Miyoshi, H., Nakamura, Y., Saito, S., Wu, C., Chai, C., Eckner, R., Lin, S., Wang, S., Wu, D., Lin, C., and Yokoyama, K. (2016) Positive Feedback Loop of OCT4 and c-JUN Expedites Cancer Stemness in Liver Cancer. *Stem Cells* **34**, 2613-2624
324. Kuijten, M., Degeling, M., Chen, J., Wiojtkiewicz, G., Waterman, P., Weissleder, R., Azzi, J., Nicolay, K., and Tannous, B. (2015) Multimodal targeted high relaxivity thermosensitive liposome for in vivo imaging. *Nature* **5**, 17220
325. Kono, K., and Takagishi, T. (2004) Temperature-Sensitive Liposomes. *Methods Enzymol* **387**, 73-82
326. Viroonchatapan, E., Sato, H., Ueno, M., Adachi, I., Tazawa, K., and Horikoshi, I. (1996) Magnetic targeting of thermosensitive magnetoliposomes to mouse livers in an in situ on-line perfusion system. *Life Sci* **58**, 2251-2261
327. Kono, K., Murakami, T., Yoshida, T., Habe, Y., Kanaoka, S., Takagishi, T., and Aoshima, S. (2005) Temperature sensitization of liposomes by use of thermosensitive block copolymers synthesized by living cationic polymerization: effect of copolymer chain length. *Bioconjug Chem* **16**, 1367-1374
328. Yang, L., Peng, X.-H., Wang, Y., Wang, X., Cao, Z., Ni, C., Karna, P., Zhang, X., Wood, W., Gao, X., Nie, S., and Mao, H. (2009) Receptor-Targeted Nanoparticles for In Vivo Imaging of Breast Cancer. *Clin Cancer Res* **15**, 4722-4732
329. Murray, A., and Luz, A. (1990) Acidophilic macrophage pneumonia in laboratory mice. *Vet Pathol* **27**, 274-281
330. Shultz, L., Coman, D., Bailey, C., Beamer, W., and Sidman, C. (1984) "Viable motheaten", a new allele at the motheaten locus. *Am J Pathol* **116**, 179-192
331. Jain, S., Mishra, V., Singh, P., Dubey, P., Saraf, D., and Vyas, S. (2003) RGD-anchored magnetic liposomes for monocytes/neutrophils-mediated brain targeting. *Int J Pharm* **261**, 43-55
332. Li, W., Su, B., Meng, S., Ju, L., Yan, L., Ding, Y., Song, Y., Zhou, W., Li, H., Tang, L., Zhao, Y., and Zhou, C. (2011) RGD-targeted paramagnetic liposomes for early detection of tumor: in vitro and in vivo studies. *Eur J Radiol* **80**, 598-606
333. Zhao, H., Wang, J., Sun, Q.-S., Luo, C.-L., and Zhang, Q. (2009) RGD-based strategies for improving antitumor activity of paclitaxel-loaded liposomes in nude mice xenografted with human ovarian cancer. *J Drug Target* **17**, 10-18
334. Caldorera-Moore, M., Liechty, W., and Peppas, N. (2011) Responsive Theranostic Systems: Integration of Diagnostic Imaging Agents and Responsive Controlled Release Drug Delivery Carriers. *Acc Chem Res* **44**, 1061-1070
335. Plank, C., Tang, M., Wolfe, A., and Szoka, F. (1999) Branched cationic peptides for gene delivery: Role of type and number of cationic residues in formation and in vitro activity of DNA polyplexes. *Hum Gene Ther* **10**, 319-332
336. Cosco, D., Bulotta, A., Ventura, M., Celia, C., Calimeri, T., Perri, G., Paolino, D., Costa, N., Neri, P., Tagliaferri, P., Tassone, P., and Fresta, M. (2009) In vivo activity of gemcitabine-loaded PEGylated small unilamellar liposomes against pancreatic cancer. *Cancer Chemother Pharmacol* **64**, 1009-1020
337. Moog, R., Burger, A., Brandl, M., Schüler, J., Schubert, R., Unger, C., Fiebig, H., and Massing, U. (2002) Change in pharmacokinetic and pharmacodynamic behavior of gemcitabine in human tumor xenografts upon entrapment in vesicular phospholipid gels. *Cancer Chemother Pharmacol* **49**, 356-366
338. Strijkers, G., Mulder, W., van Heeswijk, R., Frederik, P., Bomans, P., Magusin, P., and Nicolay, K. (2005) Relaxivity of liposomal paramagnetic MRI contrast agents. *MAGMA* **18**, 186-192
339. Ta, T., Convertine, A., Reyes, C., Stayton, P., and Porter, T. (2010) Thermosensitive liposomes modified with poly(N-isopropylacrylamide-co-propylacrylic acid) copolymers for triggered release of doxorubicin. *Biomacromolecules* **11**, 1915-1929
340. Garcia-Jimeno, S., Escribano, E., Queralt, J., and Estelrich, J. (2011) Magnetoliposomes prepared by reverse-phase followed by sequential extrusion- characterization and possibilities in the treatment of inflammation. *Int J Pharm* **405**, 181-187
341. Bornmann, C., Graeser, R., Esser, N., Ziroli, V., Jantscheff, P., Keck, T., Unger, C., Hopt, U., Adam, U., Massing, U., and von Dobschuetz, E. (2008) A new liposomal formulation of Gemcitabine is active in an orthotopic mouse model of pancreatic cancer accessible to bioluminescence imaging. *Cancer Chemother Pharmacol* **61**, 395-405

342. Vlaskou, D., Mykhaylyk, O., Krötz, F., Hellwig, N., Renner, R., Schillinger, U., Gleich, B., Heidsieck, A., Schmitz, G., Hensel, K., and Plank, C. (2010) Magnetic and Acoustically Active Lipospheres for Magnetically Targeted Nucleic Acid Delivery. *Adv Funct Mater* **20**, 3881-3894
343. Soenen, S., Brisson, A., Jonckheere, E., Nuytten, N., Tan, S., Himmelreich, U., and De Cuyper, M. (2011) The labeling of cationic iron oxide nanoparticle-resistant hepatocellular carcinoma cells using targeted magnetoliposomes. *Biomaterials* **32**, 1748-1758
344. Yang, Y., Xie, X., Xu, X., Xia, X., Wang, H., Li, L., Dong, W., Ma, P., Yang, Y., Liu, Y., and Mei, X. (2016) Thermal and magnetic dual-responsive liposomes with a cell-penetrating peptide-siRNA conjugate for enhanced and targeted cancer therapy. *Colloids Surf B Biointerfaces* **146**, 607-615
345. Martinez-Gonzalez, R., Estelrich, J., and Busquets, M. (2016) Liposomes Loaded with Hydrophobic Iron Oxide Nanoparticles- Suitable T_2 Contrast Agents for MRI. *Int J Mol Sci* **17**, 1209-1222
346. Kenworthy, A., Hristova, K., Needham, D., and McIntosh, T. (1995) Range and magnitude of the steric pressure between bilayers containing phospholipids with covalently attached poly(ethylene glycol). *Biophys J* **68**
347. Mouritsen, O., and Jorgensen, K. (1994) Dynamical order and disorder in lipid bilayers. *Chem Phys Lipids* **73**, 3-25
348. Casneuf, V., van Damme, N., Demetter, P., Robert, P., Corot, C., Duyck, P., Ceelen, W., Boterberg, T., and Peeters, M. (2011) Noninvasive Monitoring of Therapy-Induced Microvascular Changes in a Pancreatic Cancer Model Using Dynamic Contrast-Enhanced Magnetic Resonance Imaging with P846, a New Low-Diffusible Gadolinium-Based Contrast Agent. *Radiation Res* **175**, 10-20
349. Kong, G., Anyarambhatla, G., Petros, W., Braun, R., Colvin, O., Needham, D., and Dewhirst, M. (2000) Efficacy of liposomes and hyperthermia in a human tumor xenograft model: importance of triggered drug release. *Cancer Res* **60**, 6950-6957
350. Hossann, M., Wang, T., Wiggenhorn, M., Schmidt, R., Zengerle, A., Winter, G., Eibl, H., Peller, M., Reiser, M., Issels, R., and Lindner, L. (2010) Size of thermosensitive liposomes influences content release. *Journal of controlled release : official journal of the Controlled Release Society* **147**, 436-443
351. Löhr, J., Haas, S., Bechstein, W.-O., Bodoky, G., Cwiertka, K., Fischbach, W., Fölsch, U., Jäger, D., Osinsky, D., Prausova, J., Schmidt, W., and Lutz, M. (2012) Cationic liposomal paclitaxel plus gemcitabine or gemcitabine alone in patients with advanced pancreatic cancer: a randomized controlled phase II trial. *Ann Oncol* **23**, 1214-1222
352. Brusa, P., Immordino, M., Rocco, F., and Cattel, L. (2007) Antitumor activity and pharmacokinetics of liposomes containing lipophilic gemcitabine prodrugs. *Anticancer Res* **27**, 195-200
353. Immordino, M., Brusa, P., Rocco, F., Arpicco, S., Ceruti, M., and Cattel, L. (2004) Preparation, characterization, cytotoxicity and pharmacokinetics of liposomes containing lipophilic gemcitabine prodrugs. *Journal of controlled release : official journal of the Controlled Release Society* **100**, 331-346
354. Kan, P., Tsao, C.-W., Wang, A.-J., Su, W.-C., and Liang, H.-F. (2011) A liposomal formulation able to incorporate a high content of Paclitaxel and exert promising anticancer effect. *J Drug Deliv*
355. Sharma, A., and Straubinger, R. (1994) Novel taxol formulations: preparation and characterization of taxol-containing liposomes. *Pharmaceutical research* **11**, 889-896
356. Meng, S., Su, B., Li, W., Ding, Y., Tang, L., Zhou, W., Song, Y., Li, H., and Zhou, C. (2010) Enhanced antitumor effect of novel dual-targeted paclitaxel liposomes. *Nanotechnology* **21**, 415103-415109
357. Stevens, P., Sekido, M., and Lee, R. (2004) A folate receptor-targeted lipid nanoparticle formulation for a lipophilic paclitaxel prodrug. *Pharmaceutical research* **21**, 2153-2157
358. Crossasso, P., Ceruti, M., Brusa, P., Arpicco, S., Dosio, F., and Cattel, L. (2000) Preparation, characterization and properties of sterically stabilized paclitaxel-containing liposomes. *Journal of controlled release : official journal of the Controlled Release Society* **63**, 19-30
359. Sharma, A., Sharma, U., and Straubinger, R. (1996) Paclitaxel-liposomes for intracavitary therapy of intraperitoneal P388 leukemia. *Cancer Letters* **107**, 265-272
360. Zhao, L., Ye, Y., Li, J., and Wei, Y.-M. (2011) Preparation and the in-vivo evaluation of paclitaxel liposomes for lung targeting delivery in dogs. *J Pharm Pharm* **63**, 80-86
361. Cavalcanti, L., Konovalov, O., and Haas, H. (2007) X-ray diffraction from paclitaxel-loaded zwitterionic and cationic model membranes. *Chem Phys Lipids* **150**, 58-65
362. Patel, N., Rathi, A., Mongayt, D., and Torchilin, V. (2011) Reversal of multidrug resistance by co-delivery of tariquidar (XR9576) and paclitaxel using long-circulating liposomes. *Int J Pharm* **416**, 296-299
363. Zhang, J., Zhang, Z., Yang, H., Tan, Q., Qin, S., and Qiu, X. (2005) Lyophilized paclitaxel magnetoliposomes as a potential drug delivery system for breast carcinoma via parenteral administration: in vitro and in vivo studies. *Pharmaceutical research* **22**, 573-583

ACKNOWLEDGEMENTS

First of all I would like to thank Professor Ernst Wagner for the inter-university supervision of this thesis, and Professor Christian Plank and PD Dr med Rickmer Braren, for giving me the opportunity to carry our my PhD thesis in their labs, for their support and help, their time and the fruitful discussions.

Very special thanks go to Dr Olga Mykhaylyk for her outstanding support and help in all regards, and the intensive supervision with countless hours of encouraging discussions and helping with experiments and manuscripts, and the marvellous times we had on conference trips. Olga, this work would not have been possible without you!

I also would like to thank my colleagues Dr Dialechti Vlaskou, Dr Christian Koch, PD Dr Martina Anton, Dr Vroni Girbinger, Dr Mehrije Ferizi, Dr Kerstin Lohr, Sava Michailidou, Hilde Kalvelage, and all other colleagues at the Institute of Experimental Oncology and Therapy Research at the Klinikum rechts der Isar for their technical help and support and the joy I had during the time I spend at the IEOT.

Furthermore I thank my colleagues and office mates Dr Yvonne Kosanke, Dr Katja Kosanke, Dr Claudia Groß, Dr Marcus Settles, Dr Sufyan Sayyed, Dr Irina Heid, Dr Johanna Bussemer, Juliane Aichler, Florian Wille, Christoph Wörner, Barbara Cervantes, Stefan Ruschke, Michael Dieckmeyer, Anne Kluge, and Iryna Skuratovska at the Institute for diagnostic and interventional Radiology, Klinikum rechts der Isar for their help and encouragement, the chats and fun we had, and for always being there to cheer me up.

For their support and help with the experiments I performed in their labs and the discussions and warm atmosphere I thank Dr Jennifer Altomonte, Professor Oliver Ebert, MD, Dr Kim Munoz Álvarez and Dr Arturo Lopez Martinez, and Dr Marija Traikovic-Arsic, Professor Jens Siveke, MD, and Dr Nicole Teichmann at the II. Med Clinic, Klinikum rechts der Isar.

In addition, special thanks go to the whole NIM office team Dr Peter Sonntag, Dr Birgit Ziller, Silke Mayerl-Kink, Criss Hohmann and Barbara Pinto for their priceless support and help in all regards during my PhD, and my fellow NIM-GP students – I enjoyed every minute during our conferences, meetings, excursions, …
Special thanks also go to Marilena Pinto for taking care of little Benjamin!

Most of all, I thank my wonderful family Martin, Benjamin and Valentin, my parents and in-laws, and my sister for their unconditional love, support, encouragement, listening and patience!
Without you, I would not be the person I am now – Ich liebe Euch über Alles!

SCIENTIFIC COMMUNICATIONS

Peer reviewed publications

Characterization Of Magnetic Viral Complexes For Targeted Delivery In Oncology
Isabella Almstätter, Olga Mykhaylyk, Marcus Settles, Jennifer Altomonte, Michaela Aichler, Axel Walch, Ernst J. Rummeny, Oliver Ebert, Christian Plank, Rickmer Braren, *Theranostics*, 2015, 5 (7), pp 667-685.

Silica-Iron Oxide Magnetic Nanoparticles Modified for Gene Delivery: A Search for Optimum and Quantitative Criteria
Olga Mykhaylyk, Titus Sobisch, Isabella Almstätter, Yolanda Sanchez-Antequera, Sabine Brandt, Martina Anton, Markus Döblinger, Dietmar Eberbeck, Marcus Settles, Rickmer Braren, Dietmar Lerche, Christian Plank, *Pharm Res*, 2012, 29, pp 1344-1365.

Conference talk

Characterization of magnetic viral vectors by magnet resonance imaging
Isabella Almstätter, Olga Mykhaylyk, Jennifer Altomonte, Marcus Settles, Christian Plank, Rickmer Braren, *NIM/iNano Winterschool 2013*, 03/2013, Kirchberg, Tyrol, Austria

Scientific Posters

Magnetic Particle Spectroscopy Characterization of the Assemblies of Magnetic Nanoparticles
Olga Mykhaylyk, Dietmar Eberbeck, Norbert Löwa, Christian Knopke, Isabella Almstätter, Dialechti Vlaskou, Christian Plank, Rickmer Braren, Lutz Trahms, *5th International Workshop on Magnetic Particle Imaging*, 03/2015, Istanbul, Turkey

Optimization of oncolytic virus/magnetic-nanoparticle-complexes for tumor therapy
Florian Wille, Olga Mykhaylyk, Jennifer Altomonte, Juliane Dworniczak, Isabella Almstätter, Ernst Rummeny, Oliver Ebert, Christian Plank, Rickmer Braren, *4th International Workshop on Magnetic Particle Imaging*, 03/2014, Berlin, Germany

Characterization of magnetic viral vectors by magnet resonance imaging
Isabella Almstätter, Olga Mykhaylyk, Jennifer Altomonte, Marcus Settles, Christian Plank, Rickmer Braren, *NIM-GP Summer Retreat*, 08/2013, Fall, Germany

Characterization of magnetic viral vectors by magnet resonance imaging
Isabella Almstätter, Olga Mykhaylyk, Jennifer Altomonte, Marcus Settles, Christian Plank, Rickmer Braren, *NIM/iNano Winterschool 2013*, 03/2013, Kirchberg, Tyrol, Austria

Theranostische Tumortheraphie
Isabella Almstätter (representative for the "Nanosystems Initiative Munich" NIM), *Wissenswerte 2012*, 11/2012, Bremen, Germany

Characterization of magnetic viral vectors by magnet resonance imaging
Isabella Almstätter, Olga Mykhaylyk, Jennifer Altomonte, Marcus Settles, Christian Plank, Rickmer Braren, *6th Annual Symposium on Nanobiotechnology "Kyoto Cell-Material Integration 2012"*, 11/2012, Kyoto, Japan

Characterization of magnetic viral vectors by magnet resonance imaging
Isabella Almstätter, Olga Mykhaylyk, Jennifer Altomonte, Marcus Settles, Christian Plank, Rickmer Braren, *12th German Ferrofluid Workshop*, 09/2012, Benediktbeuern, Germany

Characterization of magnetic viral vectors by magnet resonance imaging
Isabella Almstätter, Olga Mykhaylyk, Jennifer Altomonte, Marcus Settles, Christian Plank, Rickmer Braren, *CeNS Workshop 2012*, 09/2012, Venice, Italy

Design and evaluation of a multifunctional nano-carrier system for targeted drug delivery in gastro-intestinal cancer
Isabella Almstätter, Olga Mykhaylyk, Marcus Settles, Christian Plank, Rickmer Braren, *NIM-GP Summer Retreat*, 06/2012, Garmisch, Germany

Characterization of magnetic viral vectors by MRI
Isabella Almstätter, Olga Mykhaylyk, Jennifer Altomonte, Marcus Settles, Christian Plank, Rickmer Braren, *9th International Conference on the Scientific and Clinical Applications of Magnetic Carriers*, 05/2012, Minneapolis, USA

Design and evaluation of a multifunctional nano-carrier system for targeted drug delivery in gastro-intestinal cancer
Isabella Almstätter, Olga Mykhaylyk, Marcus Settles, Christian Plank, Rickmer Braren, *9th International Conference on the Scientific and Clinical Applications of Magnetic Carriers*, 05/2012, Minneapolis, USA

Design and evaluation of a multifunctional nano-carrier system for targeted drug delivery in gastro-intestinal cancer
Isabella Almstätter, Olga Mykhaylyk, Marcus Settles, Christian Plank, Rickmer Braren, *<interact> 2012*, 02/2012, Munich, Germany